

**ROOM TEMPERATURE GAS SENSING CHARACTERISTICS OF
TITANIUM DIOXIDE NANOSTRUCTURES: EFFECTS OF
HYDROCHLORIC ACID ON THE STRUCTURE AND MAGNETIC
PROPERTIES**

By

ZAMASWAZI PORTIA TSHABALALA

(BSc. Hons)

A thesis submitted in fulfillment of the requirements for the degree

MAGISTER SCIENTIAE

in the

Faculty of Natural and Agricultural Sciences

Department of Physics

at the

University of Free State

Promoters: Dr. D.E. Motaung, Dr. G.H. Mhlongo

Prof. O.M. Ntwaeaborwa

JANUARY 2016

**“Sibonga isiphiwo, injabulo nesibusiso samaSwazi,
Masande”**

To my parents (Duma “Ludonga” Tshabalala and Puleng “Seboloka” Tshabalala), my brothers (Sibusiso, Siphiwe, Sandile and Spongashengu Tshabalala) and my sister (Banelisiwe Sinenjabulo Tshabalala).

DECLARATION

**“ROOM TEMPERATURE GAS SENSING CHARACTERISTICS OF
TITANIUM DIOXIDE NANOSTRUCTURES: EFFECTS OF
HYDROCHLORIC ACID ON THE STRUCTURE AND MAGNETIC
PROPERTIES”**

- (i) “I, Zamaswazi Portia Tshabalala, declare that the Master of Sciences Degree research thesis or interrelated, publishable manuscripts/published articles, or coursework Masters degree thesis that I herewith submit for the Master of Sciences Degree qualification at the University of the Free State is my independent work, and that I have not previously submitted it for a qualification at another institution of higher education.”

- (ii) “I, Zamaswazi Portia Tshabalala, hereby declare that I am aware that the copyright is vested in the University of the Free State.”

- (iii) “I, Zamaswazi Portia Tshabalala, hereby declare that all royalties as regards to intellectual property that was developed during the course of and /or in connection with the study at the University of the Free State will accrue to the University.”

In the event of a written agreement between the University and the student, the written agreement must be submitted in Lieu of the declaration by the student.

Signature:

Date:

.....

.....

ACKNOWLEDGEMENTS

“UJehova ungumalusi wami, Angiyikuswela”

AmaHubo 23:1

- To the most high God almighty, umqalisi nomphelelisi wempilo yami. Ngyabonga sonini nanini.
- My utmost gratitude goes to my supervisors Dr. D.E. Motaung (CSIR), Dr. G.H. Mhlongo (CSIR) and Prof. O.M. Ntwaeaborwa (UFS) for their support, guidance, commitment, belief and encouragement throughout the work.
- Sincere gratitude to my family mostly, to my dad for believing in me and teaching me that I am capable of breaking barriers, my mother’s endless prayers, my siblings my anchors for their support and understanding throughout the years and to my brother’s wife Mrs. Landiwe Tshabalala for being a sister and a friend to me.
- I am grateful to Dr. Malcolm Govender, Dr. George Chimowa and Mr. Amos Adeleke for discussions and advise with no complaints.
- My sincere gratitude to the Staff of NCNSM and Characterization team (CSIR) and Physics Department (UFS) for their support.
- I am indebted to Dr. Peter Makgwane (CSIR-NCNSM) for his constructive discussions.

- I am grateful to Dr. Thomas Malwela (CSIR-NCNSM) for SEM analysis and training.
- Mr. Lindokuhle Mdletshe (CSIR-NCNSM) for his assistance with BET and Raman measurements.
- Dr. Baban Dhonge (CSIR-NCNSM) for showing me how to carry out the gas sensing measurements.
- I am grateful to Dr. Modiehi Tshabalala (UFS) for her assistance and support.
- To Mr. Phila Kubheka, Ms. Katekani Shingange, and Ms Zamahlase Sibisi thank you for challenging me to be a better person and also for your support and friendship.
- Finally, I acknowledge the financial support of the CSIR (Project: HGER27S) and National Research Foundation (NRF).

ABSTRACT

**“ROOM TEMPERATURE GAS SENSING
CHARACTERISTICS OF TITANIUM DIOXIDE
NANOSTRUCTURES: EFFECTS OF HYDROCHLORIC ACID
ON THE STRUCTURE AND MAGNETIC PROPERTIES”**

Monitoring and detection of toxic and combustible gases such as methane in underground mining, carbon monoxide from burning coal in our homes and odourless gases such as nitrogen dioxide and sulphur dioxide in industries has become the subject of extensive scientific and technological research and this has been motivated by their harmful impact on the environment and human health. Early detection of these gases can help prevent fatal incidences such as fire, suffocation and death. Development of portable gas sensors with higher sensitivity and selectivity, fast response and recovery times, low detection limit and capability of operating at room temperature is one of the challenges facing researchers world-wide. Various materials such as semiconductor metal oxides (MOX), polymers, and carbon nanotubes have been used for gas sensing application. Among all the various materials, MOX such TiO_2 , ZnO , SnO_2 , Fe_2O_3 , WO_3 are the most preferred materials for gas sensing application due to their noticeable response to any change in electrical resistance when exposed to either reducing or oxidizing gas and also due to their unique properties such as

high stability and easy to synthesize. However, among the range of MOX semiconductors mentioned above, TiO₂ has emerged as the preferred MOX semiconductor for gas sensing application due to its remarkable features such as nontoxicity, biocompatibility, high photocatalytic activity and affordability. TiO₂ occurs in three crystalline forms namely: anatase, rutile and brookite. Anatase and rutile polymorphs are widely studied for technological applications.

Therefore, in this study, we investigated the gas sensing properties of TiO₂ nanoparticles annealed at 450 °C, and that annealed at various temperatures, as well as those doped with various concentrations of Mn. The undoped TiO₂ nanoparticles were synthesized from P25 Degussa via a simple hydrothermal method in an aqueous solution of sodium hydroxide (NaOH). The samples were washed with distilled water (H₂O) and different concentrations of hydrochloric acid (0.25, 0.5 and 1.0 M) which acted as the morphological controlling agent. TiO₂ doped with various concentration of Mn²⁺ were washed using 1.0 M HCl. To investigate the effect of hydrochloric acid (HCl) as a washing agent on the structure, morphology, optical, magnetic and gas sensing properties, x-ray diffraction (XRD), Raman spectroscopy, transmission electron microscopy (TEM), scanning electron microscopy (SEM), photoluminescence (PL) spectroscopy, electron paramagnetic resonance (EPR) spectroscopy, X-ray photoelectron spectroscopy (XPS), Brunauer-Emmett-Teller (BET) and Kinosistec gas sensor testing system were used for characterization. Microscopy analysis showed that the sizes of the pure TiO₂ nanoparticles were reduced when increasing the HCl concentration indicating that the particle sizes could be easily tailored and tuned

by adjusting the HCl concentration. Structural analyses revealed a phase transformation from a mixture of anatase and rutile phases to pure anatase phase at higher HCl concentration. The PL, XPS, EPR and BET analyses disclosed that the 1.0 M sample contained relatively high concentration of oxygen vacancy, Ti^{4+} and Ti^{3+} interstitial defects and it also had higher surface area which played an important role in transforming the sensing properties, resulting in higher sensing response, sensitivity and selectivity to NO_2 at room temperature.

Furthermore, the effect of thermal annealing was investigated on the structural and gas sensing properties of the pure TiO_2 nanoparticles washed with H_2O and HCl, and annealed at different temperatures (300, 450, 700 °C) in air. Surface morphology analyses revealed that the nanoparticles transformed to nanorods after annealing at 700 °C. The results showed that the sensing properties are dependent on annealing temperature. The 1.0 M TiO_2 nanostructures annealed at higher temperatures (700 °C) revealed improved sensing response to CH_4 gas at room temperature due to higher surface area of $180.51\text{ m}^2\text{g}^{-1}$ and point defects related to Ti^{3+} observed from EPR and PL analyses. In addition, the 1.0 M TiO_2 sensing material annealed at 700 °C also revealed an interstitial defect states which played a vital role in modulating the sensing properties.

To improve sensitivity, selectivity and stability of the gas sensing materials, various concentrations (1.0, 1.5, 2.0, 2.5 and 3.0 mol % denoted as S1, S2, S3, S4 and S5, respectively) of Mn-ions were loaded on the TiO_2 particles. The nanoparticles were characterised in detail using various analytical

techniques. XRD analysis showed that the structure of both pure and Mn-doped TiO_2 was tetragonal and no peaks corresponding to Mn or impurities were observed. Raman spectroscopy revealed quenching and peak broadening due to lattice disorder with increasing concentration of Mn. Optical studies revealed that the Mn loaded TiO_2 nanoparticles have enhanced UV-Vis emission and a broad shoulder at 540 nm denoting defects induced by substitution of Ti^{4+} ions by Mn^{2+} . The XPS and the EPR results revealed the presence of Ti^{4+} , Ti^{3+} and single ionised oxygen vacancies in both pure and Mn loaded nanoparticles. Additionally, a hyperfine split due to Mn^{2+} ferromagnetic ordering was observed confirming incorporation of Mn ions into the lattice. Gas sensing studies revealed that Mn^{2+} loaded TiO_2 surface improved the NO_2 and NH_3 sensing performances in terms of response and selectivity. The S1 (1.0 mol. % Mn) demonstrated an improved sensitivity of approximately 85.39 ppm^{-1} at 20 ppm NH_3 gas at room temperature.

Our findings showed that, the thermal annealing and Mn doping improve the sensitivity and selectivity and stability of the gas sensing materials. The results also validated that our sensing materials are highly sensitive and selective to CH_4 , NO_2 and NH_3 at room temperature. The observed room temperature response in this work, suggests that these TiO_2 nanostructures are possible candidates for gas sensing application in work places, mining sectors, etc. Moreover, the findings in this work give a possible solution to the issue of energy consumption of metal oxide gas sensors.

KEYWORDS

**“ROOM TEMPERATURE GAS SENSING
CHARACTERISTICS OF TITANIUM DIOXIDE
NANOSTRUCTURES: EFFECTS OF HYDROCHLORIC ACID
ON THE STRUCTURE AND MAGNETIC PROPERTIES”**

Titanium dioxide

Nanoparticles

Hydrochloric acid

P25 Degussa

Gas sensing

Structure

Morphology

Nanorods

Annealing

Oxidation gases

Reducing gases

Selectivity

Sensitivity

Stability

Magnetic

LIST OF ARTICLES INCLUDED IN THIS THESIS

- [1] Z.P. Tshabalala, D.E. Motaung, G.H. Mhlongo, O.M. Ntwaeaborwa, Facile synthesis of improved room temperature gas sensing properties of TiO₂ nanostructures: Effect of acid treatment

Sensors and Actuators B: Chemical 224 (2016) 841–856.

- [2] Z.P. Tshabalala, D.E. Motaung, G.H. Mhlongo, K. Shingange, O.M. Ntwaeaborwa, Fabrication of ultra-high sensitive and selective CH₄ room temperature gas sensing of TiO₂ nanorods: Detailed study on the annealing temperature

Sensors and Actuators B: Chemical (2016) Revised.

- [3] Z.P. Tshabalala, D.E. Motaung, G.H. Mhlongo, O.M. Ntwaeaborwa Selective Detection of Enhanced Room Temperature NO₂ and NH₃ gas Sensing Using Mn-doped TiO₂ Nanoparticles

Journal of Physical Chemistry C (2016) Submitted.

CONTENTS

| | |
|---------------------------------------------------|-----------|
| LIST OF ARTICLES INCLUDED IN THIS THESIS | 12 |
| CHAPTER ONE | 17 |
| BACKGROUND OF GAS SENSORS | 17 |
| 1.1. BRIEF HISTORY ON GAS SENSING..... | 17 |
| 1.2. EXAMPLES OF GASES..... | 18 |
| 1.3. GLOBAL DEMAND FOR SENSORS | 20 |
| 1.4. CLASSIFICATION OF GAS SENSORS..... | 20 |
| 1.5. CHARACTERISTICS OF A SENSOR..... | 22 |
| 1.6. SEMICONDUCTING METAL OXIDE GAS SENSORS | 24 |
| 1.6.1. Size and Dimension | 27 |
| 1.6.2. Surface Modification by Additives..... | 29 |
| 1.6.3. Sensing Mechanism..... | 31 |
| 1.7. AIMS AND OUTLINES..... | 36 |
| 1.7.1. Problem Statement and Novelty | 36 |
| 1.7.2. Objectives of Study | 37 |
| 1.7.3. Thesis Outline | 38 |
| 1.8. REFERENCES..... | 40 |
| CHAPTER TWO | 44 |
| LITERATURE REVIEW | 44 |

| | | |
|----------------------------|-------------------------------------------------------------|-----------|
| 2. | INTRODUCTION..... | 44 |
| 2.1. | BULK PROPERTIES OF TiO ₂ | 44 |
| 2.1.1. | Structural Properties of TiO ₂ | 45 |
| 2.1.2. | Surface properties of TiO ₂ | 48 |
| 2.1.3. | Electrical and Optical properties of TiO ₂ | 49 |
| 2.1.4. | Magnetic properties of TiO ₂ | 51 |
| 2.1.5. | Gas sensing properties of TiO ₂ | 52 |
| 2.2. | REFERENCES..... | 55 |
| CHAPTER THREE | | 59 |
| 3.1. | INTRODUCTION..... | 59 |
| 3.2. | X-RAY DIFFRACTION | 59 |
| 3.3. | RAMAN SPECTROSCOPY | 62 |
| 3.4. | ELECTRON MICROSCOPY | 65 |
| 3.4.1. | Scanning Electron Microscope | 65 |
| 3.4.2. | Transmission Electron Microscope | 68 |
| 3.5. | PHOTOLUMINESCENCE SPECTROSCOPY | 70 |
| 3.6. | ELECTRON PARAMAGNETIC RESONANCE | 72 |
| 3.7. | BRUNAUER-EMMETT-TELLER | 76 |
| 3.9. | X-RAY PHOTOELECTRON SPECTROSCOPY | 78 |
| 3.10. | GAS TESTING STATION..... | 81 |
| 3.11. | EXPERIMENTAL DETAILS | 84 |
| 3.11.1. | Materials and Chemicals..... | 84 |

| | |
|--------------------------------------------------------------------|------------|
| 3.11.2. Synthesis procedure of TiO ₂ nanoparticles..... | 85 |
| 3.12. REFERENCES..... | 86 |
| CHAPTER FOUR | 88 |
| 4.1. INTRODUCTION..... | 89 |
| 4.2. EXPERIMENT DETAILS..... | 91 |
| 4.2.1. Materials and Chemicals..... | 91 |
| 4.2.2. Synthesis procedure of TiO ₂ nanoparticles | 92 |
| 4.2.3. Sensor fabrication and testing of devices | 92 |
| 4.2.4. Characterization Techniques | 93 |
| 4.3. RESULTS AND DISCUSSION..... | 94 |
| 4.3.1. EFFECT OF ACID TREATMENT | 94 |
| 4.4. CONCLUSIONS..... | 130 |
| 4.5. ACKNOWLEDGEMENTS | 131 |
| 4.6. REFERENCES..... | 132 |
| CHAPTER FIVE..... | 137 |
| 5.1. INTRODUCTION..... | 138 |
| 5.2. EXPERIMENT DETAILS..... | 141 |
| 5.2.1. Synthesis procedure of TiO ₂ nanostructures..... | 141 |
| 5.2.2. Sensor fabrication and testing of devices | 142 |
| 5.2.3. Characterization Techniques | 142 |
| 5.3. RESULTS AND DISCUSSION..... | 143 |

| | | |
|----------------------------------------|----------------------------------------------------------------------|------------|
| 5.4. | CONCLUSION | 178 |
| 5.5. | ACKNOWLEDGEMENTS | 179 |
| 5.6. | REFERENCES..... | 180 |
| CHAPTER SIX..... | | 185 |
| 6.1. | INTRODUCTION..... | 186 |
| 6.2. | EXPERIMENTAL DETAILS..... | 188 |
| 6.2.1. | Preparation of pure and Mn-doped TiO ₂ nanoparticles..... | 188 |
| 6.2.2. | Characterization..... | 189 |
| 6.3. | RESULTS AND DISCUSSION..... | 191 |
| 6.3.1. | Structural analyses | 191 |
| 6.3.2. | Surface Morphology..... | 198 |
| 6.3.3. | BET Surface area analysis | 199 |
| 6.3.4. | Photoluminescence analysis..... | 201 |
| 6.3.5. | X-ray photoelectron spectroscopy analysis..... | 204 |
| 6.3.6. | Electron paramagnetic resonance analysis | 207 |
| 6.3.7. | Gas sensing analysis | 208 |
| 6.4. | CONCLUSION | 221 |
| 6.5. | ACKNOWLEDGEMENTS | 222 |
| 6.6. | REFERENCES..... | 223 |
| SUMMARY AND CONCLUSION..... | | 227 |

CHAPTER ONE

BACKGROUND OF GAS SENSORS

1.1. BRIEF HISTORY ON GAS SENSING

International Union of Pure and Applied Chemistry (IUPAC) define a chemical sensor as a device that transforms chemical information, ranging from the concentration of a specific sample component to the total composition analysis into an analytical useful signal [1.1]. Gas sensors can be used to detect leakages and fire and can also be used as an alarm device giving warning of the presence of hazardous gases in a work places, planes, cars and homes by monitoring changes in ambient air [1.1, 1.2]. Additionally, gas sensors are also used in food processing and storage companies, whereby they monitor and detect volatile organic compounds (VOCs) released by spoilt food [1.2]. Gas sensors are used in environmental sectors to monitor pollution that involves, for example, the release of greenhouse gases like carbon [1.2, 1.3]. Medical sector use gas sensors for early detection of diseases such as diabetes and cancer by breath analysis [1.2]. The automobile sector uses gas sensors to monitor gasoline vapour and the car ventilation [1.4]. Industrial sector uses gas sensors during and after production to ensure safety of the employees during processes such as mining, fermentation control, gas production and storage laboratories [1.5, 1.6]. Indoors air control is important in order to prevent cases of suffocation for example due to carbon monoxide (CO) [1.7].

1.2. EXAMPLES OF GASES

It is well known that some gases are a health hazard and when inhaled for longer periods they can result in death while other gases can pollute the air thereby contributing to global warming. Examples of these gases are carbon monoxide (CO), carbon dioxide (CO₂), nitrogen (N), nitrous oxide (N₂O), hydrogen sulfide (H₂S), ammonia (NH₃), chlorofluorocarbons (CFCs) and flammable gases such as methane (CH₄) [1.1- 1.7]. Monitoring such gases can help to prevent occurrences of fatal accidents such as fire and explosions.

When nitrogen oxides (NO_x, where $x \leq 2$) reacts with volatile organic compounds in the atmosphere in the presence of sunlight they form photochemical smog, contributing to air pollution that could leave people exposed to diseases such as damaged lung tissue, lung cancer, asthma, bronchitis and other respiratory diseases. Exposure to a large concentration can cause premature deaths [1.7, 1.8]. It is well known that 1 ppm of nitrogen oxide (NO) in air can be oxidized to NO₂. NO is produced during combustion when nitrogen and oxygen in the air reacts at high temperatures, during combustion in exhausts and vehicle engines and power station boilers burning coal and oil. They are also produced naturally by lightning and agricultural fertilization. When exposed to moisture nitric acid can form resulting acid rain. NO_x also contribute to ozone depletion in the stratosphere.

Carbon dioxide (CO₂) is a naturally occurring greenhouse gas. It is also a by-product of burning carbon based fuels like oil, wood, coal, hydrocarbons and

respiration of humans and animals. CO_2 is mostly used by green plants for photosynthesis. Excess of CO_2 contributes to global warming. Concentration of CO_2 in air is about 360-390 ppm. An increase in concentration can cause dizziness, blurry vision, suffocation and loss of consciousness **[1.8]**. Carbon monoxide (CO) is produced mainly from oxidation of carbon containing compounds and burning of coal. CO poses a great threat to human health and the environment. It is highly toxic and high exposure can cause fatal poisoning. CO can stop oxygen delivery into body tissues resulting in seizures and death **[1.7- 1.9]**.

Oxygen is a naturally occurring gas that supports life on earth. Plants and animals need it for respiration, but breathing air mixed with oxygen with partial pressure greater than 60 kPa can lead to permanent pulmonary fibrosis. High concentration of oxygen promotes combustion and explosions can easily start fires in mines when there is heat or a spark **[1.7]**. Hydrogen sulfide (H_2S) is a very toxic, corrosive, flammable and explosive gas. When dissolved in water or moist environment it forms a hydrosulfuric acid. H_2S occur naturally in human body as a waste product. Exposure to H_2S greater than 10 ppm can cause poisoning to various human organs like the nervous system, eye irritation, sore throat and pulmonary edema and death **[1.10]**.

1.3. GLOBAL DEMAND FOR SENSORS

As seen in [1.11], in 2009 an industrial market report in the United States of America (USA) reported that the demand for sensors increased with an annual average growth rate of 4.6% from 2004 [1.12]. Implementations of occupational health and safety standards are becoming compulsory in many countries; this act will positively influence the demand for gas sensors. Global gas sensors, detectors and analysers market 2013 reported that the market size for gas sensors was \$1,782.1 M in 2013, a Compound Annual Growth Rate (CAGR) of 5.1% is expected by 2020 [1.13].

1.4. CLASSIFICATION OF GAS SENSORS

Gas sensors consist of the sensitive layer, substrate, electrode and heater. A schematic is shown in Fig. 1.1. The sensitive layer is deposited on the substrate and interacts with the target gas. Changes caused by the presence of the analyte are measured by the electrode and displayed as an analytical signal that can be interpreted. The heater regulates the working temperature of the sensor. The material used as sensitive layer determines the working principle and type of gas sensor and the sensor performance is measured in terms of change in chemical or physical property of the sensitive layer. Table 1 lists the type of gas sensors in terms of sensitive material.

Table 1: Classification of gas sensors [1.1- 1.3, 1.5].

| | Sensitive layer | Measured property |
|----------|---------------------------|----------------------------------------------------------|
| 1 | Semiconductor metal oxide | Electrical conductivity |
| 2 | Optical sensor | Absorbance, luminescence, fluorescence, refractive index |
| 3 | Field effective | Work function |
| 4 | Calorimetric | Heat, temperature |
| 5 | Piezoelectric | Mass |
| 6 | Electrochemical | Electromotive force |

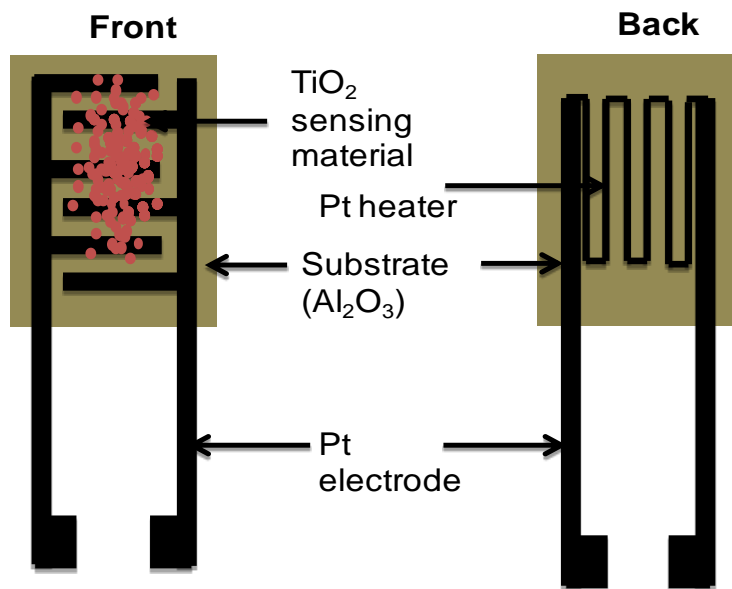


Fig. 1.1: Schematic diagram of a sensing strip deposited with a TiO_2 nanoparticles.

1.5. CHARACTERISTICS OF A SENSOR

Challenges that researchers aim to overcome are response, sensitivity, selectivity, stability and low working temperature. Below are characteristics that determine the performance of the sensing device [1.1- 1.5, 1.14, 1.15].

- Response; the sensor response (R) is defined as the ratio of the resistance change by introducing target gas in the air. When the n-type semiconducting metal oxide material is exposed to a reducing gas (equation 1.1a), the sensing resistance decreases, and when it is exposed to an oxidizing gas (equation 1.1b), the resistance of the sensor increases.

$$R(\%) = \left(\frac{R_{\text{air}}}{R_{\text{gas}}} \right) \times 100 \quad (\text{for reducing gas}) \quad (1.1a)$$

and

$$R(\%) = \left(\frac{R_{\text{gas}}}{R_{\text{air}}} \right) \times 100 \quad (\text{for oxidizing gas}) \quad (1.1b)$$

where, R_{gas} is the sensor resistance when exposed to a target gas and R_{air} is the resistance of the sensor in air. As depicted in Fig. 1.2, as the gas is injected in the chamber, the resistance increases, and when the gas is released from the chamber the resistance decreases.

- Response time is the time taken for a sensor to respond to certain gas concentration.

- Recovery time is the time taken for sensor to recover back to initial state after removal of target gas.
- Sensitivity is the minimum amount in terms of concentration of target gas that can be detected. The sensitivity (S) is given by the relationship: $S = \left(\frac{R_{\text{gas}} - R_{\text{air}}}{R_{\text{air}}} \right)$.
- Selectivity is the ability of a sensor to respond to a certain group of target gases or towards a specific one.
- Working temperature is the amount of temperature needed to heat the sensor thus resulting to maximum response.
- Detection limit (LoD) is the minimum amount of gas concentration that can be detected by the sensor and is given by: $\text{LoD} = 3 \left(\frac{\text{Noise}_{\text{rms}}}{S} \right)$.
- Stability is the ability of the sensor to resist change whether in phase due to heat or segregation of dopants and chemical change due to poisoning during reactions.
- Life time is the period at which the sensor will remain operational.

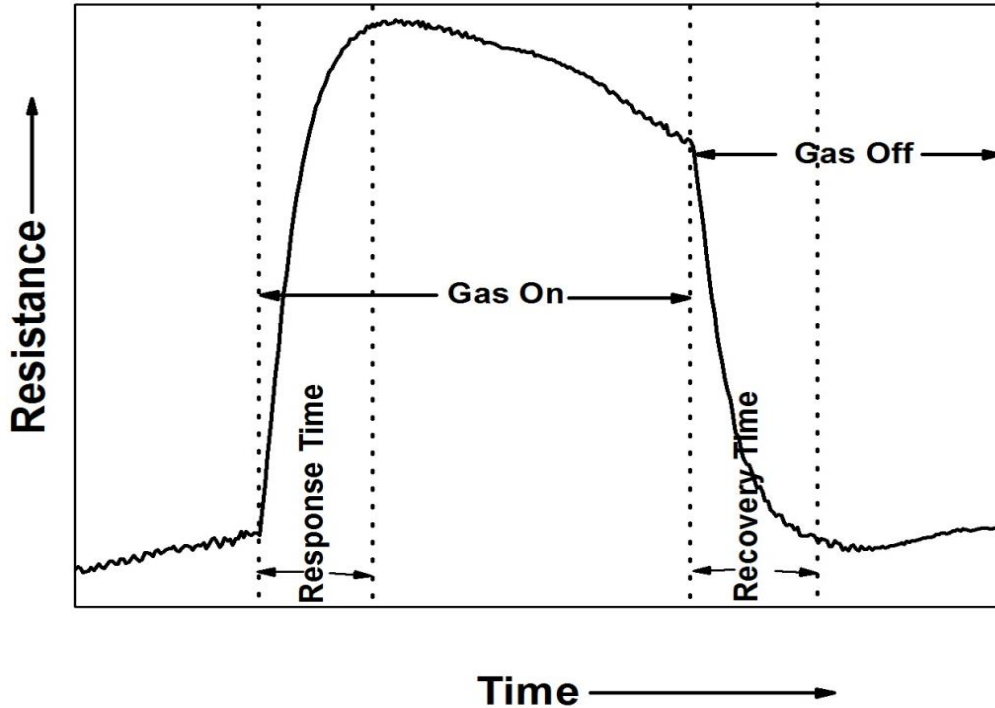


Fig 1.2: A typical resistance curve versus time of a gas sensing material.

1.6. SEMICONDUCTING METAL OXIDE GAS SENSORS

Up to date, a great deal of research has been directed towards developing portable gas sensing devices for industrial and domestic applications. Highly sensitive gas sensors that are able to detect hazardous and explosive gases at low ppm or ppb level concentration with a low working temperature to ensure less energy consumption are required. Among all the materials, metal-oxides semiconductors (MOX) appears to be the most promising materials for gas sensing due to their diverse applications in various fields such as spintronics , solar cells, photo-catalysis, gas sensors, etc. [1.3- 1.6, 1.16, 1.17]. This is due to the fact that they have a good thermal stability and can operate at high

temperatures and harsh environment [1.9-1.11, 1.14, 1.15]. The structure and morphology of metal oxides can be controlled by varying their electrical, chemical, optical and magnetic properties. Additionally, MOXs can be used in many types of gas sensors like chemiresistor, electrochemical, heterostructural, Schottky diode and surface Plasmon resonance sensors [1.18]. Such materials have different electro physical, optical, and chemical characteristics. These properties can be manipulated to enhance the performance of the sensor. MOX change their electrical resistance when in contact with an oxidising or reducing gas [1.1- 1.15].

MOXs have attracted attention of many researchers ever since 1952 where Brattain *et al.* [1.19] demonstrated a change in resistivity of germanium (Ge) with respect to the environment (mixture of gases) it was exposed to. Later, in 1962 Seyama *et al.* [1.20] reported a change in electrical conductivity of a ZnO thin film exposed to propane at 485 °C. To enhance the selectivity and sensitivity, Shaver [1.21] in 1967 explained the effect of noble metals on the electrical properties of the MOX. In 1971, Taguchi [1.22] succeeded to use SnO₂ as sensitive material and was the first to develop a chemoresistive gas sensing device. The devices were used as fire alarms by monitoring the presence of combustible and explosive gases.

Since the 1980s we have seen an intense growth in metal oxide gas sensors research with the aim of fabricating a highly sensitive, selective, stable and long life time, short response and recovery time, and low energy consumption gas sensor. A wide range of MOXs are being studied and different

synthesis methods are explored. MOXs such as SnO₂, ZnO, WO₃, In₂O₃, V₂O₅, Cr₂O₃, Fe₂O₃, TiO₂ and CuO are sensitive and electrical conductive when exposed to oxidizing and reduction gases like NO_x, O₂, CO, CO₂, CH₄, NH₃, H₂, H₂S [1.1-1.22]. SnO₂ is one of the mostly studied MOXs for gas sensing followed by ZnO (see Fig. 1.3). SnO₂ is sensitive to a large range of gases, thus rendering it less selective and has high working temperatures which require high energy consumption thus high cost [1.3]. Fig. 1.3 compares MOX that are mostly used in gas sensing.

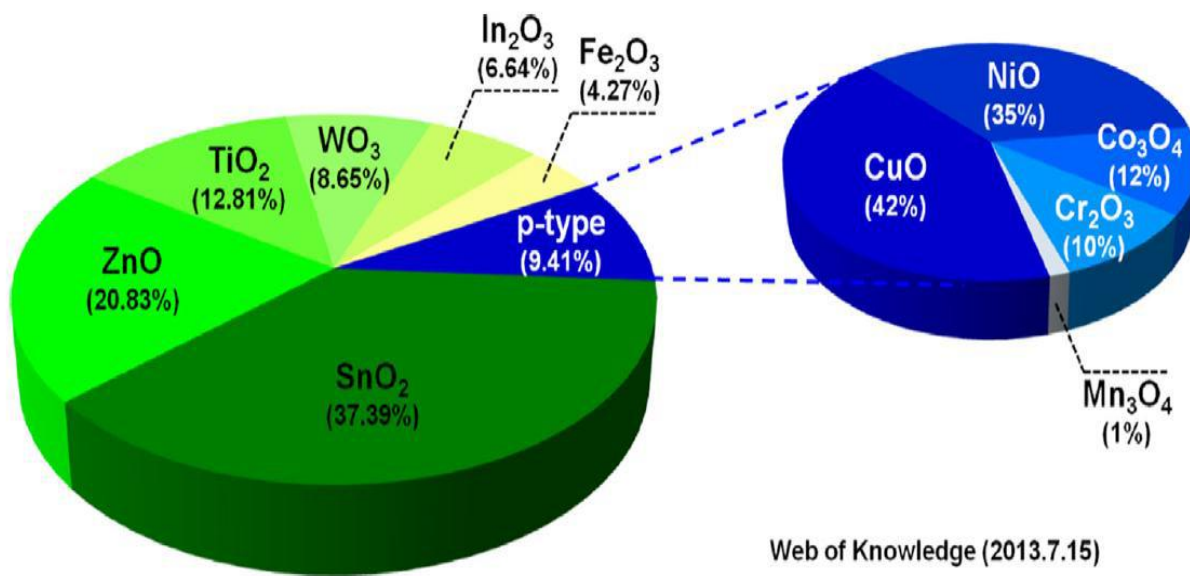


Fig 1.3: The most studied n-type and p-type MOX for gas sensor applications since 2002 to 2013 [1.5].

Factors such as structure, morphology and surface states influence the sensing layer and thus the sensor performance [1.1- 1.5]. Disadvantages of MOX

sensing material include high working temperatures, instability and cross-sensitivity [1.14- 1.22]. The working temperature of the sensor influences the sensor response if the sensitive layer requires heating in order for the gas molecules to be adsorbed on the surface of the sensing layer, such requirements increases the cost of the sensor due to high energy consumption [1.2, 1.15,]. An unstable MOX undergo phase transition at high temperature and also sensor poisoning during chemical reaction with target gas which negatively influences the sensor performance [1.2, 1.15]. Cross - sensitivity is when a sensor is sensitive to humidity and more than one gas in the environment, the sensor become less selective due to interference of the gases [1.2, 1.15].

1.6.1. Size and Dimension

By manipulating the grain size during synthesis of a material we can enhance the sensor's sensitivity. For a material with grain size (D) greater than two times the thickness (L) of the surface charge layer ($D \gg 2L$), the Schottky barriers limit the electrical conductivity resulting in poor response. Small crystallite size does not imply good sensitivity. However there is an optimum crystal size where the grain size is less than two times the thickness ($D \ll 2L$) of the surface charge layer. In this material every grain in the material is involved in space charge layer and the charge on the particle surface influences electron transport [1.1, 1.5]. A number of reports on nanomaterials reveal an enhanced sensitivity of MOX gas sensors with small grain sizes [1.1, 1.5, 1.23, 1.24]. The smaller grain sizes provide a larger surface area for the reaction to occur and

also reduce surface charge density. In this scale the chemical and electronic properties of the MOX are different from that at bulk scale. Lu *et al* [1.25] reported an enhanced response towards 500 ppm CO on SnO₂ based sensor with particle size less than 10 nm.

The sensing mechanism of MOX depends on various parameters such as the structure of the materials, effective surface area, etc. Thus the advantage of MOX is that they can be synthesised in different crystal sizes and dimension with high surface to volume ratio favourable for gas adsorption. Nanostructures such as nanospheres, nanotubes, nanorods, nanowires, nanoribbons, thin films and core/shell heterostructure have displayed enhanced properties and vast applications [1.15, 1.26, 1.27]. Nanotubes have large specific surface area which helps enhance the photocatalytic activity [1.28], Nanorods, nanowires, nanobelts and thin films have a good crystalline structure and are used in dye synthesised solar cell application [1.29]. A larger surface to volume ratio provided by the nanotubes, nanorods, and nanowires enhances the surface activity and reduce the activation energy of surface chemisorbed oxygen gas thus leading to the enhancement of target gas adsorption [1.30]. Nanoparticles thin films have a large effective surface area for adsorption of dye and solar energy and for gas sensing. The successful synthesise of these nanostructures has shown great impact in gas sensor fabrication and sensor performance [1.31, 1.32]. These nanostructures can be arranged in three different ways (as shown in Fig 1.4) during sensor fabrication namely [1.26] :

- Single nanostructure arrangement: a single nanowire, nanofiber or nanotube is used as sensitive layer. Each end of the nanowire is connected to an electrode using a focused ion beam.
- Aligned arrangement: nanostructure arrays grown on substrate of film. They can be vertically or horizontally aligned. and
- Random arrangement: Nanostructures are randomly distributed on a film.

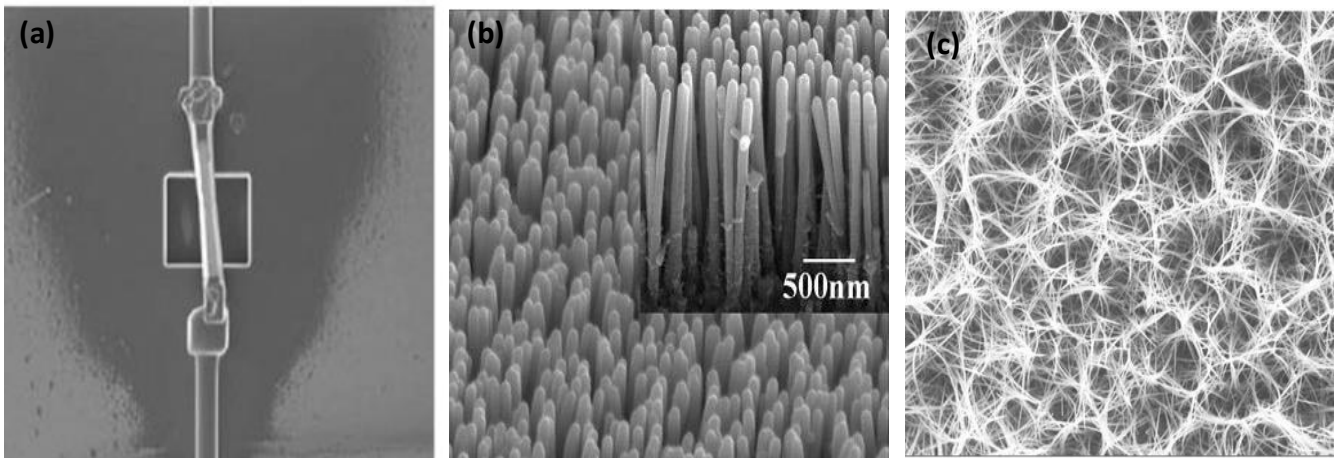


Fig 1.4: SEM images showing different arrangements of nanostructures in a sensing material. (a) Single nanostructure, (b) Aligned arrangement and (c) Random arrangement. [1.33- 1.35].

1.6.2. Surface Modification by Additives

Various ways of modifications such as dye sensitization and introducing dopants into the metal oxide have been used to modify the surface and properties of the material such as electronic properties. Moreover, previous reports have indicated that one promising approach to improve conductometric

MOX sensors is to use a mixture of MOX as composite sensor material. Since, they contain different electronic structure and chemical properties which can result in higher sensitivity and selectivity compared to the individual constituent of MOX [1.16, 1.17]. Metal oxides are doped to develop dilute magnetic semiconductor (DMS) used in applications such as spin-based light-emitting diodes, sensors and transistors [1.36]. For solar cell applications, wide band gap metal oxides like ZnO and TiO₂ are doped in order to narrow the band gap. The dopants introduce new energy states forbidden band enabling absorption of a wider range of the electromagnetic spectrum thus increasing the efficiency of the material [1.37]. Addition of dopants on the surface or volume of the metal oxide based gas sensor can substantially improve sensitivity and/or the temperature where maximum response is obtained [1.38]. Furthermore, factors such as dopant distribution and homogeneity, crystallite size, and oxidation state, influence the sensor performance.

Additives like noble metals (Pt, Ag, Pd and Au) and transitional metals (Cr, Mn, Fe, Co, Cu and Ni) can be incorporated in the MOX as dopants (≤ 1 mol %), supported in the MOX (> 1 mol %) and or decorated (deposited on the surface of the MOX). Transitional metal oxides have a partially filled d sub-shell electronic configuration [] ns² () d^m [1.39]. This partially filled level allows charge transfer from transitional metal to metal oxide surface thus resulting in enhanced conductivity. They can help to enhance photoactivity of the material by narrowing the band gap and simultaneously maintain strong redox potential [1.40]. Ahmed *et al.* [1.30] studied Mn doped ZnO nanorods for oxygen gas sensing at room

temperature. When compared to the undoped ZnO nanorods, the Mn doped nanowires displayed high sensitivity toward oxygen at room temperature as compared to undoped ZnO. They attributed the enhanced sensitivity to the reduction of rod diameter and a larger surface to volume ratio achieved by adding the Mn ions to ZnO.

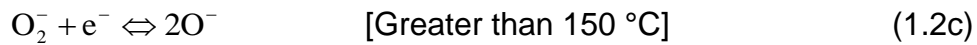
1.6.3. Sensing Mechanism

Gas sensing is a surface phenomenon and metal oxides are favourable for this process because they are non-stoichiometric with oxygen vacancies as dominant defects and also the interaction between target gas and oxide surface is reversible [1.2, 1.5]. The sensing mechanism of metal oxide gas sensors was first reported by Wolkestein [1.41] in 1961 based on electron theory of chemisorptions and catalysis. The conditions for electric charge transportation in a semiconductor exposed to target gases were later reported by Morrison (1982) [1.42], Yamazoe *et al.* (1983) [1.43] and Gopel *et al.* (1995) [1.44] and following their theories we can explain the gas sensing mechanism in semiconductor metal oxides.

There are two types of semiconductors namely: the n-type and p-type semiconductor. An n-type semiconductor (SnO_2 , ZnO, In_2O_3 , and TiO_2) has electrons as dominant charge carriers while in a p-type semiconductor (CuO , TeO_2) holes are majority charge carriers [1.27]. When these materials, both n-type and p-type, are exposed to reductive or oxidative target gas a change in resistance (either increase or decrease) is observed (as shown in Fig. 1.5). The

reaction is governed by REDOX reaction where reducing gases (H₂, CO, CH₄) donate electrons and oxidative gases (O₃, CO₂, NO₂) accept electrons from the metal oxides [1.3].

When metal oxides are exposed to ambient air, oxygen molecules are adsorbed on the surface. The O₂ is chemisorbed by accepting an electron (e⁻) from the conduction band of the metal oxide as shown in the equations (1.2 (a-d)) below and Fig. 1.5. At temperatures less than 150 °C ionized molecular (O₂⁻) dominates and at elevated temperatures greater than 150 °C atomic species (O⁻, O²⁻) dominate the surface [1.1- 1.5, 1.14, 1.15, 1.41- 1.47]. The presence of this species results into formation of depletion layer which restricts the flow of electrons and thus an increase in resistance.



When an n-type semiconductor is exposed to a reducing gas, the gas molecules are adsorbed on the surface and they react with the chemisorbed oxygen ions and donate electrons into the metal oxide as shown in equations (1.3a - 1.4b) and Fig. 1.5. The concentration of electrons will increase and the depletion layer becomes thinner restoring the flow of charge and thus decreasing

electrical resistance. With oxidising gases the opposite happens (see equations (1.5a - 1.6b)), the target gas reacts with the chemisorbed oxygen ions on the surface and extracts electrons. The depletion layer increases as there is less electron flow and the electrical resistance increases further. In the case of p-type semiconductor metal oxides exposed to reducing gas the electrical resistance increases. When exposed to oxidising gas electrical resistance decreases [1.1-1.5, 1.14, 1.15, 1.41- 1.47].

In the presence of reducing gases such as H₂ or CO [1.47, 1.48]:



In the presence of oxidizing gases such as CO₂ or NO₂ [1.47-1.50].



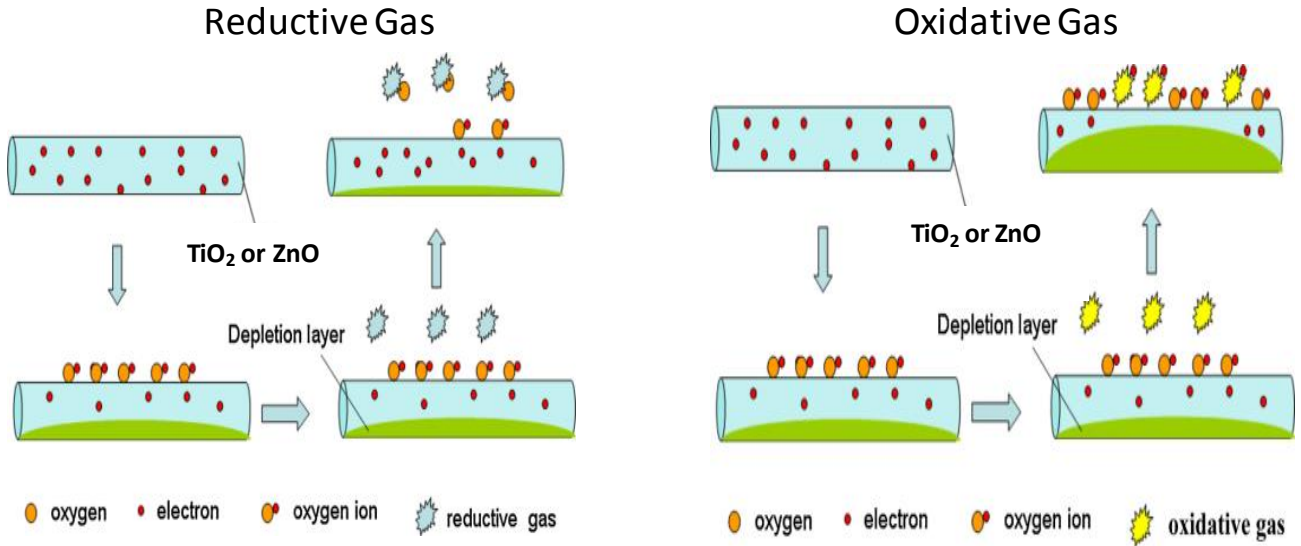


Fig. 1.5: Schematic diagram of sensing mechanism of TiO_2 or ZnO nanorods when exposed to a reducing (or reductive) gas or oxidizing (oxidative) gas [1.46].

Fig. 1.6a and b shows the importance of size and dimension in a gas sensing performance. Generally, gas sensors are strongly dependent on size and geometry of the crystallites and their interconnectivity. Yamazoe *et al.* [1.51] demonstrated that nanostructures with smaller crystallites size (L), that are smaller than the Debye length, typically of the order of 10-15 nm, show significant improvement on the sensor performance or sensitivity (see Fig. 1.6b).

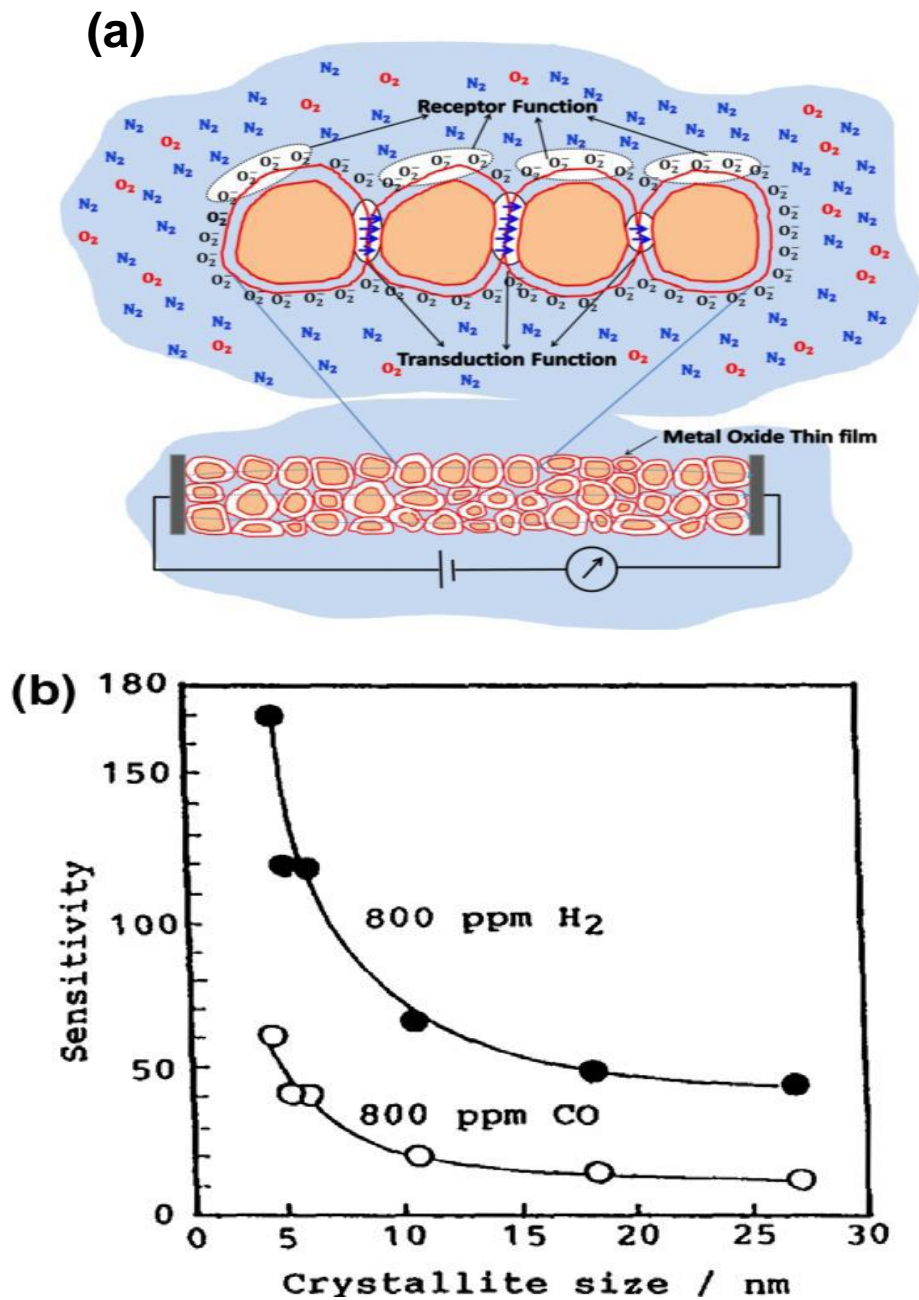


Fig. 1.6: (a) Schematic diagram illustrating the sensing mechanism of a metal oxide, and (b) plot depicting the effect of crystallite size on the sensitivity of nanocrystalline SnO₂ gas sensors [1.47, 1.48].

The thickness of the space charge region acts as a potential barrier in the electron conduction process between the grains, a thinner space region promotes charge flow over a small period thus quick response time and an enhanced sensor response and sensitivity. Advances of nanotechnology play a major role in the development of gas sensors as they enable scientists to synthesize metal oxides with crystallite size meeting these conditions.

1.7. AIMS AND OUTLINES

1.7.1. Problem Statement and Novelty

Monitoring and detection of toxic and combustible gases in residential areas and different workplaces like industry and mining environment has generated interest in the past decade. Therefore, sensors with high selectivity, sensitivity, with long term stability and that can operate at room temperature are required. Currently, gas sensors employing metal oxide (MOX) semiconductors are receiving more attention, due to their noticeable change in electrical resistance when exposed to either reducing or oxidizing gas. However, despite many successes that have been obtained, there are few reports on gas sensors operating at room temperature with high selectivity and sensitivity. Moreover, there are limited reports on the comparison between magnetization and gas sensing based on TiO_2 nanostructures; both undoped and doped with transitional metals prepared using a simple hydrothermal microwave assisted method. Furthermore, there are no reports on the room temperature CH_4 gas sensing of TiO_2 nanostructures. Therefore, in this dissertation, we report probably for the

first time the room temperature CH₄ gas sensing of pure TiO₂ nanostructures, and without any use of UV-light or dopants. In addition, we have shown previously, that in a TiO₂ structure, anatase phase is more active than the rutile phase. However, in this work, the 1.0 M sample annealed at 700 °C with 30 % rutile content shows an increase in response towards CH₄ and NO₂ gas compared to pure anatase sample (annealed at 450 °C). In this work, the structure, magnetic and gas sensing properties of TiO₂ and the effect of doping with transitional metals were investigated. The issue of energy consumption of metal oxide gas sensors with high working temperature is still unresolved hence the TiO₂ nanostructures prepared in this work display potential solutions.

1.7.2. Objectives of the Study

Objectives of this study:

- Synthesis of the TiO₂ nanostructures using the microwave assisted hydrothermal method
- Study the effect of annealing temperature
- Evaluate effects of surface modification of TiO₂ with Mn,. Comparison of pure TiO₂ with Mn doping.
- Study the structural properties of the material with XRD, Raman and TEM
- Study the optical and morphological properties of the material using SEM and Nanolog
- Design optimization and fabrication of TiO₂ gas sensor

- Testing of the device for highly sensitive CO, CH₄, NO₂, NO, H₂S, etc, detection, study of the electrical resistivity and gas response mechanism on TiO₂ films in a wide temperature range
- Investigate a link between magnetization and sensing properties using electron spin resonance and gas sensing system.

1.7.3. Thesis Outline

The thesis contains seven chapters:

Chapter One: Background of gas sensors

- This chapter discusses the history and characteristics of gas sensor and semiconductor metal oxides.
- The sensing mechanism related to MOX
- Aims and objectives

Chapter Two: Literature review

- Chapter two focuses on the literature review of TiO₂. The characteristics, different properties, structure and particle morphology that can be achieved and their effect on the gas sensing properties.

Chapter Three: Characterization Techniques

- This chapter gives the theoretical background of the analytical techniques which were used in this thesis.

Chapter Four:

- Preparation of TiO₂ nanoparticles washed with different concentrations of hydrochloric acid (HCl). The aim here was to evaluate the effect of washing agent such as distilled water and HCl on the structure and morphology, defect related emission, paramagnetic defect and sensing properties of the nanoparticles.

Chapter Five:

- In this chapter, the TiO₂ powders obtained in chapter four were calcined at different temperatures (300, 450 and 700 °C). The effect of annealing temperature on the structure, crystallite size, morphology and sensing properties of TiO₂ were investigated in detail using various analytical techniques.

Chapter Six:

- Chapter six focuses on the preparation of undoped and Mn-TiO₂ doped nanoparticles washed with 1.0 M HCl. The effect Mn additives on the structure, morphology, magnetic and sensing properties of the TiO₂ nanoparticles were studied.

Chapter Seven:

- This chapter summarises all the work carried out in this thesis.

1.8. REFERENCES

- [1.1] V. E. Bochenkov and G. B. Sergeev, , Chapter 2, Vol 3, American Scientific Publishers, (2010), pages 31-52.
- [1.2] S. Capone, A. Forleo, L. Francioso, R. Rella, P. Siciliano, J. Spadavecchia, D.S. Presicce, A.M. Taurino, J. Optoelectron. Adv. M. 5 (2003) 1335-1348.
- [1.3] X. Liu, S. Cheng, H. Liu, S. Hu, D. Zhang, H. Ning, Sensors 12 (2012) 9635-9665.
- [1.4] A. M. Ruiz, A. Cornet., K. Shimano, J.R. Morante, N Yamazoe, Sens. Actuators, B 109 (2005) 7-12.
- [1.5] G. Neri, Chemosensors 3 (2015) 1-20.
- [1.6] T. Cottineau, S. N. Pronkin, M. Acosta, C. Meny, D. Spitzer, V. Keller, Sens. Actuators, B 182 (2013) 489-497.
- [1.7] M. Gorguner, M. Akgun, EAJM 42 (2010) 28-35.
- [1.8] <http://global.britannica.com/EBchecked/topic/279097/hydroxide>
- [1.9] A. Ruiz, J. Arbiol, A. Cornet, J.R. Morante, Mater. Sci. Eng., C 19 (2002) 105-109.
- [1.10] M. Kaur, N. Jain, K. Sharma, S. Bhattacharya, M. Roy, A.K. Tyagi, S.K. Gupta, J.V. Yakhmi, Sens. Actuators, B 133 (2008) 456-461.
- [1.11] G. Kiriakidis, K. Moschovis, I. Kortidis, V. Binas, Vacuum 86 (2012) 495-506.
- [1.12] Gubpta BL. GB-200N industrial sensor technologies and markets. Nowalk, US: Business Communication Company, Inc.; 2004.

- [1.13] <http://www.ishn.com/articles/101421-gas-sensors-market-forecasts-to-2020>
- [1.14] C. Wang, L. Yin, L. Zhang, D. Xiang, R. Gao, *Sensors* 10 (2010) 2088-2106.
- [1.15] K.J. Choi, H.W. Jang, *Sensors* 10 (2010) 4083-4099.
- [1.16] B. Mondal, B. Basumatari, J. Das, C. Roychaudhury, H. Saha, N. Mukherjee, *Sens. Actuators B* 194 (2014) 389–396.
- [1.17] L. Zhang, et al., *Sens. Actuators B: Chem.* (2015), <http://dx.doi.org/10.1016/j.snb.2015.07.113>.
- [1.18] G. Korotcenkov, *Chemical Sensors Comprehensive Sensor Technologies*, Vol 4, Momentum Press, 2011.
- [1.19] W.H. Brattain, J. Bardeen, *Bell Syst. Tech. J.* 32 (1952) 1-41.
- [1.20] T. Seyama, A. Kato, *Anal. Chem.* 34 (1962) 1502-1503.
- [1.21] P.J. Shaver, *Appl. Phys. Lett.* 11 (1967) 255-257.
- [1.22] N. Taguchi, U.S. Patent 3, 631, 436, 28 December 1971.
- [1.23] G. Korotcenkov, *Sens. Actuators, B* 107 (2005) 209-232.
- [1.24] M.-I. Baraton, L. Merhari, *Mater. Trans.* 42 (2001) 1616-1622.
- [1.25] F. Lu, Y. Liu, M. Dong, X.P. Wang, *Sens. Actuators, B* 66 (2000) 225-227.
- [1.26] M.M. Arafat, B. Dinah, S.A. Akbar, A.S.M.A. Haseeb, *Sensors*, 12 (2012) 7207-7258.
- [1.27] J. Huang, Q. Wan, *Sensors*, 9 (2009) 9903-9924.

- [1.28] D. Aphairaj, T. Wirunmongkol, S. Niyomwas, S. Pavasupree, P. Limsuwan, *Ceram. Int.* 01 (2014) 145.
- [1.29] I. Tacchini, A. Anson-Casaos, Y. Yu, M. T. Martinez, M. Lira-Cantu, *Mater. Sci. Eng., B* 177 (2012) 19-29.
- [1.30] F. Ahmed, N. Arshi, M.S. Anwar, R. Danish, B. H. Koo, *Current Applied Physics* 13 (2013) 64-68.
- [1.31] O. Lupan, G. Chai, L. Chow, *Microelectron. J.* 38 (2007) 1211-1216.
- [1.32] Y.-J. Choi, I.-S. Hwang, J.-G. Park, K.J. Choi, J.-H. Park, J.-H. Lee, *Nanotechnology* 19 (2008) 095508.
- [1.33] O. Lupan, G. Chai, L. Chow, *Microelectron. Eng.* 85 (2008) 2220-2225.
- [1.34] O.K. Varghese, D. Gong, M. Paulose, K.G Ong, C.A. Grimes, *Sens. Actuators, B* 93 (2003) 338-344.
- [1.35] S.N. Das, J.P. Kar, J. Xiong, J.-M. Myoung, Chapter 2, <http://dx.doi.org/10.5772/5457>
- [1.36] S.J. Pearton, D P. Norton, M.P. Ivill, A. F. Hebard, J.M. Zavada, W.M. Chen, I. A. Buyanova, *IEEE Transactions on Electron Devices* 54(5) (2007) 1040-1048.
- [1.37] Q.R. Deng, X.H. Xia, M.L. Guo, Y. Gao, G. Shao, *Mater. Lett.* 65 (2011) 2051-2054.
- 1.38] W. Chen, Q. Zhou, L. Xu, F. Wan, S. Peng, W. Zeng, *Journal of Nanomaterials* (2013) <http://dx.doi.org/10.1155/2013/173232>
- [1.39] <http://goldbook.iupac.org/T06456.html>

- [1.40] Y. Wang, R. Zhang, J. Li, L. Li and S. Lin, *Nanoscale Research Letters* 9 (2014) 46-53.
- [1.41] F.F. Wolkenstein, *Discuss. Faraday Soc.* 31 (1961) 209-218.
- [1.42] R.S. Morrison, *Sens. Actuators* 2 (1982) 329-341.
- [1.43] N. Yamazoe, Y. Kurokawa, T. Seiyama, *Sens. Actuators, B* 4 (1983) 283-289.
- [1.44] W. Gopel, K. Schierbaum, *Sens. Actuators, B* 26-27 (1995) 1-12.
- [1.45] S. Basu, P.K. Basu, *Journal of Sensors* (2009), doi:10.1155/2009/861968.
- [1.46] A. Wei, L. Pan, W. Huang, *Mater. Sci. Eng., B* 176 (2011) 1409-1421.
- [1.47] P. Shankar, J.B.B. Rayappan, *Science Jet* 4 (2015) 126-144.
- [1.48] Xu CN, Tamaki J, Miura N, Yamazoe N. *Sens Actuators B* 3 (1991) 147.
- [1.49] D. E. Motaung, G. H. Mhlongo, I. Kortidis, S. S. Nkosi, G. F. Malgas, B. W. Mwakikunga, S. Sinha Ray, G. Kiriakidis, *Appl. Surf. Sci.* 279 (2013) 142-149.
- [1.50] M.R. Mohammadi, D.J. Fray, *Sens. Actuators, B* 150 (2010) 631-640.
- [1.51] N. Yamazoe, *Sens. Actuators, B* 5 (1991) 7-19.

CHAPTER TWO

LITERATURE REVIEW

2. INTRODUCTION

This chapter gives an insight on the proposition of titanium (IV) dioxide (TiO_2) as a metal oxide based gas sensor for detection of hazardous and explosive gases at low temperature. A detailed review on the structure, optical, surface properties of TiO_2 including the magnetic properties and a brief literature survey on the room temperature TiO_2 gas sensing performance is also discussed.

2.1. BULK PROPERTIES OF TiO_2

TiO_2 has widely been known for its photocatalysis ability since Fujishima's water spilling demonstration in 1972 [2.1]. TiO_2 is nontoxic, highly stable under various conditions, corrosion resistant, biocompatible, and cost-effective and is available in abundance in South Africa. It is preferred for environmental, energy and health applications compared to other materials [2.2-2.4]. It is used in applications such as water purification and removal of heavy metals [2.5], electrochromic devices [2.6], hydrogen storage [2.7], solar cells [2.8], gas sensor [2.9], paint pigments and sunscreens [2.10]. The properties that make TiO_2 favourable are discussed in the following sections:

2.1.1. Structural Properties of TiO₂

TiO₂ is a naturally occurring mineral and it exists in three crystal structures known as Anatase, Rutile and Brookite [2.11- 2.15]. Other structures exist at high pressure. The brookite face is metastable and transforms to rutile at high temperatures. As for brookite not much technological advances and application have been reported. Rutile TiO₂ is the most stable polymorph and is widely used for high temperature applications such as methane gas sensing in mining industry [2.16]. Anatase TiO₂ is very stable at low temperatures and transforms to rutile at higher temperature. Besides being stable in nanoscale, anatase TiO₂ displays higher photocatalytic activity resulting in vast applications in photocatalytic devices [2.12]. Both anatase and rutile have I₄₁/amd and P₄₂/mmm tetragonal structure and brookite has an orthorhombic structure [2.11- 2.15]. Their unit cell contains an octahedral configuration of a titanium atom surrounded by six oxygen atoms and the lattice parameters are given by the lattice vector *a* and *c* [2.11, 2.13, 2.14]. The Ti–O bonding is largely ionic with some covalent contribution. Fig. 2.1a and b show the anatase and rutile unit cells, and Table 2.1 lists the basic properties of anatase and rutile TiO₂. In anatase, the octahedrons share four edges, hence the four-fold axis, with Ti atoms situated at (0, 0, 0) and (0, ½, ¼) while, the O atoms are situated at (0,0,u). (0,0,ū), (0, ½, u+ ¼) and (0, ½, ½ -u). Where u = 0.305 at 15 K [2.11, 2.14]. However, in rutile, the Ti atoms are at (0, 0, 0) and (½, ½, ½) and the O atoms at ± (u, u, 0) and ± (u+ ½, ½-u, ½). The titanium oxide shares two edges

of the octahedron with other octahedrons and form chains and the chains rearranged themselves into a four-fold symmetry [2.14].

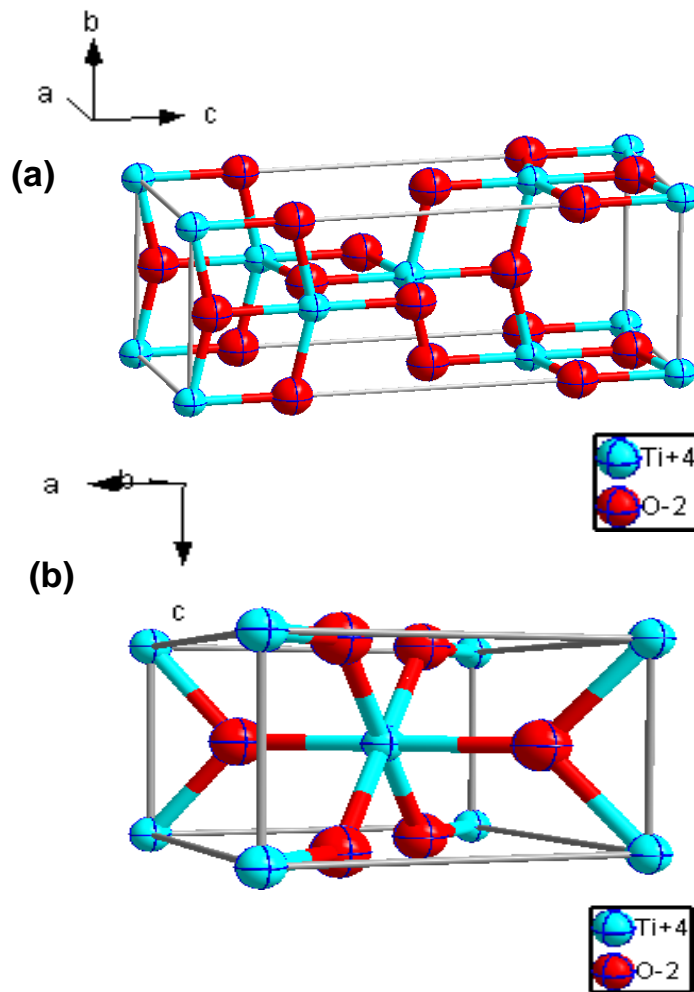


Fig. 2.1: (a) Anatase and (b) Rutile TiO₂ unit cells. The Ti and the O ions are represented by the blue and red balls, respectively.

Table 2.1: Summary of the basic properties of TiO₂ polymorphs.

| Properties | Anatase | Rutile | References |
|-------------------------------------|--------------------------------------------------|----------------------|---------------|
| Crystal structure | Tetragonal | Tetragonal | [2.17, -2.19] |
| Atoms per unit cell | 4 | 2 | [2.19, 2.20] |
| (Z) | | | |
| Lattice parameters | a= 0.3785 | a= 0.4594 | [2.17-2.20] |
| (nm) | c= 0.9514 | c= 2.9587 | |
| Space group | I4 ₁ /amd | P4 ₂ /mnm | [2.11- 2.15] |
| Ti-O bond length | 1.937(4) | 1.949(4) | [2.19] |
| (nm) | 1.965(2) | 1.980(2) | |
| Density (kg. m⁻³) | 3894 | 4250 | [2.19, 2.20] |
| Refractive index | 2.52 | 2.71 | [2.18- 2.20] |
| Melting point | Transform to rutile at higher temperatures | 1870 | [2.10, 2.18] |
| Solubility in HF | soluble | Insoluble | [2.21] |
| Solubility in H₂O | insoluble | Insoluble | [2.17] |
| Hardness (Mohs) | 5.5 - 6 | 6 -6.5 | [2.18] |
| Bulk Modulus | 183 | 206 | [2.22] |
| (GPa) | | | |
| Theoretical band | | | [2.23] |
| gap | | | |
| (eV) | 3.23 | 3.0 | |
| (nm) | 387 | 413 | |

2.1.2. Surface properties of TiO₂

The surface plays an important role in nanomaterials, since it enables interaction between reagents and the material. The surface chemistry of TiO₂ is influenced by the fact that it has a mixture of ionic and covalent bonding. The anatase (101), (001), and (100) surfaces and the rutile (110) surface are the most studied single crystalline TiO₂ surfaces [2.12]. Surface properties can be manipulated to improve the material's performance. The surface can be modified by adding impurities (dopants) on the TiO₂ surface [2.12, 2.13], by sensitizing (dye sensitization for solar cell) [2.8], and by manipulating the size (nanoscale, quantum dots) of the sensing material. Incorporation of impurities cause lattice distortion and induces additional defect states when they replace Ti⁴⁺ ions in the lattice. Fig. 2.2 shows intrinsic and dopants induced defects in the TiO₂ lattice. Many researchers have reported that nanostructured materials exhibit significantly different physical and chemical properties from those in bulk form [2.24, 2.25]. This is because grains of nanostructured metal oxides are almost depleted of charge carriers since most are trapped on the surface. When exposed to target gases they exhibit great conductivity compared to air [2.26]. Porosity is also an influencing factor, because it allows the reagent to pass through the pores and interact with the outer and inner surface of the material. Additionally, size and dimensions of nanomaterials also play an important role on the performance of the material. It has been reported that small particle sizes are beneficial to TiO₂ based- devices [2.8]. Quantum confinement effect governs the transport properties of phonons and photons and thus electrons and holes

movement within the material. Moreover, previous results have also shown that, the specific surface area increases with a decrease in particle size and also change the surface stability and phase transitions [2.15, 2.25]. A large surface to volume ratio increases the interaction between the material and the medium. Fig. 2.3 shows SEM micrographs of TiO_2 with different morphologies and dimensions, such as one dimensional (1-D) nanotubes [2.27], nanowires [2.28], nanorods [2.29], nanoribbons [2.30], nanofibers [2.31] synthesized using various methods.

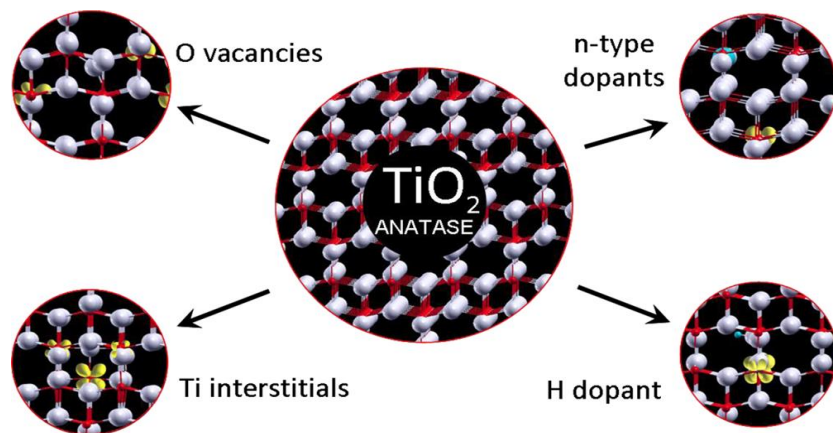


Fig. 2.2: Ball and stick figure showing Intrinsic and dopant induced defects of TiO_2 . The red balls represent Ti atoms, grey balls represent O atom and the yellow balls represent defects [2.12].

2.1.3. Electrical and Optical properties of TiO_2

The anatase phase has an indirect bandgap of about 3.2 eV, while rutile phase has a bandgap of approximately 3.0 eV [2.23]. Anatase has a more reducing power than rutile. For example, it can reduce molecular oxygen into superoxide radicals. Changes in stoichiometry results to an increase in oxygen

vacancies (V_O) and creation of Ti^{3+} in the lattice. High concentration of (V_O) is the reason why TiO_2 is an n-type semiconductor (see Fig 2.2) [2.12, 2.15]. Such stoichiometric deviations allow electron flow, hence the conductivity of the material [2.32]. The optical properties of TiO_2 are strongly influenced by intrinsic defects states. Oxygen vacancies, titanium interstitials, and oxygen Interstitials strongly influence the reactivity of the material [2.12]. The defects are good electron trapping sites. TiO_2 absorbs below 380 nm wavelength and when excited a broad visible photoluminescence in the green range is observed.

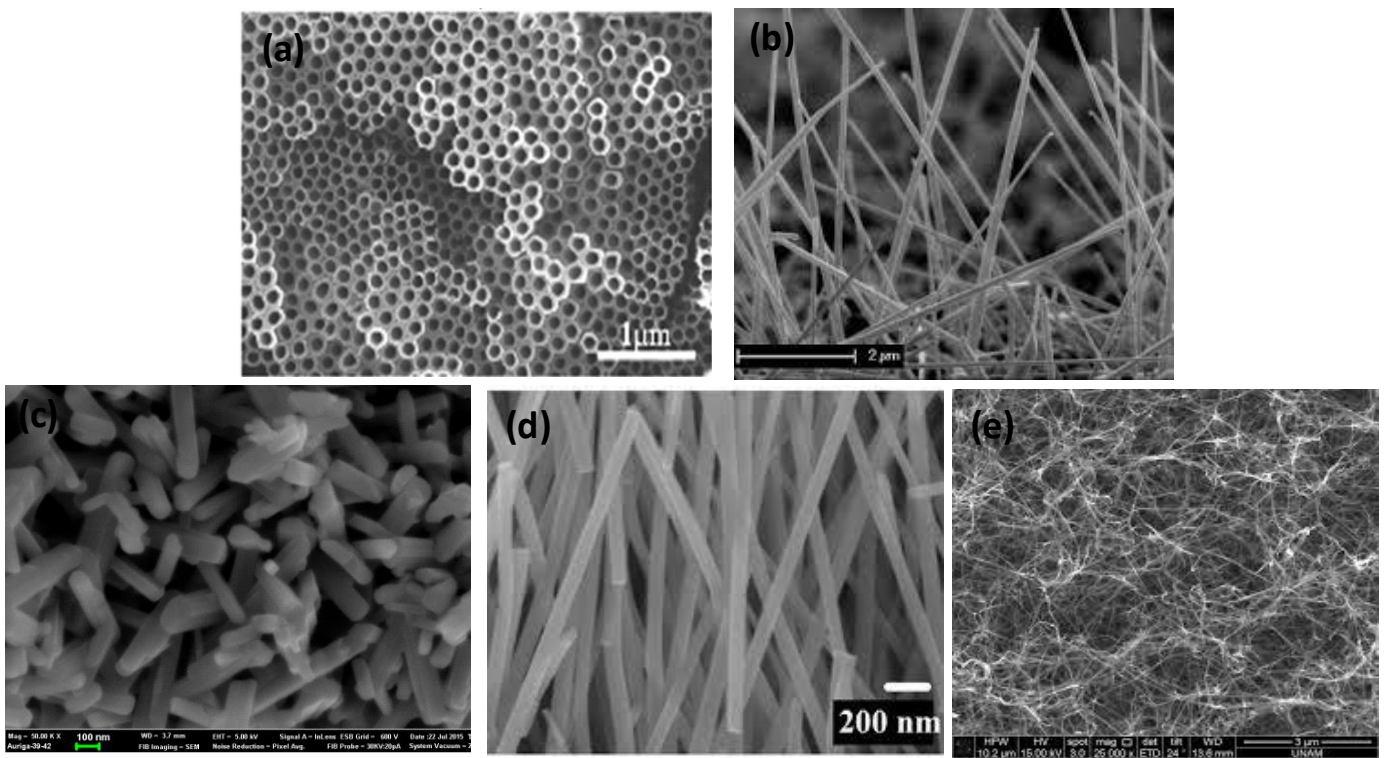


Fig. 2.3: 1-D TiO_2 (a) nanotubes [2.27], (b) nanowires [2.28], (d) nanorods [2.29], (d) nanoribbons [2.30], and (e) nanofibers [2.31].

2.1.4. Magnetic properties of TiO₂

Since the discovery of ferromagnetism (FM) in Co-doped TiO₂ [2.33], a lot of studies have been done to determine the magnetic properties of undoped TiO₂. Scientists reported that room temperature ferromagnetism (RTFM) in undoped oxides such as TiO₂ is related to surface defects and/or interface defects [2.34] which maybe induced during the preparation process. Previous reports indicated that the FM observed in undoped TiO₂ largely originates from the d-orbitals of low-charge-state Ti cations converted from Ti⁴⁺ cations, which are induced by the surface (V_O) [2.35, 2.36]. Fig. 2.4 shows the magnetic characterization of the milled TiO₂ nanostructures measured at various temperatures showing a clear magnetic hysteresis loops which demonstrates a RTFM recorded at different isothermal temperatures 4–300 K [2.37].

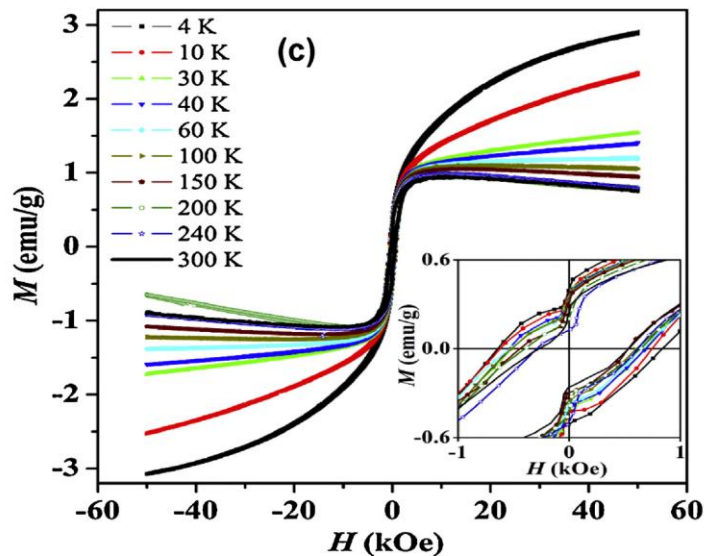


Fig. 2.4: Magnetic properties of 120 h milled TiO₂ nanoparticles measured at various temperatures. The inset depicts the magnified image.

2.1.5. Gas sensing properties of TiO₂

TiO₂ has been reported to be one of the most promising material for gas sensing application because it is nontoxic, biocompatible, affordable, and it is highly stable and corrosion resistant. Hence, it can operate in harsh conditions and has long life cycle. Moreover, TiO₂ can be easily synthesized using several methods, such as chemical vapour deposition (CVD) [2.38] anodization [2.39], electrospinning [2.31], microwave and autoclave hydrothermal [2.29]. TiO₂ contains donor type defects such as oxygen vacancies and titanium interstitials occupying interstices between the atomic sites [2.24]. Oxygen vacancies (V_O) are formed by transfer of an oxygen atom on a normal site to a gaseous state. Fig. 2.5 shown a schematic diagram of the sensing mechanism of TiO₂ nanoparticles exposed to oxidative and reductive gases. When oxygen molecules are absorbed on the surface of TiO₂ they extract electrons from the conduction band and trap the electrons in form of oxygen species O₂⁻, O⁻ or O²⁻ at the surface. This leads to band bending and an increase depletion layer. Since TiO₂ is n-type, when exposed to a reducing gas such as H₂, H₂S, CH₄, the oxygen ions react with the gas and donate electrons into the surface, this decreases the resistance and reverses the band bending thus increasing conductivity. When exposed to oxidizing gases such as NO_x, O₂, O₃ TiO₂ behaves oppositely [2.24, 2.40, 2.41].

For gas sensing application; sensitivity, selectivity, high operating temperature and stability are the most pressing challenges faced by researchers on improving gas sensor performance. Despite, all the work that has been done

on gas sensors, there are few reports on pure TiO_2 sensing material with higher sensing response, improved sensitivity and selectivity at room temperature (RT). Lin *et al.* [2.42] reported gas sensing response of vertically grown TiO_2 nanotube arrays synthesized using an electrochemical anodization process. Their sensor showed a good response to 10-50 ppm concentrations of formaldehyde and a reasonable selectivity to gases such as ethanol and ammonia at room temperature. Dhivya *et al* [2.43] reported an enhanced response towards NH_3 in the concentration range of 5–100 ppm at room temperature with sensitivity of $S=7857$ and this was attributed to high surface-to-bulk ratio and crystal structure of reactive DC magnetron sputtered TiO_2 films.

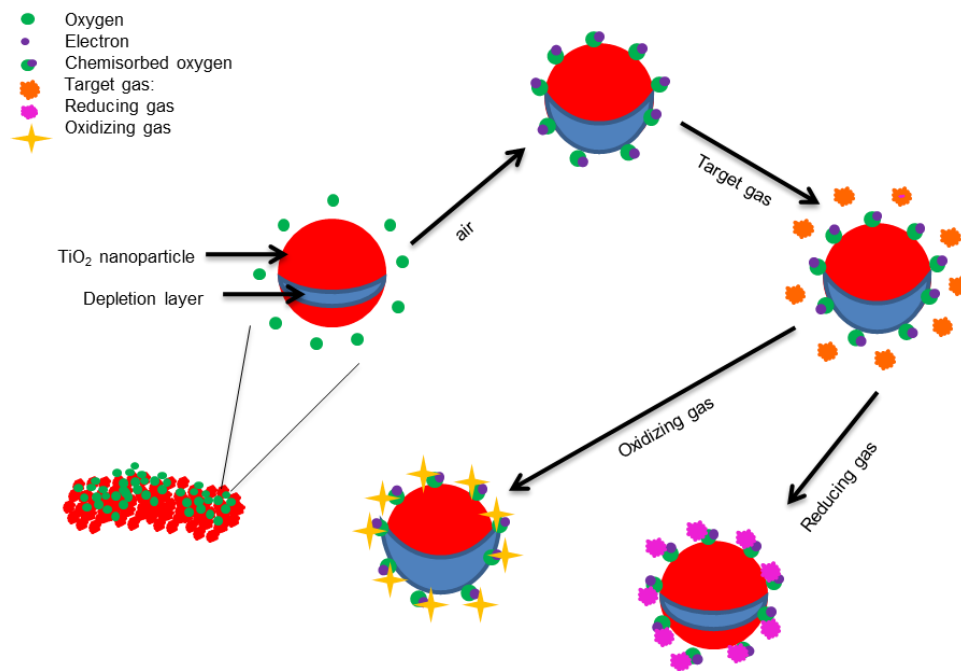


Fig. 2.5: Sensing mechanism of TiO_2 [2.24, 2.40, 2.41].

Table 2.2 gives a literature survey on the room temperature gas sensing of undoped and TiO_2 doped with different noble metals and transitional metals

prepared using different methods. It is worth mentioning that regardless of the work carried so far, there are no reports on the sensing properties of Mn-doped TiO₂. Therefore in this work we investigated the room temperature gas sensing properties of TiO₂ doped with different concentrations of Mn.

Table 2.2: A summary of reports on room temperature TiO₂ based gas sensors

| Sensing element | Synthesis method | Working temperature (°C) | Gas | Gas concentration (ppm) | Response | Reference |
|----------------------------------------------------------------|-----------------------------|--------------------------|------------------------------------|-------------------------|-------------|-----------|
| TiO ₂ nanotubes | Electrochemical anodization | RT | HCHO Ethanol NH ₃ | 10-50 50 1000 | | [2.42] |
| TiO ₂ nanoparticles | | RT | NH ₃ | 0.15-100 | 7857 | [2.43] |
| TiO ₂ nanoparticles | hydrothermal | RT | NO ₂ NH ₃ | 5-40 5-40 | 1093 750 | [2.44] |
| TiO ₂ nanotubes | | RT | H ₂ | 100-500 | 239 | [2.45] |
| TiO ₂ nanotubes | anodizing | RT-UV radiation assisted | HCHO | 50 | 80 | [2.46] |
| TiO ₂ nanotubes | anodizing | RT-UV assisted | H ₂ | 1000 | | [2.39] |
| NiO-TiO ₂ nanocomposite | | RT-UV illumination | NH ₃ | 10-100 | 500 | [2.47] |
| Cellulose/TiO ₂ nanoparticles/PANI nanofibers | Electrospinning Sol-gel | RT | NH ₃ | 10-250 | 6335 | [2.48] |
| Al/TiO ₂ /Al ₂ O ₃ /p-Si film | | RT-UV illumination | NO ₂ | 20-100 | 190 | [2.49] |
| Pd-TiO ₂ nanoparticles | | RT | H ₂ | | | [2.50] |
| Ag-TiO ₂ core-shell nanoparticles | | RT | ethanol | 5 | | [2.51] |

2.2. REFERENCES

- [2.1] A. Fujishima, K. Honda, *Nature* 23 (1972) 37-38.
- [2.2] Y. Jun, H. Kim, J. Lee, S. Hong, *Sens. Actuators, B* 120 (2006) 69-73.
- [2.3] D. Aphairaj, T. Wirunmongkol, S. Niyomwas, S. Pavasupree, P. Limsuwan, *Ceram. Int.* 40(7) (2014) 9241-9247.
- [2.4] A. M. Ruiz, A. Cornet, J. R. Morante, *Sens. Actuators, B* 100 (2004) 256-260.
- [2.5] S.C. Xu, S.S Pan, Y. Xu, Y.Y. Luo, Y.X. Zhang, G.H. Li, *J. Hazard. Mater.* 283 (2015) 7-13.
- [2.6] D.K. Hwang, J.H. Moon, Y.G. Shul, K.T. Jung, D. H. Kim, D.W. Lee, *J. Sol-Gel Sci. Technol.* 26 (2003) 783.
- [2.7] G.K Mor, M.A. Carvalho, O.K. Varghese, M.V. Pishko, C.A. Grimes, *J. Mater. Res.* 19 (2004) 628-634.
- [2.8] S. Ito, S.M. Zakeeruddin, R. Humphry-Baker, P. Liska, R. Charvet, P. Comte, M.K. Nazeeruddin, P. Penchy, M. Takata, H. Miura, S. Uchida, M. Gratzel, *Adv. Mater.* 18 (2006) 1202-1205.
- [2.9] M.-H. Seo, M. Yuasa, T. Kida, J.-S. Huh, K. Shimano, N. Yamazoe, *Sens, Actuators, B* 137 (2009) 513.
- [2.10] A. Fujishima, K. Hashimoto, T. Watanabe, BKC Inc, 1999.
- [2.11] J. Muscat, V. Swamy, N. Harrison, *Phys. Rev. B* 65 (2002) 224112.
- [2.12] F. De Angelis, C. Di Valentin, S. Fantacci, A. Vittadini, A. Selloni, *Chem. Rev.* 114 (2014) 9708-9753.
- [2.13] U. Diebold, *Surf. Sci. Rep.* 48 (2003) 53-229.

- [2.14] D.A.H. Hanaor, C.C. Sorrell, *J. Mater. Sci.* 46 (2011) 855-874.
- [2.15] X. Chen, S.S. Mao, *Chem. Rev.* 107 (2007) 2891-2959.
- [2.16] S. Sharma, M. Madou, *Phil. Trans. R. Soc. A* 370 (2011) 2448-2473.
- [2.17] J. Fisher, T.A. Egerton, Wiley, New York (2001)
- [2.18] G.V. Samsonov, IFI/Plenum Press, New York (1982).
- [2.19] S.D. Mo, W.Y. Ching, *Phys. Rev. B* 51 (1995) 13023-13032.
- [2.20] J.K. Burdett, T. Hughbanks, G.J. Miller, J.W. Jr Richardson, J.V. Smith, *J. Am. Chem. Soc.* 109 (1987) 3639.
- [2.21] T. Ohno, K. Sarukawa, M. Matsumura, *J. Phys. Chem. B* 105 (2001) 2417.
- [2.22] H. Wang, J.P. Lewis, *J. Phys.: Condens. Matter* 18 (2006) 421.
- [2.23] L. Kavan, M. Gratzel, S.E. Gilbert, C. Klemenz, H.J. Scheel, *J. AM. Chem. Soc.* 118 (1996) 6716.
- [2.24] W. Zhou, H. Liu, R.I. Boughton, G. Du, J. Lin, J. Wang, D. Liu, *J. Mater. Chem.* 20 (2010) 5993-6008.
- [2.25] N. Yamazoe, *Sens. Actuators, B* 5 (1991) 7-19.
- [2.26] J. Huang, Q. Wan, *Sensors* 9 (2009) 9903-9924.
- [2.27] A. Hu, C. Cheng, X. Li, J. Jiang, R. Ding, J. Zhu, F. Wu, J. Liu, X. Huang, *Nanoscale. Res. Lett.* 6 (2011) 2-6.
- [2.28] L. Francioso, A.M. Taurino, A. Forlo, P. Siciliano, *Sens. Actuators B Chem.* 130 (2008) 70-76.
- [2.29] L. M. Sikhwivhil, S. Mpelane, B. W. Mwakikunga, S. Sinha Ray, *ACS Appl. Mater. Interfaces* 4 (2012) 1656-1665.

- [2.30] B. Santara, P.K. Giri, S. Dhara, K. Imakita, M. Fujii, J. Phys. D: Appl. Phys. 47 (2014) 235304.
- [2.31] Y. Aykut, C.D. Saquing, B. Pourdeyhimi, G.N. Parsons, S.A. Khan, ACS Appl. Mater. Interfaces 4 (2012) 3837-3845.
- [2.32] R.T. Williams, K.S. Song, J. Phys. Chem.: Solids 51 (1990) 679-716.
- [2.33] Y. Matsumoto, M. Murakami, T. Shono, T. Hasegawa, T. Fukumura, M. Kawasaki, P. Ahmet, T. Chikyow, S. Koshihara, H. Koinuma, Science 291 (2001) 854.
- [2.34] M. Venkatesan, C.B. Fitzgerald, J.M.D. Coey, Nature 430 (2004) 630.
- [2.35] A. Sundaresan, R. Bhargavi, N. Rangarajan, U. Siddesh, C.N.R. Rao, Phys. Rev. B 74 (2006) 161306–161309.
- [2.36] T. Wu, H. Sun, X. Hou, L. Liu, H. Zhang, J. Zhang, Mater. 190(2014) 63–66.
- [2.37] A. S. Bolokang, F.R. Cummings, B.P. Dhonge, H.M.I. Abdallah, T. Moyo, H.C. Swart, C.J. Arendse, T.F.G. Muller, D.E. Motaung, Appl. Surf. Sci. 331 (2015) 362-372.
- [2.38] J.J. Wu, C.C. Yu, J. Phys. Chem. B 108 (2004) 3377.
- [2.39] G. K. Mor, O. K. Varghase, M. Paulose, C. A. Grimes, Sensor Lett. 1 (2003) 42-46.
- [2.40] C. Wang, L. Yin, L. Zhang, D. Xiang and R. Gao, Sensors 10 (2010) 2088-2106.
- [2.41] H. Wua, L. Wanga, J. Zhou, J. Gao, G. Zhang, S. Xu, Y. Xie, L. Li, K. Shi, J. Colloid Interface Sci. 466 (2016) 72–79.

- [2.42] S. Lin, D. Li, J. Wu, X. Li, S.A. Akbar, *Sens. Actuators B* 156 (2011) 505–509.
- [2.43] P. Dhivya, A.K. Prasad, M. Sridharan, *Ceram. Int.* 40 (2014) 409-415.
- [2.44] Z.P. Tshabalala, D.E. Motaung, G.H. Mhlongo, O.M. Ntwaeaborwa, *Sens. Actuators B* 224 (2016) 841–856.
- [2.45] K. Chen, K. Xie, X. Feng, S. Wang, R. Hu, H. Gu, Y. Li, *Int. J. Hydrogen Energy* 37 (2012) 13602-13609.
- [2.46] L. Liu, X. Li, P.K. Dutta, J. Wang, *Sens. Actuators B* 185 (2013) 1-9.
- [2.47] C. Xiang, Z. She, Y. Zou, J. Cheng, H. Chu, S. Qiu, H. Zhang, L. Sun, F. Xu, *Ceram. Int.* 40 (2014) 16343-16348.
- [2.48] Z. Pang, Z. Yang, Y. Chen, J. Zhang, Q. Wang, F. Hang, Q. Wei, *Colloids Surf., A* <http://dx.doi.org/10.1016/j.colsurfa.2016.01.024>
- [2.49] I. Karaduman, D.E. Yildiz, M.M. Sincar, S. Acar, *Mater. Sci. Semicond. Process.* 28 (2014) 43-47.
- [2.50] S. Mun, Y. Chen, J. Kim, *Sens. Actuators B* 171-172 (2012) 171-172, 1186-1191.
- [2.51] Z. Zhu, C.-T. .Kao, R.-J. Wu, *Appl. Surf. Sci.* 320 (2014) 348-355.

CHAPTER THREE

CHARACTERIZATION TECHNIQUES

3.1. INTRODUCTION

To gain insight on the structural, electrical, optical, chemical, magnetic and sensing properties of the synthesized material, various characterization techniques such as x-ray diffraction (XRD), Raman spectroscopy, scanning electron microscope (SEM), transmission electron microscope (TEM), physisorption analysis, photoluminescence (PL), and gas testing station were used. Therefore, in this chapter the theories and principles behind the instruments are discussed.

3.2. X-RAY DIFFRACTION

X-ray diffraction (XRD) is a simple and powerful instrument used to determine the crystalline structure, and estimate the crystallite size, lattice strain and lattice parameters of the material. This technique is based on the x-rays beam incident on a material as shown in Fig. 3.1. The atoms in the material cause the incident beam of X-rays to diffract into many specific directions. Depending on the wavelength, incident and scattering angles these waves cancel one another out through destructive interference or they add constructively in a

few specific directions governed by Bragg's law (equation 3.1) [3.1]. Each crystalline material has a unique XRD pattern to identify its crystal structure. The XRD patterns observed represent the orientation and arrangement of a particular set identified by Miller indices (h, k, l) [3.2].

$$n\lambda = 2d\sin\theta \quad (3.1)$$

where n is an integer, which normally equals to 1, and $\lambda = 1.5418 \text{ \AA}$ is the wavelength of the beam corresponding to Cu $K\alpha$ emission, d is the lattice spacing between diffracting planes, θ is the angle of incidence,

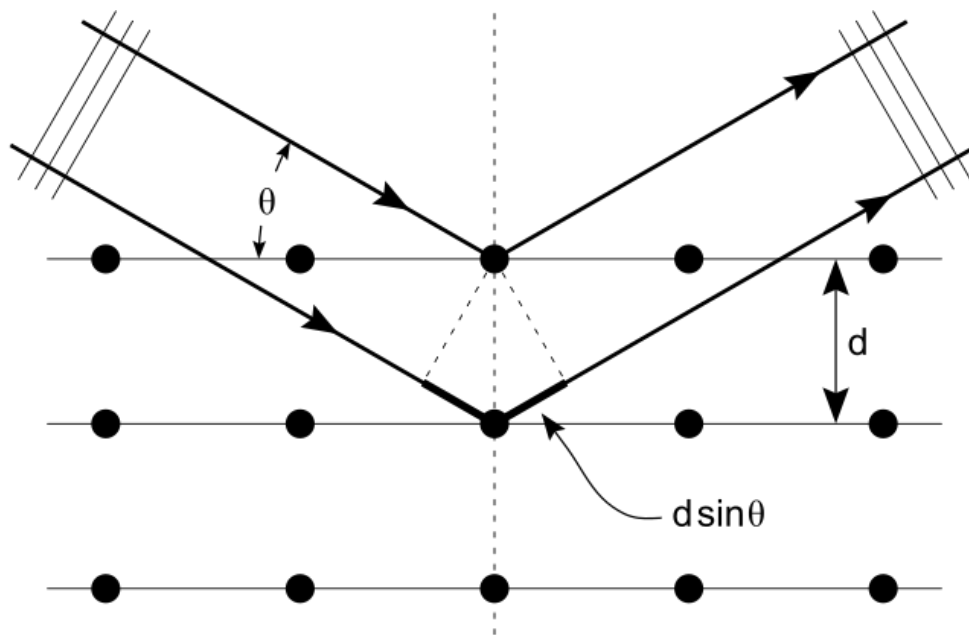


Fig. 3.1: Schematic diagram of diffraction pattern based on Bragg's law

[3.1].

By examining the diffraction patterns, the broadness of the peaks given by the full width at half maximum (β measured in radians) and intensity help estimate the crystallite size (L) from Debye – Scherrer model shown in equation 3.2 [3.3, 3.4].

$$L = \frac{K\lambda}{\beta \cos\theta} \quad (3.2)$$

where K is a constant equals to 0.94,

Williamson and Hall also proposed a model, known as the Williamson - hall method shown in equation 3.3 and 3.4 [3.4] which takes into account the strain (ε) induced by crystal imperfections and lattice distortion.

$$\beta_{hkl} = \frac{k\lambda}{L \cos\theta} + 4\varepsilon \tan\theta \quad (3.3)$$

Rearranging equation 3.3 gives:

$$\beta_{hkl} \cos\theta = \frac{k\lambda}{L} + 4\varepsilon \sin\theta \quad (3.4)$$

In this study, the XRD measurements were conducted using a PanAlytical X'pert PRO PW3040/60 X-ray diffractometer fitted with a Cu $K\alpha$ monochromated radiation source. As shown in Fig. 3.2 the detector is placed on the circumference of a circle centred at the specimen stage rotating about an axis (into the page), X-rays diverge from the X-ray tube source and are diffracted by

the specimen to form a convergent diffracted beam at the slit before entering the detector. The two slits define and collimate the incident and diffracted beams.

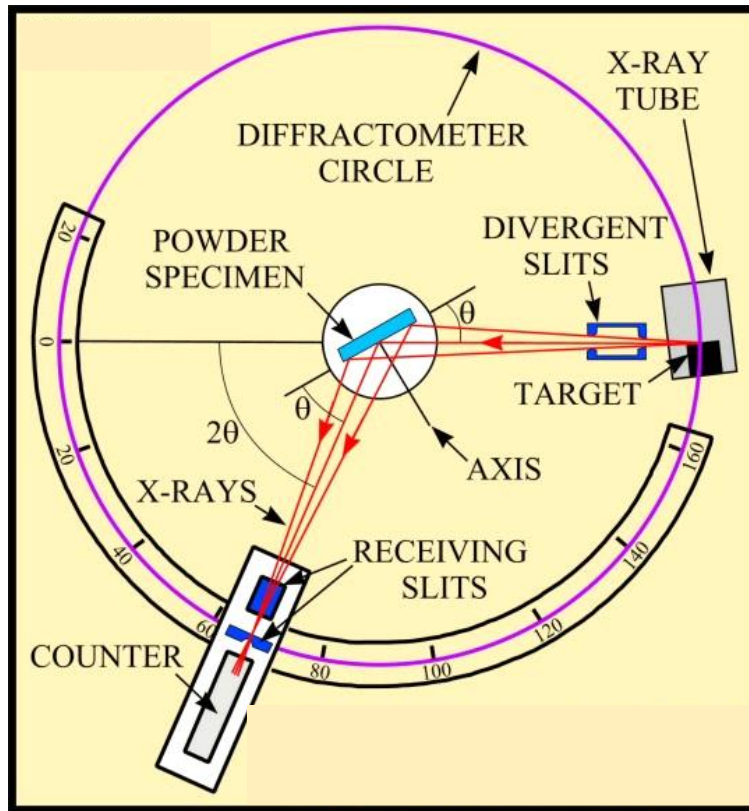


Fig. 3.2: Schematic diagram of X-ray spectrometer [3.2].

3.3. RAMAN SPECTROSCOPY

Raman spectroscopy is a technique based on Raman effect where a monochromatic light is in-elastically scattered by atoms or molecules in a medium (sample) [3.5]. The technique enables the study (or investigation) of vibrational states of molecules and molecular bond structure. Typically, Raman spectroscopy uses a laser radiation in the visible or near- infrared frequency to excite the sample. When the incident light interacts with the sample, the sample

molecules are excited to a virtual energy state by absorbing photons from the incident light and later de-excited by reemit the photon elastic or in-elastic [3.6]. When the scattered light is strong and has the same frequency as that of the incident light elastic scattering occurs, this behaviour is also known as Rayleigh scattering. However in Raman scattering, the reemitted light has lower or higher frequency than the incident light which is categorised as Stokes and anti-Stokes scattering [3.6, 3.7].

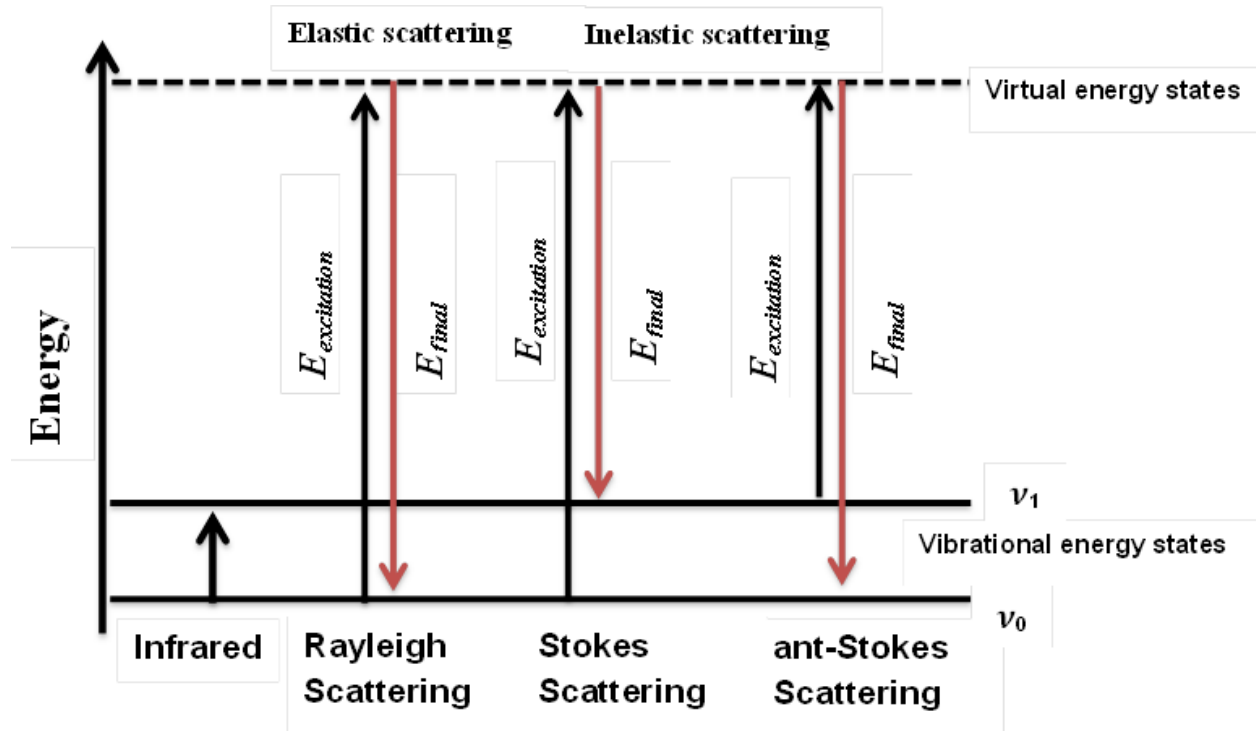


Fig. 3.3: Illustration of Rayleigh and Raman scattering [3.7].

When a Raman- active molecule absorb a photon part of the photon's energy is transferred to the Raman active modes and the scattered photon has reduced energy. This frequency is called Stokes frequency [3.6, 3.7]. However if

the Raman active mode already in the excited vibrational state absorb a photon, light at higher frequency called anti-Stokes frequency is scattered and the molecules return to vibrational ground state (see Fig. 3.3) [3.6, 3.7]. Fig. 3.4 shows the system setup .The incident beam from 514.5 nm excitation laser is directed onto the sample. The monochromatic laser beam is passed through a pinhole and measured in a spectrometer, and then reflected by the mirrors towards the Notch filter. From the Notch filter the light is then focused to the sample and directed to the monochromator, light entering the monochromator is directed towards a diffraction grating, which can be rotated to direct light of different wavelengths to the exit slit. As the grating is rotated the light is then directed to the coupled charge detector (CCD) and a spectrum is easily recorded. Thus, a Horiba Jobin – Yvon HR800 Raman microscope was used to characterize our TiO₂ materials.

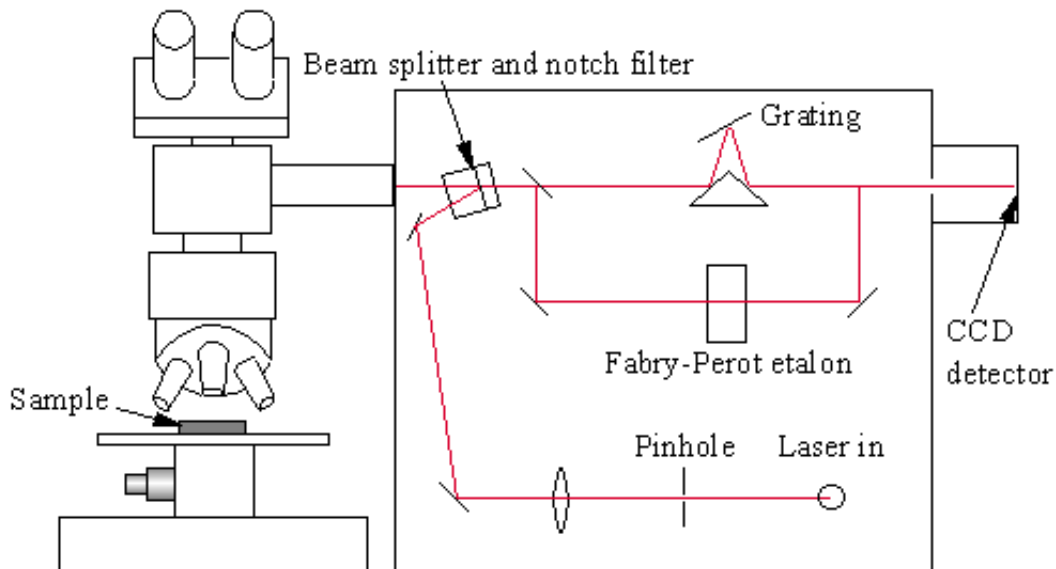


Fig. 3.4: Schematic diagram of Raman spectroscopy [3.6].

3.4. ELECTRON MICROSCOPY

Electron microscopes are beneficial in the field of nanoscience and nanotechnology because a beam of accelerated electrons is used as a probing source. Electrons are highly energetic (very low wavelength $\approx 0.05 \text{ \AA}$) [3.8] and enable the microscope to operate in higher magnification and resolution where else light microscopes have limited wavelength thus limiting the possible magnification of the microscope. In this work, the scanning electron microscope (SEM) and transmission electron microscope (TEM) were used to study surface morphology and topography, particle distribution and crystallinity of the synthesized materials.

3.4.1. Scanning Electron Microscope

In a scanning electron microscope (SEM) electrons are emitted from a field-emitter in an electron gun located at the top of the column. The electrons form a cloud of electrons which is focused and directed by electromagnetic lenses (objective and condenser lens), coils, and apertures. The electrons are accelerated in a vacuum by high voltage (5-20 kV) into a fine probe that scans over the surface of the material. The magnetic fields are also used to shape and control the beam. When the beam of electron interacts with the material, it loses energy in various ways each carrying information about the sample as seen in Fig. 3.5. Some of the lost energy is converted into heat, emitted as secondary electrons (low energy), backscattered electrons (high energy) or X-ray emission (see Fig. 3.5) [3.9, 3.10]. The detectors convert them into a signal that is directed

to a screen with intensity corresponding to the position of the beam on the sample. Additionally, the x-rays ejected are characteristic of the atoms of the sample and are used in energy dispersive x-ray spectroscopy (EDS).

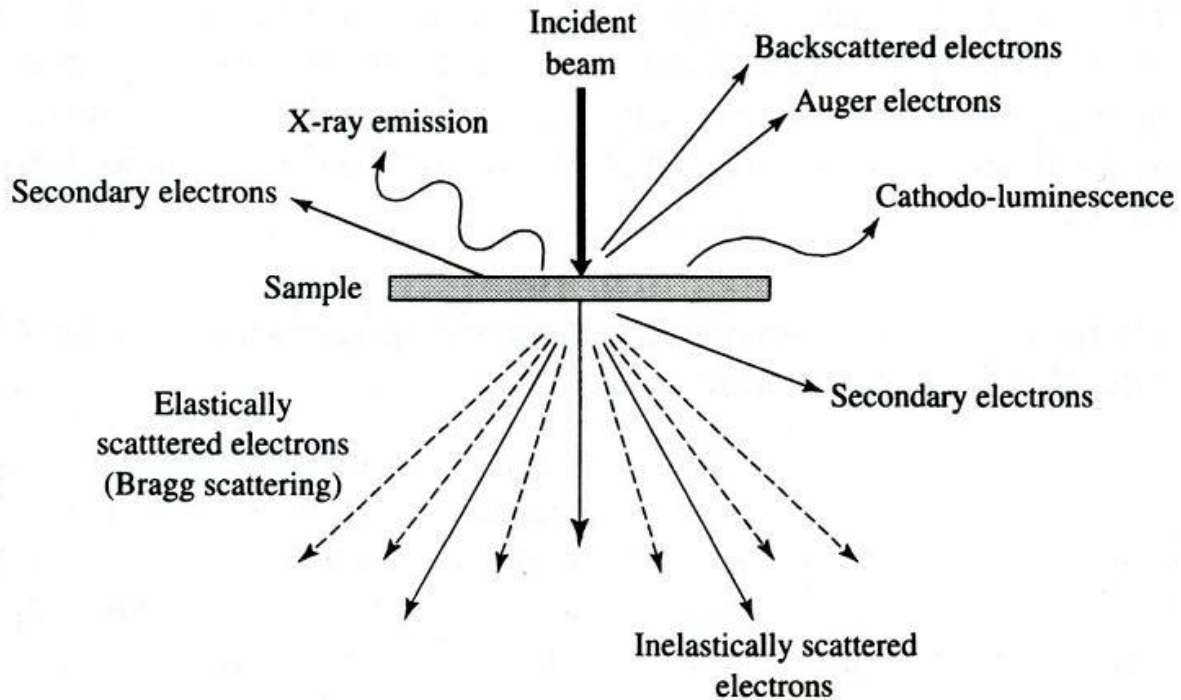


Fig. 3.5: Electron-specimen interaction [3.9].

The apparatus's resolution, working distance and spherical aberration influence the quality and focusing of the image [3.10]. During sample preparation the samples are coated by a conducting layer in order to obtain a non-conductive (often said to be charging) image. If not properly coated excess electrons build up and are released as sudden flashes interfering with image formation. The coating increases conductivity and the release of secondary and backscattered electrons and also limits sample damage by excessive heat of the beam. In this

study, the SEM images of the TiO_2 powders were obtained from the Auriga ZEISS SEM. Fig. 3.6 shows the schematic diagram of the scanning electron microscope.

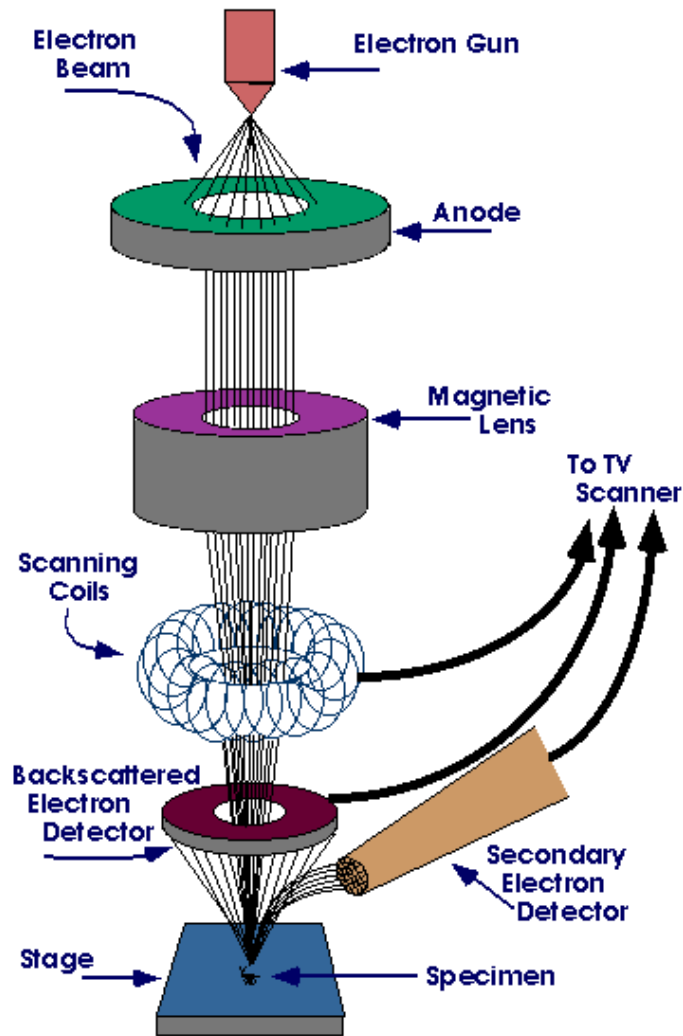


Fig. 3.6: Schematic diagram of a SEM [3.11].

3.4.2. Transmission Electron Microscope

Transmission electron microscope (TEM) is a vital analysis method in the scientific field both physical and biological sciences. It can be used to characterize nanomaterials to obtain information about the particle size, shape, crystallinity, and interparticle interaction. This technique differs from SEM in that; the primary electron beam is transmitted through the sample instead of being backscattered or knocking out secondary electrons [3.8]. A very energetic beam of electrons typically from a tungsten source is directed through a very thin sample and the interactions of the electrons with the atoms give information about the crystalline structure.

A TEM schematic diagram is shown in Fig. 3.7. A hot cathode in the electron gun emits high accelerated electrons through an anode with a potential difference between 100 to 300 kV. The electrons are focused into a small, thin and coherent beam by passing through a condenser lens and form a parallel beam before passing through the sample. The condenser aperture excludes high angle electrons from interacting with the sample. The objective lens magnifies the information about the sample and the image may be viewed on the screen. The lighter areas on the image represent the areas where more electrons were transmitted through while the darker areas represent areas where fewer electrons were transmitted. By obeying De Broglie's hypothesis on wave –particle duality [3.9], increasing the accelerating potential of the electrons, the electron wavelength shrinks. As a result the highly energetic transmitted electrons enable high magnification and high resolution image of about 1 Å with regularity.

In this study high resolution transmission electron microscopy (HR-TEM) analyses were carried out at 200 kV using JEOL JEM-2100 HR-TEM. The TiO_2 powders were dispersed in ethanol and ultra-sonicated until homogeneously dissolved. The solution was then deposited (drop) on a holey-carbon copper grid and dried at room temperature. Selected area electron diffraction (SAED) patterns were obtained from TEM for both amorphous and crystalline TiO_2 samples. Crystalline patterns can be divided into two groups: monocrystalline and polycrystalline. The electron diffraction patterns obtained are distinctly different: monocrystalline diffraction patterns have a bright spot due to the transmitted beam at the centre surrounded by regularly spaced spots of lower intensity. The distinct arrangements of the spots on the pattern are consistent with various directions due to arrangement or pattern of the atoms in the material. Polycrystalline diffraction patterns differ in that the bright central spot is more diffuse; the surrounding spots have lower intensity and are arranged in concentric rings. The distance between each concentric ring to the centre of the bright spot corresponds to a particular plane. Additionally, amorphous diffraction patterns consist of a very diffuse bright central spot surrounded by diffuse concentric ring or rings.

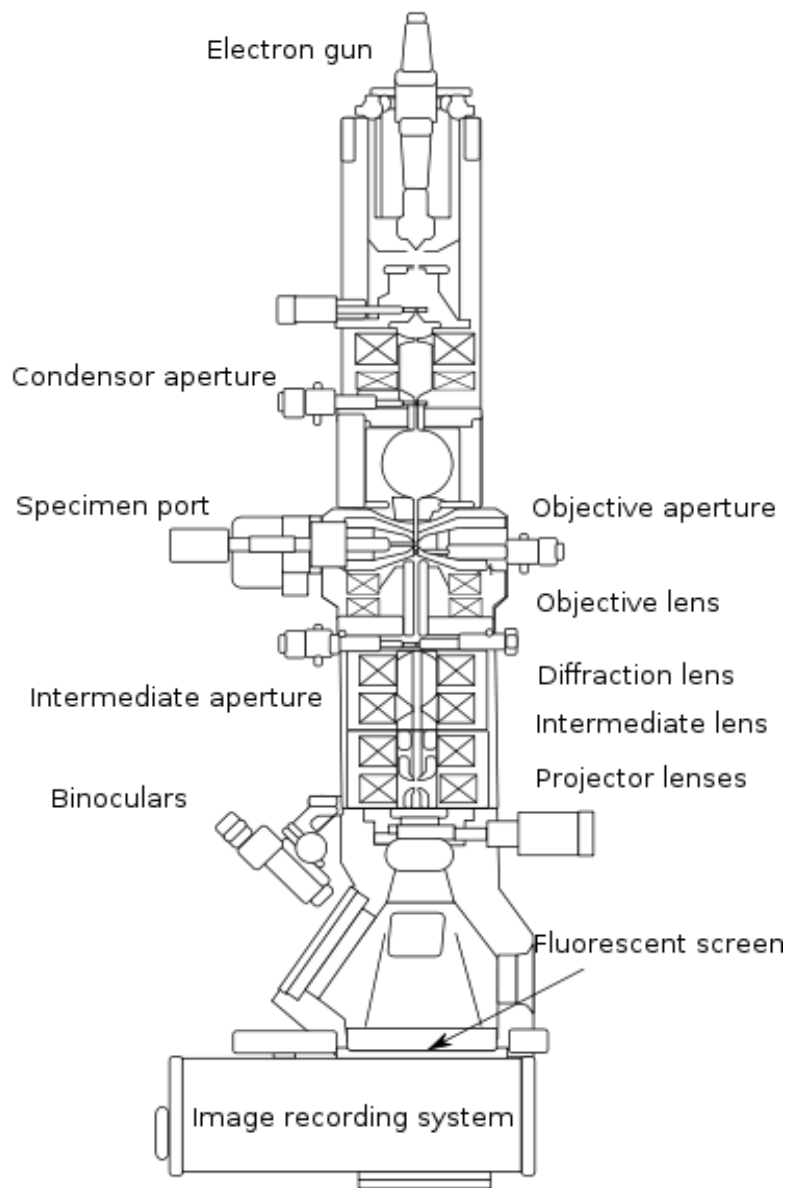


Fig. 3.7: The schematic diagram of a TEM [3.1].

3.5. PHOTOLUMINESCENCE SPECTROSCOPY

Photoluminescence spectroscopy (PL) is an important technique in the study of the surface defects states, donor and acceptor states and induced

trapping states present within the band gap of materials . When a photon, with energy greater or equals the band gap of a material is absorbed by a material it excites a valence electron which then transit to the conduction band. The excited electron returns back to initial state by losing the energy by emitting a photon which is observed in a form of radiation [3.6, 3.12]. The photon absorption process is strongly influenced by whether the material has a direct or indirect band. In a direct band: a valence electron gains energy and momentum from the incoming photon without changing its wave vector and vertically transit to the conduction band. Electrons and holes are formed in the conduction and valence bands respectively. However, in an indirect band gap material the excited electron needs additional energy in order to reach the band gap therefore the transition involve a phonon in other to conserve momentum [3.12]. During relaxation process the excitons loose energy and re-radiate photons. The PL spectrum indicates the transitions that were populated by excitons during excited state. The luminescence may be due to radiative recombination of excitons and the Coulomb bound electron hole pair [3.12]. In this study a room temperature PL analysis was performed using a Horiba Jobin-Yvon iHR 320 NanoLog spectrometer with a Symphony® cryogenic detector using a Xenon lamp as a continuous energy supply excited at 325 nm. The schematic is shown in Fig. 3.8.

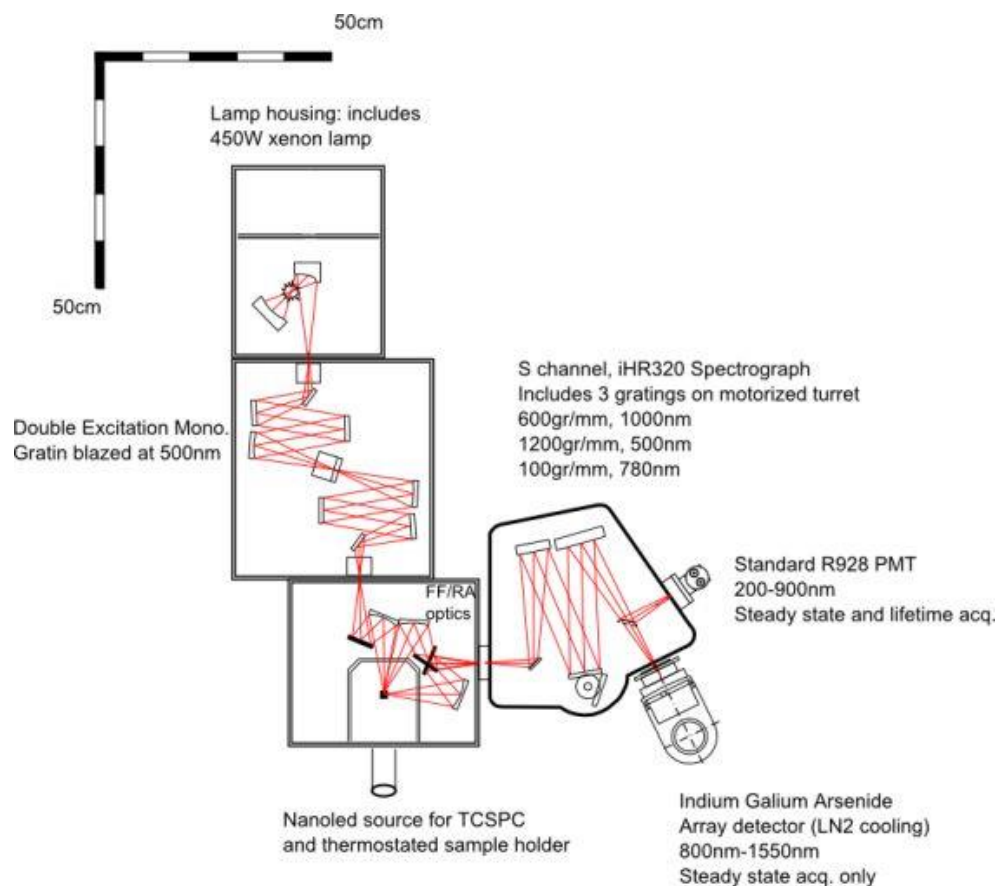


Fig. 3.8: The schematic of NanoLog [3.13].

3.6. ELECTRON PARAMAGNETIC RESONANCE

Electron paramagnetic resonance (EPR) spectroscopy which is based on the transitions between quantized states of the resulting magnetic moment was firstly demonstrated by the Russian physicist Zavoisky in 1944 following the quantum mechanics interpretation of the Zeeman Effect [3.14]. This technique is used for the structural characterization of nanoscale samples and gives information about the paramagnetic centres on various oxide surfaces, including diamagnetic oxides, nitroxides and transition metal ions. The paramagnetic

centres observed include surface defects, radicals, metal cations or supported metal complexes and clusters [3.14, 3.15]. Changes in specific location of the species on a surface of the material is highly influenced by the presence of other species in the system for example dopants or impurities, the size of the metal particles, post treatment conditions such as annealing and also the measurement conditions [3.15].

When a compound with an unpaired electron associated with a spin interacts with a strong magnetic field. The spin of the unpaired electron can be aligned in only two possible orientations. The two orientations have different magnetic potential energy which induces a lift in degeneracy of electron spin states as shown in Fig.3. 9 below. The spin alignment can either be parallel to the magnetic field with low energy state $m_s = -1/2$ or antiparallel to the magnetic field corresponding to high energy state $m_s = +1/2$ [3.15, 3.16]. The energy difference ΔE is given by:

$$\Delta E = E_+ - E_- = h\nu = g_e \mu_B B \quad (3.5)$$

$$\mu_B = \frac{e\hbar}{2mc} \quad (3.6)$$

where h is the Planck's constant ($6.626 \times 10^{-34} \text{ J s}^{-1}$), ν = the frequency of radiation, μ_B is the Bohr magneton ($9.274 \times 10^{-24} \text{ J T}^{-1}$), B is the magnetic field strength in Tesla, and g_e is the electron spin g-factor [3.16].

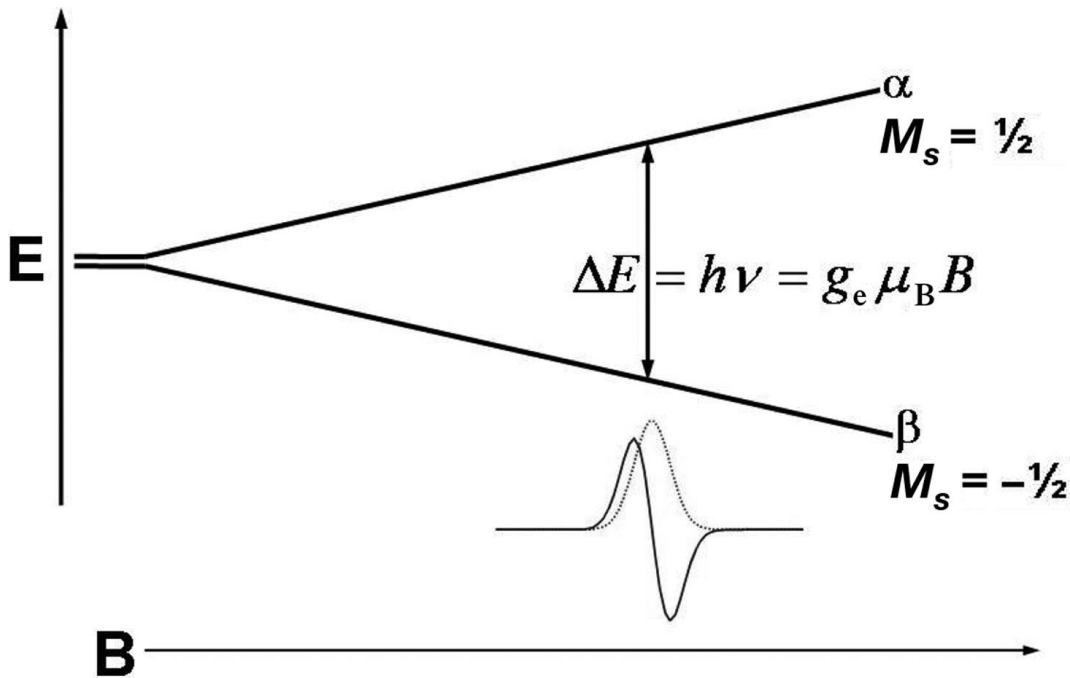


Fig. 3.9: Energy levels for an electron spin ($m_s = \pm 1/2$) in an applied magnetic field B [3.16].

During the EPR measurement the sample is exposed to a fixed microwave irradiation in-between linear magnetic field in order to excite some of the electrons in the lower energy level to the upper energy level. Unpaired electrons have a small magnetic field thus they align themselves parallel to the applied magnetic field (which is larger). The microwave irradiation induces a change in orientation of some of the unpaired electrons at a certain magnetic field strength resulting to separation of energy states as seen in Fig. 3.9 and is known as resonance condition [3.15]. The EPR spectrum we observe is a product of spectroscopic detection of this resonance.

There are three basic components to the EPR system (as shown in Fig. 3.10) namely: the magnetic field source, Microwave Bridge (resonator) and the signal detector. The generated microwave frequency is transmitted through a waveguide to the sample situated between the magnets. EPR spectroscopy can be carried out by varying the magnetic field and keeping the frequency constant or by varying the frequency and keeping the magnetic field constant. In this work the JOEL electron paramagnetic resonance (EPR) spectrometer operating at 9.4 GHz (X- band) at room temperature was used.

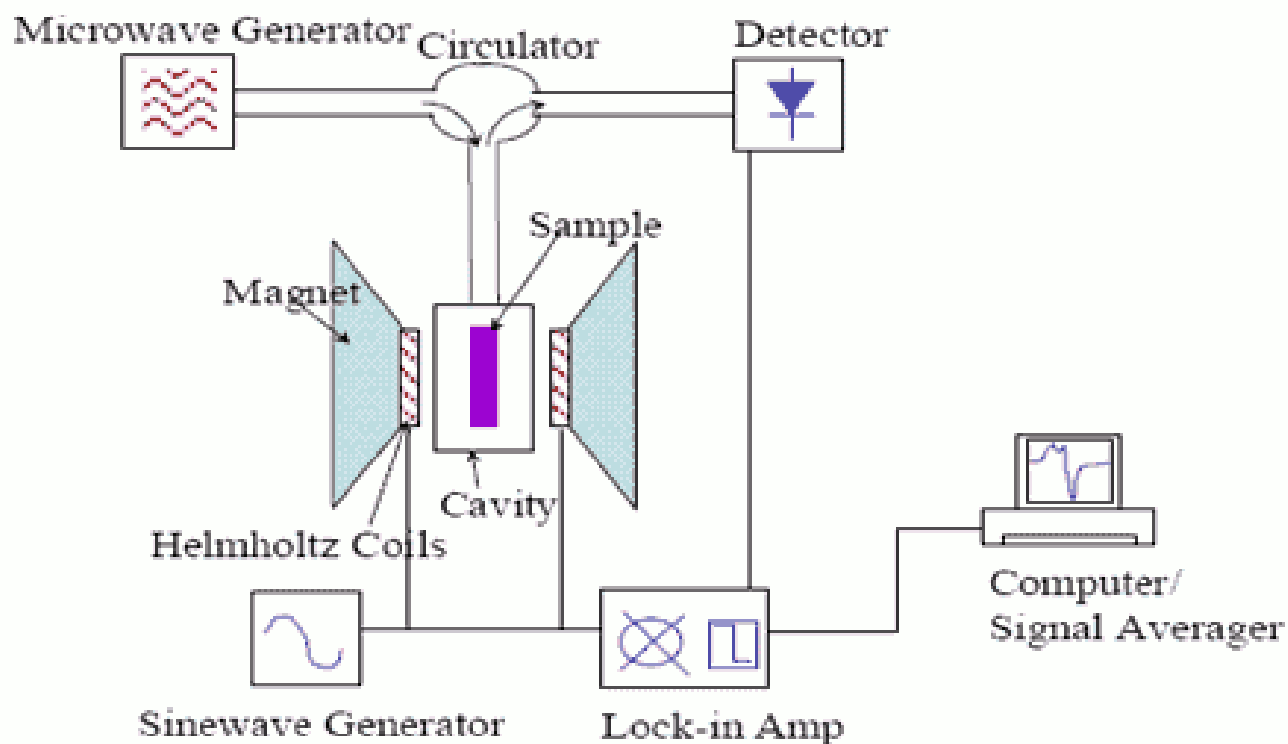


Fig. 3.10: Electron paramagnetic resonance set-up [3.17].

3.7. BRUNAUER-EMMETT-TELLER

The Brunauer-Emmett-Teller (BET) analysis is a vital technique based on the adsorption of gas molecules on solid surface. The technique gives information on surface characteristics such as the specific surface area, pore diameter and pore volume of nanomaterials. The BET theory was developed by Stephen Brunauer, Paul Emmett, and Edward Teller in 1938 as an extension of the Langmuir theory, developed by Irving Langmuir in 1916 [3.18]. The Langmuir theory assumed that the adsorbate behaves as an ideal gas at isothermal conditions, amount of adsorbed adsorbate is a function of pressure or concentration, all surface sites have the same adsorption energy for the adsorbate, each active site can be occupied only by one particle and the adsorbates form a monolayer. While the BET theory refers to infinite-layer adsorption, no interaction between each layer and the Langmuir theory holds on each layer. Non-corrosive gases like nitrogen, argon, carbon dioxide, etc. are normally used as adsorbates. The BET equation is given by (3.7):

$$\frac{1}{N((p_o/p)-1)} = \frac{c-1}{N_m c} \left(\frac{p}{p_o} \right) + \frac{1}{N_m c} \quad (3.7)$$

where N is the is the adsorbed gas quantity, N_m is the monolayer adsorbed gas quantity, p and p_o are the equilibrium and saturation pressures of the adsorbate at the temperature of adsorption and c is the BET constant. The adsorption

isotherms can be plotted as $1/(N((p_o/p)-1))$ against the partial pressure (p_o/p)

[3.18, 3.19].

In equation (3.7)

$$\frac{c-1}{N_m c} = \text{slope} \quad (3.7a)$$

$$\frac{1}{N_m c} = y - \text{intercept} \quad (3.7b)$$

Solving for $N_m c$ in (3.7b) and substitute into (3.7a) and solve for c we obtain:

$$c = \frac{\text{slope}}{y - \text{intercept}} + 1 \quad (3.7c)$$

Now by substituting (3.7c) into (3.7b) we get:

$$N_m = \frac{1}{\text{slope} + y - \text{intercept}} \quad (3.7d)$$

And the BET surface area is given by:

$$S_{\text{BET}} = \frac{N_m N_A}{V a} \quad (3.8)$$

where N_m is the monolayer adsorbed gas, N_A is Avogadro's number, V is molar volume of adsorbate gas and a is the mass of the adsorbent **[3.18]**.

In this work, the BET surface area, pore diameter and pore volume of the samples were measured by nitrogen (N_2) physisorption using a Micromeritics TRISTAR 3000 surface area analyser. To maintain accuracy, the samples were degassed for 2 hours at 110 °C to extract water molecules and impurities before BET analyses were carried out. In order to maintain accuracy, the glass cell (sample holder) must be properly cleaned to minimize contamination.

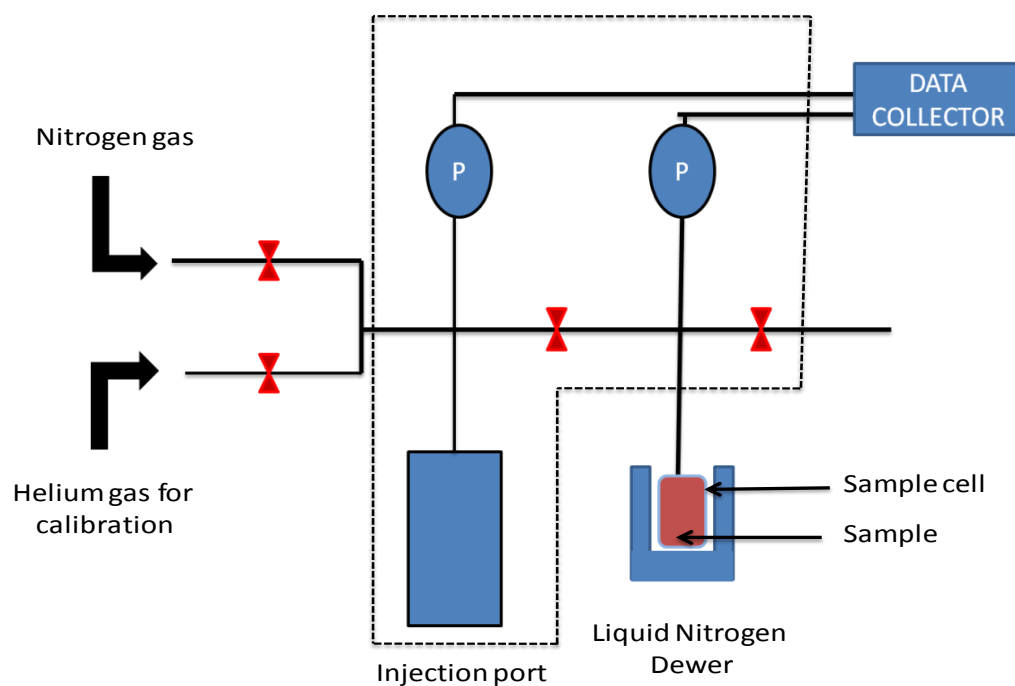


Fig. 3.11: Schematic diagram of the BET apparatus [3.19].

3.9. X-RAY PHOTOELECTRON SPECTROSCOPY

X-ray photoelectron spectroscopy (XPS) is a surface technique that measures the surface states, elemental composition, chemical and electronic

states of the elements within a material and is commonly known as electron spectroscopy for chemical analysis (ESCA) [3.20]. The technique was first reported by Siegbahn in 1967 based on the photoelectric effect outlined by Einstein in 1905 [3.21]. He later won a Nobel Prize in 1969 for producing the first commercial monochromatic XPS instrument with his research group at the University of Uppsala, Sweden.

The photoelectric effect describes the ejection of electrons from a metal surface when irradiated by light. Einstein proposed that light is not a wave propagating through space but a collection of wave packets called photons with energy (E) given by $E = h\nu$ where h is the Planck constant, ν is the frequency. For an electron to be ejected the photon energy must be greater than the materials work function (ϕ), if the energy is less no electron will be ejected. Thus, the photoelectric effect equation [3.22] is defined as:

$$E_{k(\max)} = h\nu - \phi \quad (3.9)$$

Where $E_{k,\max}$ is the maximum kinetic energy of the ejected electron. The excited electrons move from the core state into the continuum, leaving holes in the molecule resulting to an ion (X^+). The kinetic energy of the ejected electron is measured by a detector. XPS is dependent on photoemission due to x-rays with energy range at 100 eV to 100 keV, therefore with the knowledge of the x-ray excitation energy, the binding energy (BE) of the specific orbital from which an electron is ejected can be evaluated by using the Einstein equation of

photoelectric effect. Ernest Rutherford proposed equation 3.10 in other get the BE of each of the emitted electrons **[3.22]**:

$$BE = E_p - E_{k(\max)} - \phi \quad (3.10)$$

where E_p is the energy of the x-ray photon irradiated on the material.

The characteristic spectral peaks observed on the XPS spectrum correspond to the electronic configuration (1s, 2s, 2p, 3s,) in the atoms and each peak represents the amount of element contained. Fig. 3.12 shows a schematic diagram of the XPS setup. The XPS detectors in the instrument require ultra-high vacuum to operate, in order to compensate for the long path length (1 m) between detectors and the material. Only the electrons that have been ejected and reached the detector are measured. The excited electrons can undergo recombination, trapping in excited states or inelastic collision within the material and loose kinetic energy resulting to less electrons escaping. It is noteworthy that the XPS cannot detect hydrogen and helium **[3.23]**.

In this work the XPS analysis for TiO₂ nanostructure in powder form were performed using a PHI 5000 Versaprobe – Scanning ESCA Microprobe. Less volatile materials are preferred for XPS analysis.

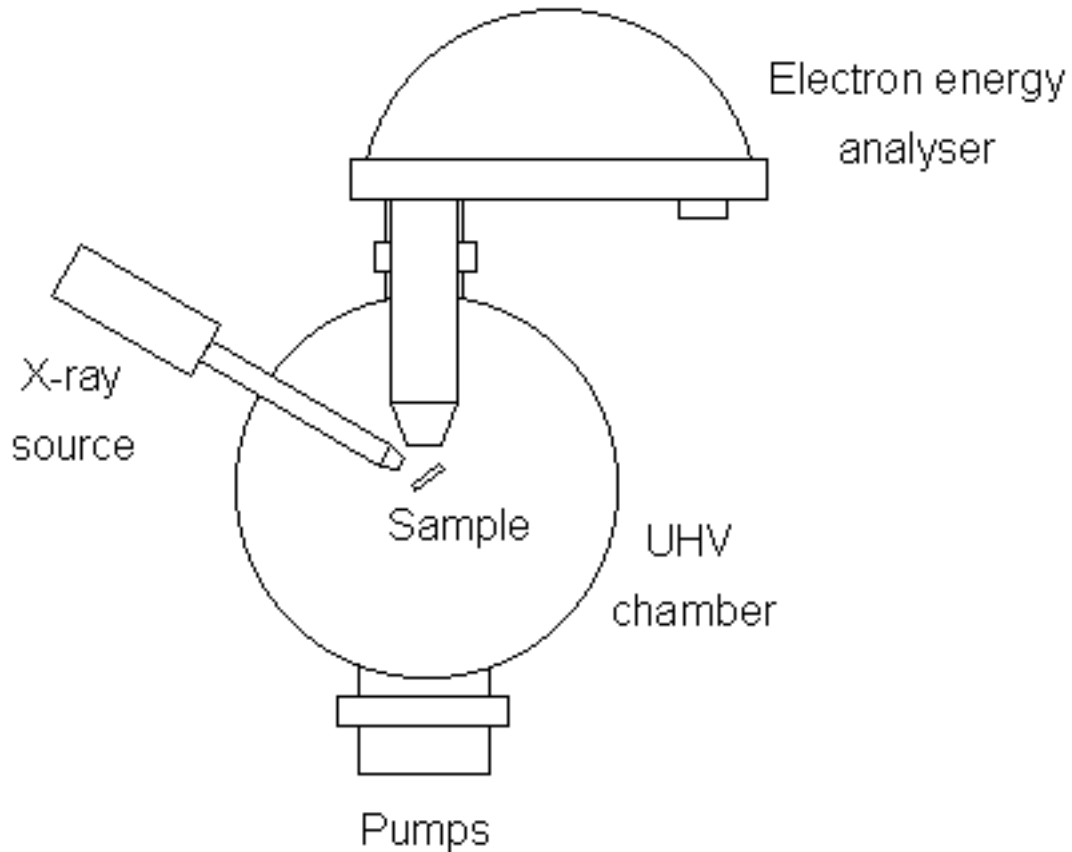


Fig. 3.12: Schematic diagram of the XPS system [3.24].

3.10. GAS TESTING STATION

Gas sensing device is used to detect and monitor the presence of gases in the environment; it can be work places like underground mining, homes and public places. The gases can be harmful, combustible and pose a threat to human health and the ecosystem. These devices are used to detect gas leaks and are incorporated with an alarm to alert people giving them chance to evacuate and take proper safety precautions and some can initiate automatic

shut down. Earlier people relied on their noses to detect gases however some gases are odourless and are dangerous when inhaled at high concentrations and prolonged period thus, a number of life threatening incidents and fatal deaths occurred before modern day electronic sensors. Gas detectors can be classified according to the operation mechanism such as electrochemical, semiconductor, infrared, ultrasonic and holographic [3.26].

A KENOSISTEC KSGAS6S Italy gas sensing instrument set-up used in this work is shown in Fig. 3.13. The system consists of a sensing chamber with sample stages, an air mixer and a dry air inlet carrying dry air into the mixer, four different gas inlets, mass flow controllers to control the amount of gas into the chamber, two thermostatic baths, one supplies wet air into the mixer during humidity measurements and the second is for volatile gas measurements, six KEITHLEY picoammeters for the conductance measurement and six heaters that supply voltage across the sample, gas inlet and outlets including a vent outlet. Fig. 3.13b shows the image of the system's main window. The gas sensing measurements were conducted by pasting homogenous paste of the sample on one side of interdigitated electrode and fixed it to the sample stage in the sensing chamber. The samples were then exposed to gases and humidity in the chamber over a period of time. The picoammeters record the conductance for various gases and humidity concentrations and the heater supplies voltage across the sample.

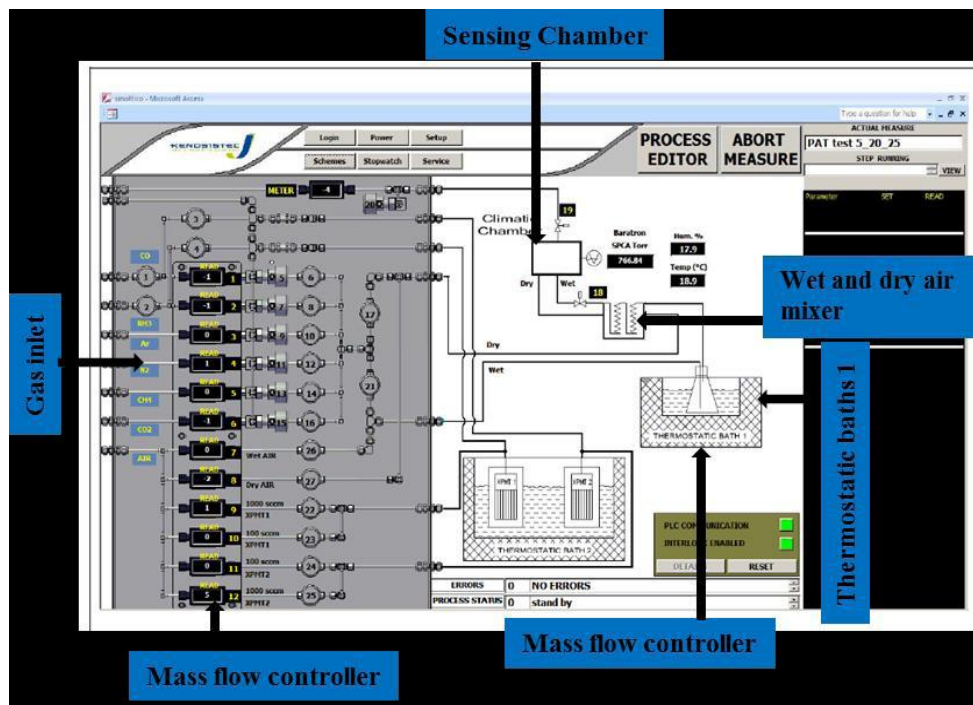
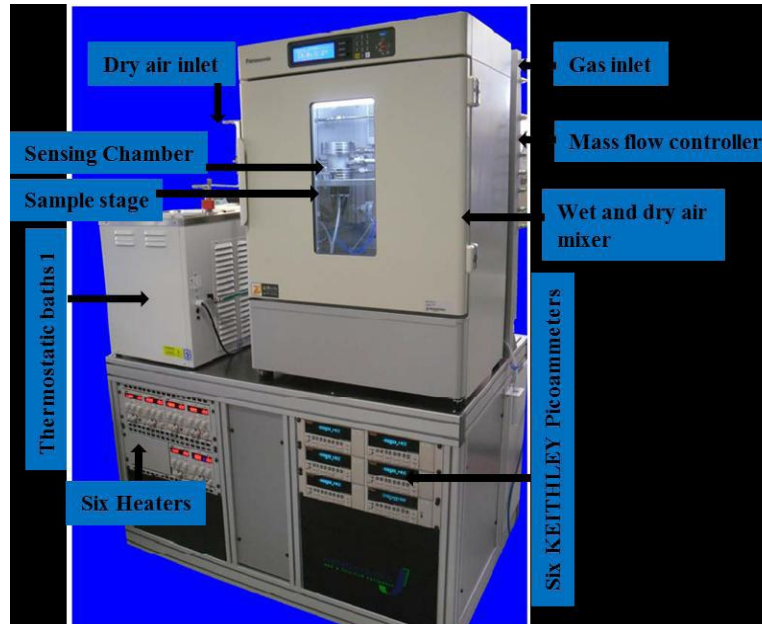


Fig.3.13: KENOSISTEC (a) gas sensing station and (b) Main operational window (or set-up). KENOSISTEC UHV & THIN FILM EQUIPMENT [3.27].

3.11. EXPERIMENTAL DETAILS

3.11.1. Materials and Chemicals

P25 TiO₂ Degussa (99.9 % purity), manganese (II) nitrate tetrahydrate (Mn(NO₃)₂ · 4H₂O), sodium hydroxide (NaOH) (99.9 % purity), hydrochloric acid (37 % purity) were purchased from Sigma-Aldrich and used as received without any purification.

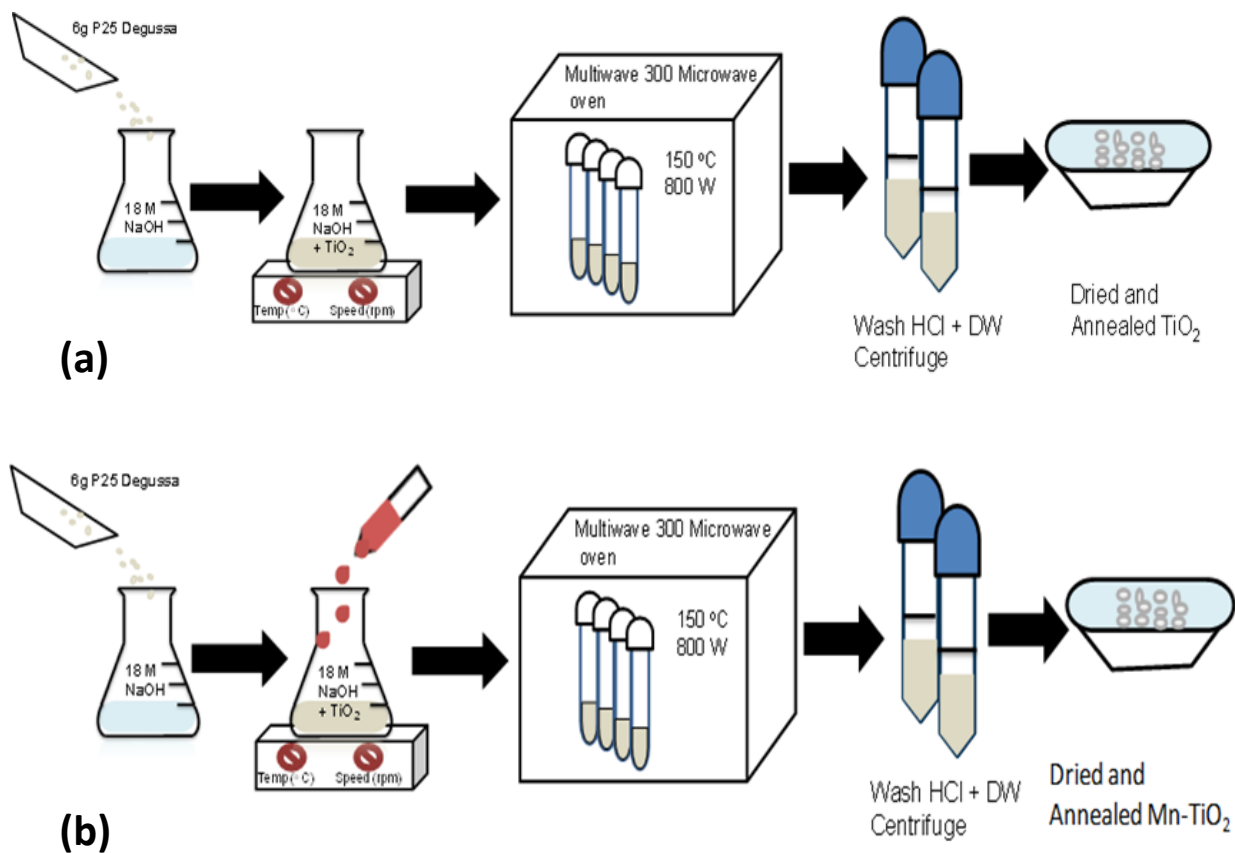


Fig. 3.14: Synthesis procedure for both (a) undoped and (b) Mn-doped TiO₂ nanoparticles

3.11.2. Synthesis procedure of TiO₂ nanoparticles

For pure TiO₂ nanostructures, microwave assisted hydrothermal method was followed to synthesize TiO₂ nanoparticles. As shown on the Schematic diagram in Fig.3.14a, 6g of commercial P25 TiO₂ powder used as a starting material was added into 100 mL of 18 M NaOH. The mixture was stirred for 10 minutes to ensure that it is homogeneous and transferred into 4 100 ml Teflon vessels. The mixture was then subjected to microwave irradiation for 15 minutes in a (Perkin Elmer/Anton Paar Multiwave 3000) Microwave oven. The products were allowed to cool down at room temperature. For comparison, separate products were washed with distilled water (H₂O), while the rest were washed with 0.25, 0.5 and 1.0 M HCl until the desired pH of 8 was obtained. The final product was then filtered and dried in a vacuum oven at 120 °C for 14 hours. The samples were then calcined for 3 hours at 450 °C and characterized in detail using various analytical techniques.

For the annealing study, the as-synthesized TiO₂ nanostructures were post annealed at 300, 450 and 700 °C for 3 hours.

For Mn doped TiO₂ nanoparticles the same procedure was followed however for the doped samples (see Fig.3.14b), 1.5, 2.0, 2.5, and 3.0 mol % of Mn (NO₃)₂ 4H₂O were dissolved in 10 mL distilled water and added drop wise while stirring before subjecting to microwave and washed with 1.0 M HCl.

3.12. REFERENCES

- [3.1] B. Fultz, J. Howe, Springer (2003).
- [3.2] B.D. Cullity, Addison Wesley, (1956).
- [3.3] J.R. Connolly, for EPS400-002, Springer (2007)
- [3.4] B.R. Rehani, P.B. Joshi, K.N. Lad, A. Pratap, Indian J. Pure & App. Phy. 44 (2006) 157 – 161.
- [3.5] C.V. Raman, K.S. Krishnan, Indian J. Phys. 2 (1928) 387-398.
- [3.6] E. Smith and G. Dent, Wiley and Sons Ltd., Great Britain (2005)
- [3.7] J.R. Ferraro, K. Nakamoto, C.W. Brown, Elsevier (2003).
- [3.8] D.B. Williams and C.B Carter, Springer (2009).
- [3.9] R.F. Egerton, Springer (2005).
- [3.10] J. Goldstein, Third Edition, Springer (2003).
- [3.11] <http://www.microtechsciences.com/images/sem-diagram.gif>
- [3.12] P. Bamfield, M.G. Hutchings, 2nd edn., The Royal Society of Chemistry, Cambridge (2010).
- [3.13] <http://fluorescence.ttk.pte.hu/nanologseminar2013/devices.php>
- [3.14] P.L. Hall, Clay Minerals 15 (1980) 321-335.
- [3.15] D.M. Murphy, Chapter 1, WILEY-VCH Verlag GmbH & Co. KGaA, Weinheim (2009).
- [3.16] J. Weil and J. Bolton, second edition. J. Wiley, USA (2007).
- [3.17] <http://stanford.edu/courses/2007/ap272/thareja1/>
- [3.18] S. Brunauer, P.H. Emmett, E. Teller, J. Am. Chem. Soc, 60 (2) (1938) 309–319.

- [3.19] A.R. Barron, *Connexions* (2014).
- [3.20] K. Siegbahn, K.I. Edvarson, *Nuclear Physics* 1 (8) (1965) 137–159.
- [3.21] A. Einstein, *Ann. Physik* 17 (1905) ,132. 1921 Nobel Prize in Physics.
- [3.22] Iris and Wolfgang E. S Unger, 7 (2003) 519.
- [3.23] L.C. Feldman, J.W. Mayer, (1986).
- [3.24] http://www.chem.qmul.ac.uk/surfaces/scc/scat5_3.htm
- [3.25] S. Capone, A. Forleo, L. Francioso, R. Rella, P. Siciliano, J. Spadavecchia, D.S. Presicce, A.M. Taurino, *Journal of Optoelectronic and Advanced Materials* 5 (2003) 1335-1348.
- [3.26] KENOSISTEC UHV & THIN FILM EQUIPMENT (ITALY)

CHAPTER FOUR

Facile synthesis of improved room temperature gas sensing properties of TiO₂ nanostructures: Effect of acid treatment¹

ABSTRACT

TiO₂ nanoparticles were synthesized via a simple hydrothermal method in a sodium hydroxide (NaOH) aqueous solution and washed with distilled water and different concentrations of hydrochloric acid which acted as the morphological/crystallographic controlling agent. Microscopy analysis showed that the size of the TiO₂ nanoparticles could be easily tailored and tuned by varying the HCl concentration. The phase transformation from a mixture of anatase and rutile phases to pure anatase phase was observed at higher HCl concentration. The particle sizes were reduced while the Brunauer-Emmett-Teller surface area increased when increasing the HCl concentration, thus resulting in higher sensing response and selectivity to NO₂ at room temperature. The X-ray photoelectron spectroscopy, photoluminescence and electron paramagnetic resonance studies also revealed that the 1.0 M sample contain high relative concentration of oxygen vacancy and Ti⁴⁺ and Ti³⁺ interstitial defect states which played a vital role modulating the sensing properties.

¹The content of this paper has been published in: Sensors and Actuators B: Chemical 224 (2016) 841–856

Keywords: TiO₂, morphology; HCl, gas sensing; NO₂.

4.1. INTRODUCTION

Gas sensing devices that will control air quality during combustible processes, industrial emissions, and auto motive vehicles are required [4.1]. Such devices need to be reliable, low cost, portable and compatible to micro electronics systems [4.2, 4.3]. A great deal of research has focused on the development of gas sensors that are highly sensitive, selective, stable, and have low working temperatures and provide short response-recovery time [4.4-4.8]. In addition global warming is increasing at a high rate due to air pollution. Pollutants such as carbon monoxide (CO), carbon dioxide (CO₂), nitrogen monoxide (NO_x), ammonia (NH₃), hydrogen (H₂) hydrogen sulfide (H₂S) and hydrocarbons emitted from cars and industries can cause respiratory diseases and may results in fatalities if inhaled in higher concentration [4.5, 4.6].

Numerous semiconducting metal oxides (MOX) have been studied as gas sensors including ZnO, SnO₂, WO₃, V₂O₅ and Fe₂O₃. Among them, TiO₂ has been one of the attractive materials due to its various properties such as wide band gap, high photocatalytic activity, biocompatibility, chemical stability, high melting point and its enhanced surface reactivity [4.1-4.7]. TiO₂ has three crystalline phases, namely anatase, brookite and rutile. The rutile phase is stable thereby enabling TiO₂ to operate at harsh environment. Anatase phase is metastable and is popular for photocatalytic activity [4.3, 4.5- 4.7]. TiO₂ nanoparticles have optical and electrical properties different from those of its bulk

form thus synthesis of TiO₂ nanostructures enables manipulation of such properties and vast application such as sensing. The ability of a MOX to sense can be determined by the change in electrical resistance when exposed to different concentration of a target gas. In order to increase selectivity and sensitivity of the gas sensor different materials have been introduced as dopants. Generally dopants alter some properties of the host material such as altering the band gap, electrical resistivity and inhibit particle growth [4.8]. Corotta *et al.* [4.8] studied TiO₂ doped with Niobium thick film gas sensors for environmental monitoring. The sensors showed great response to low concentrations of CO up to 850 °C working temperature. Recently, Meng *et al.* [4.9] reported gas sensing properties of Pd-doped TiO₂ nanowires exposed to different concentrations of H₂. They indicated that Pd doped samples exhibited higher response to H₂ at 200 °C working temperature.

Irrespective of the great body of research achieved to date, there are still few or no reports on room temperature gas sensing of H₂, NH₃, NO₂ and CH₄ using undoped TiO₂ nanoparticles in a pure anatase phase. Chen *et al.* [4.10] reported a room temperature H₂ gas sensing on highly ordered TiO₂ nanotube arrays through anodization. Dhivya *et al.* [4.11] reported a room temperature gas sensing of NH₃ using mixed phase TiO₂ nanoparticles deposited on a glass substrate at -100 V bias voltage. Besides, studies have attempted to reduce the sensing operating temperature by introducing various dopants and using mixed oxides. A room temperature NO₂ gas sensing on Al/TiO₂/Al₂O₃/p-Si film using UV-light irradiation was reported by Karaduman *et al.* [4.12] Chen *et al.* [4.13]

reported a room temperature NH_3 gas sensing on NiO-wrapped mesoporous TiO_2 microspheres under UV- irradiation. A room temperature gas H_2 sensing on TiO_2 nanotubes decorated with Pd nanoparticles was reported Xiang *et al.* [4.14]. Mun *et al.* [4.15] reported a room temperature NH_3 gas sensing on cellulose- TiO_2 -multiwall carbon nanotube nanocomposite.

In this work we investigate the room temperature gas sensing of H_2 , NH_3 , NO_2 and CH_4 on pure anatase TiO_2 nanoparticles synthesized using microwave-assisted hydrothermal method in an 18 M NaOH aqueous solution and washed with H_2O and various concentrations of hydrochloric acid. The alterations on microstructures of TiO_2 nanostructures, induced by the acid washing process are also studied. We show in detail that by increasing HCl concentration up to 1.0 M, the sensing properties improves at room temperature compared to commercial P25 showing higher response at higher operating temperature. The PL, XPS and EPR are conducted to study the defects states contributing to the sensing properties.

4.2. EXPERIMENT DETAILS

4.2.1. Materials and Chemicals

P25 TiO_2 Degussa (99.9 % purity), sodium hydroxide (NaOH) (99.9 % purity), hydrochloric acid (37 % purity) were purchased from Sigma-Aldrich and used as received without any purification.

4.2.2. Synthesis procedure of TiO₂ nanoparticles

Microwave assisted hydrothermal method was employed to synthesize TiO₂ nanoparticles. 6g of commercial P25 TiO₂ powder used as a starting material was added into 100 mL of 18 M NaOH. The mixture was stirred for 10 minutes to ensure that it is homogeneous and transferred into 4 100 ml Teflon vessels. The mixture was then subjected to microwave irradiation for 15 minutes in a Microwave oven (Perkin Elmer/Anton Paar Multiwave 3000). The products were allowed to cool down at room temperature. For comparison, separate products were washed with distilled water (H₂O), while the rest were washed with 0.25, 0.5 and 1.0 M HCl until the desired pH of 8 was obtained. The final product was then filtered and dried in a vacuum oven at 120 °C for 14 hours. The samples were then calcined for 3 hours at 450 °C.

4.2.3. Sensor fabrication and testing of devices

For gas sensing measurements, TiO₂ nanoparticles were dispersed in ethanol and drop-coated on alumina substrates (size: 2 mm × 2 mm) with two Pt electrodes (on its top surface) and a micro-heater (on its bottom surface). The deposited sensitive layer was heated to 450 °C to remove the organic solvent used and to obtain good adhesion. The sensing measurements were carried out at RT, 250, 300, 350 and 400 °C by varying the voltage. A flow-through technique with a constant flow rate of 250 ml/min was used to test the electrical and gas-sensing properties of the sensing films. A constant flux of synthetic air of 0.5 l/min was used as gas carrier into which the desired concentration of H₂, CH₄,

NH₃ and NO₂ gases. The measurements were carried out in a dry air atmosphere (79% nitrogen and 21% oxygen). The gas sensing response of the device was examined when monitoring the variation of the resistance of the sensors using a gas sensing station KSGAS6S (KENOSISTEC, Italy).

4.2.4. Characterization Techniques

The TiO₂ crystallographic structure was examined using Panalytical X'pert PRO PW 3040/60 X-ray diffractometer (XRD) equipped with a Cu-K α ($\lambda = 0.154$ nm) monochromatized radiation source. A Horiba Jobin-Yvon HR800 Raman microscope with 514.5 nm excitation laser was used for Raman studies. High-resolution transmission electron microscopy (HR-TEM) analyses were carried out at 200 kV with a JEOL-TEM 2100 instrument to investigate the localized phase formation and crystal growth of the TiO₂ nanostructures. TiO₂ powders were deposited on holey-carbon-coated Cu grids from alcohol suspensions. Scanning electron microscopy (SEM) micrographs of the TiO₂ nanoparticles were measured at an accelerating voltage of 3 keV using an Auriga ZEISS. The specific surface area and the pore volume of the samples were measured by nitrogen (N₂) physisorption using a Micromeritics TRISTAR 3000 surface area analyzer. Before the analysis, the samples were degassed at 110 °C for 2 hours under a continuous flow of N₂ gas to remove adsorbed contaminants. The Photoluminescence (PL) spectra were determined using Jobin-Yvon NanoLog spectrometer. A PHI 5000 Versaprobe-Scanning ESCA Microprobe was used to carry out X-ray photoelectron spectroscopy (XPS) analysis. A JEOL X-band

electron paramagnetic resonance (EPR) spectrometer was used for microwave absorption measurements of the TiO₂ samples at constant frequency (9.4 GHz) and at room temperature (298 K).

4.3. RESULTS AND DISCUSSION

4.3.1. Effect of acid treatment

X-ray diffraction analysis was carried out to study the structure of the P25 TiO₂ nanoparticles and that washed with distilled water (H₂O) and different concentrations of HCl aqueous solution. As shown in Fig. 4.1, the starting material, P25 Degussa, has a mixture of both Anatase and Rutile phases of TiO₂. After hydrothermal treatment, the intensity of the diffraction peaks was reduced. Wang *et al.* [4.16] indicated that while treated in aqueous NaOH, TiO₂ crystals become amorphous because the Ti–O bond gets broken and Ti–O–Na or Ti–OH bonds forms. The broad peak observed at 30.5 ° for the samples washed with H₂O only and 0.25 M HCl is related to H₂Ti₃O₇ [4.17]. After the samples were washed with higher concentration of HCl, the peaks assigned to TiO₂ anatase structure as seen in JCPDS File No. 76-1940 were observed. No other peaks are observed that can be assigned to impurities indicating pure TiO₂. To quantify the phase transformation in the sample, peak intensity ratios were extracted from XRD spectra and the amount of rutile phase was computed with the empirical relationship used by Depero *et al.* [4.18]:

$$W_R = \frac{1}{1 + (1.26 I_R / I_A)^{-1}} \quad (4.1)$$

where W_R is the fraction of rutile phase, I_R is the value of the highest XRD peak of Rutile and I_A is the highest anatase peak. The rutile fraction was found to be 21.28 % for the commercial P25 sample and while the hydrothermally treated samples showed no rutile phase. The low HCl concentration acts as a catalyst that decreases the activation energy for the formation of rutile TiO_2 during crystal growth. Previous reports [4.19] indicated that at lower HCl concentration, the formation of anatase is favoured, while, at high concentration, the formation of anatase is inhibited and formation of the rutile phase is preferred. This is due to that at higher HCl concentration, the surface of the titania becomes protonated, and the titania gets solubilized. As a result this promotes a dissolution precipitation mechanism to take place, resulting in the formation of rutile phase. However, it should be pointed out that, some formation of anatase phase will exist, due to the solid-state mechanism [4.19, 4.20]. Hence, the formation of rutile at elevated temperatures (>600 °C) which is a result of higher solubility and faster reaction kinetics induced by higher temperature, resulting to an increase of the rate of the dissolution/precipitation mechanism more than the solid-state mechanism. This mechanism has been described in more detail by Yanagisawa *et al.* [4.19]. Increasing the HCl concentration to 1.0 M affects the O-Ti-O bond structure causing rearrangement of the octahedral [4.21]. This suggests that the HCl concentration promotes phase transition and the crystallinity of the

nanoparticles. Table 4.1 shows a summary of the crystallite sizes and lattice strain of the samples calculated using the William – Hall equation [4.22]:

$$\beta \cos \theta = \frac{k\lambda}{L} + 4\varepsilon \sin \theta \quad (4.2)$$

where L is the crystallite size, k is a constant equals to 0.9, λ is the wavelength of the X-ray radiation equals to 0.154056 nm, β is the peaks full width at half maximum and θ is the diffraction angle. The distance between adjacent crystal planes d , was calculated using Bragg's equation $\lambda = 2d \sin \theta$ [4.23], and the values are listed in Table 4.1.

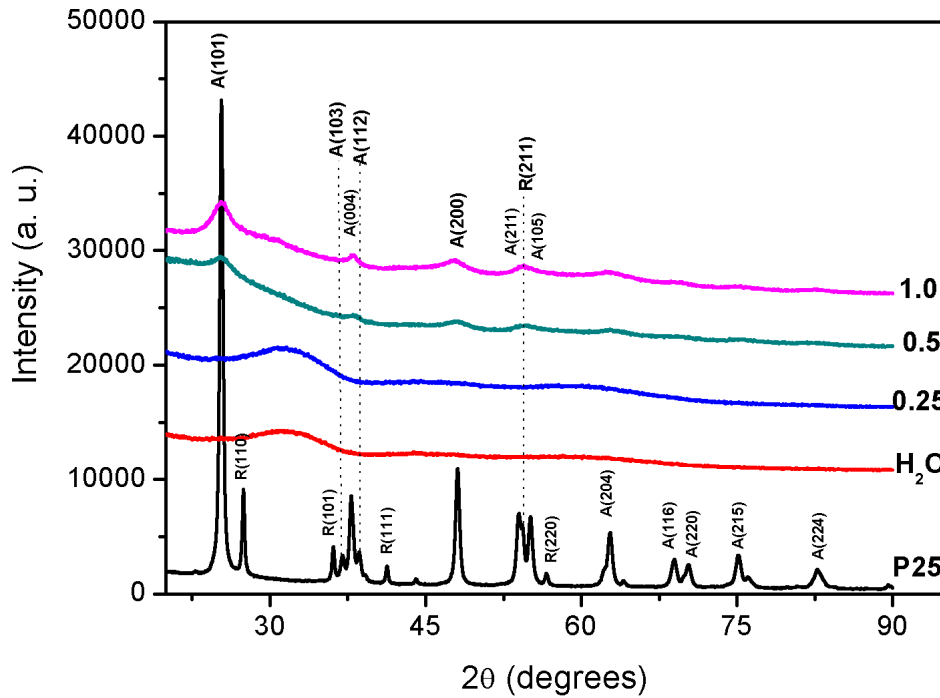


Fig. 4.1: XRD patterns of TiO₂ nanoparticles washed with H₂O and different concentrations of HCl. **Note: R represents rutile and A anatase**

Trinh *et al.* [4.24] indicated that the response of the metal-oxide gas sensors also depends mainly on the crystallite size of the sensing materials. This denotes that, if the size of the crystallite size is close to the size of the Debye length ($L \geq L_{\text{Debye}}$), then the sensing material can display excellent sensing response. However, if the crystallite size is significantly larger than the L_{Debye} , then the response of an oxide semiconductor is independent of the crystallite size. Therefore, Table 4.1 shows that, when the grain size decreases, the lattice strain increases.

Table 4.1: Summary of crystallite size (L) and strain of TiO_2 samples washed with H_2O and different concentrations of HCl .

| Sample | h k l | 2θ | d_{hkl} (nm) | L (nm) | strain |
|-----------------------|-------|-----------|----------------|--------------|---------|
| P25 | (101) | 25.34 | 0.351 | 20.09 | 0.00746 |
| | (110) | 27.45 | 0.324 | | |
| H₂O | (101) | - | - | - | - |
| | (110) | - | - | - | - |
| 0.25 M | (101) | - | - | - | - |
| | (110) | - | - | - | - |
| 0.5 M | (101) | 25.24 | 0.352 | 4.46 | 0.23764 |
| | (110) | - | - | - | - |
| 1.0 M | (101) | 25.24 | 0.353 | 6.46 | 0.23432 |
| | (110) | - | - | - | - |

Fig. 4.2 shows the Raman spectra of the TiO_2 nanoparticles washed with distilled H_2O and different HCl concentrations. The P25 sample shows strong Raman active modes $E_{g(1)}$, $E_{g(2)}$, $B_{1g(1)}$, A_{1g} , $B_{1g(2)}$ and $E_{g(3)}$ at 141.7, 193.2, 392.5,

513.4 and 634.5 cm^{-1} corresponding to anatase and rutile phases of TiO_2 [4.25-4.27]. The H_2O and 0.25 M samples show amorphous behavior with a broad shoulder at 197.06 and 650.59 cm^{-1} corresponding to $E_{g(2)}$ and $E_{g(3)}$, respectively. The 1.0 M sample shows more resolved peaks. Moreover, the $E_{g(2)}$ peak at 196.30 cm^{-1} becomes more visible compared to the rest. The increase in the peak intensity is due to improved crystallinity, while the broadening of XRD peaks could be induced by the smaller particle size as demonstrated by the TEM results and particle size distribution shown in Figs. 4.3 and 4.4, respectively [4.28]. This increase in intensity with higher washing HCl concentration correlates with the XRD results. When HCl concentration increases, a blue shift is observed from 140.37 to 144.96 cm^{-1} , which is probably due to phonon confinement effects.

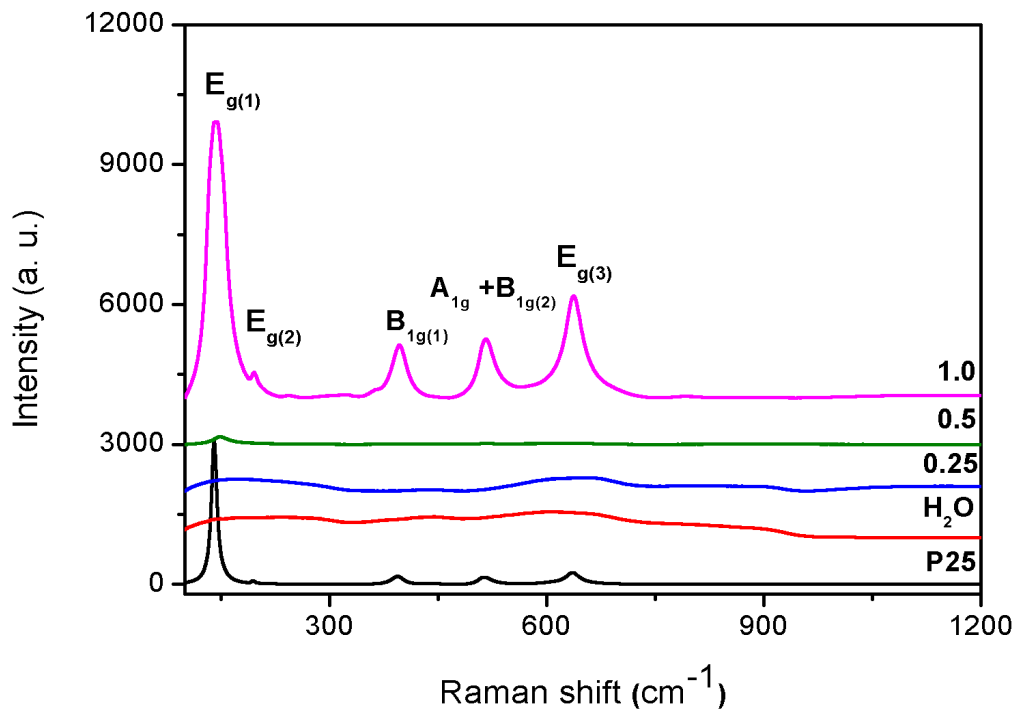


Fig. 4.2: Raman spectra of TiO_2 nanoparticles washed with H_2O and different concentrations of HCl.

Fig. 4.3 shows TEM micrographs and selected area electron diffraction (SAED) patterns of commercial P25 TiO₂ nanoparticles compared with those treated hydrothermally and washed with H₂O and different concentrations of HCl aqueous solution. Fig 4.3a shows that the P25 sample consists of nanoparticles with an average particles size of ~18 nm as depicted in the particle size distribution (Fig. 4.4a). HR-TEM image in Fig. 4.3b shows lattice fringes with d-spacing's of 0.329 nm and 0.355 nm corresponding to (101) anatase phase. It can be seen on SAED patterns (Fig. 4.3b, inset), that the nanoparticles are polycrystalline.

The hydrothermally treated samples washed with H₂O reveal agglomerated particles with irregular shapes. Upon washing the samples with HCl, the particle size decreases and this is confirmed by particle size distribution in Fig 4.4c-e. SAED patterns, (Fig. 4.3d) show diffused Debye-rings denoting that the material contain an amorphous phase. This is in agreement with XRD results which showed that samples washed with H₂O, 0.25 and 0.5 M are dominated by amorphous phase. When HCl concentration increases (1.0 M), lattice fringes with d-spacing's of 0.349 nm and 0.362 nm corresponding to (101) anatase are observed. The presence of an amorphous phase is shown by arrows. SAED patterns in the inserts of Fig. 4.3h depict that the samples are polycrystalline with diffused rings.

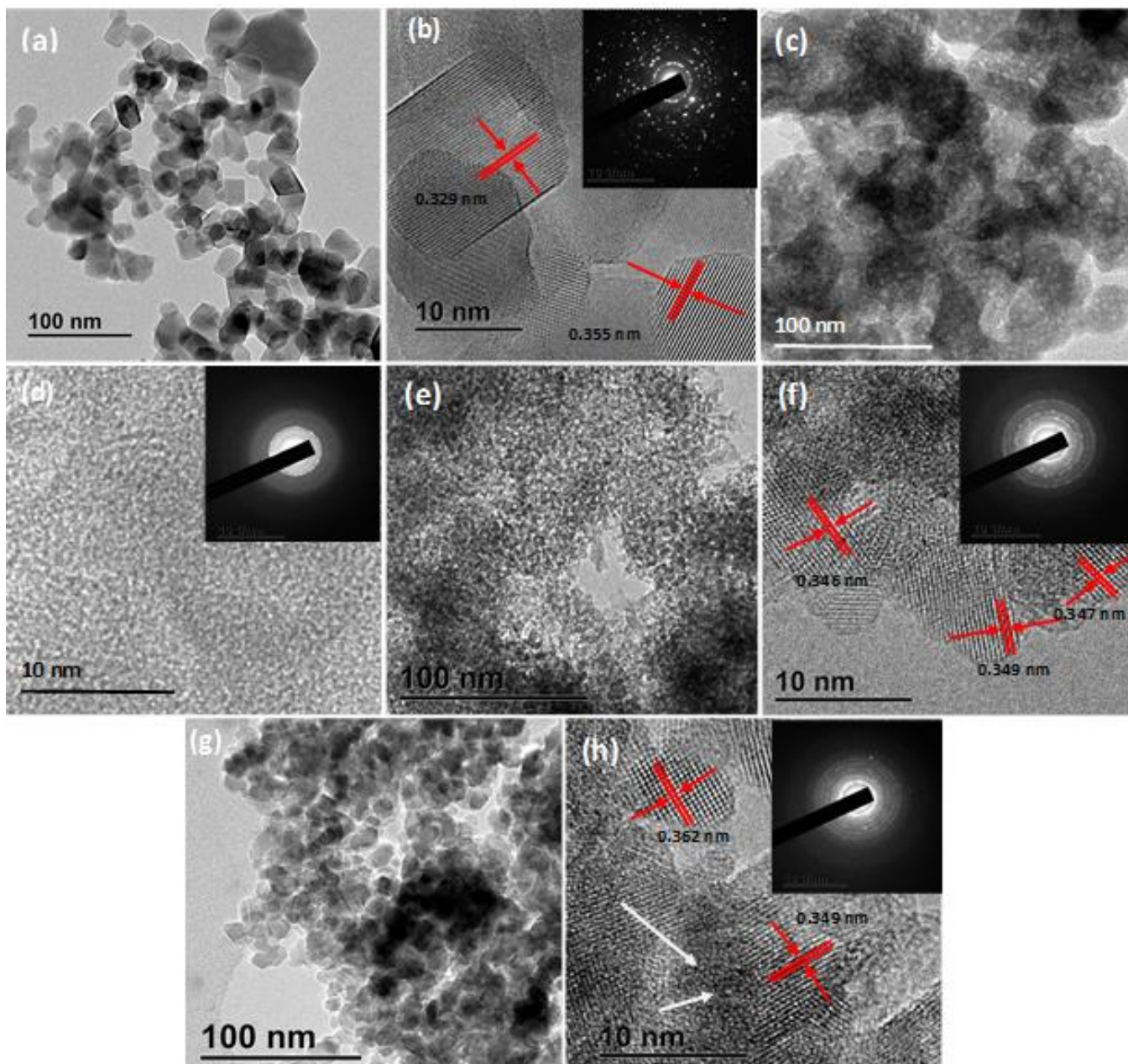


Fig. 4.3: TEM images of TiO_2 (a-b) commercial P25, washed with (c-d) H_2O , (e-f) 0.5 M and (g-h) 1.0 M.

The SEM images of P25 Degussa compared with that washed with H₂O and various concentrations of HCl aqueous solution are shown in Fig. 4.5. After hydrothermal treatment of the P25 Degussa, the agglomerated nanoparticles formed a porous surface which might be beneficial for the sensing properties resulting in adsorption of high quantities of a gas. The particle size of the samples decreased as the concentration of the HCl was increased as seen in Fig. 4.5c-e and this is consistent with the particle size distribution in Fig. 4.4c-e. The results indicate that when the grain size increases, grain boundaries decrease providing a large surface area thus increasing the sensing properties. Furthermore, the texture of the 0.5 and 1.0M HCl samples changes showing the “fibril-like” or fluffy structures as depicted by the arrows in Fig. 4.5e. In addition, the surface becomes more porous.

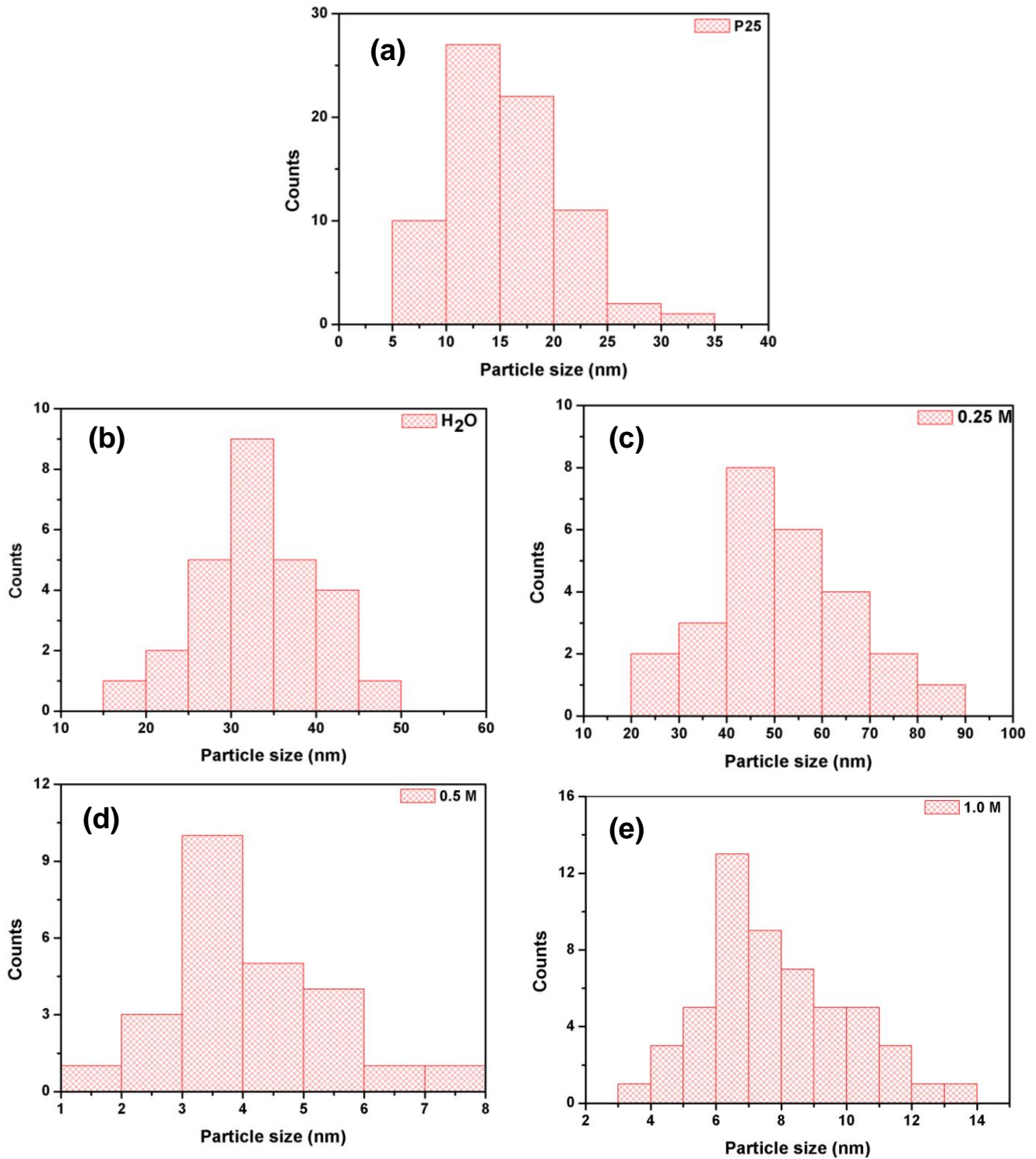


Fig. 4.4: Particle size distribution of TiO_2 nanostructures (a) P25, washed with (b) H_2O (c) 0.25 M, (d) 0.5 M and (e) 1.0 M HCl.

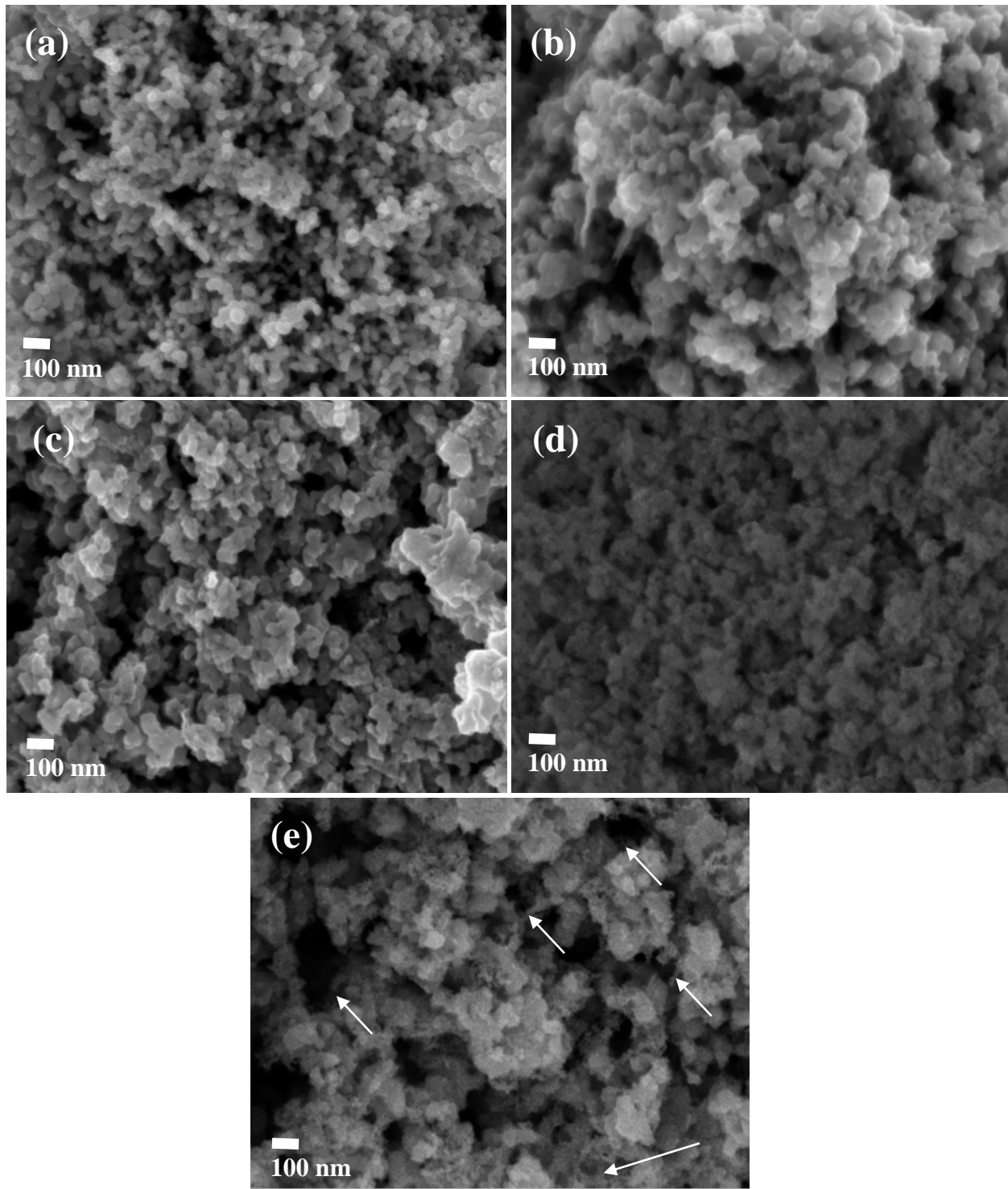


Fig. 4.5: SEM images of TiO₂ nanoparticles (a) P25 Degussa, nanoparticles washed with (b) H₂O, and nanoparticles washed with (c) 0.25 M, (d) 0.5 M and (e) 1.0 M HCl.

Fig. 4.6 shows the nitrogen adsorption isotherms of TiO₂ nanoparticles. It is well known that the hysteric activity is associated with both connectivity and the broadening of the pore size distribution in porous materials. Fig. 4.6 shows that the hysteresis loop of the hydrothermally treated sample subsequently washed with H₂O displays larger pore diameter and smaller surface area (Table 4.1) compared to P25. It is clear that the hysteresis loop of the samples washed with HCl shifts up when increasing the HCl concentration. More interestingly, there is a peculiar behavior observed in the 0.5 M sample showing a radical increase in the BET surface area while the pore diameter decreases. This is consistent with the XRD results in Table 4.1 showing that as the crystallite size decrease larger surface area get exposed. When the HCl concentration is increased to 1.0 M the surface area decreases while the pore diameter increases significantly as compared to 0.5 M. These observations are in good agreement with the sensing results (as discussed later) where we observed that the 1.00 M sample has good response than the 0.50 M sample. A large surface area alone does not result in good sensing however a porous surface (with large pore size) allows larger volume of the target gases to be adsorbed into the entire sensing layer thus enhancing the sensor response. A summary of BET surface area and pore diameter is shown in Table 4.2.

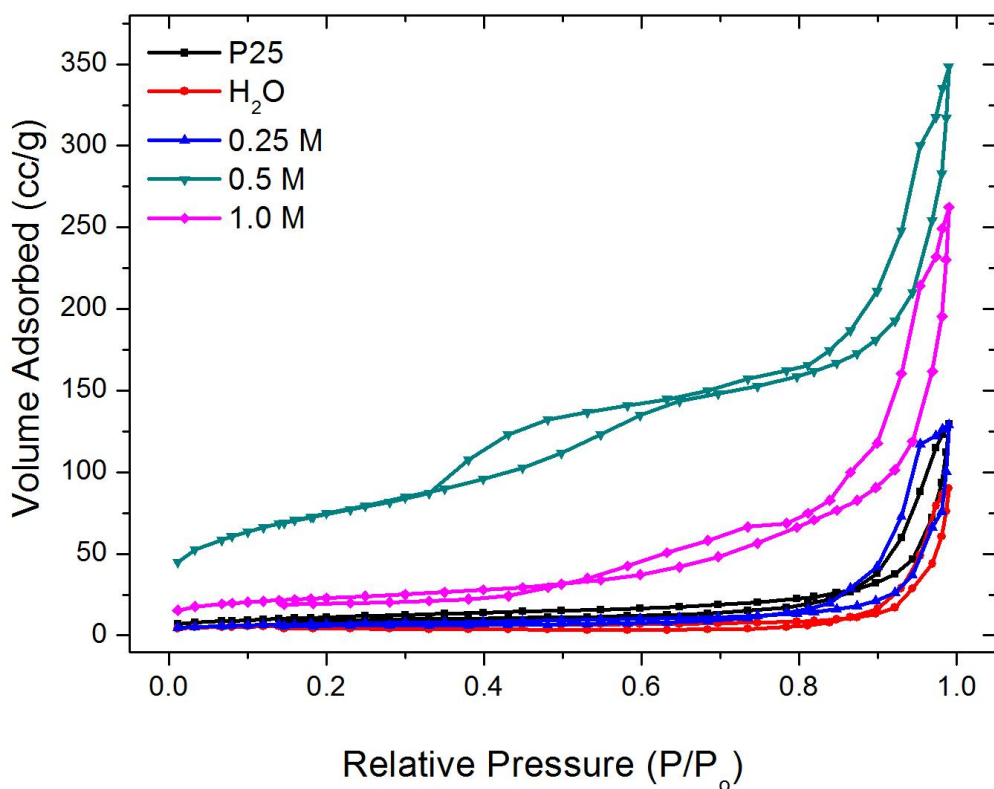


Fig. 4.6: N₂ adsorption isotherms for TiO₂ samples.

Table 4.2: Summary of BET specific surface area, pore volume (V_{pore}) and pore diameter (d_{pore}) of commercial TiO₂ nanoparticles (P-25) and those hydrothermally treated and washed with HCl.

| Materials | BET (m ² g ⁻¹) | V_{pore} (cm ³ g ⁻¹) | d_{pore} (nm) |
|-----------------------|------------------------------------------|---------------------------------------------------------|---------------------------|
| P25 | 40.5127 ± 0.0502 | 0.201464 | 25.4748 |
| H₂O | 20.1677 ± 0.2290 | 0.140103 | 48.2508 |
| 0.25 M | 24.9224 ± 0.1132 | 0.196439 | 44.0710 |
| 0.50 M | 270.5217 ± 0.4123 | 0.545816 | 9.2939 |
| 1.00 M | 80.3301 ± 0.5149 | 0.417041 | 21.5196 |

To analyse the surface chemistry, elemental composition, chemical state and electronic states of the elements in the TiO₂ nanoparticles washed with H₂O and HCl aqueous solution, X-ray photoelectron spectroscopy (XPS) analysis was carried out. The broad scan survey spectrum in Fig. 4.7a depicts that the surface mainly contains Ti, O and C elements and no other elements were observed as impurities. The observed carbon peak (C 1s) around 284 eV is probably due to exposure of the sample to atmospheric hydrocarbons and carbon tape on which the powders were mounted for XPS measurements.

High resolution XPS spectra of Ti 2p core levels of commercial P25, H₂O, 0.5 and 1.0 M samples are shown in Fig. 4.7b-e. The commercial P25 spectrum in Fig. 7b shows a Ti 2p_{3/2} and 2p_{1/2} doublets centred at 458.55 and 464.15 eV respectively, assigned to Ti⁴⁺ interstitials. The XPS spectrum of the nanoparticles washed with H₂O shown in Fig. 4.7c reveals two peaks centred at 458.21 and 463.86 eV corresponding to Ti⁴⁺ 2p_{3/2} and Ti³⁺ 2p_{1/2} [4.29- 4.31]. The samples washed with HCl in Fig. 4.7c-d show peaks at 458.53 and 464.22 eV for 0.5 M and 458.08 and 463.76 eV for 1.0 M. The observed peaks at 458.53 and 458.08 are assigned to Ti⁴⁺ 2p_{3/2} and Ti³⁺ 2p_{3/2} respectively while the peaks at 464.22 and 463.76 are assigned to Ti⁴⁺ 2p_{1/2} and Ti³⁺ 2p_{1/2} respectively [4.27, 4.30, 4.32]. The 1.0 M sample shows a shift to lower binding energy signalling an increase in Ti³⁺ vacancies.

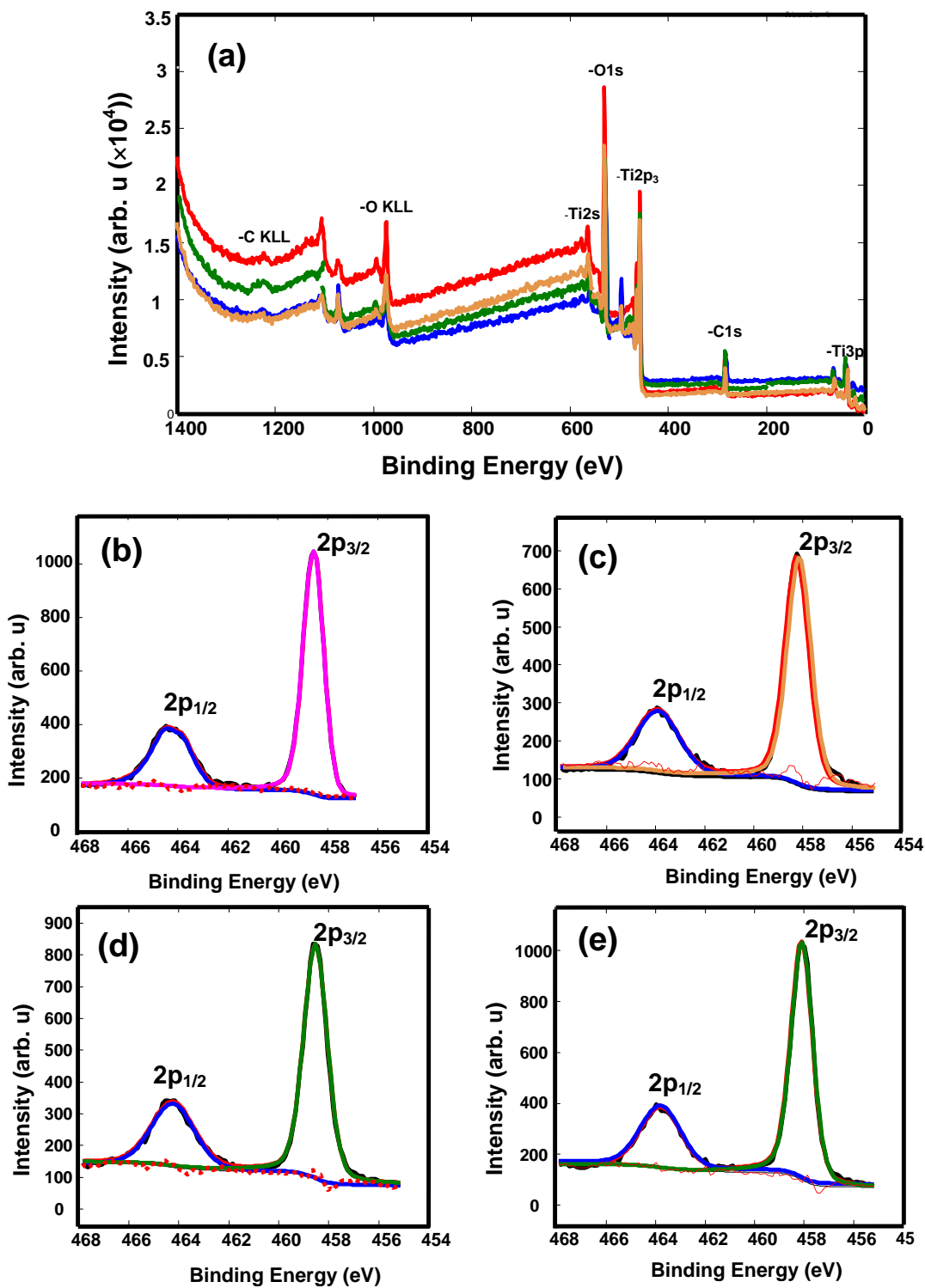


Fig. 4.7: (a) XPS survey scan of various TiO_2 nanoparticles, and deconvoluted core level spectra of Ti_{2p} for TiO_2 samples (b) P25, washed with (c) H_2O , (d) 0.5 M and (e) 1.0 M HCl.

Fig. 4.8a-d shows the O 1s core level spectra of commercial P25, H₂O, 0.5 and 1.0 M samples. The deconvoluted spectra using Gaussian fit show two peaks O₁ and O₂ centred at 529.80 and 531.30 eV assigned to Ti⁴⁺ and Ti³⁺ oxygen vacancies on the surface and subsurface regions for the commercial P25. Similar behaviour is observed for H₂O sample revealing two peaks located at 529.82 and 531.63 eV as shown in Fig 8b [4.27, 4.29, 4.30, 4.33]. At higher HCl concentration Fig. 4.8d, the peaks shifted to lower energies 529.31 and 530.58 eV. The peak at 529.31eV is due to Ti⁴⁺ oxygen vacancies on the surface and the one at 530.58 is due to O²⁻ ions in the TiO₂ crystal lattice [4.27, 4.29-4.32]. The comparison spectra for O and Ti in Fig. 4.8e and f respectively, clearly confirm a peak shift to lower energies when increasing the HCl concentration. The calculated Ti-O ratio is 1:1.97, which implies that, a portion of oxygen ions is not in the stoichiometric Ti-O bonding. Therefore, this denotes that there are oxygen vacancies on the TiO₂ surface. These results are consistent with the PL and EPR results in Fig. 4.9 and 4.10 (below) showing that oxygen vacancy defect states are dominating but are not the only contributing defects as there are Ti³⁺ interstitials [4.29- 4.31].

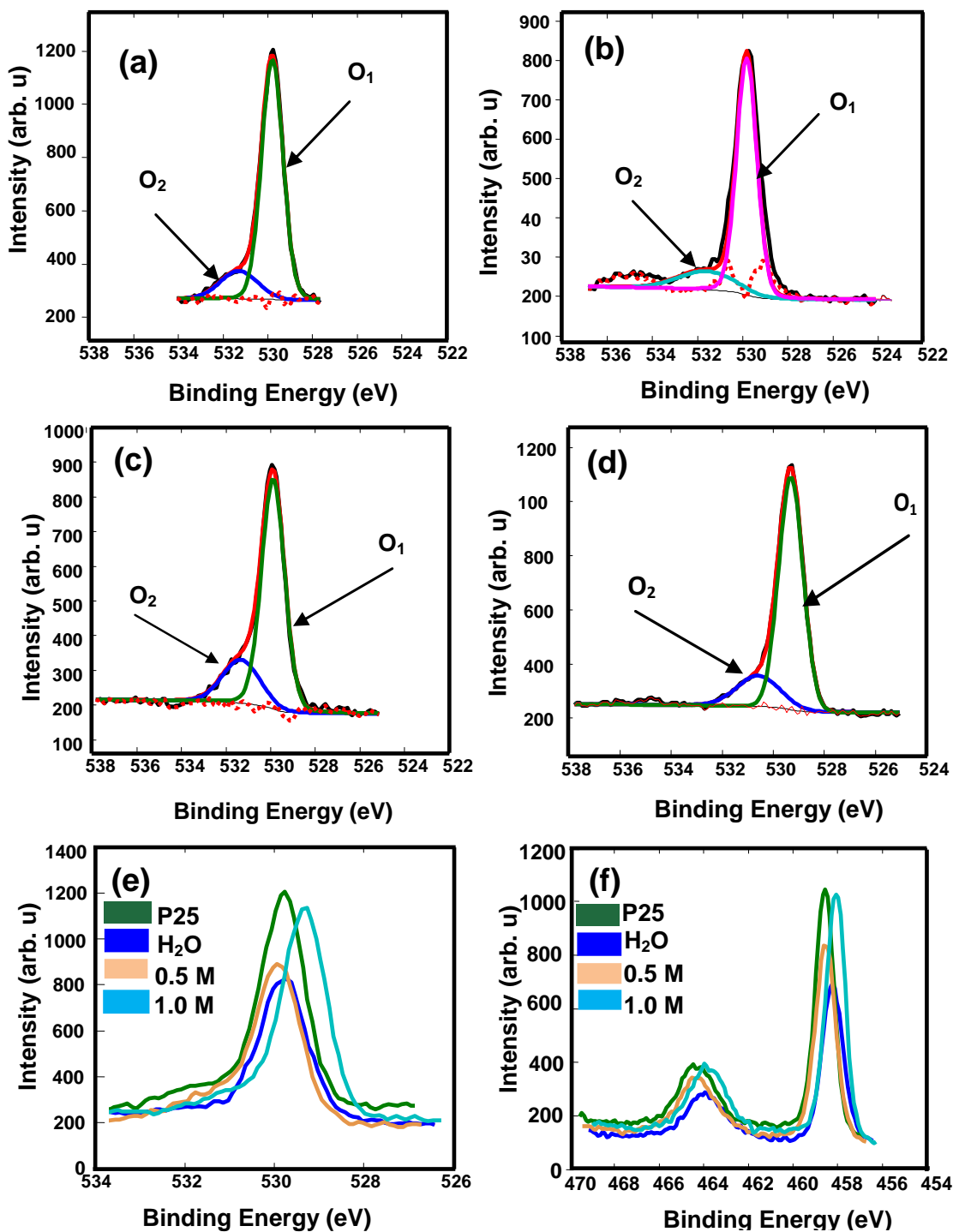


Fig. 4.8: Experimental and fitted curves for normalized O 1s XPS spectra of TiO₂ (a) P25, washed with (b) H₂O, (c) 0.5 M and (d) 1.0 M HCl. Note (e-f) are comparison spectra of O and Ti respectively.

In order to analyse the key factors influencing sensing performance, the native defects in TiO_2 such as oxygen vacancy and Ti interstitial were studied in detail by room temperature photoluminescence which is an effective way to study the defect structure of the semiconductor metal oxides. Fig. 4.9 shows TiO_2 nanoparticles washed with H_2O and different concentrations of HCl. It can be seen that the P25 and hydrothermally treated samples washed with H_2O and HCl have broad PL peaks in the range of 380-550 nm. Their intensity increases with increasing the HCl concentration. The emission shifts as the particle size is reduced with increasing HCl concentration, and this is probably due to quantum confinement effect [4.28]. This blue shift is in good agreement with the Raman analyses.

It is well known that defects states of TiO_2 can be due to (a) self-trapped excitons located at the TiO_6 octahedra, (b) oxygen vacancies (V_o) and (c) surface states. Anatase TiO_2 has indirect band gap, thus no free exciton recombination defects are observed. Therefore, to analyse the role of each defect on the sensing properties of TiO_2 the broad visible spectra were deconvoluted using a Gaussian fitting method. The deconvoluted spectra in Fig. 4.8b show five emission bands at 391.5 (Peak 1), 402.6 (Peak 2), 419.1 (Peak 3), 443.2 (Peak 4) and 490 nm (Peak 5) for the P25 sample. According to the literature the PL emission bands in Peak 1-3 originate from self-trapped excitons located at the TiO_6 octahedron, while Peak 4 and 5 are assigned to shallow trapped oxygen vacancies (V_o) associated with Ti^{3+} centre below the conduction band [4.29, 4.30, 4.34, 4.35]. When a TiO_2 lattice loses an O atom an electron pair remains

trapped in the vacancy cavity and leaves behind a pair of electrons that forms an F centre. One of the electrons in the F centre occupies the nearest Ti^{4+} ion resulting in Ti^{3+} and F^+ centres which will form shallow and deep trap states as shown in equations (4.3- 4.6) below [4.29- 4.31, 4.34, 4.35]:



In Fig. 4.9b-d we observe changes in the intensity of peak 4 and peak 5. The peak intensity is enhanced after hydrothermal treatment. Additionally when introducing 1.0 M HCl the PL intensity related to V_o is enhanced as compared to the rest denoting that the samples contain higher percentage of V_o on the TiO_2 surface after hydrothermal treatment.

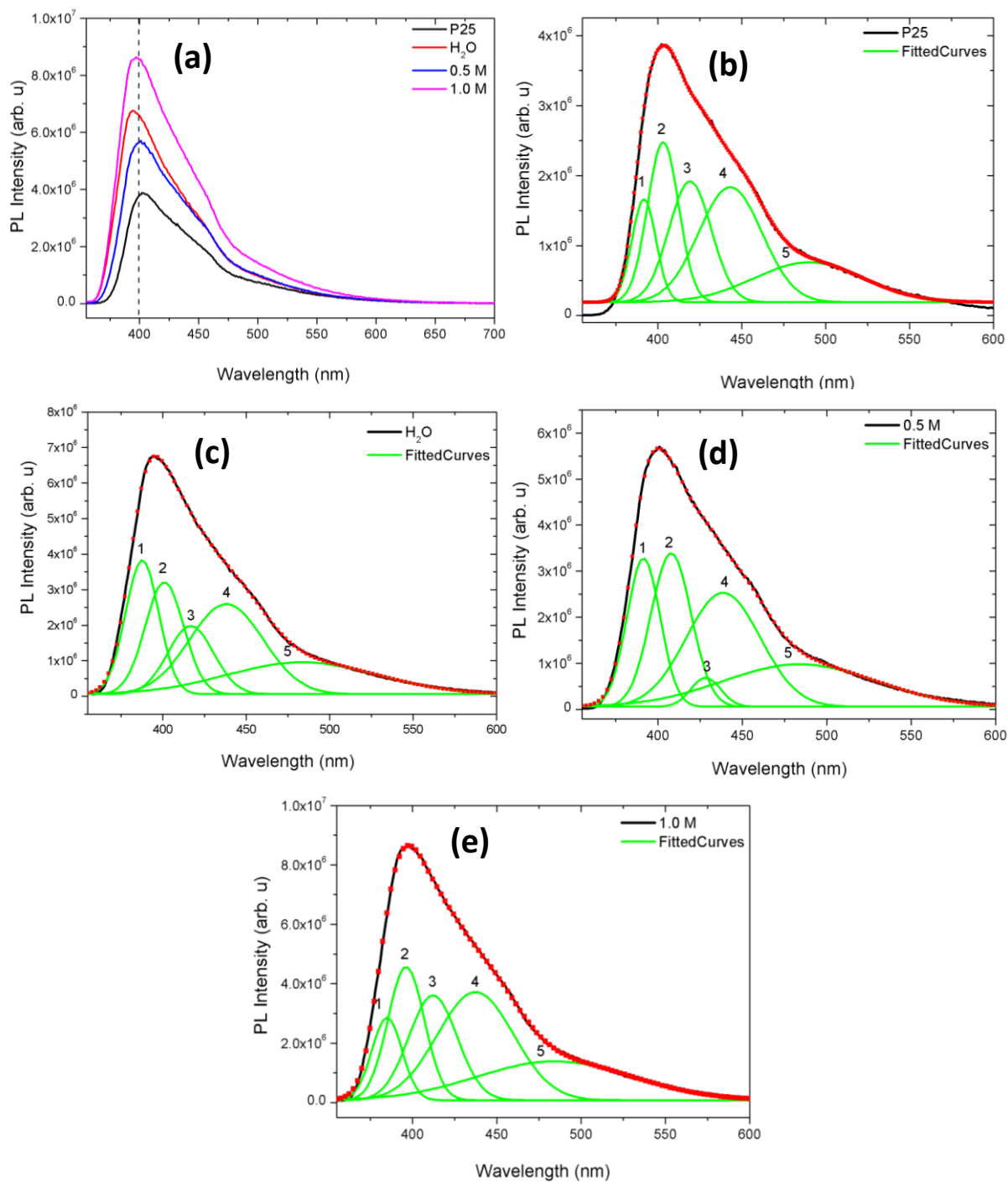


Fig. 4.9: (a) PL spectra of TiO₂ nanoparticles and (b-e) correspond to Gaussian fits of each PL spectrum (the black lines and red circles are the experimental results and Gaussian fits respectively).

To complement the PL and XPS results the electron paramagnetic resonance (EPR) analyses were conducted. The technique allows us to study magnetic properties of a material by analysing the nature and interactions of magnetic species present in the material. Previous results reported that TiO₂ nanostructures have surface hole trapping sites, surface bound hole trapping sites, lattice electron trapping sites and interfacial sites [4.36- 4.40]. Room temperature EPR spectra of TiO₂ nanoparticles are shown in Fig. 4.10. An isotropic signal showing an S-shape signal related to ferromagnetic resonance (FMR) is clearly observed in Fig. 4.10 for the commercial P25 with a g-factor of 2.0320. An increase in FMR intensity is observed for samples washed with H₂O. More remarkably, when washing the sample with HCl a trivial shift to higher field is observed.

At higher HCl concentration (1.0 M) the FMR signal is more enhanced showing a hyperfine structure with a g-factor of 1.9738. This hyperfine structure coupling may be due to interactions between unpaired electrons magnetic moments and those of surrounding nuclei. As shown in Table 4.3, the number of spins (N_s) contributing to the FM ordering also increases when increasing the HCl concentration. According to the previous results, the FM ordering of the system originates from regions of correlated and isolated spins [4.41]. While the magnetization that is due to the uncorrelated spins is paramagnetic. It should be noted that the N_s was calculated using the following formula [4.42]:

$$N_s = 0.285I(\Delta H)^2 \quad (4.7)$$

where, “ I ” is the peak-to-peak height and ΔH is the line width. Cybula *et al.* [4.36] showed resonance signals with g values = 2.018, =2.014 and 2.004 assigned to $(\text{Ti}^{4+}\text{-O}^- \text{-Ti}^{4+}\text{-OH}^-)$ hole trapping in the subsurface (O_B) of the valence band. The g -values of 2.028, 2.015 and 2.003 are attributed to $(\text{Ti}^{4+}\text{-O}^{2-}\text{-Ti}^{4+}\text{-O}^-)$ surface oxygen ions (O_S). The signal with $g=1.989$ and $g=1.958$ are assigned to Ti^{3+} trapping site within the anatase lattice. In addition, Giannakas *et al.* [4.37] reported an EPR signal with g values ranging from 2.0033 to 2.0248 assigned to O^{2-} hole trapping ions. They also observed g -values $g_{\parallel}=1.990$, $g_{\parallel}=1.964$, $g_{\perp}=1.940$ assigned to Ti^{3+} lattice ions and $g_{\parallel}=1.972$, $g_{\parallel}=1.954$, $g_{\perp}=1.930$ to surface Ti^{3+} ions. Prokes *et al.* [4.39] reported two resonance signals at $g=2.06$ and $g=2.0035$ assigned to surface adsorbed O^{2-} and oxygen hole centre respectively. Therefore, we suggest that the resonance signals observed in our work with $g > 2.0$ can be attributed to surface hole trapping sites and while that at $g < 1.99$ Ti^{3+} is assigned to lattice trapping sites.

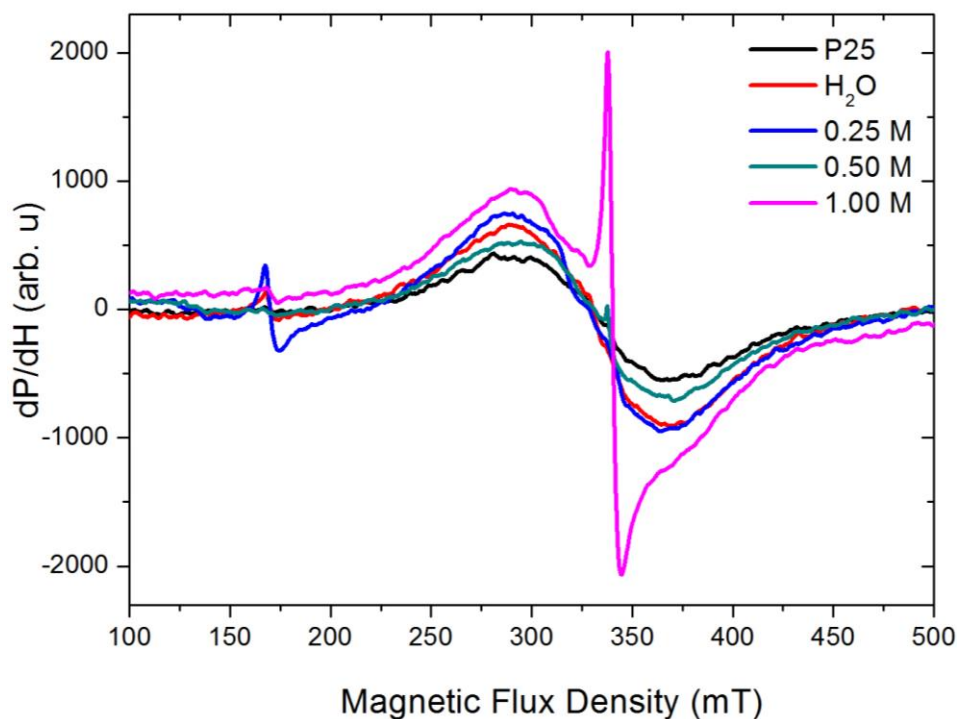


Fig. 4.10: EPR measurements of various TiO_2 nanostructures taken at room temperature with a microwave power of 5 mW.

These results are consistent with PL and XPS results. More remarkably, there is a peculiar signal observed at lower fields (167. mT) for H_2O , 0.25 M and 1.0 M with g-factors of 4.1627, 4.1325 and 4.1325, respectively. The same behaviour was observed by Yu *et al.* [4.43] in Fe-doped TiO_2 nanoparticles with $g = 4.30$ assigned to oxygen vacancies created by isolated rhombic Fe^{3+} cations. In addition, a FMR signal with $g = 4.76$ in undoped TiO_2 samples assigned to Ti^{3+} in the distorted octahedral was reported by Santara *et al.* [4.31]. These authors speculated that this signal is due to oxygen vacancies contributing to orbital

overlapping of $3d^1$ spin of Ti^{3+} and $1s^1$ spin of F^+ centre within the oxygen vacancy.

Table 4.3: Summary of the EPR results showing the FMR field, g-factor, line width (ΔH_{EPR}) and number of spins (N_s) TiO_2 nanostructures.

| Sample | FMR Field (mT) | g-factor | ΔH_{EPR} (mT) | N_s ($\times 10^6$) |
|------------------|----------------|----------|-----------------------|-------------------------|
| P25 | 315.403 | 2.0320 | 80.04 | 1.73 |
| H ₂ O | 314.384 | 2.0393 | 75.24 | 2.51 |
| 0.25 M | 314.382 | 2.0379 | 74.30 | 2.65 |
| 0.5 M | 316.425 | 2.0251 | 74.49 | 1.90 |
| 1.0 M | 324.597 | 1.9738 | 74.34 | 3.47 |

The response of MOX semiconductor gas sensors typically depends on the operating temperature. Therefore to examine the optimum operating temperature, all the sensors were tested at different temperatures (25-400 °C) for different gases and the results are shown in Fig. 4.11. As shown in Fig.4.11a and d, a commercial P25 sensing material shows a low response at room temperature when exposed to H₂ and NO₂ gas; the response increases with temperature and has maximum at 400 °C. A very low response is observed for P25 sensing material in Fig 4.11b and c when exposed to NH₃ and CH₄ showing a maximum response of 100 at 250 °C and 49 at 400 °C for the respective gases. It is interesting to indicate that the hydrothermally treated TiO₂ samples (H₂O, 0.5 and 1.0 M) shown in Fig. 4.11a-d show a higher response to all gases

at room temperature. When increasing the working temperature from RT to 400 °C, their response decreases drastically denoting that their optimum working temperature is RT (25 °C), this observation clearly confirms that these materials are indeed room temperature sensing materials. The decrease in response may be due to the adsorption saturation, as the operating temperature increases the target gas is desorbed before interaction with oxygen ions on the TiO₂ surface, thus decreasing the response [4.44]. More interesting, a 1.0 M (Fig. 4.11a-d) sensing material shows a higher response to all gases at RT compared to other sensors. According to BET results, although the 0.5 M sample showed higher surface area compared to 1.0 M, it is clear that the surface area alone does not warrant a higher sensing response. Thus, the pore diameter and volume should also be improved, hence the higher pore diameter and volume of the 1.0 M sample justify the observed higher sensing response, since they could provide more sites for surface adsorption and desorption of the gas molecules (see BET results). Furthermore, based on the PL and EPR results, we suggest that the higher relative concentration of V_O, Ti⁴⁺ and Ti³⁺ defects are the most favorable adsorption sites for oxygen species, which can enhance the possibility of interaction with gas molecules. Therefore, we conclude that the relative concentration of V_O, Ti⁴⁺ and Ti³⁺ play a vital role in modulating both the sensing and magnetic properties of TiO₂ nanoparticles [4.45, 4.46]. Moreover, the observed low sensing response of P25 at room temperature is probably due to absence of Ti³⁺ and low relative concentration of V_O observed from the PL and

EPR (Fig. 4.9 and 4.10) compared to other samples. Wang *et al.* [4.47] also showed that P25 Degussa contains defects related to V_O .

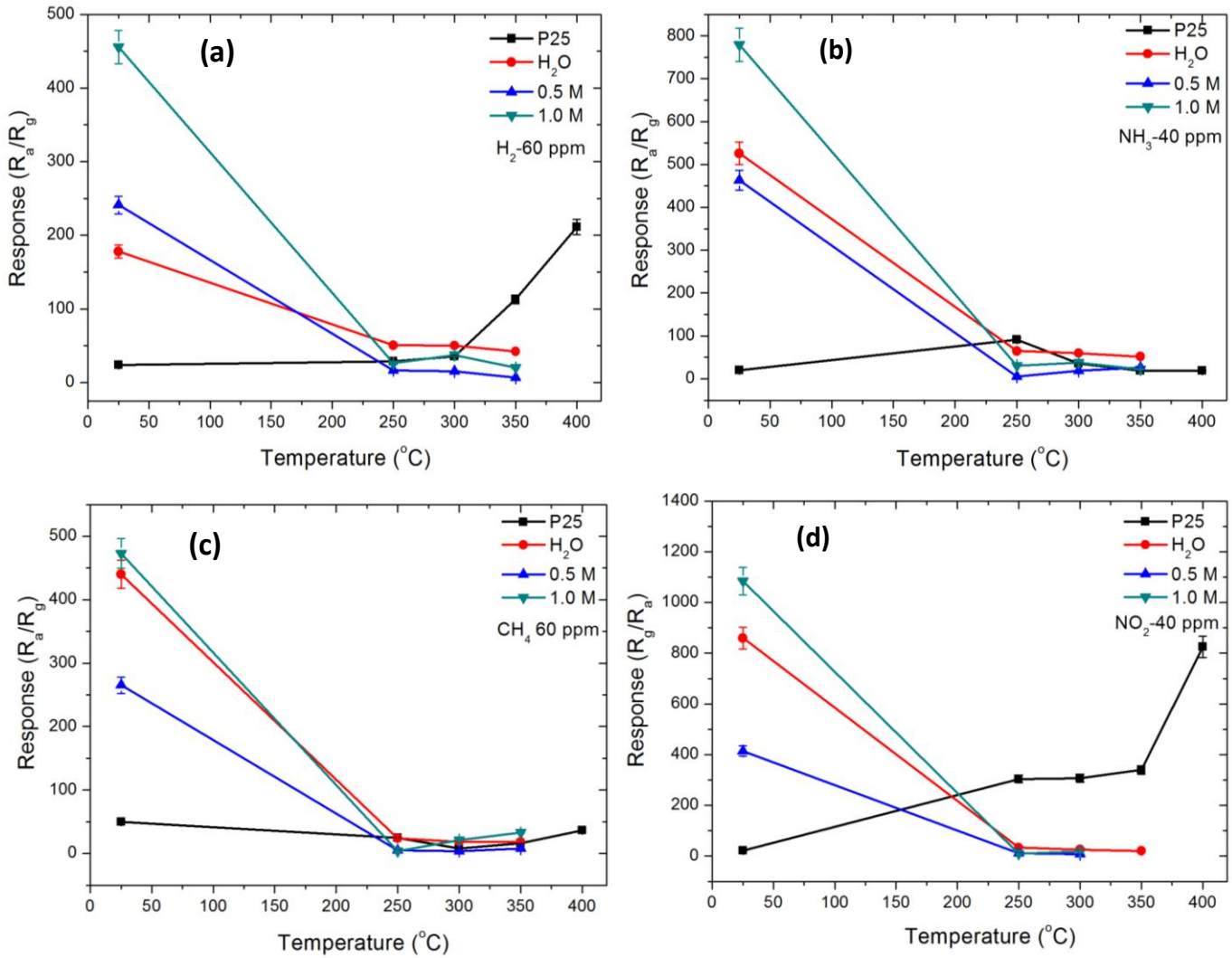


Fig. 4.11: Response versus temperature for TiO_2 nanoparticles exposed to various gases (a) H_2 , (b) NH_3 , (c) CH_4 and (d) NO_2 .

Fig 4.12 shows the sensor response as a function of concentration at room temperature (RT). When the P25 sensor is exposed to either H_2 or NH_3 gas, a

maximum sensing response is observed at 10 ppm and 20 ppm respectively and saturates thereafter. A very low response is observed when the P25 is exposed to NO_2 . The hydrothermally treated sensing materials display a good response to all the gases and their response increases with concentration up to 60 ppm for CH_4 and H_2 (results not shown) while they saturate at 40 ppm for NO_2 and NH_3 denoting that they have reached their optimum detection level. It can be seen from Fig. 4.12 that the material washed in 1.0 M HCl shows enhanced response than those washed in water and other concentrations of HCl. Gas sensing is a surface phenomenon, changes on the surface affects the sensitivity/response of the sensor. Thus, at low gas concentration we observe a low response because less area is covered, as the gas concentration increases a larger surface area get exposed to the gas, hence, an increase in a sensor response is observed. When an optimum concentration (40 ppm) is reached the sensor response saturates and starts decreasing with an increase in gas concentration. It is clear from the results that the HCl concentration has an effect on the structure and surface of the materials. Thus we propose that, after hydrothermal treatment, the nanostructures formed contain Na ions located at the octahedral sites of titania. When the acid and water are introduced the Na ions are removed and replaced by protons and water molecules resulting in a more accessible space for gas adsorption, thus inducing higher sensing response [4.48].

To further validate a correlation between the gas sensing, magnetic properties and defects, a number of spins were plotted as a function of response as shown in Fig. 4.12c. As revealed in Fig. 4.12c, when the number of spins

increases, the sensing response also increases denoting that both properties are also dependent on the defects. Therefore, our results confirm that the defects such as V_O , Ti^{4+} and Ti^{3+} play a crucial role on the gas sensing properties.

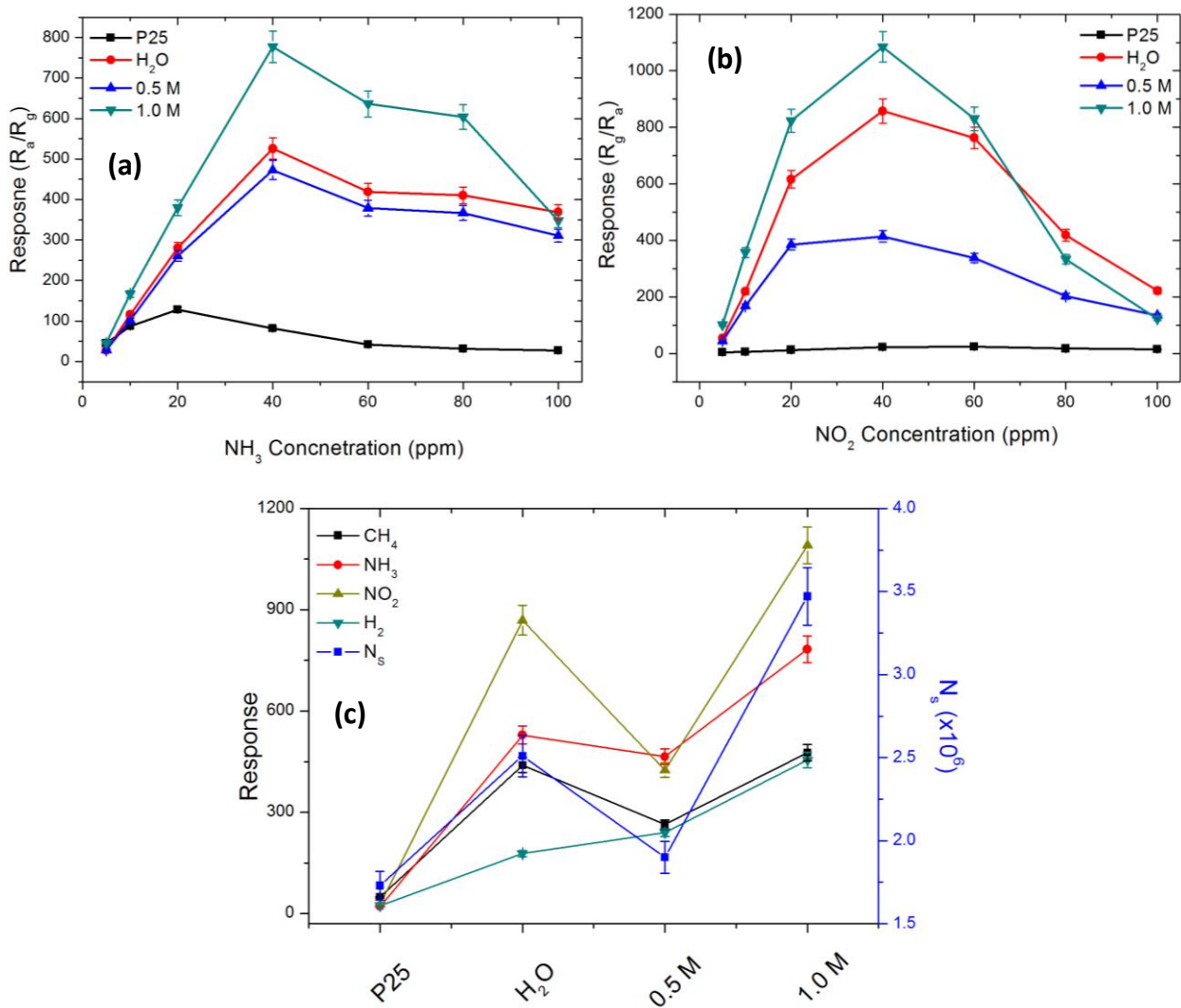


Fig. 4.12: Response versus concentration for TiO₂ nanoparticles exposed to various gases (a) NH₃, (b) NO₂ (c) response as a function of number of spins.

Table 4.4 shows the room temperature NO₂ and NH₃ gases sensing ability of TiO₂ nanostructures synthesized in this work compared with those of other types of pure and doped TiO₂ materials from the literature. From Table 4.4, it is observed that our sensing materials are more sensitive to NO₂ compared to those reported in the literature.

Table 4.4: Literature survey on NO₂ and NH₃ gas sensors based on TiO₂ nanostructures compared with the current work

| Sensing element | Type of Gas | Operating Temp. | Gas Concentration (ppm) | Response* | Refs. |
|----------------------------------------------------------------|-----------------|-----------------------------|-------------------------|-----------|--------------|
| TiO ₂ nanotubes | H ₂ | RT | 100-500 | 239.4 | 4.10 |
| TiO ₂ nanoparticles | NH ₃ | RT | 0.15-100 | 7857 | 4.11 |
| Al/TiO ₂ /Al ₂ O ₃ /p-Si film | NO ₂ | RT-UV illumination assisted | 20-100 | 190 | 4.12 |
| NiO-TiO ₂ nanocomposite | NH ₃ | RT-UV illumination assisted | 10-100 | 500 | 4.13 |
| TiO ₂ nanoparticles | NO ₂ | RT | 5-40 | 1093 | In this work |
| TiO ₂ nanoparticles | NH ₃ | RT | 5-40 | 750 | In this work |

*Note: the sensor response is defined as R_a/R_g (for reducing gas), R_g/R_a , (for oxidation gas) where R_a is the resistance of the sensor in air and R_g is the resistance of the sensor when exposed to a target gas [4.49].

The response–recovery behavior is an imperative characteristic that determines the performance of gas sensors. To obtain a deeper insight into the gas sensing behavior, the dynamic response of TiO₂ nanoparticles prepared using hydrothermal route and washed with pure distilled H₂O and various concentrations of HCl aqueous solution was studied as shown in Fig. 4.13. The sensing materials were exposed to various concentrations of H₂, CH₄, CO, NH₃ and NO₂ gases and measured at different working temperatures (RT, 250, 300, 350 and 400 °C). Fig. 4.13 shows the dynamic response of TiO₂ nanoparticles washed with H₂O and 1.0 M tested to NO₂ at various concentrations and temperatures. It is observed in Fig. 4.13 that when NO₂ target gas is exposed to a sensing material (TiO₂) the sensor response increases and saturates at a certain value. When the gas is released the response decreases as the sensor recovers back to baseline revealing a good sensing material. Fig. 4.13c demonstrates the absolute resistance (or current) of P25 sensing material tested to NH₃ gas at room temperature. It is clear from Fig. 4.13 that the current increases when introducing the NH₃ gas and further decreases when the tested gas is release confirming that the P25 sensing does indeed show a response when tested at room temperature.

Table 4.5 shows the response time (the time taken for the sensor resistance to reach saturation level after being exposed to a gas) and recovery time (the time taken for the resistance to recover to its initial value (baseline) after removal of the target gas) of TiO₂ nanoparticles exposed to various gases **[4.50]**. As

shown in Table 4.5, the sensing materials show better response-recovery times towards NO_2 and NH_3 compared to other gasses. More specifically, the 1.0 M showed the shortest response time of 33 s towards NH_3 . In addition, the 0.25 M showed response-recovery times of 35 and 58s towards NH_3 , while the 1.0 M reveals response-recovery times of 48 and 52 s towards NO_2 gas.

To estimate the sensitivity of the TiO_2 sensing materials, the slope of the curves in Fig. 4.12 was used [4.51, 4.52]. As depicted in Fig. 4.12 that the response of all the sensors (except the P25) increases linearly in the range of 5-40 ppm, then start to saturate above 40 ppm. While the P25 shows a linear increase in the range of 5-20 ppm, then starts to saturate thereafter. As a result, from Table 4, it is observed that the 1.0 M shows the highest sensitivity of 47.85 ppm^{-1} at 40 ppm to NO_2 when compared to other gases and other sensing materials. Thus this shows that the 1.0 M is more sensitive to NO_2 . The higher sensitivity of the 1.0 M gas sensor is attributed to smaller grain size and higher pore diameter. Previous reports [4.53–4.54] have stated that the diameter of the nanostructures can significantly affect the gas sensitivity performance.

The limit of detection (LoD) of all the sensors was estimated by calculating the sensor noise using the fluctuation in the gas response at baseline using the root-mean-square deviation (rms). To extract the rms deviation, 30 points were used at the baseline without analyte gas. Based on the IUPAC definition, the LoD can be estimated using the following relation, $3(\text{noise}_{\text{rms}}/\text{slope})$, where the first derivative of the graphs in Fig. 4.12 gives the slope [4.51, 4.52, 4.55, 4.56]. It is

observed from Table 4.5 that the sensing materials washed with H₂O and 1.0 M HCl, show very small LoD values, compared to their counterparts. Previous studies [4.52, 4.56] indicated a low LoD value can be employed to detect a leakage at the beginning, and it is very useful in various applications related to safety.

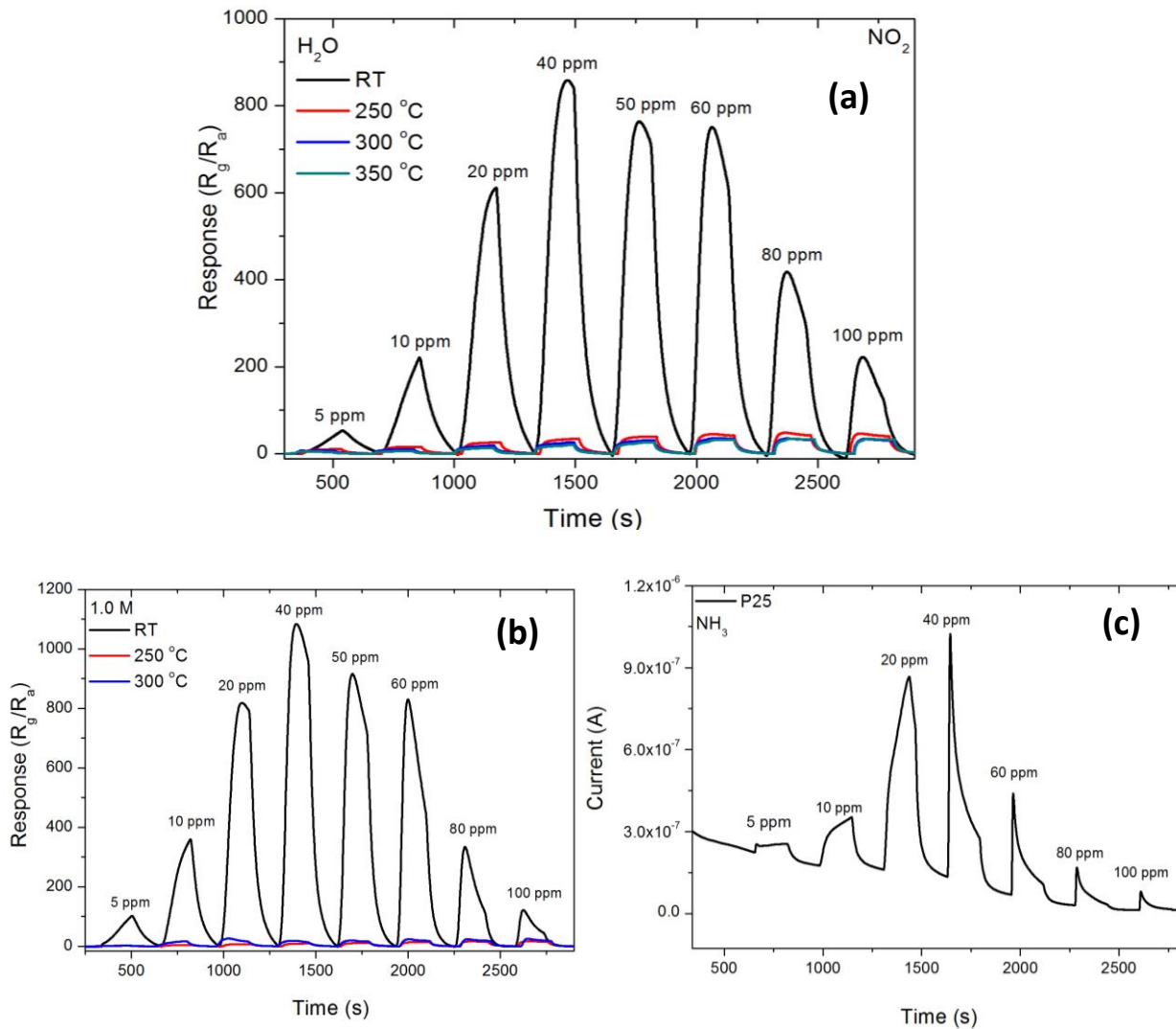


Fig 4.13: The response of TiO₂ sensor to NO₂ (a) H₂O and 1.0 M TiO₂ samples, and (c) current vs time for P25 TiO₂ sensing material tested to NH₃ at room temperature.

Table 4.5: Summary of the Response (t_{res}) and Recovery (t_{rec}) time, sensitivity (S), and LoD for TiO₂ nanoparticles tested at various gases at room temperature, at 40 ppm gas concentration.

| Materials | H ₂ (40 ppm) | | | | NO ₂ (40 ppm) | | | | CH ₄ (40 ppm) | | | | NH ₃ (40 ppm) | | | |
|-----------------------|----------------------------|------------------|------|------|-----------------------------|------------------|-------|------|-----------------------------|------------------|-------|------|-----------------------------|------------------|-------|------|
| | t_{res} (s) | t_{rec} (s) | *S | LoD | t_{res} (s) | t_{rec} (s) | S | LoD | t_{res} (s) | t_{rec} (s) | S | LoD | t_{res} (s) | t_{rec} (s) | S | LoD |
| P25 | 106 | 148 | 5.91 | 0.14 | 75 | 103 | 0.58 | 2.23 | 57 | 53 | 1.60 | 0.17 | 40 | 108 | 5.35 | 0.47 |
| H₂O | 90 | 98 | 2.34 | 0.55 | 64 | 86 | 37.47 | 0.01 | 74 | 99 | 7.73 | 0.24 | 58 | 111 | 16.80 | 0.06 |
| 0.25 M | 65 | 56 | 7.61 | 0.23 | 60 | 63 | 13.90 | 1.62 | 161 | 169 | 2.30 | 1.86 | 35 | 58 | 19.06 | 0.06 |
| 0.5 M | 90 | 96 | 3.26 | 0.71 | 62 | 102 | 22.70 | 0.29 | 114 | 95 | 7.69 | 1.64 | 72 | 121 | 15.53 | 0.23 |
| 1.0 M | 72 | 82 | 7.26 | 0.14 | 48 | 52 | 47.85 | 0.02 | 72 | 54 | 12.45 | 0.96 | 33 | 101 | 22.19 | 0.14 |

*Note: Units for sensitivity (S) and LoD are ppm⁻¹ and ppm, respectively

Fig. 4.14a shows the response curve cycling of the 1.0 M TiO₂ nanostructures exposed to 40 ppm NO₂ at room temperature. As shown from the spectrum, the sensor reveals a good reversibility and repeatability towards 40 ppm NO₂ gas. Moreover, it is observed that the response values, response and recovery times of sensors are almost the same during the testing through three times circulation of NO₂. For practical application, the stability of response is of critical importance. Therefore, to evaluate the stability, the 1.0 M sensing material was tested every day towards NO₂ for 40 days. As shown in Fig. 4.14b, the 1.0 M TiO₂ sensing material displays almost a constant electrical signal to the target

gas over 40 days. This shows that the 1.0 M TiO₂ nanostructures have a good stability and may be suitable for the practical application.

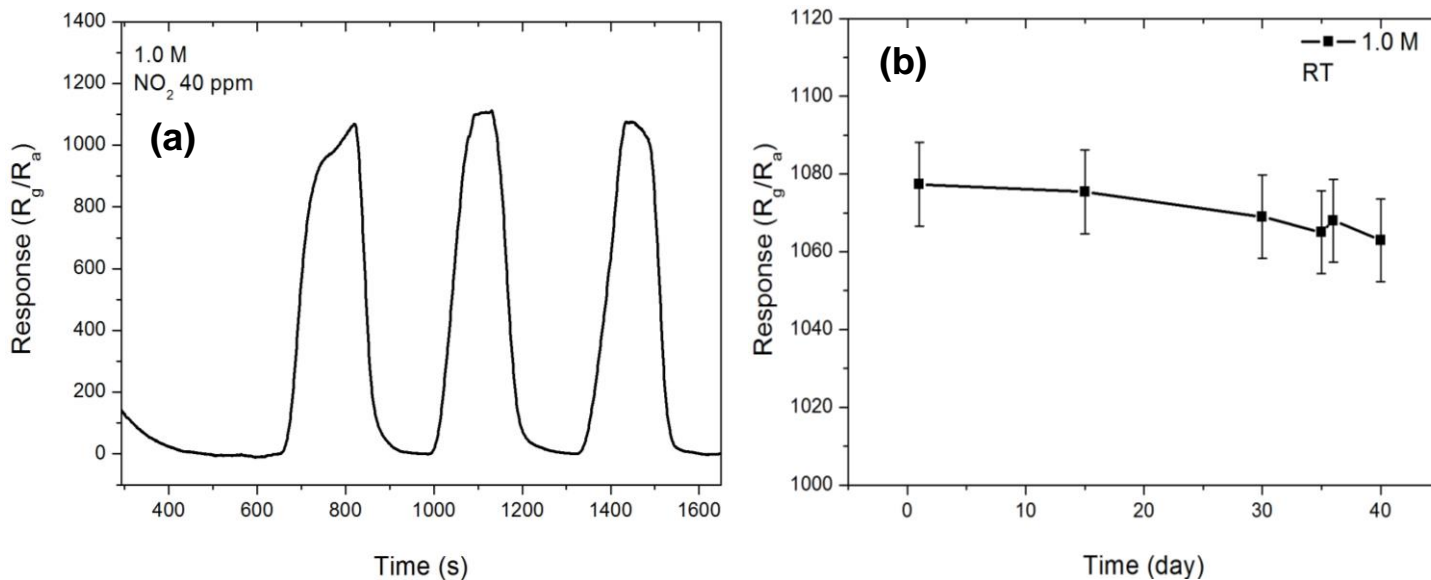


Fig. 4.14: (a) Typical response curve cycling of the 1.0 M TiO₂ nanostructures exposed to 40 ppm NO₂; (b) The sensing stability of long-term response values of the 1.0 M TiO₂.

Selectivity in gas sensing is another essential parameter that is required for a real-time practical application. Therefore, the responses of the TiO₂ nanoparticles treated with various concentrations of HCl were tested towards 40 ppm H₂, CH₄, NH₃, CO and NO₂ at room temperature and 250 °C, as shown in Fig. 4.15. It is clear from Fig. 4.15a that the nanoparticles washed with 1.0 M of HCl shows improve response of 1093 to NO₂ at room temperature, indicating that they have a very good selectivity to NO₂.

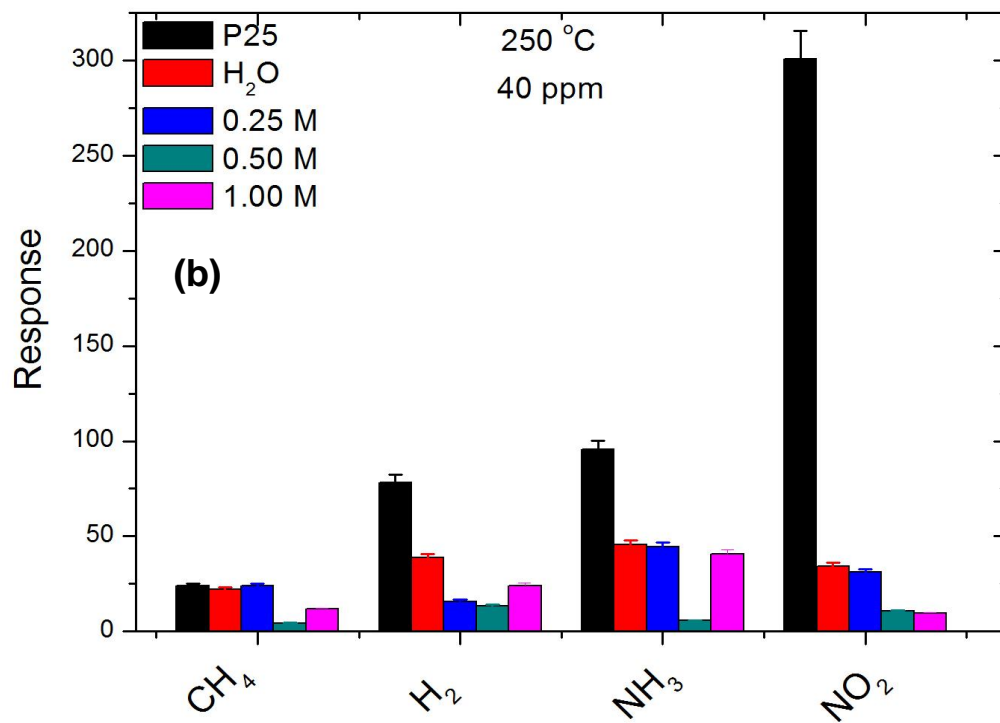
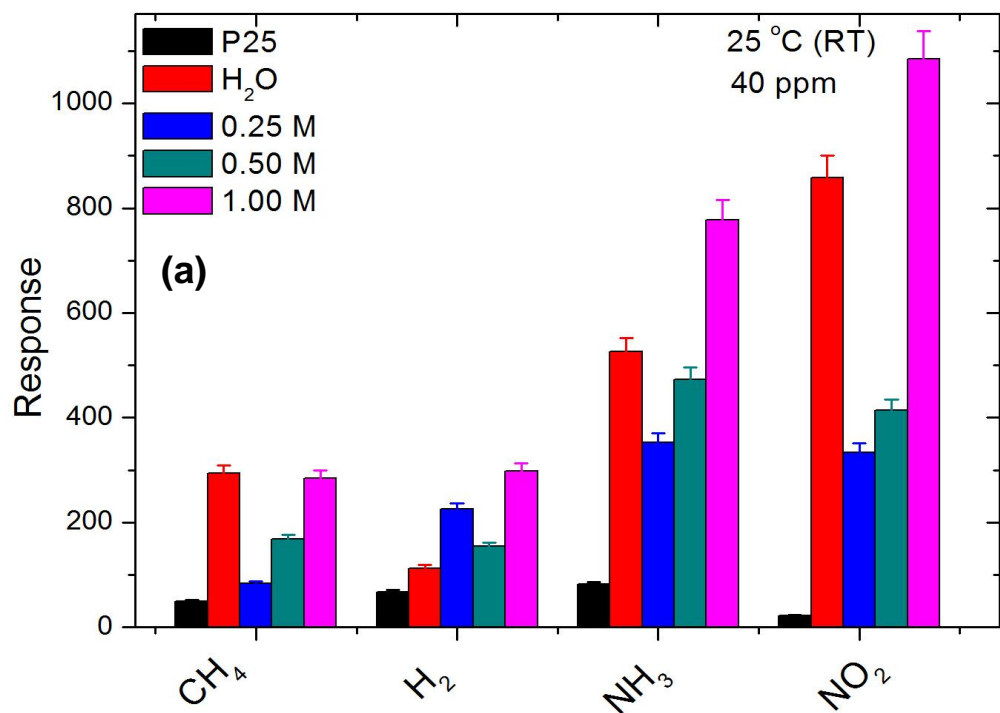
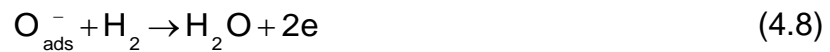


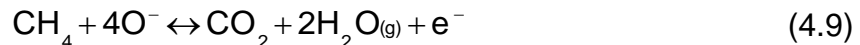
Fig. 4.15: The selectivity test toward 40 ppm of CH₄, H₂, NH₃, and NO₂ at (a) 25 °C (RT) and (b) 250 °C.

Robust response, fast recovery, and good selectivity of nanoparticles washed with 1.0 M of HCl support their promising applications at the industrial level with minimal cost. When the sensing materials were tested at 250 °C, P25 nanoparticles (Fig. 4.15b) revealed improved response to NO₂ denoting that they are only sensitive at higher temperature.

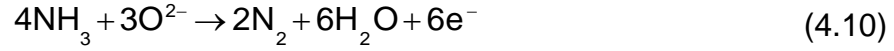
Based on literature, sensing is a surface phenomenon and TiO₂ contains donor type defects such as oxygen vacancies and titanium interstitials occupying interstices between the atomic sites [4.26]. Oxygen vacancies (V_o) are formed by transfer of an oxygen atom on a normal site to a gaseous state. When molecules are absorbed on the surface of TiO₂ they extract electrons from the conduction band and trap the electrons in the form of ions at the surface. This leads to band bending and an electron depletion region layer increases. When exposed to a reducing gas such as H₂, the atoms react with the gas and replace the oxygen molecules with other molecules; this decreases the resistance and reverses the band bending thus increasing conductivity and the following reaction occurs [4.57]:



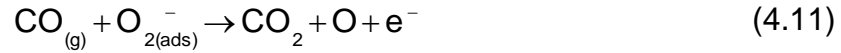
When the sensing material is exposed to CH₄, it will dissociate at the O₂ sites on the TiO₂ nanoparticles according to the following reaction:



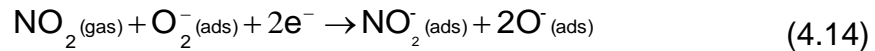
When the TiO₂ sensing material is exposed to NH₃, the gas–solid interaction lead to the following reaction **[4.58]**:

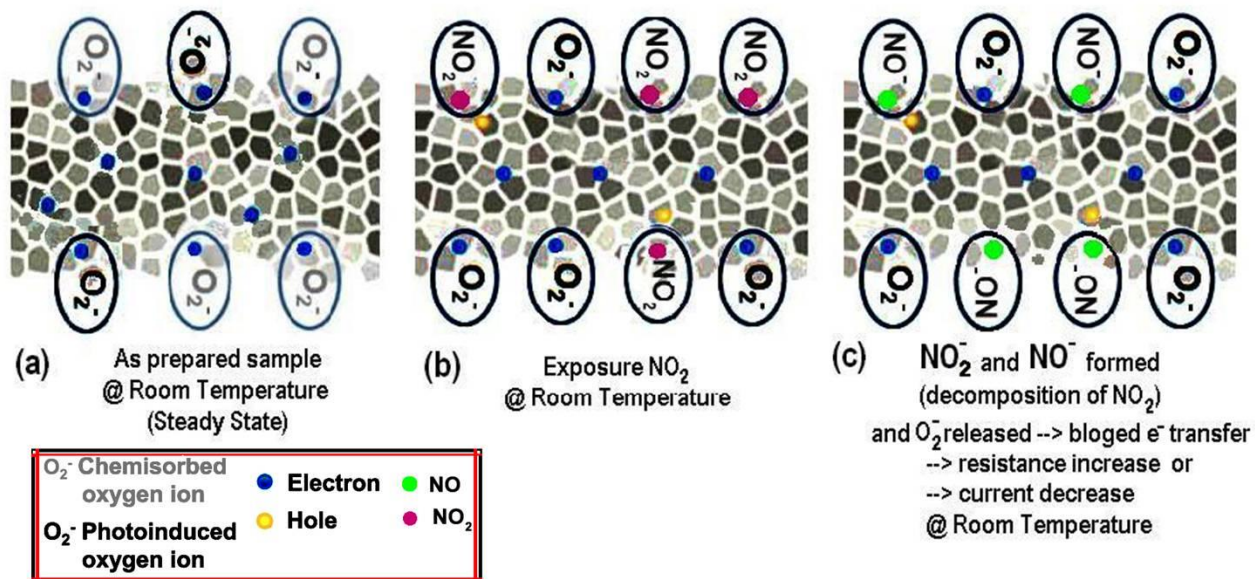


TiO₂ has oxygen species (O₂⁻, O⁻, O²⁻) adsorbed on its surface from the atmosphere. When exposed to CO (a reducing gas) the gas reacts with the oxygen ions and releases an electron to the material and produces CO₂ **[4.59]**. The conductivity of the material increases due to increase of electrons. This reaction process can be expressed by the following chemical equations:



However, when TiO₂ sensing material is exposed to oxidative gas such as NO₂, the NO₂ gas is adsorbed in the form of NO₂⁻(ads) and NO⁻(ads) (see reactions 4.13, 4.14 and Scheme 4.1), and with the pre-ion oxygen adsorbates (O, O²⁻, O₂⁻), results to an increase in the depletion layer. Therefore, the sensor resistance increased upon exposure to the NO₂ gas **[4.60]**.





Scheme 4.1: Schematic diagram showing sensing mechanism of NO_2 gas

4.4. CONCLUSIONS

Morphology control of the TiO_2 nanoparticles was demonstrated using a simple hydrothermal method and washing the samples using concentrated HCl aqueous solution. The nanoparticles size and crystallization behavior of TiO_2 were shown to be dependent on the concentration of HCl. Structural analysis revealed a phase transformation from mixture of both anatase and rutile in commercial P25 to pure anatase phase after hydrothermal treatment. An amorphous structure was observed on the TiO_2 nanoparticles after hydrothermal treatment and their crystallinity improved with an increase in HCl concentration. The hydrothermal treatment caused agglomeration of particles with highly porous surfaces and the particle size decreased as the acid was introduced resulting in higher surface area. The 1.0 M sample showed greater response toward target

gases at room temperature than the other samples. This may be attributed to high surface porosity allowing more interaction of the adsorbed gas with the sensing material. Additionally, XPS, PL and EPR showed that the 1.0 M contains relatively high concentration of V_o and Ti^{3+} defects states which contributed to the sensing properties of the nanoparticles.

4.5. ACKNOWLEDGEMENTS

This work was supported by the Department of Science and Technology (DST) and the Council for Scientific and Industrial Research (CSIR). The NCNSM characterization team and Dr. Baban Donge are acknowledged for the HRTEM, SEM and sensing measurements.

4.6. REFERENCES

- [4.1] A.M. Ruiz, A. Cornet, K. Shimanoe, J.R. Morante, N. Yamazoe, *Sens. Actuators B* 109 (2005) 7-12.
- [4.2] Y. Jun, H. Kim, J. Lee, S. Hong, *Sens. Actuators B* 120 (2006) 69-73.
- [4.3] A.M. Ruiz, A. Cornet, J.R. Morante, *Sens. Actuators B* 100 (2004) 256-260.
- [4.4] K. Vijayalakshmi, S.D. Jereil, *Ceram. Int.* 41 (2015) 3220-3226.
- [4.5] A.M. Ruiz, J. Arbiol, A. Cornet, J.R. Morante, *Mater. Sci. Eng., C* 19 (2002) 105-109.
- [4.6] M. Kaur, N. Jain, K. Sharma, S. Bhattacharya, M. Roy, A.K. Tyagi, S.K. Gupta, J.V. Yakhmi, *Sens. Actuators, B* 133 (2008) 456-461.
- [4.7] D. Aphairaj, T. Wirunmongkol, S. Niyomwas, S. Pavasupree, P. Limsuwan, *Ceram. Int.* 40 (2014) 9241–9247.
- [4.8] M.C. Corotta, M. Ferroni, D. Gnani, V. Guidi, M. Merli, G. Martinelli, M.C. Casale, M. Notaro, *Sens. Actuators, B* 58 (1999) 310-317.
- [4.9] D. Meng, T. Yamazaki, T. Kikuta, *Sens. Actuators B* 190 (2014) 838-843.
- [4.10] K. Chen, K. Xie, X. Feng, S. Wang, R. Hu, H. Gu, Y. Li, *Int. J. Hydrogen Energy* 37 (2012) 13602-13609.
- [4.11] P. Dhivya, A.K. Prasad, M. Sridharan, *Ceram. Int.* 40 (2014) 409-415.
- [4.12] I. Karaduman, D.E. Yildiz, M.M. Sincar, S. Acar. 28 (2014) 43-47.
- [4.13] N. Chen, S. Lin, J. Wang, J. Zhang, *Sens. Actuators B* 209 (2015) 729-734.

- [4.14] C. Xiang, Z. She, Y. Zou, J. Cheng, H. Chu, S. Qiu, H. Zhang, L. Sun, F. Xu, *Ceram. Int.* 40 (2014) 16343-16348.
- [4.15] S. Mun, Y. Chen, J. Kim, *Sens. Actuators B* 171-172 (2012) 1186-1191.
- [4.16] Y.L. Wang, S. Tan, J. Wang, Z.J. Tan, Q.X. Wu, Z. Jiao, M.H. Wu, *Chin. Chem. Lett.* 22 (2011) 603–606.
- [4.17] M.H. Seo, M. Yuasa, T. Kida, J.S. Huh, K. Shimano, N. Yamazoe, *Sens. Actuators B* 137 (2009) 513–520.
- [4.18] L.E. Depero, L. Sangaletti, B. Allieri, E. Bontempi, R. Salari, M. Zocchi, C. Casale, M. Notaro, *J. Mater. Res.* 13 (1998) 13, 1644-1649.
- [4.19] K. Yanagisawa, J. Ovenstone, *J. Phys. Chem. B* 103 (1999) 7781-7787.
- [4.20] T.-D. Nguyen Phan, H.-D. Pham, T.V. Cuong, E.J. Kim, S. Kim, E.W. Shin, *J. Cryst. Growth* 312 (2009) 79–85.
- [4.21] S. Dai, Y. Wu, T. Sakai, Z. Du, H. Sakai, M. Abe, *Nanoscale Res. Lett.* 5 (2010) 1829-1835.
- [4.22] Y.T. Prabhu, K.V. Rao, V.S.S. Kumar, B.S. Kumari, *World Journal of Nano Science and Engineering* 4 (2014) 21-28.
- [4.23] A.K. Zak, M.E. Abrishami, W.H.A. Majid, R. Yousefi, S.M. Hosseini, *Ceram. Int.* 37 (2011) 393-398.
- [4.24] T.T. Trinha, N.H. Tu, H.H. Le, K.Y. Ryu, K.B. Le, K. Pillai, J. Yi, *Sens. Actuators B* 152 (2011) 73–81
- [4.25] F. Tian, Y. Zhang, J. Zhang, C. Pan, *J. Phys. Chem. C* 116 (2012) 7515-7519.
- [4.26] C.Y. Xu, P.X. Zhang, L. Yan, *J. Raman Spectrosc.* 32 (2001) 862-865.

- [4.27] W. Ma, Z. Lu, M. Zhang, *Appl. Phys.*, A 66 (1998) 612-627.
- [4.28] A.S. Bolokang, F.R. Cummings, B.P. Dhonge, H.M.I. Abdallah, T. Moyo, H.C. Swart, C.J. Arendse, T.F.G. Muller, D.E. Motaung, *Appl. Surf. Sci.* 331 (2015) 362-372.
- [4.29] B. Santara, P.K. Giri, K. Imakita, M. Fujii, *Nanoscale* 5 (2013) 5476-5488.
- [4.30] B. Santara, P.K. Giri, K. Imakita, M. Fujii, *J. Phys. Chem. C* 117 (2013) 23402-23411.
- [431] B. Santara, P.K. Giri, S. Dhara, K. Imakita, M. Fujii, *J. Phys. D: Appl. Phys.* 47 (2014) 235304-235317.
- [4.32] P.I. Liu, L.C. Chung, H. Shao, T.M. Liang, R.Y. Horng, C.C.M. Ma, M.C. Chang, *Electrochimica Acta* 96 (2013) 173-179.
- [4.33] B.K. Sarma, A.R. Pal, H. Bailing, J. Chutia, *J. Phys. D: Appl. Phys.* 45 (2012) 275401.
- [4.34] Y. Lei, L.D. Zhang, *J. Mater. Res.* 16 (2001) 1138-1144.
- [4.35] H. Zhang, M. Zhou, Q. Fu, B. Lei, W. Lin, H. Guo, M. Wu, Y. Lei, *Nanotechnology* 25 (2014) 275603-275613.
- [4.36] A. Cybula, J.B. Priebe, M. M. Pohl, J.W. Sobczak, M. Schneider, A. Zielinska-Jurek, A. Bruckner, A. Zaleska, *Appl. Catal. B* 152-153 (2014) 202-211.
- [4.37] A.E. Giannakas, E. Seristatidou, Y. Deligiannakis, I. Konstantinou, *Appl. Catal. B* 132-133 (2013) 460-468.
- [4.38] D.C. Hurum, A.G. Agrios, S.E. Crist, K.A. Gray, T. Rajh, M.C. Thurnauer, *J. Electron. Spectrosc. Relat. Phenom.* 150 (2006) 155-163.

- [4.39] S.M. Prokes, J.L. Gole, X. Chen, C. Burda, W.E. Carlos, *Adv. Funct. Mater.* 15 (2005) 161-167.
- [4.40] X. Xin, T. Xu, J. Yin, L. Wang, C. Wang, *Appl. Catal. B* 176 (2015) 354-362.
- [4.41] M. El-Hilon, A.A. Dakhel, *J. Magn. Magn. Mater.* 323 (2011) 2202–2205.
- [4.42] R.V. Sagar, S. Buddhudu, *Spectrochim. Acta, Part A* 75 (2010) 1218-1222.
- [4.43] S. Yu, H.J. Yun, D.M. Lee, J. Yi, *J. Mater. Chem.* 22 (2012) 12629.
- [4.44] S. Basu, P.K. Basu, *Sensors* 86 (2009) 1968-1988.
- [4.45] V.B. Kamble, A.M. Umarji, *Appl. Phys. Lett.* 104 (2014) 251912-4.
- [4.46] S. Ghosh, G.G. Khan, K. Mandal *ACS Appl. Mater. Interfaces* 4 (2012) 2048-2056.
- [4.47] C. Wang, H. Liu, Y. Liu, G. He, C. Jiang, *Appl. Surf. Sci.* 319 (2014) 2–7.
- [4.48] R. Menzel, A.M. Peiro, J.R. Durrant, M.S.P. Shaffer, *Chem. Mater.* 18 (2006) 6059-6068.
- [4.49] A. Wei, L. Pan, W. Huang, *Mater. Sci. Eng. B* 176 (2011) 1409-1421.
- [4.50] Y.J. Chen, G. Xiao, T.S. Wang, F. Zhang, Y. Ma, P. Gao, C.L. Zhu, E. Zhang, Z. Xu, Q.H. Li, *Sens. Actuators B* 156 (2011) 867-874.
- [4.51] M. Tonezzer, T.T. Le Dang, N. Bazzanella, V.H. Nguyen, S. Iannotta, *Sens. Actuators B* 220 (2015) 1152–1160.
- [4.52] M. Tonezzer, S. Iannotta, *Talanta* 122 (2014) 201–208.
- [4.53] C.S. Rout, M. Hegde, A. Govindaraj, C.N.R. Rao, *Nanotechnology* 18 (2007) 205504.

- [4.54] Y.J. Chen, C.L. Zhu, G. Xiao, *Nanotechnology* 17 (2006) 4537.
- [4.55] M. Meyyappan, *Carbon Nanotubes: Science and Applications*, CRC Press (2004) page 220 -221
- [4.56] M. Hjiri, L. El Mira, S.G. Leonardi, A. Pistone, L. Mavilia, G. Neri, *Sens. Actuators B* 196 (2014) 413–420.
- [4.57] D.E. Motaung, G.H. Mhlongo, I. Kortidis, S.S. Nkosi, G.F. Malgas, B.W. Mwakikunga, S.S. Ray, G. Kiriakidis, *Appl. Surf. Sci.* 279 (2013) 142-149.
- [4.58] G.K. Mani, J.B.B. Rayappan, *Appl. Surf. Sci.* 311 (2014) 405-412.
- [4.59] M.R. Mohammadi, D.J. Fray, *Sens. Actuators, B* 150 (2010) 631-640.
- [4.60] A. Sharma, M. Tomar, V. Gupta, *J. Mater. Chem.* 22 (2012) 23608–23616.

CHAPTER FIVE

Fabrication of ultra-high sensitive and selective CH₄ room temperature gas sensing of TiO₂ nanorods: Detailed study on the annealing temperature¹

ABSTRACT

Applications of ultra-highly sensitive and selective methane (CH₄) room temperature gas sensors are important for various operations especially in underground mining environment. Therefore, this study set out to investigate the effect of annealing temperature on the sensitivity and selectivity of TiO₂-based sensors for detection of CH₄ gas at room temperature. TiO₂ nanoparticles synthesized using hydrothermal methods were annealed at various temperatures. Surface morphology analyses revealed that the nanoparticles transformed to nanorods after annealing at 700 °C. The results showed that the sensing properties are annealing temperature dependent. The 1.0 M TiO₂ nanostructures annealed at higher temperatures (700 °C) revealed improved sensing response to CH₄ gas at room temperature due to higher surface area of 180.51 m²g⁻¹ and point defects related to Ti³⁺ observed from electron paramagnetic resonance (EPR) and photoluminescence (PL) analyses. In

¹ The content of this chapter has been submitted to Sensors and Actuators B (2016) Revised

addition, the 1.0 M TiO₂ sensing material annealed at 700 °C also revealed an excellent sensitivity and selectivity to CH₄ gas at room temperature compared to other gases (H₂, NH₃, and NO₂), indicating that the TiO₂ nanoparticles are possible candidates for monitoring CH₄ at low concentration of ppm level.

Keywords: TiO₂; nanorods; annealing; CH₄; selectivity; gas sensing

5.1. INTRODUCTION

Monitoring and detection of toxic and combustible gases in residential areas and different workplaces like industry and mining environment has generated interest in the past decade. Enhanced sensitivity and selectivity for specific type of gases, fast response and recovery at low temperature and concentration [5.1-5.7] are fundamental characteristics of modern age gas sensing devices of toxic and often odourless gases such as oxygen (O₂), nitrogen dioxide (NO₂), sulphur dioxide (SO₂), methane (CH₄), radon (Rn) gas, ammonium (NH₃) and carbon monoxide (CO), among others. An early detection of these gases in residential, workplaces and automobiles can prevent occurrences of fatal incidents such as fire, explosions, and poisoning. For instance high concentration of O₂ in underground mines and also the mixture of air and fuel in automobile engines poses a threat as it promotes combustion and therefore it needs to be monitored continuously [5.5]. High concentration (>25 ppm) of poisonous NH₃ in products such as fertilizers, pesticides and bleach is dangerous and if inhaled it can cause respiratory problems and may lead to fatal death [5.7].

Semiconducting metal oxides (MOX) are the promising gas sensing materials because of the change in electrical resistance when exposed to either reducing or oxidizing gas [5.8]. Tin oxide (SnO_2) is one of the mostly studied MOx for gas sensing applications followed by zinc oxide (ZnO), tungsten trioxide (WO_3), titania (TiO_2), indium oxide (In_2O_3) and vanadium pentoxide (V_2O_5) [5.9]. Among them, TiO_2 has generated a lot of research interest due to its numerous applications such as photocatalytic water splitting [5.10], renewable energy (solar cells) [5.11], electrochromic devices, biomedical coating, drug delivery and gas sensing [5.12, 5.13]. TiO_2 is an n-type semiconductor with 3 crystalline phases, namely anatase, rutile and brookite. The anatase phase is known for its high photocatalytic activity. It is highly unstable and transforms to rutile phase at relatively high temperatures (above 600 °C) depending on the synthesis method. The rutile phase is stable and has got useful applications in different environments [5.12, 5.13].

One of the challenges of MOX gas sensors is energy consumption by sensors with high working temperature. Structural modification by phase transformation or additives can influence the gas sensing properties of TiO_2 . Post-preparation thermal treatment promotes phase transformation from amorphous to crystalline form and from anatase to rutile phase. The development of gas sensors that are highly sensitive at room temperature has drawn attention of many researchers worldwide. For example, Rao *et al.* [5.14] explored the gas sensing capability of Pd-doped ZnO thick films and they observed their high sensitivity to NH_3 at room temperature with a very short response time at 30 ppm

NH₃. Ag-TiO₂ core/shell nanoparticles have been found to display enhanced room temperature sensitivity and selectivity towards ethanol at very low concentration (< 5 ppm) [5.15]. Recently, Lin *et al.* [5.16] synthesized TiO₂ nanotube arrays for room temperature detection of formaldehydes. The nanotubes were synthesized by electrochemical anodization process and they showed very good response to the formaldehydes in the range of 10-50 ppm including 1000 ppm NH₃ and 50 ppm ethanol. Titania- nanotubes array were used for hydrogen gas sensing at room temperature responding to up to 1000 ppm. The sensor was able to self-clean when exposed to UV-light allowing complete release of the gas and avoiding sensor poisoning [5.17]. In this work we studied the structural transformation of TiO₂ nanoparticles annealed at various temperatures and their room temperature gas sensing properties. Previously, [5.18] we carried out sensing analyses at various operating temperatures (25, 250, 300, 350 and 400 °C) and various gases, after annealing the samples at 450 °C, and we found that the sensing response decreases when increasing the operating temperature (>25 °C) denoting that 25 °C is optimum temperature. In this study we investigate the effect of post-preparation annealing temperature on the gas sensing performance of TiO₂ nanostructures. We demonstrate for the first time that the TiO₂ nanostructures annealed at higher temperatures (700 °C) display improved sensing response, higher sensitivity and selectivity at room temperature compared to those annealed at lower temperatures. Previously [5.18], we found that the 1.0 M sample annealed at 450 °C shows a higher sensing response to NO₂ gas at room temperature. Therefore,

herein we show that upon annealing the samples at various temperatures, the 1.0 M annealed at 700 °C shows a higher sensing response to CH₄ gas at room temperature. We show in detail that the annealing our TiO₂ nanostructures at different temperatures influences their sensing performance.

5.2. EXPERIMENT DETAILS

5.2.1. Synthesis procedure of TiO₂ nanostructures

Microwave assisted hydrothermal method was used to synthesise TiO₂ nanoparticles. 6g of commercial P25 TiO₂ Degussa powder (purchased from Sigma-Aldrich, 99.9% purity) used as a starting material was added into 100 mL of 18 M of sodium hydroxide (NaOH) (also purchased from Sigma-Aldrich, 99.9% purity). The mixture was stirred for 10 minutes to ensure that it is homogeneous and was transferred into 4 Teflon vessels. The mixture was then microwave irradiated (Perkin Elmer/Anton Paar Multiwave 3000) for 15 minutes. The obtained products were allowed to cool at room temperature. For comparison, separate products were washed with distilled water, while the rest were washed with 0.25, 0.5 and 1.0 M hydrochloric acid (HCl, 37 % purity) until the desired pH of 8 was obtained. The final product was then filtered and dried in vacuum in an oven kept at 120 °C for 14 hours. The samples were then annealed for 3 hours at 300, 450 and 700 °C.

5.2.2. Sensor fabrication and testing of devices

Gas sensing measurements were carried out by dispersing TiO₂ nanoparticles in ethanol and drop-coated on alumina substrates (size: 2 mm × 2 mm) with two Pt electrodes (on their top surfaces) and a micro-heater (also on its bottom surface). For all the samples, including the as-prepared, the deposited TiO₂ layer was heated to 120 °C for 24 hours to remove the organic solvent used and to obtain good adhesion. All the sensing measurements were carried out at room temperature (25 °C). A constant flux of synthetic air of 0.5 l/min was used as gas carrier into which the desired concentrations of H₂, CH₄, NH₃ and NO₂ gases were added. The gas sensing response of the device was examined when monitoring the variation of the electrical resistance of the sensors using a KSGAS6S gas sensing station (KENOSISTEC, Italy).

5.2.3. Characterization Techniques

The TiO₂ crystallographic structure was examined using a Panalytical X'pert PRO PW 3040/60 X-ray diffractometer equipped with a Cu-K α ($\lambda = 0.154$ nm) monochromated radiation source. A Horiba Jobin-Yvon HR800 Raman microscope with an Ar⁺ laser (514.5 nm) was used as an excitation source for Raman measurements. The internal structure was analysed using a JEOL-JEM 2100 high-resolution transmission electron microscopy (HR-TEM) at 200 kV. For TEM analysis, TiO₂ powders were deposited on holey-carbon-coated Cu grids from ethanol suspensions. The surface morphology of the nanoparticles was analysed using a Auriga ZEISS scanning electron microscopy (SEM) operated at

an accelerating voltage of 5 KeV. The specific surface area and the pore volume of the samples were measured by nitrogen (N_2) physisorption using a Micromeritics TRISTAR 3000. X-ray photoelectron spectroscopy (XPS) analysis was carried using a PHI 5000 Versaprobe-Scanning ESCA Microprobe. The photoluminescence (PL) measurements were characterized using a Horiba Jobin-Yvon NanoLog spectrometer at an excitation wavelength of 325 nm. Magnetic properties were investigated using a JOEL electron paramagnetic resonance (EPR) spectrometer operating at 9.4 GHz at room temperature.

5.3. RESULTS AND DISCUSSION

Fig. 5.1 shows the XRD patterns of the as-prepared and annealed TiO_2 nanoparticles prepared using NaOH and washed with H_2O and different concentrations of HCl solution. Commercial TiO_2 (P25 Degussa) in Fig. 5.1a was used as a reference for the prepared samples. It is observed in Fig 5.1a-d that, as the annealing temperature increases, the peak intensity also increases and the peaks become narrow as the sample becomes more crystalline. The intensity of the R(110) rutile phase improves, while the A(101) peak related to anatase decreases especially at 700 °C. This indicates that increasing the annealing temperature promotes a phase transformation. As demonstrated in Fig. 5.1b, the hydrothermally treated sample washed with distilled water reveals an amorphous behavior before annealing. Wang *et al.* [5.19] indicated that, when treated in aqueous NaOH, TiO_2 crystals become amorphous, since the Ti–O bond gets broken and Ti–O–Na or Ti–OH bonds forms. When annealing the samples at 300

°C and 450 °C, a few broad peaks are observed. At 700 °C, phase transformation occurred and the rutile phase is dominating and this is seen by the intensity increase of the R(110) and R(101) rutile peaks. However, when washing the samples with HCl aqueous solution, the anatase phase dominated even at higher annealing temperature as observed in Fig.5.1 c and d. To quantify the percentage of anatase and rutile from XRD spectra, an empirical equation used by Sangaletti *et al.* [5.20] was used:

$$W_R = \frac{1}{1 + \left(1.26 \frac{I_R}{I_A}\right)^{-1}} \quad (5.1)$$

where W_R the fraction of rutile phase, I_R is the most intense rutile peak and I_A is the most intense anatase peak. The rutile fraction listed in Table 5.1 indicates that the samples undergo phase transformation and the ratio of rutile phase increases with an increase in annealing temperature. However, the amount of rutile phase decreased with washing procedure from P25 Degussa to H₂O, 0.5 M and 1.0 M respectively. The crystallite sizes and the strain of the samples were calculated using the Debye Scherrer equations (5.2) and (5.3) [5.21].

$$D = \frac{k\lambda}{\beta \cos\theta} \quad (5.2)$$

$$\varepsilon = \frac{\beta \cos\theta}{4} \quad (5.3)$$

where D is the crystallite size, k is a constant equals to 0.9, λ is the wavelength of the X-ray radiation equals to 0.154056 nm, β is the peaks full width at half

maximum and θ is the diffraction angle. The distance between adjacent crystal planes d , was calculated using Bragg's equation $n\lambda = 2d \sin\theta$ and the values are listed in Table 5.1.

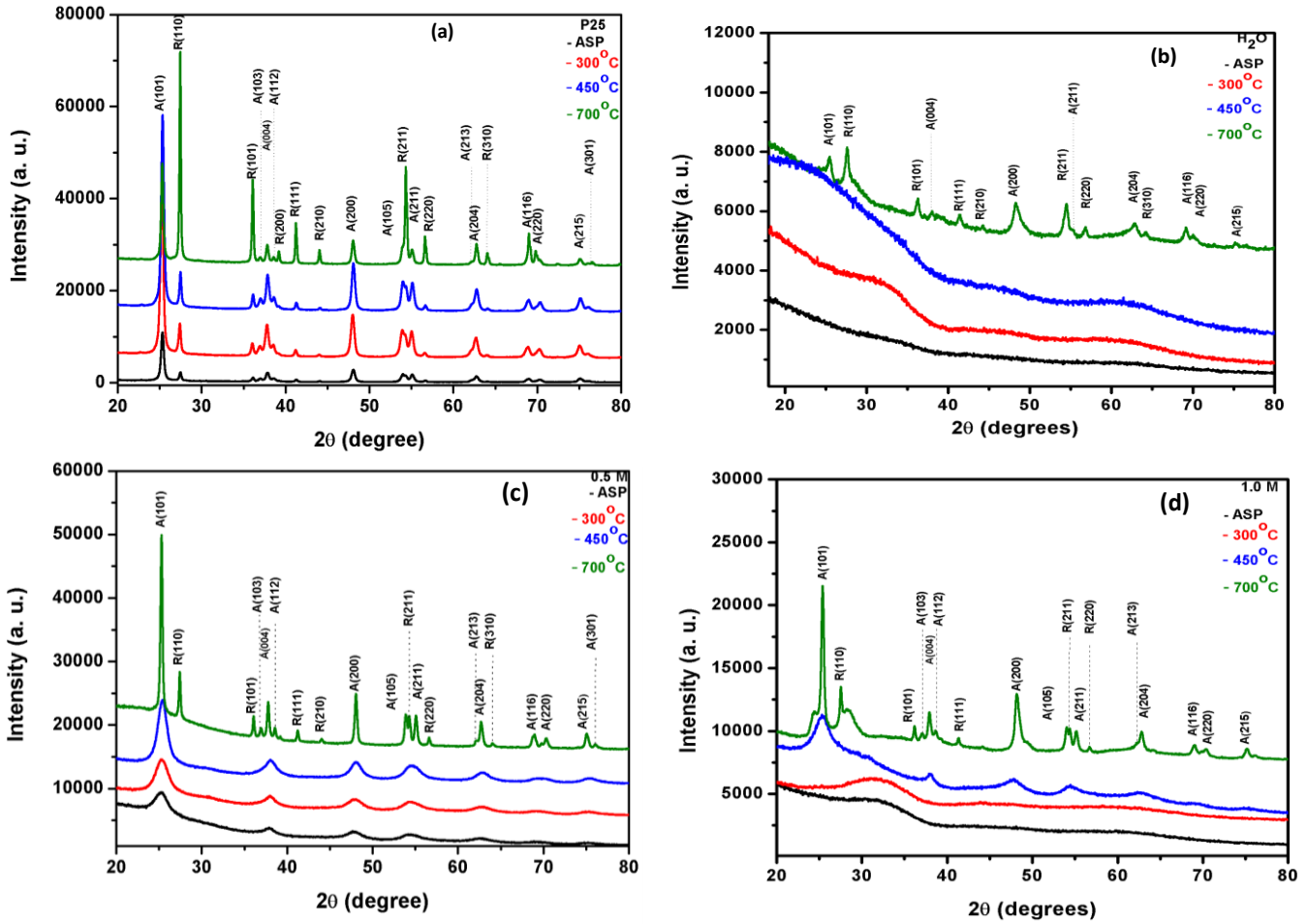


Fig. 5.1: XRD spectra of (a) P25, (b) H_2O , (c) 0.5 M and (d) 1.0 M TiO_2 nanostructures. Please note that A and R are related to anatase and rutile phase, while the ASP in the figures refers to as-prepared.

Table 5.1: Summary of crystallite size, strain, and rutile phase percentage in P25 Degussa and the synthesized TiO₂ nanoparticles annealed at various temperatures.

| Sample | Annealing temperature (°C) | D (nm) | Strain | W _R (%) | d (nm) |
|-----------------------|----------------------------|-----------|-----------|--------------------|-----------|
| P25 | ASP | 18.94 | 0.00183 | 19.97 | 0.352 |
| | 300 | 20.02 | 0.00173 | 20.88 | 0.351 |
| | 450 | 20.09 | 0.00746 | 21.28 | 0.351 |
| | 700 | 25.02 | 0.00139 | 72.32 | 0.352 |
| H₂O | ASP | Amorphous | Amorphous | Amorphous | Amorphous |
| | 300 | Amorphous | Amorphous | Amorphous | Amorphous |
| | 450 | Amorphous | Amorphous | Amorphous | Amorphous |
| | 700 | 6.16 | 0.00563 | 57.69 | 0.352 |
| 0.5 M | ASP | 4.01 | 0.00864 | Anatase | 0.351 |
| | 300 | 4.64 | 0.00747 | Anatase | 0.352 |
| | 450 | 4.46 | 0.23764 | Anatase | 0.352 |
| | 700 | 28.32 | 0.00124 | 32.56 | 0.352 |
| 1.0 M | ASP | Amorphous | Amorphous | Amorphous | Amorphous |
| | 300 | Amorphous | Amorphous | Amorphous | Amorphous |
| | 450 | 6.64 | 0.23432 | Anatase | 0.353 |
| | 700 | 21.20 | 0.00164 | 30.07 | 0.351 |

To study the phase composition, phonon confinement and defect-related emission and as well as to supplement the XRD, Raman analyses were carried out on the TiO₂ nanoparticles annealed at different temperatures. Six active Raman modes, E_{g(1)}, E_{g(2)}, B_{1g(1)}, A_{1g}, B_{1g(2)}, and E_{g(3)} corresponding to anatase and rutile phase are observed at 143, 195, 393, 512 and 637 cm⁻¹ for P25 Degussa as shown in Fig. 5.2a. As the annealing temperature increases to 450 °C the E_g peaks intensity increases and become narrow. At 700 °C, a broad shoulder around 230 cm⁻¹ is observed and the peaks at 446 and 600 cm⁻¹ assigned to E_g and A_{1g} Raman active modes of rutile phase [5.22, 5.23] are also observed and this is in agreement with XRD results (Fig. 5.1a). The as-prepared samples (before annealing) washed with distilled water and various concentrations of HCl (Fig. 5.2b-d) show amorphous behaviour and this observation is consistent with the XRD results. Upon annealing, few broad peaks corresponding to E_g modes at low frequency regions are observed and become more intense with increasing annealing temperature. Additionally, the main anatase peak in Fig. 5.2c shows a redshift in wavenumbers from 140.49 to 134.67 cm⁻¹ after annealing at 700 °C, which is probably due to particle growth as the phase transition progresses or due to phonon confinement effect of the nanoparticles. A pure anatase phase at 700 °C showing all six Raman active modes is also observed, and also is in agreement with the XRD results.

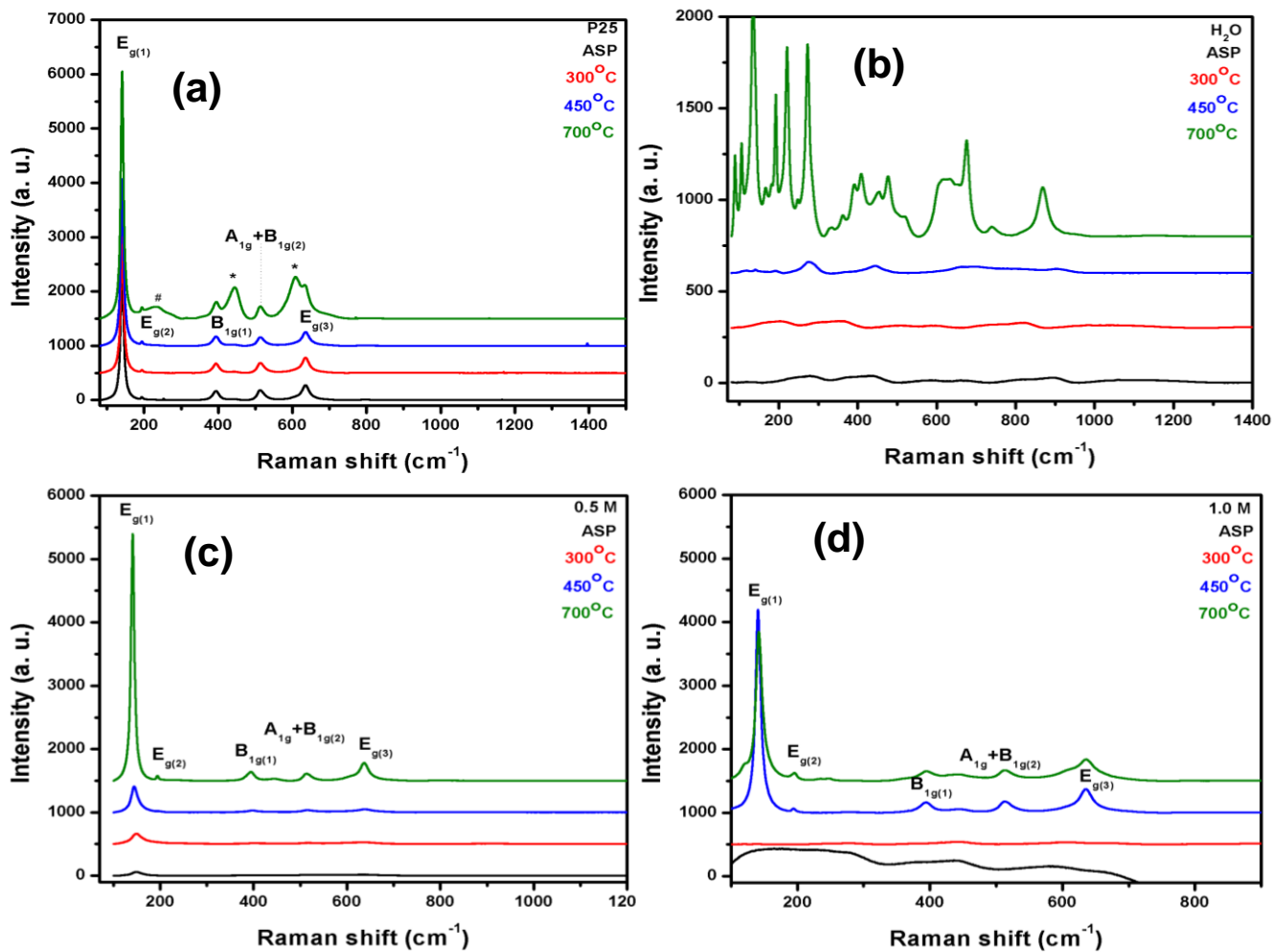


Fig. 5.2: Raman spectra for (a) P25, (b) H₂O, (c) 0.5 M and (d) 1.0 M TiO₂ nanostructures. Note: the ASP in the figures refers to as-prepared.

The TEM micrographs and selected area electron diffraction (SAED) patterns of commercial P25 and the hydrothermally treated samples washed with H₂O and 1.0 M HCl and annealed at 700 °C are depicted in Fig. 5.3 a-i. The P25 nanoparticles in Fig. 5.3a-d are polycrystalline as seen on the SAED insert. We observe a transformation in morphology as the particles become rod-like at 700 °C. The hydrothermally treated samples are agglomerated and showing an

amorphous behaviour. The amorphous samples show diffused Debye-rings in the SAED patterns in Fig. 5.3f and Fig. 5.3j. This is in agreement with the XRD observations in Fig. 5.1b and d, showing that the amorphous phase is dominating. After annealing at 700 °C, the H₂O nanoparticles becomes more crystalline while the 1.0 M sample transform to rod-like structure, showing a single crystalline behaviour as presented in Fig. 5.3l.

Detailed investigations on the surface morphology of P25 Degussa and the TiO₂ nanoparticles washed with various concentrations of HCl and that annealed at 700 °C was carried out using SEM analyses. Fig. 5.4 shows the SEM micrographs of the as-prepared and annealed samples. Fig. 5.4a shows that commercial P25 nanoparticles have small grain size. It is observed that after annealing at 700 °C the particle size increased and formed a mixture of rod and particles as seen in Fig. 5.4b. After hydrothermal treatment the as-prepared samples in Fig. 5.4c and e show clusters on nanoparticles with small particle size. As the annealing temperature increased the particles agglomerated into irregular shapes and particles grew bigger as observed in the particle size distribution (Fig. 5.5). The 1.0 M sample transformed to rods at 700 °C showing a diameter distribution of 20-35 nm. Thus we can conclude that annealing temperature promotes phase and morphology transformation. This observation is in good agreement with the XRD results shown in Table 5.1 which depicts that the diameter of particle decreases with an increase in concentration of HCl [5.18], and after annealing at 700 °C the diameter of the particle increases due to agglomeration.

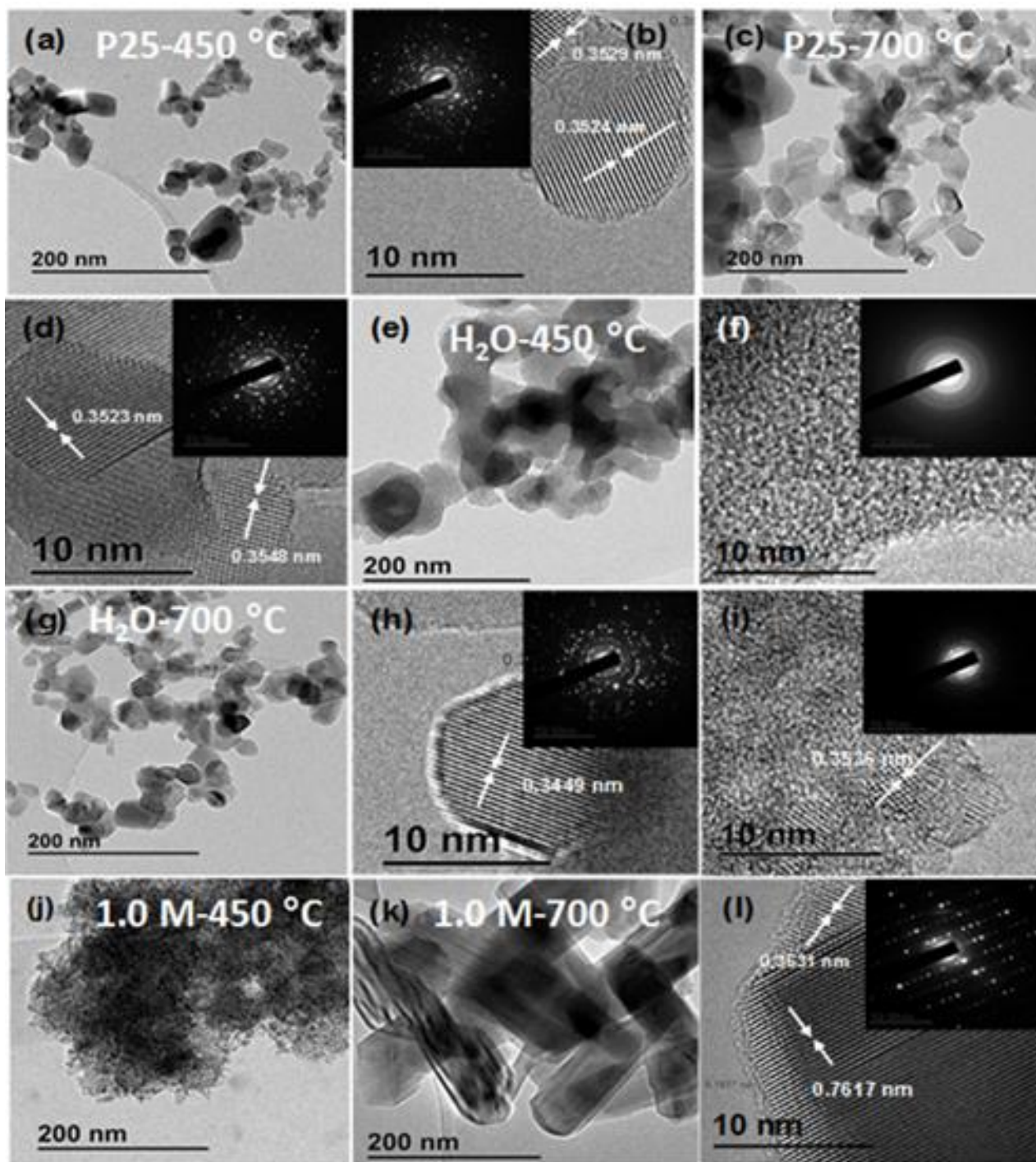


Fig. 5.3: TEM images of TiO_2 (a-b) pure P25, (c-d) P25 annealed at 700 °C, (e-f) washed with H_2O (g-h) H_2O annealed at 700 °C, (i-j) washed with 1.0 M and (k-l) 1.0 M annealed at 700 °C.

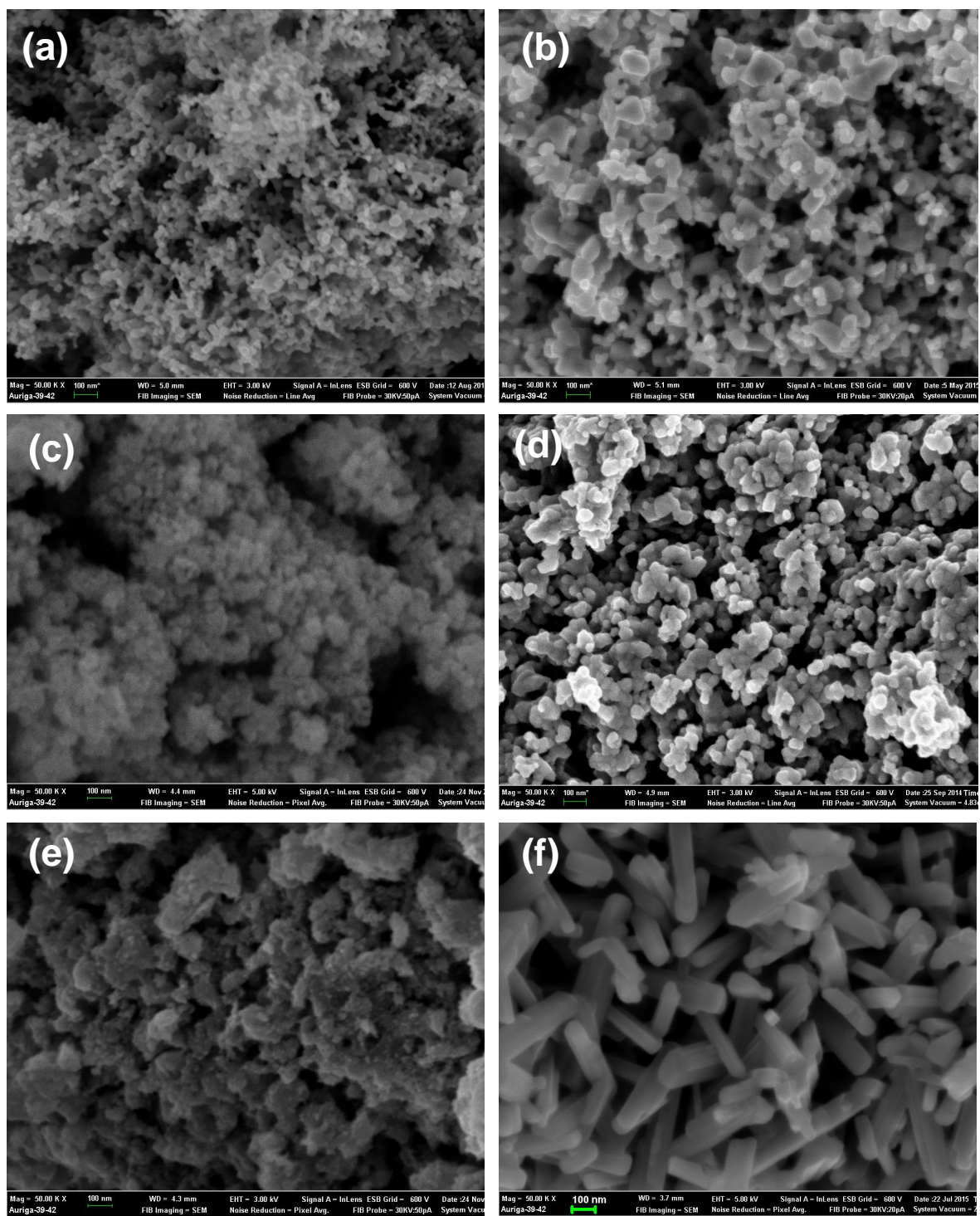


Fig. 5.4: SEM images of TiO₂ nanoparticles (a) P25, (b) P25- 700 °C, (c) as prepared TiO₂ washed with 0.5 M HCl (d) 0.5 M HCl annealed at 700 °C, (e) as-prepared TiO₂ washed with 1.0 M HCl, (f) 1.0 M HCl annealed at 700 °C.

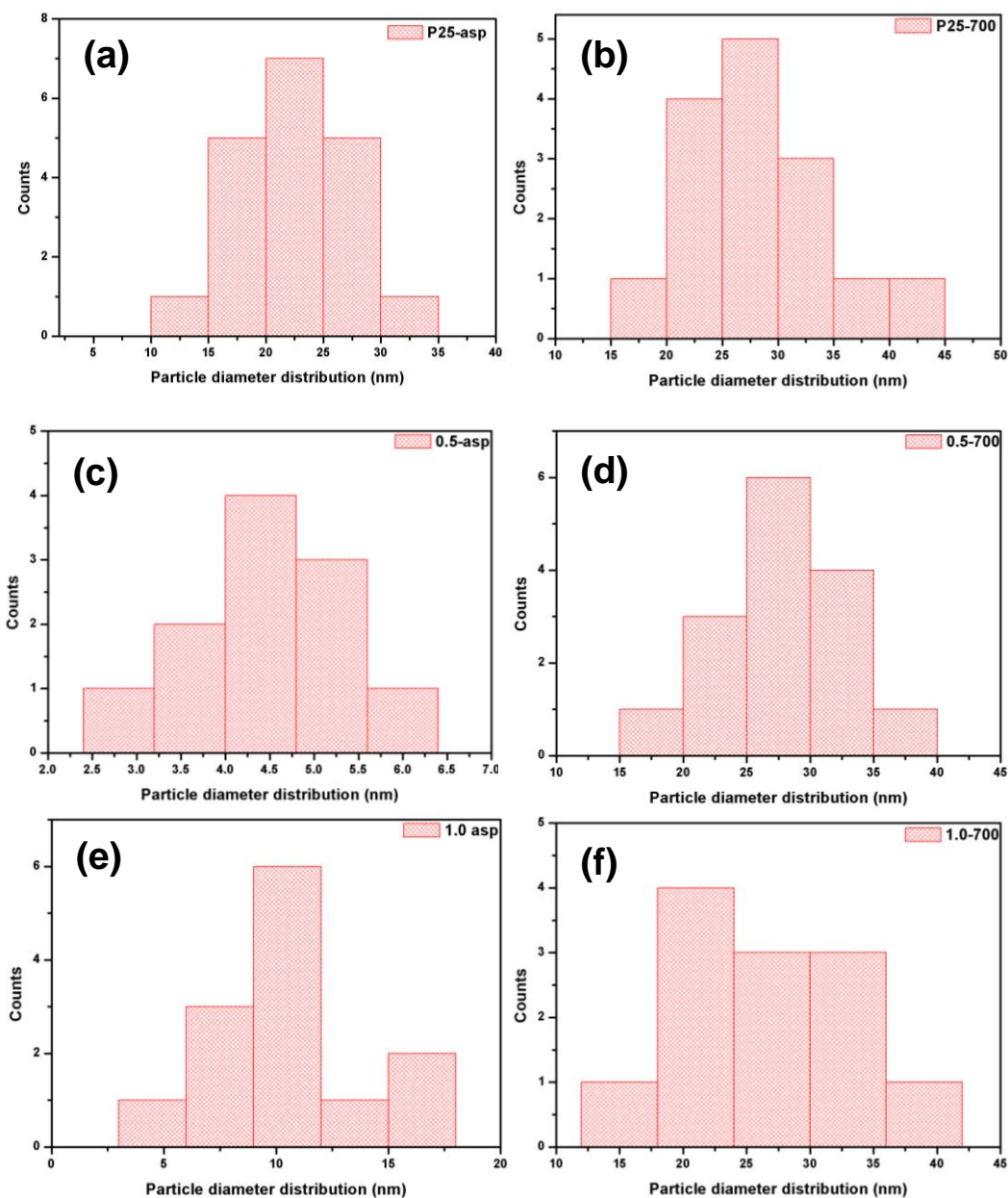


Fig. 5.5: Particle size distribution of TiO₂ nanostructures as-prepared (a) P25, (c) 0.5 M HCl (e) 1.0 M HCl and samples (b, d and f) annealed at 700 °C. Note: the ASP in the figures refers to as-prepared.

Nitrogen physisorption characteristics of the TiO₂ nanostructures annealed at 700 °C is shown in Fig. 5.6 and the Brunauer, Emmett and Teller or BET surface area, pore volume and diameter value of the as-prepared and annealed TiO₂ nanostructures at various temperatures are listed in Table 5.2. The hysteresis loops in Fig. 5.6 shifts upwards as the surface area increases. It is observed in Table 5.2 that the surface area increases with annealing temperature up to 450 °C and decrease with further increase in the annealing temperature to 700 °C and this is due to agglomeration and increase in particle size. However, it is noteworthy that the 1.0 M sample shows an increase in surface area when annealed at 700 °C.

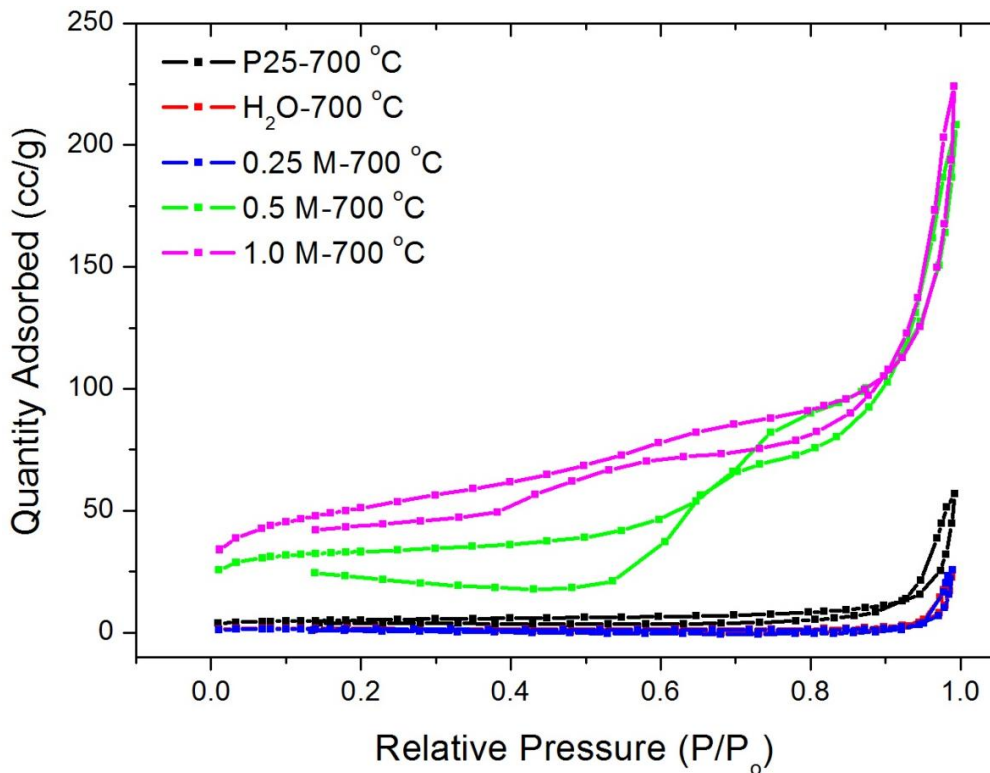


Fig. 5.6: N₂-adsorption isotherms for TiO₂ nanostructures annealed at 700 °C.

Table 5.2: Summary of BET surface area, pore volume (V_{pore}) and pore diameter (d_{pore}) of P-25 TiO_2 and those hydrothermally treated and washed with HCl and annealed at different temperatures.

| Materials | Annealing Temperature ($^{\circ}\text{C}$) | BET (m^2g^{-1}) | V_{pore} (cm^3g^{-1}) | d_{pore} (nm) |
|-----------------------|----------------------------------------------|-----------------------------------|--------------------------------------------------|------------------------|
| P25 | As-prepared | 36.2569 ± 0.2877 | 0.167776 | 35.1473 |
| | 450 | 40.5127 ± 0.0502 | 0.201464 | 25.4748 |
| | 700 | 17.7128 ± 0.1052 | 0.082904 | 40.2603 |
| H₂O | As-prepared | 15.7956 ± 0.133 | 0.106365 | 51.2793 |
| | 450 | 20.1677 ± 0.2290 | 0.140103 | 48.2508 |
| | 700 | 5.0287 ± 0.1557 | 0.035483 | 62.7267 |
| 0.25 M | As-prepared | 71.5402 ± 0.2846 | 0.268972 | 21.9579 |
| | 450 | 24.9224 ± 0.1132 | 0.196439 | 44.0710 |
| | 700 | 4.2453 ± 0.1308 | 0.040558 | 72.2514 |
| 0.50 M | As-prepared | 6.5018 ± 0.0594 | 0.012662 | 11.4886 |
| | 450 | 270.5217 ± 0.4123 | 0.545816 | 9.2939 |
| | 700 | 112.6772 ± 1.8639 | 0.330572 | 14.2425 |
| 1.00 M | As-prepared | 6.8000 ± 0.5479 | 0.040989 | 106.6081 |
| | 450 | 80.3301 ± 0.5149 | 0.417041 | 21.5196 |
| | 700 | 180.5129 ± 1.1993 | 0.388520 | 12.6592 |

We have reported previously [5.18] that the 1.0 M sample annealed at 450 $^{\circ}\text{C}$ showed good response with surface area of $80 \text{ m}^2\text{g}^{-1}$ and largest (among the samples) pore diameter of 21.52 nm. The high response was said to be due to

the porosity of the sample. In this work, the 1.0 M sample annealed at 700 °C has a surface area of about 180.51 m²g⁻¹ and pore diameter of approximately 12.66 nm. The increase in surface area and decrease in pore size is due to the transformation of the nanoparticles to nanorods as seen on TEM images. 1-dimensional nanostructures have high surface to volume ratio (which results from a high nanostructure aspect ratio), which enables the adsorption of oxygen groups and hasty transport of charge carriers.

X-ray photoelectron spectroscopy (XPS) analysis was carried out in order to study the chemical state of TiO₂ nanostructures annealed at 700 °C. The XPS survey spectrum in Fig. 5.7a shows the presence of Ti, O, C, etc. No contaminants were present; all the peaks have been calibrated with respect to C1s peak. Fig. 5.7b-e show the high resolution XPS spectra of Ti 2p and O 1s for H₂O and 1.0 M HCl annealed at 700 °C. At 450 °C, the Ti 2p_{3/2} and 2p_{1/2} peaks were centred at 458.21 eV and 463.86 eV respectively for H₂O sample and at 458.08 eV and 463.76 eV for 1.0 M sample [5.18]. However, with further annealing (up to 700 °C) the peaks shifted to lower energy and became broad. The spin orbital splitting between the Ti 2p peaks for H₂O sample is 5.51 eV, which is less than the standard value of 5.70 eV in anatase indicating that the shift to lower energy is due to the phase transformation from anatase to rutile phase [5.24, 5.25].

As depicted in Fig. 5.7 b, the Ti 2p_{3/2} peak can be fitted with one peak centred at 458.15 eV associated with Ti⁴⁺ octahedral and the 2p_{1/2} peak be fitted

with two peaks centred at 463.1 eV and 464.24 eV assigned to Ti^{3+} in the H_2O sample annealed at 700 °C . The Ti 2p core spectrum of 1.0 M sample annealed at 700 °C displays broad peaks that could be fitted with two peaks. The $2p_{3/2}$ and $2p_{1/2}$ were deconvoluted into 2 peaks each centred at 457.29 eV and 462.94 eV assigned to Ti^{3+} and 458.34 eV and 464.07 eV assigned to Ti^{4+} valence state [5.24- 5.26]. The peak shift was observed by Santara *et al* [5.27] and explained it as the effect of the surface Ti^{4+} and the near surface Ti^{3+} interstitial defects. When annealing at high temperatures, the surface Ti^{3+} defects interact with oxygen in air and get oxidised to Ti^{4+} resulting in $2p_{3/2}$ peak broadening as the Ti^{4+} concentration increases. More interesting, a spin orbital splitting between the Ti 2p peaks for 1.0 M sample annealed at 700 °C is 5.69 eV, showing superiority of the anatase phase.

Fig. 5.7d-e shows the O 1s spectra of the H_2O and 1.0 M samples annealed 700 °C. An asymmetric curve and a broad shoulder towards higher binding energy are observed on both samples. The O 1s spectra were deconvoluted into three peaks. The peaks centred at 529.73 eV and 528.96 eV for H_2O and 1.0 M respectively were assigned to O^{2-} oxygen in the TiO_2 crystal lattice. While the peaks centred at 531.66 eV and 530.27 eV are assigned to Ti-O-Ti bond on the surface and near surface. The 534.99 eV and 534.0 eV peaks were assigned to C-O bond [5.24, 5.27, 5.28]. The shift to lower binding energy as the annealing temperature increases was also observed by Wang *et al.* [5.24] and Santara *et al.* [5.27] were ascribed to the decrease in oxygen vacancies and increase in Ti^{4+} content.

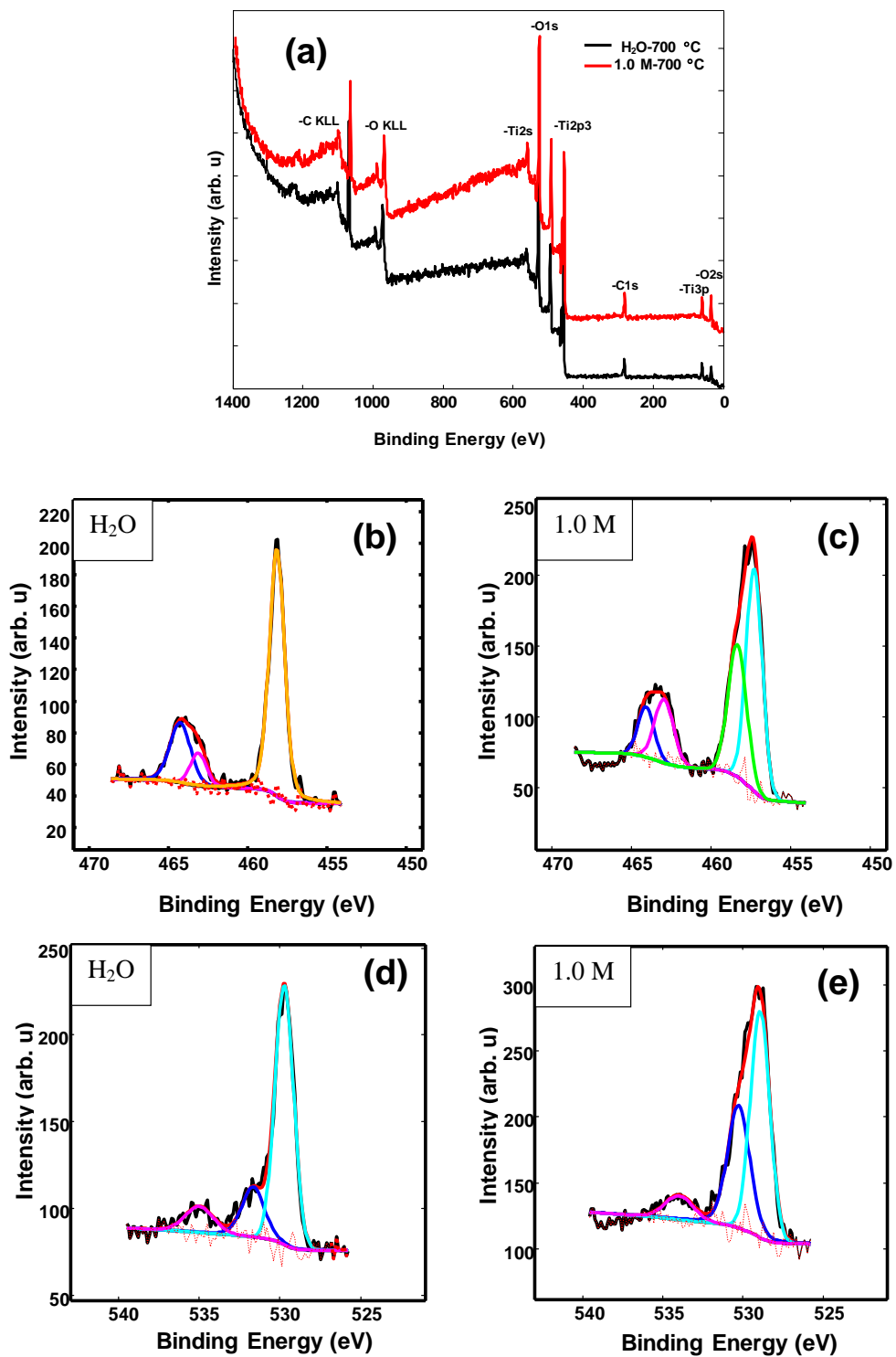


Fig. 5.7: The survey, Ti 2p and O 1s XPS spectra for TiO₂ nanostructures washed with H₂O and 1.0 M HCl annealed at 700 °C.

To investigate the defect states present in the as-prepared and annealed TiO₂ nanostructures influencing the sensing properties of the sample, photoluminescence (PL) measurements were performed. Fig. 5.8a-c shows the PL emission spectra of the commercial P25 and TiO₂ samples washed with H₂O and various concentrations of HCl. The as-prepared samples were compared to samples annealed at 300, 450 and 700 °C. A broad visible emission band is observed for all the samples. We have demonstrated in our previous work [5.18] that the intensity increases with HCl concentration. In this work we observe that the intensity of the visible band weakens when annealing at 300°C and increase when annealing at 450 °C as the annealing temperature increases to 700°C the peak intensity further decrease. This is due to the change in defect levels induced by phase transformation from amorphous phase at 300°C to pure anatase at 450 °C and the co-existence of both anatase and rutile phases at 700°C. Crystalline materials have high defects levels as compared to amorphous materials. The same behaviour was observed by Aykut *et al.* [5.29] in TiO₂ nanofibers annealed up to 800°C and they attributed the decrease in intensity to phase transformation which induces a change in types of defects forming oxygen vacancies to intrinsic defects as it transforms from anatase to rutile phase. Furthermore, Ghosh *et al.* [5.30] reported that oxygen vacancy defects present in anatase phase are responsible for the visible band emission.

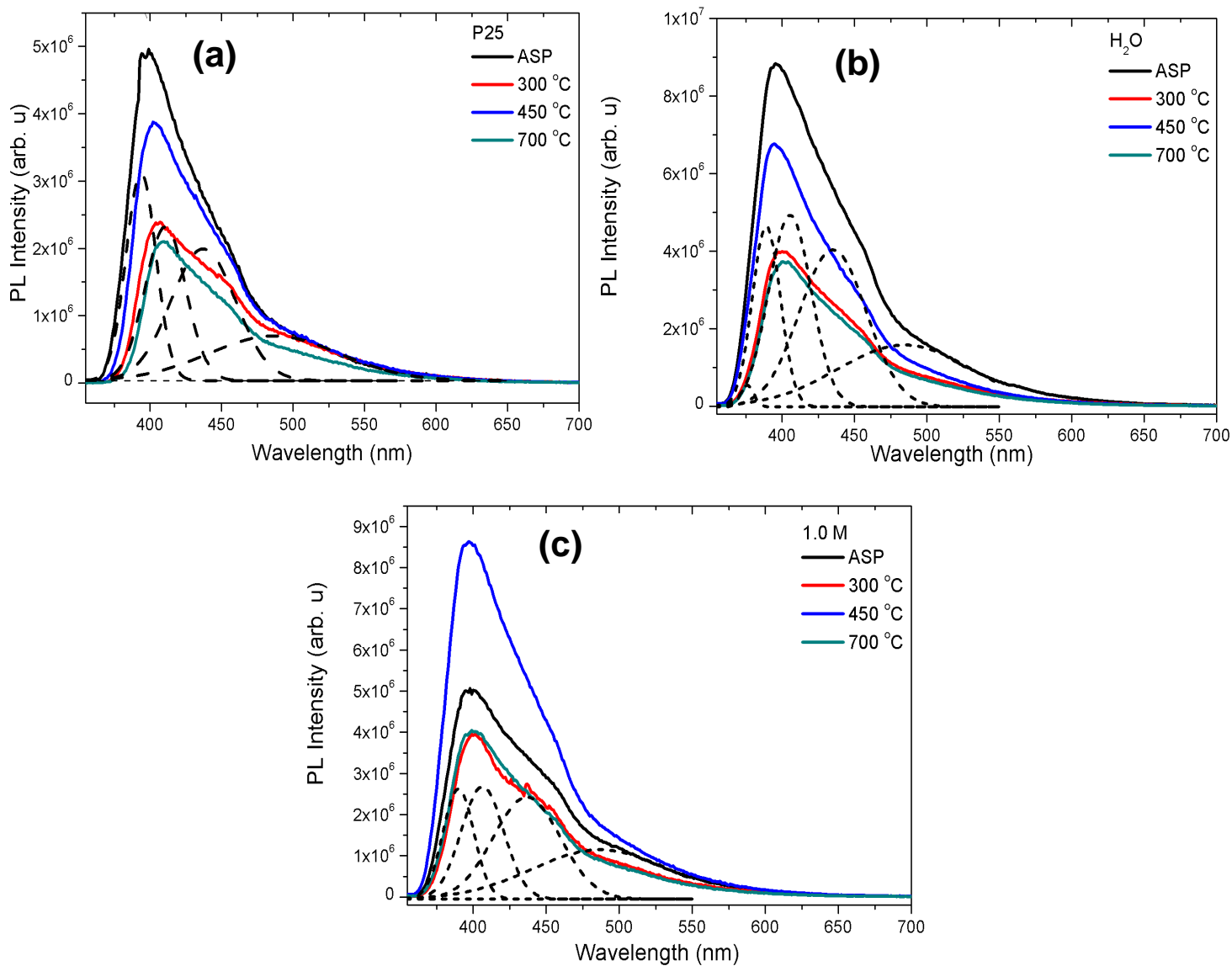


Fig. 5.8: PL spectra of TiO₂ nanoparticles (a) P25, (b) washed with distilled H₂O and (c) 1.0 M HCl. Note: the ASP in the figures refers to as-prepared.

During annealing at high temperatures (900 °C) the oxygen defects decreases and the near infrared emission attributed to intrinsic defects intensifies

due to pure rutile phase. This observation is consistent with the XPS analyses (Fig. 5.7). It has been reported in the literature [5.29- 5.34] that there are three physical origins of defects states, self-trapped excitons, oxygen vacancies and surface states that can be present in TiO₂ both anatase and rutile. The defects states can be influenced by change in surface of the sample due to annealing [5.31]. As shown in Fig. 5.8a-c, the broad peaks were deconvoluted using a Gaussian fit and fitting into four emission peaks. The peaks have been assigned and are presented in Table 5.3 below.

Table 5.3: Summary of PL emission bands and defect type.

| Peak | P25 | H ₂ O | 1.0 M | Defect type |
|------|-----------|------------------|-----------|-----------------------------------------------------------------------------------------------------------|
| 1 | 393.66 nm | 389.27 nm | 389.93 nm | Band edge emission [5.29, 5.32] |
| 2 | 410.67 nm | 405.47 nm | 406.41 nm | Self-trapped excitons at TiO ₆ octahedral [5.27, 5.28] |
| 3 | 437.22 nm | 435.09 nm | 436.72 nm | Self-trapped excitons at TiO ₆ octahedral [5.27, 5.28] |
| 4 | 486.70 nm | 485.66 nm | 487.12 nm | Shallow trap states originating from oxygen vacancies associated with Ti ³⁺ [5.32, 5.27, 5.28] |

The EPR was used to study the behaviour and interactions of magnetic species due to the presence of defects. It has been reported that TiO₂ nanostructures have defect sites such as lattice electron trapping, surface electron trapping and surface bound hole trapping sites [5.18]. Fig. 5.9a-c shows the microwave adsorption derivative (dP/dH) as a function of magnetic flux density of commercial P25 and TiO₂ nanoparticles washed with H₂O and 1.0 M HCl annealed at various temperatures. As shown in Fig. 5.9a, P25 displays an isotropic signal related to ferromagnetic (Fig. 9a 700°C) and a sharp peak related to paramagnetic behaviour and this paramagnetic signal is more visible in all the samples annealed at 300 °C. This indicates that calcining the samples at 300 °C results in a magnetic transition in which some spins related to ferromagnetic (FM) transform to paramagnetic. A similar behaviour has been observed by Nkosi *et al.* [5.33] for nickel oxide at room temperature induced by substrate annealing. A significant shift towards larger magnetic field and a reduction on the FM intensity as the annealing temperature increases to 700°C is observed in Fig 5.9a and c. The g-factor values and number of spins contributing to the magnetic behaviour of the samples are listed in Table 5.3. It should be pointed out that the number of spins (N_s) contributing to the FM ordering were calculated using a formula shown in ref. [5.18, 5.35] It is clear from Table 5.3, that the annealed samples show a g-factor in the range of 1.97-1.98 related to Ti³⁺. De Angelis *et al.* [5.34] reported that thermal annealing results in removal of a neutral oxygen atom from stoichiometric bulk anatase which leaves two excess electrons in the lattice which becomes reduced partially while forming Ti³⁺ species.

Kumar *et al.* [5.36] investigated EPR properties of TiO₂ nanoparticles annealed at temperatures ranging from 100-1000 °C. For the samples annealed at temperatures below 700 °C they reported the g-values of $g_1 = 2.016$, $g_2 = 2.012$, $g_3 = 2.002$, $g_{\parallel} = 1.958$ and $g_{\perp} = 1.988$; where g_1 , g_2 , g_3 were assigned to surface hole trapping sites and g_{\parallel} , g_{\perp} were assigned to surface electron trapping (Ti³⁺) sites in the anatase TiO₂. They also observed a reduction on the EPR intensity with an increase in annealing temperature and attributed the change to the removal of electrons by adsorbed oxygen thus stabilizing the trapped holes by preventing charge recombination. As the annealing temperature increases to 700°C, a new hole signal with $g = 2.026$ was observed and assigned to Ti⁴⁺O²⁻ Ti⁴⁺O⁻ radicals. Two major features of mixed phase in commercial P25 were reported by Hurum *et al.* [5.37] with g-values of $g = 1.990$ and 1.957 assigned to lattice electron trapping sites in anatase, while the g-values of $g = 1.975$ and 1.940 were assigned to lattice electron trapping site in rutile. This is in agreement with the observations made by Li *et al.* [5.38] The presence of surface and lattice Ti³⁺ at $g = 1.98$ and $g = 1.93$ respectively in Ti³⁺ self-doped TiO_{2-x} anatase nanoparticles was reported by Liu *et al.* [5.39] and a paramagnetic signal at $g = 2.03$ responsible for the interaction with O₂ to form O₂⁻ species. Thus, the signal observed in this work with g-values $g \leq 2.02$ and $g \geq 2.03$ can be attributed to surface hole trapping sites in anatase and in rutile respectively while $g \leq 1.990$, $g \leq 1.957$ are attributed to lattice and surface electron trapping site in anatase and $g \leq 1.975$, $g \leq 1.940$ attributed to lattice and surface electron trapping site in rutile.

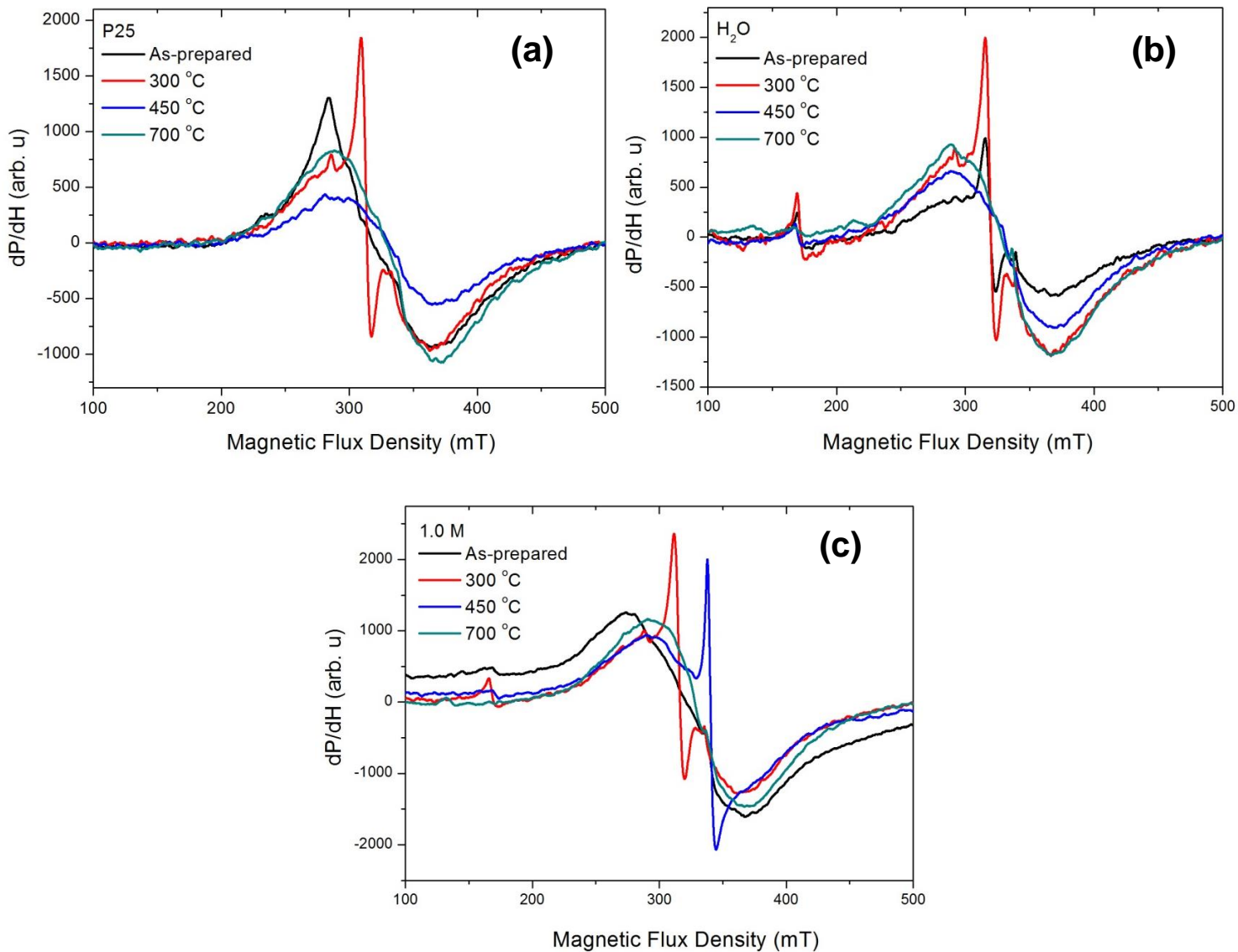


Fig. 5.9: EPR measurements of TiO₂ nanostructures annealed at various temperatures.

Table 4: The g-factor values and number of spins contributing to the magnetic behaviour of the samples.^{33,34, 36-41}

| Sample | ΔH (mT) | $N_s \times 10^6$ | g-factor | Assigned to |
|-------------------------|-----------------|-------------------|----------------------------|------------------------------------------------------------------------------------------------------|
| P25-ASP | 76.83 | 3.53 | 2.0248 | Surface hole trapping sites |
| P25-300 °C | 77.09 | 2.58 | 2.0245 1.9802 | Surface hole trapping sites |
| P25-450 °C | 80.04 | 1.73 | 2.0320 | surface hole trapping sites |
| P25-700 °C | 76.10 | 2.95 | 2.0348 1.9803 | Surface hole trapping sites Ti ³⁺ in rutile |
| H ₂ O-ASP | 73.74 | 1.47 | 2.0192 1.9912 4.1233 | Surface hole trapping Ti ³⁺ in anatase Ti ³⁺ in the distorted octahedral |
| H ₂ O-300 °C | 79.93 | 3.53 | 2.0249 1.9800 4.1171 | Surface hole trapping Ti ³⁺ in anatase Ti ³⁺ in the distorted octahedral |
| H ₂ O-450 °C | 75.24 | 2.51 | 2.0393 4.1459 | Surface hole trapping Ti ³⁺ in the distorted octahedral |
| H ₂ O-700 °C | 77.61 | 3.61 | 2.0334 4.1528 | Surface hole trapping Ti ³⁺ in the distorted octahedral |
| 0.25 M-ASP | 76.89 | 4.49 | 2.0340 | Surface hole trapping |
| 0.25 M-300 °C | 87.24 | 7.61 | 2.0349 1.9803 4.1154 | Surface hole trapping Ti ³⁺ in anatase Ti ³⁺ in the distorted octahedral |
| 0.25 M-450 °C | 74.30 | 2.65 | 2.0379 4.1924 | Surface hole trapping Ti ³⁺ in the distorted octahedral |
| 0.25 M-700 °C | 79.24 | 2.98 | 2.0578 4.2552 | Surface hole trapping Ti ³⁺ in the distorted octahedral |
| 0.5 M-ASP | 76.62 | 2.41 | 2.0245 | Surface hole trapping |
| 0.5 M-300 °C | 88.08 | 2.15 | 2.0391 | Surface hole trapping |
| 0.5 M-450 °C | 74.49 | 1.90 | 2.0251 | Surface hole trapping |
| 0.5 M-700 °C | 83.05 | 3.79 | 2.0301 1.9971 | Surface hole trapping Ti ³⁺ in anatase |
| 1.0 M-ASP | 93.53 | 7.17 | 1.9788 2.0247 | Ti ³⁺ in rutile Surface hole trapping |
| 1.0 M-300 °C | 79.59 | 3.89 | 2.0253 1.9852 4.1308 | Surface hole trapping Ti ³⁺ in anatase Ti ³⁺ in the distorted octahedral |
| 1.0 M-450 °C | 74.34 | 3.47 | 1.9738 | Ti ³⁺ in anatase |

The gas sensing characteristics of TiO₂ nanoparticles prepared using hydrothermal treatment and washed with distilled water and various concentrations of HCl (0.25, 0.5 and 1.0 M) and annealed at 300, 450 and 700 °C were studied. We have previously [5.18] determined the optimum working temperature for all the samples to be room temperature (25 °C) when exposed to NH₃, NO₂, H₂ and CH₄. Fig. 5.10a-d shows the sensing response of TiO₂ sensing materials versus the annealing temperature tested to 40 ppm NH₃, NO₂, H₂ and CH₄. As shown in Fig. 5.10, as the annealing temperature increases, a gradual increase in response is observed for the samples washed with H₂O and HCl when tested for NH₃ and NO₂ gases, showing their maximum response at the annealing temperature of 450 °C, indicating that 450 °C is their optimum annealing temperature. However, the 1.0 M showed a maximum response of 1300 at 700 °C for NO₂ detection. We have shown in ref. [5.18] that, when the 1.0 M sample was annealed at 450 °C, a maximum response of 1093 at 40 ppm NO₂ was observed. This increase in response with an increase in annealing temperature shows that the sensing materials (especially the 1.0 M) are dependent on the annealing temperature. As shown in Fig. 5.10a-c, no response was observed for P25 sample. It was shown in the XRD, SEM and TEM results that the grain sizes and the content/percentage of rutile phase in the sample increase with an increase in annealing temperature (see Table 5.1). This results in a decrease in a sensor response of P25 samples towards all the gases and displays no response after annealing at 700 °C. It is reported in the literature [5.42] that, anatase is favourable for gas sensing since it contains more defects

and the anatase surface is more active than the rutile surface. When exposed to H₂ gas, a significant increase in response for 1.0 M from 295 at 450 °C to 1433 at 700 °C annealing temperature was observed. However, when the 1.0 M samples were exposed to CH₄ gas a peculiar behaviour observed, the 1.0 M sample demonstrated a remarkable increase in sensor response, showing a response of approximately 4500 at 40 ppm CH₄ after annealing at 700 °C. The increase in sensing response for 1.0 M annealed at 700 °C is most likely a result of the diffusion/adsorption effects of the different surface morphologies. HR-TEM analysed showed that the 1.0 M TiO₂ nanoparticles annealed at 700 °C transformed to “rod-like” structure. Thus, the 1.0 M TiO₂ nanorod has a much higher surface area (see BET results), than the TiO₂ nanoparticles (observed for other materials even after annealing), with narrow inter-nanorod spaces, providing more sites for surface adsorption and desorption of the gas molecules.

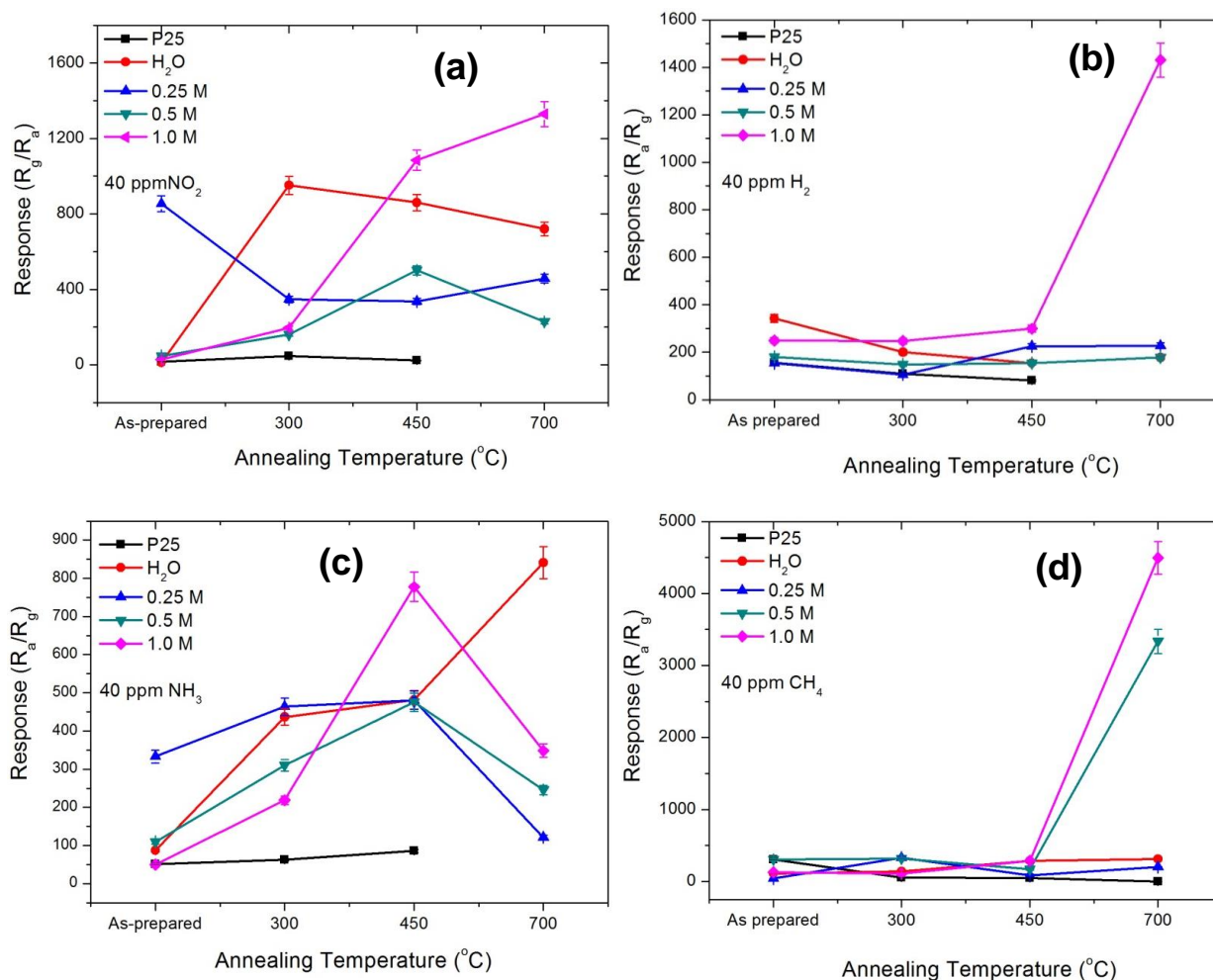


Fig. 5.10: Response versus temperature for TiO₂ sensors exposed to 40 ppm: (a) NO₂, (b) H₂, (c) NH₃ and (d) CH₄ gases.

Furthermore, the higher sensing response observed for 1.0 M to CH₄ gas, may be attributed to the smaller binding energy of the CH₄ (see Table 5.5) compared to the rest of the gases which makes it easier to break down and participate in the reaction with the sample. Motaung *et al.* [5.43] observed the same behaviour in ZnO nanostructures evaluated for room temperature gas sensing of CH₄ and H₂ gases. They attributed the enhanced sensor response

towards CH₄, to polarization of CH₄ molecules making it easier to be absorbed by the surface thus increasing conductivity.

Table 5.5: Properties of the tested gas molecules [5.44- 5.45].

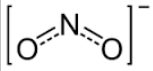
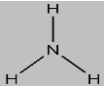
| Gas type | Structural formula | Bond | Bonding energy (kJ/mol) |
|-----------------|-----------------------------------------------------------------------------------|-------------------|-------------------------|
| NO ₂ |  | O-N-O | 473 |
| H ₂ | H-H | H-H | 436 |
| NH ₃ |  | H-NH ₂ | 435 |
| CH ₄ |  | H-CH ₃ | 431 |

Fig. 5.11a–b shows the sensor response against H₂ and CH₄ gases concentration for the samples annealed at 700°C. As depicted in Fig.5.11a, no response is observed for P25 tested to H₂ gas at 700°C. Furthermore, when P25 is exposed to CH₄, no response is observed at low concentration (< 40 ppm). As demonstrated in Fig. 5.11a and b, the sensing response of the 1.0 M increases linearly with an increase in gas concentration up to 20 ppm, showing maximum values of 1430 at 40 ppm H₂ and 6905 at 60 ppm CH₄ gas. The sensor response saturates above 40 ppm H₂ and 60 ppm CH₄ gases and start decreasing, establishing that 40 and 60 ppm is the optimal detection level. Moreover, the 1.0 M fabricated sensor exhibits a great response of 987, even at low concentration of 5 ppm CH₄ gas. Thus, this confirms that the as-fabricated gas sensor can be considered to be the most promising candidate for CH₄ gas sensor in mining application.

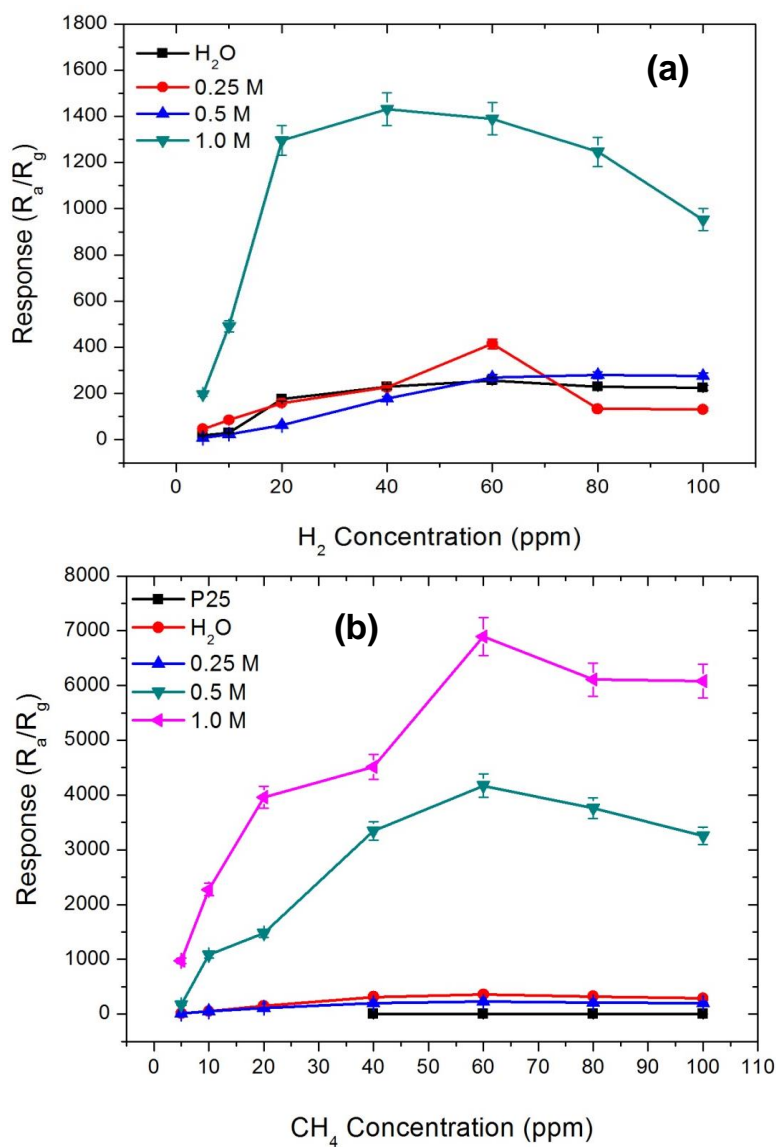


Fig. 5.11: The response curves of 700 °C annealed TiO₂ nanostructures exposed to different concentrations of (a) H₂ and (b) CH₄ gas at room temperature.

The response and recovery dynamics of the sensor is shown in Fig. 5.12 for 1.0 M annealed at 700°C exposed to 5 - 100 ppm CH₄. The sensor response increases when the gas is introduced in the chamber and when the gas is

removed, the response decreases back to the initial value confirming reversibility and prevents sensor poisoning. The response time is the time taken for the sensor resistance to reach saturation when exposed to a target gas and recovery time is the time taken for the sensor resistance to recover to its initial baseline value after removal of target gas. When exposed to 40 ppm CH₄ gas, the 1.0 M sensor shows a response time of 45 s and recovery time of 33 s at room temperature, suggesting that the sensor respond quickly to both the injection and removal of the target gas in air.

Furthermore, sensitivity which is defined as the change of a measured signal per analyte concentration unit was estimated by calculating the slope of the 0.5 M and 1.0 M curves in Fig. 5.11a and b [5.18, 5.46, 5.47]. As depicted in Fig. 5.11, the 1.0 M sample is highly sensitive to CH₄ gas as compared to other sensors with a maximum sensitivity of 199 ppm⁻¹ at 20 ppm CH₄ gas, while the 0.5 M showed a sensitivity of 132 ppm⁻¹ at 20 ppm. When the sensing materials are exposed to H₂ gas, a sensitivity of 73 and 5.19 ppm⁻¹ is observed for 1.0 M and 0.5 M, respectively. Therefore, we can conclude that the 1.0 M is more sensitive to CH₄ gas. The higher sensitivity of the 1.0 M gas sensor is due to high surface to volume ratio associated with the TiO₂ nanorods [5.48]. It was reported previously that, the diameter and geometry of the nanostructures play a vital role on the gas sensitivity performance [5.49, 5.50].

To determine the limit of detection (LoD) of the 0.5 M and 1.0 M sensors when exposed to H₂ and CH₄, the sensor noise and slope (sensitivity) were

extracted from Fig. 5.12. According to the IUPAC definition, $LoD = 3(\text{Noise}_{\text{rms}}/\text{slope})$. The sensor noise was extracted from the root-mean-square (rms) deviation of the response fluctuation using 30 points at the baseline without any target gas and the slope was calculated from the linear part in Fig. 5.11a and b. We observed very low LoD values of about 0.106 and 0.149 for 0.5 M and 1.0 M sensors, respectively, when exposed to H_2 gas. In the presence of CH_4 , the 0.5 M reveals the highest LoD value of approximately 1.663, while the 1.0 M sample shows 0.329 LoD. A low LoD value has been reported to be useful in detecting the leakage at the beginning in various application related to safety [5.47, 5.51].

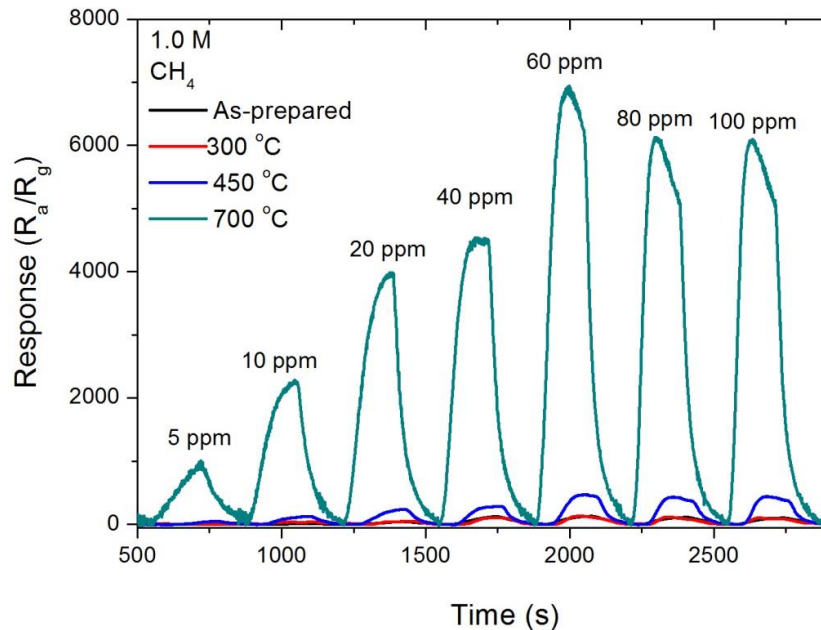


Fig. 5.12: The response curve of annealed TiO_2 nanostructures at various temperatures and exposed to different concentrations of CH_4 gas.

Table 5.6 shows a literature survey on the room temperature CH₄ gas sensing properties of various MOX compared to our current work based on TiO₂ nanorods washed with 1.0 M HCl and calcined at 700 °C. As shown in Table 5.6, there is a limited literature on the room temperature CH₄ gas sensing of metal oxides sensing elements. More remarkably, there is no single literature on the room temperature CH₄ gas sensing of TiO₂ nanostructures. Therefore, we validate that, we report for the first time on the room temperature CH₄ gas sensing on pure TiO₂ nanostructures, and without any use of UV-light or dopants. Most remarkably, it can clearly be seen that our TiO₂ sensors show higher sensing response compared to other metal oxides sensing materials tested to CH₄ gas at room temperature, indicating that they are more sensitive and reliable sensors.

Table 5.6: Literature survey on various MOX on room temperature gas sensing of CH₄ gas.

| Sensing element | CH ₄ Concentration (ppm) | Response ^a | Refs. |
|------------------|-------------------------------------|-----------------------|--------------|
| ZnO | 100 | 80 % | 5.43 |
| SnO ₂ | 2500 | 0.58 | 5.52 |
| PANI/PdO | 800 | 45 | 5.53 |
| ZnO/UV-LED Light | 1000 | 95 % | 5.54 |
| Pd-SWCNT | 100 | 0.045 | 5.55 |
| TiO ₂ | 60 | 6905 | In this work |

^aNote: The sensor response is defined as R_a/R_g for a reducing gas, and R_g/R_a for oxidation gas, where R_a is the sensor resistance in air and R_g is the sensor resistance when exposed to a target gas.

It has been reported previously, that in a TiO_2 structure, anatase phase is more active than the rutile phase. However, in this work, the 1.0 M sample annealed at 700 °C with 30 % rutile content shows an increase in response towards CH_4 and NO_2 gas compared to pure anatase sample (annealed at 450 °C). Table 5.7 lists the mixed phases (anatase and rutile) of TiO_2 gas sensors and their sensing responses to various tested gases. As shown in Table 5.7, the mixed phases sensors show poor sensing response compared to the one obtained in this work and more remarkably they were tested at higher operating temperature and gas concentration. It should be pointed out that the amount of rutile content was not stated in refs [5.56, 5.58, 5.59].

Repeatability and stability are few of the challenging factors for gas sensing materials. Fig. 5.13a shows the repeatability curve for the 1.0 M TiO_2 annealed at 700 °C and tested to 60 ppm CH_4 gas at room temperature. It can clearly be seen that the cycle is repeatable over time with a response ≥ 6000 . To establish stability of the sensor, the sensor response measurements were conducted over a long period (30 days) exposed to CH_4 gas. The results display a fairly constant response indicating the stability and repeatability of the sensor throughout the test, which indicates that the fabricated TiO_2 sensor has potential industrial applications.

Table 5.7: Effect of TiO₂ phase (anatase (A) and rutile (R)) content on the sensing response of a TiO₂ based sensor.

| Morphology | Annealing Temperature (°C) | Operating Temperature (°C) | Gas | Gas Concentration (ppm) | Response | Refs. |
|-------------------------------|----------------------------|----------------------------|-----------------|-------------------------|----------|--------------|
| Nanoparticles | 900 | 600 | CH ₄ | 500 | 0.92 | 5.56 |
| | | 450 | CO | 500 | | |
| Nanotubes (Rutile dominating) | 700 | 400 | NO ₂ | 100 | 418 | 5.57 |
| Nanoparticles | 800 | 500 | CO | 100 | 1.8 | 5.58 |
| Nanorods | 900 | 350 | H ₂ | - | 0.4 | 5.59 |
| Nanorods (30% R and 70% A) | 700 | RT | CH ₄ | 60 | 6905 | In this work |
| | | | NO ₂ | 40 | 1300 | |

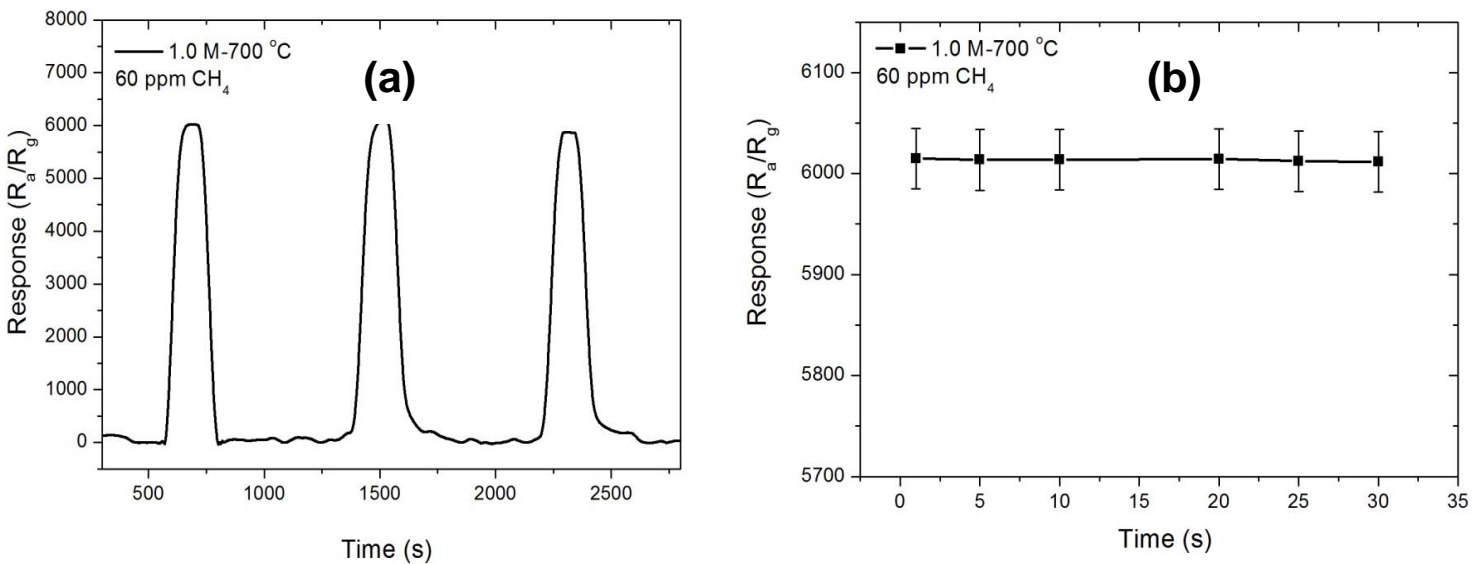


Fig. 5.13: (a) Typical repeatability curve and (b) Sensing stability of long-term response of the 1.0 M TiO₂ annealed at 700 °C exposed to 60 ppm CH₄.

Selectivity is usually defined as the ability of the gas sensor to differentiate between different kinds of target gases and it is a vital parameter for gas sensing in practical application. The selectivity of the as-prepared TiO₂ nanoparticles treated with various concentrations of HCl and that annealed at 700 °C was established by testing the sensing device to interfering test gases like 40 ppm NH₃, NO₂, H₂ and CH₄ at room temperature. As shown in Fig. 5.14, the selectivity histogram of the sensor is quantitatively displayed by plotting the sensor responses toward all gases at 40 ppm. It is clearly shown in Fig. 5.14 that the TiO₂ samples have different response to different gases and that the response is highly influenced by the annealing temperature. As shown in Fig. 5.14a, the as-prepared 0.25 M TiO₂ sensor exhibits the highest sensing response towards NO₂ gas. From our previous results, [5.18] we found that after thermal annealing at 450 °C the 1.0 M sample showed a distinct selectivity towards NO₂ at room temperature with a response of ~1093. However, in the current work after annealing at 700 °C the 1.0 M sample (Fig. 5.14 b) shows a very high sensing response of 4500 towards 40 ppm CH₄ gas, signifying that it is highly selective to CH₄ gas even at low concentration. The observed dynamic response and higher sensitivity and selectivity make the 1.0 M sensing materials annealed at 700 °C to be the most promising candidate for CH₄ gas sensing application.

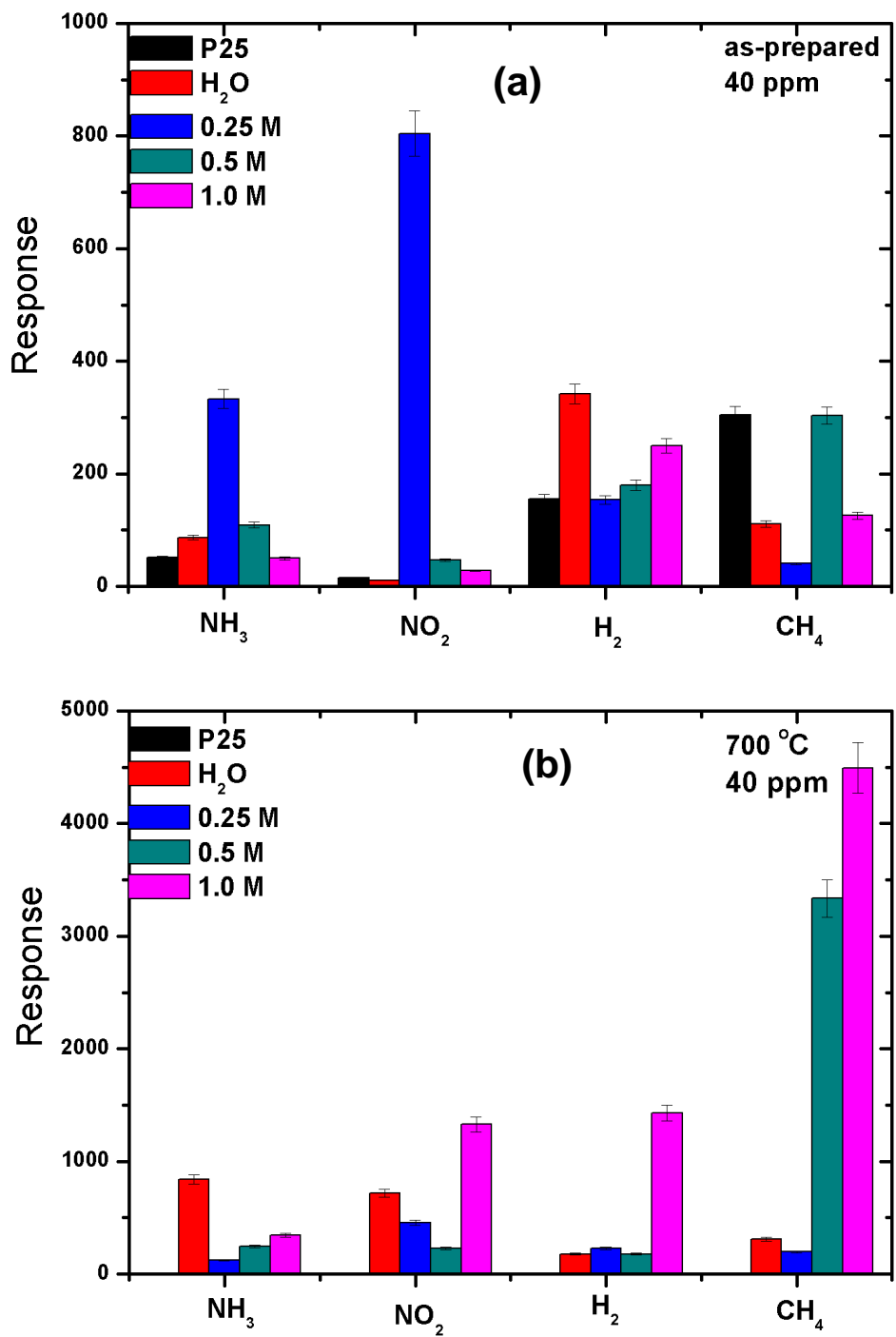
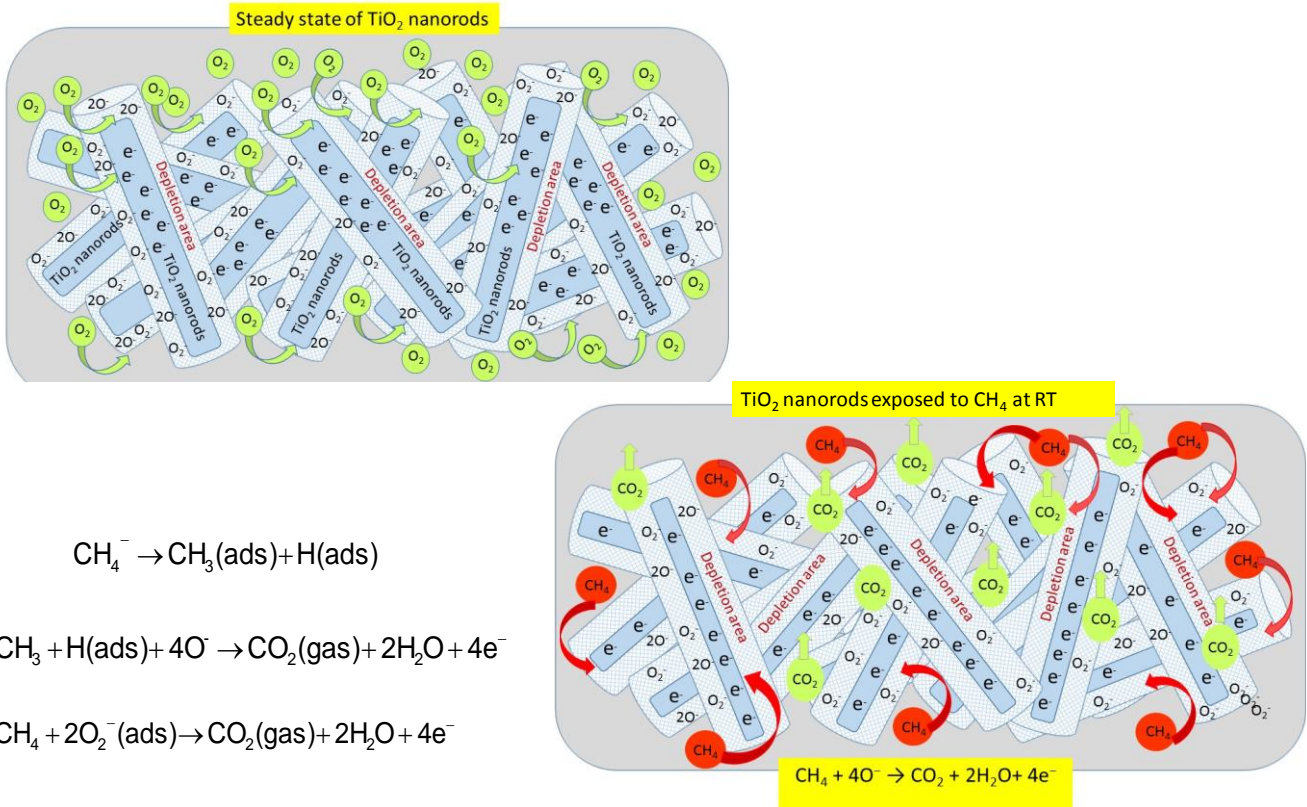


Fig. 5.14: Selectivity plots of the (a) as-prepared and (b) annealed at 700 °C TiO₂ when exposed to 40 ppm and CH₄.

It is well known that the gas sensing mechanism is dependent on the electrical properties of TiO_2 and surface boundaries between the grains which are affected by the adsorption and desorption of gaseous molecules, which plays a vital role in the sensing mechanisms. Due to high sensitivity the 1.0 M sample displays potential for detecting reductive gases hence we observe high/great response towards CH_4 and H_2 . Oxygen molecules in air (atmosphere) adsorbed on the TiO_2 surface or grain boundary, they extract electrons from the conduction band and trap the electrons in the form of oxygen ions at the surface, thus leading to an increase of the depletion layer increasing the sensor resistance. However, in the presence of a reducing gas CH_4 ; the gas molecules react with TiO_2 surface and replace the oxygen ions with electrons deposited into the material. The depletion layer decreases, while the resistance decreases (**see scheme 5.1) [5.12]**).



Scheme 5.1: Schematic diagram demonstrating the sensing mechanism of CH₄ gas on TiO₂ nanorods.

5.4. CONCLUSION

In conclusion, ultra-high sensitive and selective TiO₂-based sensors for selective detection of CH₄ gas at room temperature were synthesised using a hydrothermal method in a sodium hydroxide aqueous solution and washed with distilled water and different concentrations of hydrochloric acid annealed at various temperatures. Our findings demonstrated that the sensing properties are dependent on the annealing temperature. The 1.0 M TiO₂ nanostructures annealed at higher temperatures (700 °C) exhibited a response time of 45 s and

recovery time of 33 s and higher selectivity of 199 ppm^{-1} at room temperature due to their higher surface area of $180.51 \text{ m}^2\text{g}^{-1}$ and point defects related to Ti^{3+} observed from the EPR and PL analyses. Moreover, the results validated that the 1.0 M sensing material is highly selective to CH_4 gas and thus, it should be a strong candidate for monitoring of CH_4 gas at low concentration in the range of ppm level in mining sectors.

5.5. ACKNOWLEDGEMENTS

This work was financially supported by the Department of Science and Technology (DST) and the Council for Scientific and Industrial Research (CSIR) (Project No. HGER27S). We would also like to thank NCNSM characterization facility for microscopy and sensing measurements.

5.6. REFERENCES

- [5.1] H.-J. Kim, J.-H. Lee, *Sens. Actuators B* 192 (2014) 607– 627.
- [5.2] X. Liu, S. Cheng, H. Liu, S. Hu, D. Zhang, H. Ning, *Sensors* 12 (2012) 9635-9665.
- [5.3] C. Wang, L. Yin, L. Zhang, D. Xiang, R. Gao, *Sensors* 10 (2010) 2088-2106.
- [5.4] S. Capone, A. Forleo, L. Francioso, R. Rella, P. Siciliano, J. Spadavecchia, D.S. Presicce, A.M. Taurino, *J. Optoelectron. Adv. Mater.* 5 (2003) 1335-1348.
- [5.5] H.-R. Kim, Kwon-Il Choi, J.-H. Lee, S.A. Akbar, *Sens. Actuators B* 136 (2009) 138–143.
- [5.6] Y.-J. Chen, G. Xiao, T.-S. Wang, F. Zhang, Y. Ma, P. Gao, C.-L. Zhu, E. Zhang, Z. Xu, Q.-H. Li, *Sens. Actuators B* 156 (2011) 867-874.
- [5.7] M. Zarifi, S. Farsinezhad, M. Abdolrazzaghi, M. Daneshmand, K. Shankar, *Nanoscale* (2016) DOI: 10.1039/C5NR06567D
- [5.8] V. Galstyan, E. Comini, G. Faglia, G. Sberveglieri, *Sensors* 13 (2013) 14813-14838
- [5.9] V.B. Kamble, A.M. Umarji, *Appl. Phys. Lett.* 104 (2014) 251912-4.
- [5.10] A. Fujishima, K. Honda, *Nature* (1972) 37-38.
- [5.11] I. Tacchini, A. Anson-Casaos, Y. Yu, M.T. Martinez, M. Lira-Cantu, *Mater. Sci. Eng. B* 177 (2012) 19-26.
- [5.12] X. Chen, S.S. Mao, *Chem. Rev.* 107 (2007) 2891-2959.

- [5.13] P. Roy, S. Berger, P. Schmuki, *Angew. Chem. Int. Ed.* 50 (2011) 2904-2939.
- [5.14] G.S.T. Rao, D.T. Rao, *Sens. and Actuators B*, 55(1999) 166-169.
- [5.15] Z. Zhu, C.-T. Kao, R.-J. Wu, *Appl. Surf. Sci.* 320 (2014) 348-355.
- [5.16] S. Lin, D. Li, J. Wu, X. Li, S.A. Akbar, *Sens. and Actuators B*, 156 (2011) 505–509.
- [5.17] G.K. Mor, O.K. Varghase, M. Paulose, C.A. Grimes, *Sensor Letters* 1 (2003) 42-46.
- [5.18] Z.P. Tshabalala, D.E. Motaung, G.H. Mhlongo, O.M. Ntwaeaborwa, *Sens. Actuators B* 224 (2016) 841–856.
- [5.19] Y.L. Wang, S. Tan, J. Wang, Z.J. Tan, Q.X. Wu, Z. Jiao, M.H. Wu, *Chin. Chem. Lett.* 22 (2011) 603–606.
- [5.20] L. Sangaletti, L.E. Depero, B. Allieri, E. Bontempi, R. Salari, M. Zocchi, C. Casale, M. Notaro, *J. Mater. Res.* 13 (1998) 1644.
- [5.21] D. Cullity, Reading, MA, 1956, 363.
- [5.22] F. Tian, Y. Zhang, J. Zhang, C. Pan, *J. Phys. Chem. C* 116 (2012) 7515-7519.
- [5.23] W. Ma, Z. Lu, M. Zhang, *Appl. Phys., A* 66 (1998) 612-627.
- [5.24] Q. Wang, X. Wei, J. Dai, J. Jiang, X. Huo, *Mater. Sci. Semicond. Process.* 21 (2014) 111-115.
- [5.25] A. Lapcha, C. Maccato, A. Mettenborger, T. Andreu, L. Mayrhofer, M. Walter, S. Olthof, T.-P. Ruoko, A. Klein, M. Moseler, K. Meerholz, J. R.

- Morante, D. Barreca, and S. Mathur, *J. Phys. Chem. C* 119 (2015) 18835-18842.
- [5.26] A. S. Bolokang, F.R. Cummings, B.P. Dhonge, H.M.I. Abdallah, T. Moyo, H.C. Swart, C.J. Arendse, T.F.G. Muller, D.E. Motaung, *Appl. Surf. Sci.* 331 (2015) 362-372.
- [5.27] B. Santara, P.K. Giri, K. Imakita, M. Fujii, *J. Phys. Chem. C* 117 (2013) 23402-23411.
- [5.28] B. Santara, P.K. Giri, K. Imakita, M. Fujii, *Nanoscale* 5 (2013) 5476-5488.
- [5.29] Y. Aykut, C.D. Saquing, B. Pourdeyhimi, G.N. Parsons and S.A. Khan, *Appl. Mater. Interfaces* 4 (2012) 3837-3845.
- [5.30] S. Gosh, G.G. Khan, K. Mandal, A. Samanta, P.M.G. Nambissan, *J. Phys. Chem. C* 117 (2013) 8458-8467.
- [5.31] M. Zacharias, P. M. Fauchet. *Appl. Phys. Lett.* 71 (1997) 380.
- [5.32] M.C. Mathpal, A.K. Tripathi, M. K. Singh, S.P. Gairola, S.N. Pandey, A. Agarwal, *Chem. Phys. Lett.* 555 (2013) 182-186.
- [5.33] S.S. Nkosi, B. Yalisi, D.E. Motaung, J. Keartland, E. Sideras-Haddad, A. Forbes, B.W. Mwakikunga, *Appl. Surf. Sci.* 265 (2013) 860-864
- [5.34] F. De Angelis, C. Di Valentin, S. Fantacci, A. Vittadini, A. Selloni, *Chem. Rev.* 114 (2014) 9708–9753.
- [5.35] D.E. Motaung, G.H. Mhlongo, S.S. Nkosi, G.F. Malgas, B.W. Mwakikunga, E. Coetsee, H.C. Swart, H.M.I. Abdallah, T. Moyo, S.S. Ray, *ACS Appl. Mater. Interfaces* 6 (2014) 8981–8995.

- [5.36] C.P. Kumar, N.O. Gopal, T.C. Wang, M.-S. Wong, S.C. Ke, J. Phys. Chem. B 110 (2006) 5223-5229.
- [5.37] D.C. Hurum, A.G. Agrios, S.E. Crist, K.A. Gray, T. Rajah, M.C. Thurnauer, J. Electron. Spectrosc. Relat. Phenom. 150 (2006) 155-163.
- [5.38] G. Li, S. Ciston, Z.V. Saponjic, L. Chen, N.M. Dimitrijevic, T. Rajh, K.A. Gray, J. Catal. 253 (2008) 105-110.
- [5.39] X. Liu, H. Xu, L. R. Grabstanowicz, S. Gao, Z. Lou, W. Wang, B. Huang, Y. Dai, T. Xu, Catal. Today 225 (2014) 80-89.
- [5.40] X. Xin, T. Xu, J. Yin, L. Wang, C. Wang, Appl. Catal. B 176 (2015) 354-362.
- [5.41] B. Santara, P.K. Giri, S. Dhara, K. Imakita, M. Fujii, J. Phys. D: Appl. Phys. 47 (2014) 235304-235317.
- [5.42] H. Tang, K. Prasad, R. Sanjines, F. Levy, Sens. Actuators B 26 (1995) 71-75.
- [5.43] D.E. Motaung, G.H. Mhlongo, et al., Appl. Surf. Sci. 279 (2013) 142-149.
- [5.44] Z.S. Hosseni, A. Irajizad, A. Mortezaali, Sens. Actuators B 207 (2015) 865-871.
- [5.45] Z. Liu, T. Fan, D. Zhang, X. Gong, J. Xu, Sens. Actuators B 136 (2009) 499-509.
- [5.46] M. Tonezzer, T.T. Le Dang, N. Bazzanella, V.H. Nguyen, S. Iannotta, Sens. Actuators B 220 (2015) 1152-1160.
- [5.47] M. Hjiri, L. El Mira, S.G. Leonardi, A. Pistone, L. Mavilia, G. Neri, Sens. Actuators B 196 (2014) 413-420.

- [5.48] J.X. Wang, X.W. Sun, Y. Yang, H. Huang, Y.C. Lee, O.K. Tan, L. Vayssieres, *Nanotechnology* 17 (2006) 4995–4998.
- [5.49] Y.J. Chen, C.L. Zhu, G. Xiao, *Nanotechnology* 17 (2006) 4537.
- [5.50] C.C. Li, L.M. Li, Z.F. Du, H.C. Yu, Y.Y. Xiang, Y. Li, Y. Cai, T.H. Wang, *Nanotechnology* 19 (2008) 035501.
- [5.51] M. Tonezzer, S. Iannotta, *Talanta* 122 (2014) 201–208.
- [5.52] A. Biaggi-Labios, F. Sola, M. Lebron-Colon, L. J. Evans, J. C. Xu, G. W. Hunter, G. M. Burger and J. M. Gonzalez, *Nanotechnology* 23 (2012) 455501.
- [5.53] G. Xie, P. Sun, X. Yan, X. Du, Y. Jiang, *Sens. Actuators B* 145 (2010) 373-377.
- [5.54] B.P.J. de Lacy Costello, R.J. Ewen, N.M. Ratcliffe, M. Richards, *Sens. Actuators B* 134 (2008) 945-952.
- [5.55] Y. Lu, J. Li, J. Han, H.-T. Ng, C. Binder, C. Partridge, M. Meyyappan, *Chem. Phys. Lett.* 391 (2004) 344-348.
- [5.56] Z. M. Seeley, A. Bandyopadhyay, S. Bose, *Thin Solid Films* 519 (2010) 434-438.
- [5.57] Y. Gonullu, G.C.M. Rodriguez, B. Saruhan, M. Urgen, *Sens. Actuators B* 169 (2012) 151-160.
- [5.58] A. M. Ruiz, A. Cornet, K. Shimano, J.R. Morante, N. Yamazoe, *Sens. Actuators B* 109 (2005) 7-12.
- [5.59] L.M. Sikhwivhilu, S. Mpelane, B.W. Mwakikunga, S. Sinha Ray, *ACS Appl. Mater. Interfaces* 4 (2012) 1656–1665.

CHAPTER SIX

Selective Detection of Enhanced Room Temperature and NH₃ gas Sensing of Mn-doped TiO₂ Nanoparticles

ABSTRACT

Fabrication of highly sensitive and selective ammonia (NH₃) and nitrogen dioxide (NO₂) gas sensors at room temperature remains an important scientific challenge in the gas sensing field and is motivated by their harmful impact on the human health and environment. Therefore, herein we report on the gas sensing properties of Mn doped TiO₂ nanoparticles with various concentrations of Mn (1.0, 1.5, 2.0, 2.5 and 3.0 mol % presented as S1, S2, S3, S4 and S5) synthesized using hydrothermal method. Structural analyses showed that the structure of both pure and Mn –doped TiO₂ is tetragonal. Optical studies revealed that the Mn doped TiO₂ nanoparticles have enhanced UV-Vis emission and a broad shoulder at 540 nm signifying induced defects by substituting Ti⁴⁺ ions with Mn²⁺. The X-ray photoelectron spectroscopy and the electron paramagnetic resonance studies revealed the presence of Ti⁴⁺, Ti³⁺ and single ionized oxygen vacancies in both pure and Mn doped nanoparticles. Additionally a hyperfine split due to Mn²⁺ ferromagnetic ordering was observed confirming incorporation of Mn ions into the lattice. The sensitivity, selectivity, operating temperature, and response-recovery time, were thoroughly evaluated according to the alteration in

the materials electrical resistance in the presence of the target gases. Gas sensing studies revealed that Mn²⁺ doped on the TiO₂ surface improved the NO₂ and NH₃ sensing performances in terms of response, sensitivity and selectivity. The S1 (1.0 mol. %) revealed a higher sensitivity of 85.39 ppm⁻¹ at 20 ppm NH₃ gas.

Keywords: Mn-doped TiO₂, NO₂ selectivity, gas sensing

6.1. INTRODUCTION

Since Fujishima and Honda [6.1] discovered the photocatalytic water splitting phenomenon of TiO₂, a significant amount of research has been conducted focusing on TiO₂ nanomaterials. This is because of its promising applications in various fields such as energy, health, industrial and environmental sectors. The applications range from photocatalysis [6.2], electrochromic [6.3], renewable energy [6.4], pigments, sunscreens [6.5], Hydrogen storage [6.6], gene therapy [6.7] to gas sensing [6.8], just to name a few. The vast ranges of applications are enabled by the excellent physical and chemical properties of TiO₂ at nanoscale. Furthermore, TiO₂ is very stable, nontoxic, affordable and biocompatible [6.2- 6.8]. It's interaction with various hazardous gases in the environment such as CH₄, NH₃, CO, O₂, H₂S and NO₂ enables us to monitor and control these pollutants. Some of the gases are oxidized by TiO₂ to harmless compounds such as H₂O and O₂ in the presence of UV radiation [6.9, 6.10].

TiO₂ occurs in three crystallographic forms namely anatase, rutile and brookite. The anatase and brookite phases are metastable and transform to rutile at higher temperatures. Various processes have been done to modify the structure and properties of TiO₂ such as thermal annealing, sensitizing and metal ion doping in order to enhance/ tune its performance [6.4, 6.11, 6.12]. Thermal annealing promotes crystallization of the material and also promotes phase transformation, change in morphology and crystallite size. Such changes affect the gas sensing characteristics of the material. Intrinsic modifications such as introduction of dopants such as transitional metals (Mn, Co, Cu, Fe, and Cr) can hinder or promote phase transformation and enhance sensitivity and/or selectivity of the sensing material [6.2, 6.13]. Furthermore factors such as dopant distribution and homogeneity, crystallite size, and oxidation state are of great importance when incorporating dopants.

Materials used as bases for gas sensing rely on good conductivity. However, TiO₂ is n-type and has a wide band gap which results in very low conductivity in the range of $10^{-6} \Omega^{-1} \text{ cm}^{-1}$ at room temperatures [6.14, 6.15]. Incorporation of Mn ions into semiconducting metal oxides has been reported to alter/influence factors such photo activity and room temperature ferromagnetism of the MOx. Mn has a potential in narrowing the band gap and also introduce intermediate bands in the forbidden band thus improving the absorption range of TiO₂ [6.16]. Lu *et al.* [6.17] demonstrated significant improvement in optical and electrical properties of Mn doped TiO₂ by changing the band gap. Binas *et al.* [6.18] reported on enhanced photocatalytic activity of Mn doped TiO₂ by

degradation of methylene Blue dye under UV and visible light with Mn to TiO₂ ratio equals to 0.1:100. Other studies have attributed this behaviour to impurities, oxygen vacancy, structural disorder and aggregates of dopants [6.19- 6.21]. Li *et al.* [6.22] reported that incorporation of Ni²⁺ into TiO₂ lattice induce inversion of conductivity and this promoted good sensing towards H₂ gas ranging from 50 ppm to 2% H₂ at room temperature. Mn-ZnO nanorods were employed by Ahmed *et al.* [6.23] for oxygen gas sensing at room temperature. The doped ZnO displayed high aspect ratio and high sensitivity as compared to the pure.

Previously, we have showed that TiO₂ nanoparticles washed with 1.0 M HCl and annealed at 450 °C display good response at room temperature [6.24]. Therefore, in this study, we report for the first time on the ultra highly sensitivity and selectivity ammonia (NH₃) and nitrogen dioxide (NO₂) gas sensing properties of Mn doped TiO₂ nanoparticles prepared by hydrothermal method. The synthesized TiO₂ powders were characterized in detail, in order to investigate the influence of Mn doping on the TiO₂ structure, surface area, photoluminescence, magnetic and gas sensing properties.

6.2. EXPERIMENTAL DETAILS

6.2.1. Preparation of pure and Mn-doped TiO₂ nanoparticles

Microwave assisted hydrothermal method was followed to synthesize TiO₂ nanoparticles. 6g of commercial P25 TiO₂ powder used as a starting material was added into 100 mL of 18 M NaOH for pure sample. For the doped samples, 1.0, 1.5, 2.0, 2.5, and 3.0 mol % of Mn (NO₃)₂ 4H₂O were dissolved in 10 mL

distilled water and added dropwise. It should be pointed out that the doped samples, 1.0, 1.5, 2.0, 2.5, 3.0 mol % were denoted as S1, S2, S3, S4 and S5 respectively. The mixture was stirred for 10 minutes to ensure that it is homogeneously dissolved and transferred into 5 100 ml Teflon vessels. The mixture was then subjected to microwave irradiation for 15 minutes in a (Perkin Elmer/Anton Paar Multiwave 3000) microwave oven. The products were allowed to cool down at room temperature. The pure and doped TiO₂ products were washed with 1.0 M HCl, and distilled water until the desired pH of 8 was obtained. The final products were then filtered and dried in a vacuum oven at 120 °C for 14 hours. The samples were then calcined for 3 hours at 450 °C.

6.2.2. Characterization

The TiO₂ crystallographic structure was examined using Panalytical X'pert PRO PW 3040/60 X-ray diffractometer (XRD) equipped with a Cu-K α ($\lambda = 0.154$ nm) monochromatized radiation source. A Horiba Jobin-Yvon HR800 Raman microscope with 514.5 nm excitation laser and spectral resolution 10/10 acquisition was used for Raman studies. High-resolution transmission electron microscopy (HR-TEM) analyses were carried out on TiO₂ powders deposited on holey-carbon-coated Cu grids from alcohol suspensions at 200 kV using a Technai TEM instrument. Surface morphology analyses were examined using an Auriga ZEISS scanning electron microscopy (SEM) at an accelerating voltage of 3 KeV. The specific surface area and the pore volume of the samples were measured by nitrogen (N₂) physisorption using a Micromeritics TRISTAR 3000

surface area analyser. Before the analysis, the samples were degassed at 110 °C for 2 h under a continuous flow of N₂ gas to remove adsorbed contaminants. The optical properties were determined using Jobin-Yvon NanoLog Photoluminescence (PL) spectrometer equipped with a Jobin-Yvon PMT detector. A PHI 5000 Versaprobe-Scanning ESCA Microprobe was used to carry out X-ray photoelectron spectroscopy (XPS) analysis. A JEOL X-band electron paramagnetic resonance (EPR) spectrometer was used for microwave absorption measurements of the TiO₂ samples at constant frequency (9.4 GHz) and at room temperature (298 K).

A gas sensing measurements were carried out on TiO₂ nanoparticles dispersed in ethanol and drop-coated on alumina substrates (size: 2 mm × 2 mm) with two Pt electrodes (on its top surface) and a micro-heater (on its bottom surface). The deposited Mn-TiO₂ layer was heated to 450 °C to remove the organic solvent used and to obtain good adhesion. The sensing measurements were carried out at RT, 250, 300, 350 and 400 °C by varying the voltage. A flow-through technique with a constant flow rate of 250 ml/min was used to test the electrical and gas-sensing properties of the sensing films. A constant flux of synthetic air of 0.5 l/min was used as gas carrier into which the desired concentration of H₂, CH₄, NH₃ and NO₂ gases. The gas sensing response of the device was examined when monitoring the variation of the resistance of the sensors using a gas sensing station KSGAS6S (KENOSISTEC, Italy).

6.3. RESULTS AND DISCUSSION

6.3.1. Structural analyses

The X-Ray Diffraction pattern for pure and Mn-doped TiO₂ nanoparticles is shown in Fig. 6.1. The diffraction peaks were indexed according to the JCPD card no: 89-4203 and JCPD card no: 89-4202 for anatase and Rutile TiO₂ respectively. No peaks corresponding to impurities or Mn clusters were observed. The pure TiO₂ demonstrate pure anatase phase, with broad peaks due to smaller crystallite size as confirmed by calculations using Debye Scherrer formula on the (101) diffraction peak tabulated in Table 6.1. It can be clearly seen in Fig. 6.1 that S1 shows an amorphous behaviour. However, the rest of the Mn-doped TiO₂ nanoparticles display high crystallinity with narrow and intense diffraction peaks. The (110) rutile peak positioned at 27.4° is observed in S3 and S4, and the intensity increases with Mn concentration in S4. Two more rutile peaks are observed in S4 positioned at 36.1° and 41.3° corresponding to (101) and (111). Arroyo *et al* [6.13] observed a similar behaviour. At low concentration (≤ 1.0 mol %) of Mn dopants, anatase phase was preserved, however when increasing the concentration to 2.5 mol %, a phase transformation to rutile is accelerated. They attributed the stabilization of anatase phase to Mn²⁺ cations occupying the Ti interstitials and further stated that the anatase –rutile transformation is due to Mn²⁺ cations in substitutional position. However, in this work we observed a pure anatase phase for S2 and S5 equals to 1.5 and 3 mol%. This may denotes that there is an optimum concentration of Mn cations promoting either anatase stabilization or anatase–rutile transformation.

As shown in the inset of Fig. 6.1, a shift to higher angles is observed on the anatase (101) and (200) diffraction peaks for samples S2 and S3. However, as Mn concentration increases (S4 and S5) a noticeable shift to lower angles is observed. A shift to higher angles after Mn incorporation signals lattice contraction in the *a*-axis, and a shift to lower angles suggest lattice expansion [6.17]. The content of Mn in the sample influences the growth in crystallite size. As tabulated in Table 6.1, the crystallite size for the pure TiO₂ nanoparticles is ~ 6.5 nm, and upon doping, the crystallite sizes increased.

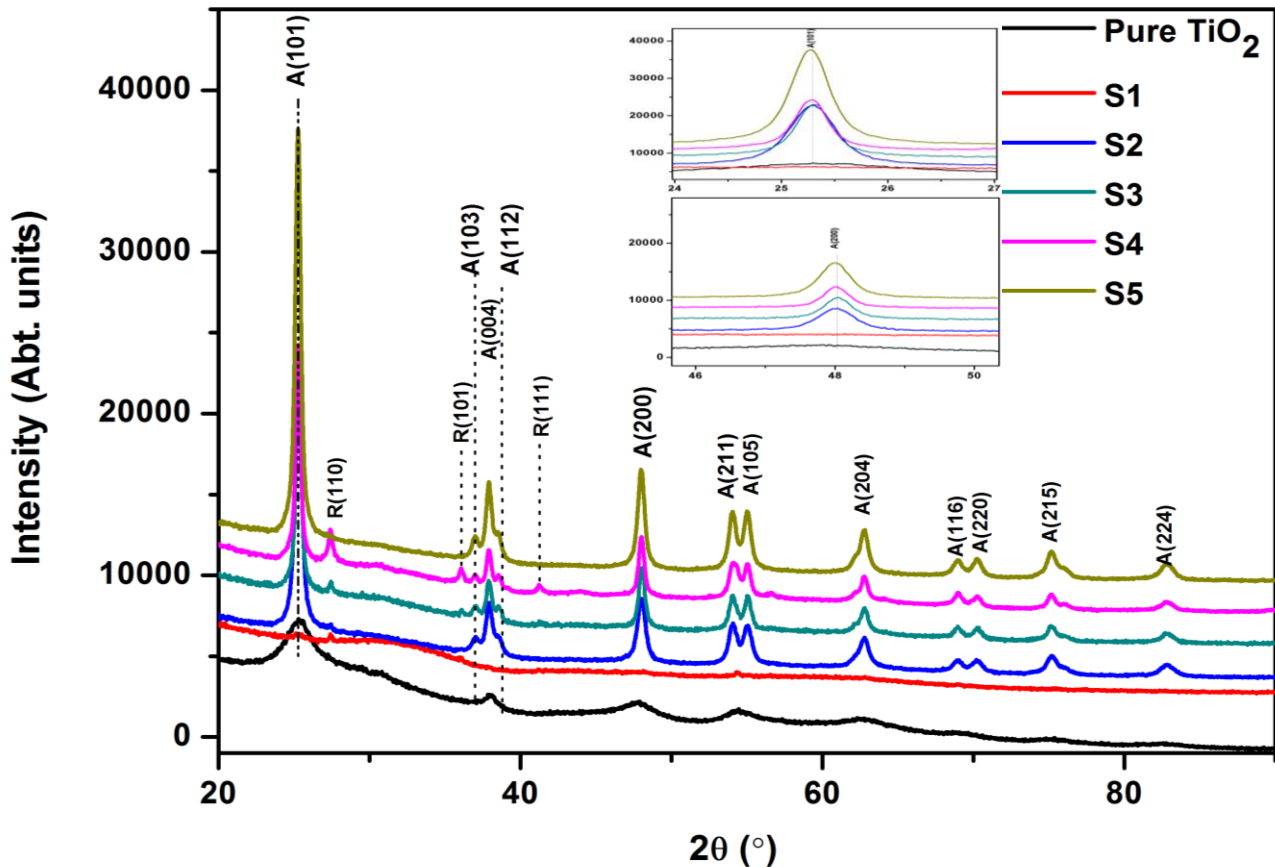


Fig. 6.1: X-Ray Diffraction spectra for pure and Mn doped TiO₂ nanoparticles.

Based on the XRD data, the lattice parameters a , c and v were determined from the most intense peak using the tetragonal equation and Vegard's law [6.25]. In theory the lattice parameters a and c for anatase are equal to 0.3785 nm and 0.9514 nm respectively and 0.4595 nm and 0.2962 nm for rutile TiO_2 [6.12, 6.26]. The lattice parameter a , contracts as Mn concentration increases, while c increases, indicating lattice growth. The Mn dopants incorporated within the interstitials lead to lattice expansion (Mn ions substitutes Ti^{4+} ions). Although the S4 sample shows the presence of rutile, the lattice parameters do not due to the fact that anatase phase is dominating (see Table 6.1).

Table 6.1: Summary of d-spacing, crystallite size, strain, lattice parameters and Rutile content at different Mn concentrations.

| Sample | 2θ ($^\circ$) | d₁₀₁ (nm) | D₁₀₁ (nm) | strain | a (nm) | c (nm) | V (nm)³ | W_R (%) |
|---------------|-------------------------------------------------------|---------------------------------|---------------------------------|---------------|-------------------|-------------------|-------------------------------|------------------------------|
| Pure | 25.24 | 0.3526 | 6.46 | 0.2343 | 0.3803 | 0.9403 | 0.1360 | 0 |
| S1 | - | - | - | - | - | - | - | Amorphous |
| S2 | 25.29 | 0.3519 | 24.48 | 0.1416 | 0.3758 | 1.0023 | 0.1416 | 0 |
| S3 | 25.30 | 0.3517 | 32.71 | 0.1060 | 0.3743 | 1.0198 | 0.1429 | 7.49 |
| S4 | 25.28 | 0.3520 | 35.23 | 0.0984 | 0.3723 | 1.0808 | 0.1502 | 13.32 |
| S5 | 25.26 | 0.3523 | 30.99 | 0.1075 | 0.3713 | 1.1151 | 0.1537 | 0 |

Raman spectroscopy measurements were performed on Pure and Mn doped TiO_2 nanoparticles to study and identify phase and structural transformation. As shown in Fig. 6.2 that the samples are crystalline except for

the S1, which reveals an amorphous phase. As demonstrated in Fig. 6.2; six Raman active modes are observed on the pure sample corresponding to anatase phase, situated at $E_{g(1)} = 142.74 \text{ cm}^{-1}$, $E_{g(2)} = 196.48 \text{ cm}^{-1}$, $B_{1g(1)} = 396.43 \text{ cm}^{-1}$, $A_{1g} = 515.56 \text{ cm}^{-1}$, $B_{1g(2)} = 515.56$ and $E_{g(3)} = 636.85 \text{ cm}^{-1}$. The E_g peaks are due to symmetric stretching vibrations, the B_{1g} peaks are due to symmetric bending vibrations and the A_{1g} peaks are due to antisymmetric bending vibrations of the O-Ti-O bond in the TiO_2 lattice [6.27, 6.28]. When introducing different concentrations of Mn, the peaks intensity decreases with increase in concentration. The anatase Raman active modes are still observed, however there is a shift in the $E_{g(1)}$ peak to higher frequency as the Mn concentration increases. Frequency shift from 142.74 cm^{-1} (for pure) to 143.70 cm^{-1} , 144.18 cm^{-1} , 146.09 cm^{-1} and 143.26 cm^{-1} is observed for S2, S3, S4 and S5, respectively. Furthermore, a gradual decrease in $E_{g(1)}$ peak intensity from 5913.67 for pure to as low as 1173.89 in Mn doped TiO_2 samples is evident. The decrease in intensity and broadness of the peaks indicate a disorder in the structure as the dopant concentration increases. Similar behaviour was observed by Xu *et al.* [6.29] on Mn doped TiO_2 samples. No rutile peak was observed on the sample S4, because of the quenching in intensity as the dopant concentration increases making it difficult to identify the rutile vibration modes.

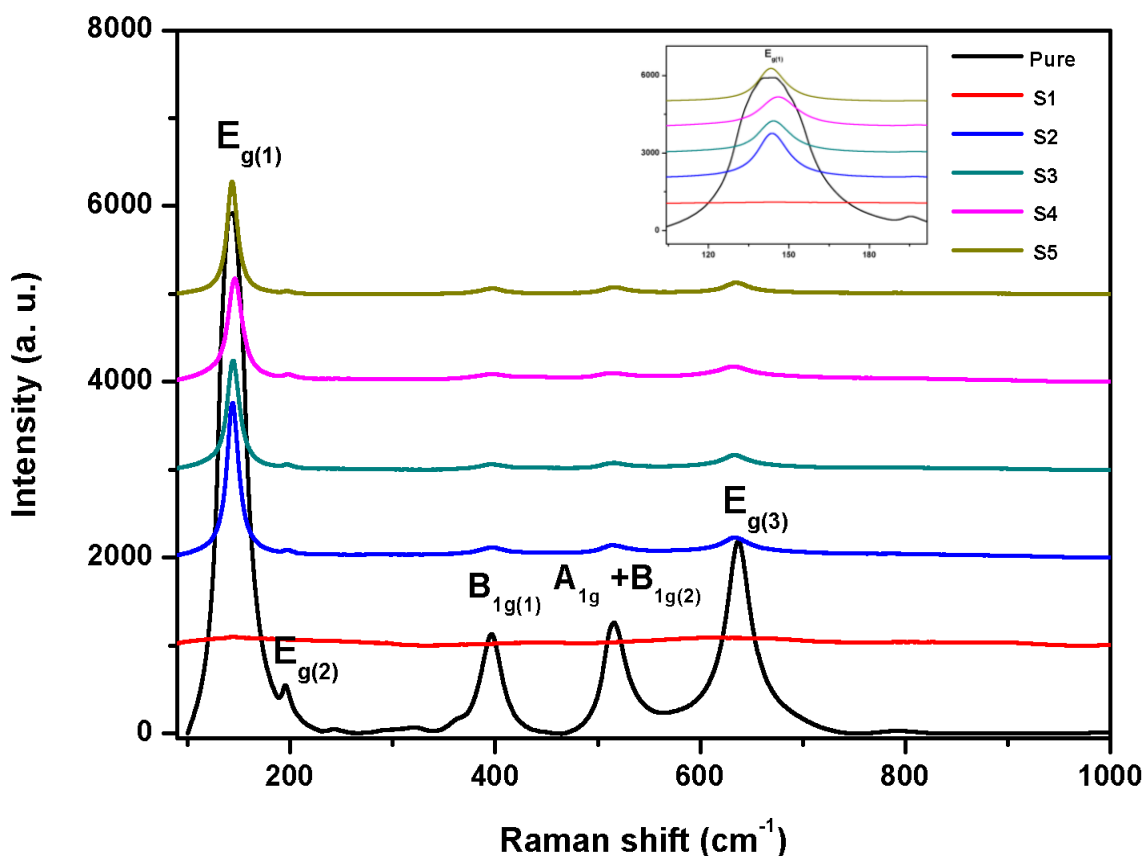


Fig. 6.2: Raman spectra for pure and Mn doped TiO₂ nanoparticles.

To further study the morphology and crystal structure of the nanoparticles, TEM analysis was carried out. TEM micrographs and selected area electron diffraction (SAED) patterns for the undoped and Mn doped TiO₂ nanoparticles are shown in Fig. 6.3. The images displayed formation of nanoparticles consistent with the SEM observations. As depicted in Fig. 6.2d-f, when incorporating the Mn ions in the TiO₂ (S1), no fringes are observed; only an amorphous behaviour is visible. Fig. 6.3e and f show diffused Debye rings due to amorphous structure. These observations are in agreement with the XRD results in Fig. 6.1. At higher doping level (S2-S5), lattice fringes disclosing d-spacings of

0.352 nm were clearly visible. It is observed that the incorporation of Mn promotes the particle growth. The SAED patterns in Fig. 6.3c, i, l, o and r show polycrystalline structure with bright distinct rings. Additionally, the SAED patterns confirmed that, the TiO_2 anatase phase transforms to rutile phase upon incorporating Mn in to the TiO_2 surface, by disclosing the (110) plane related to rutile.

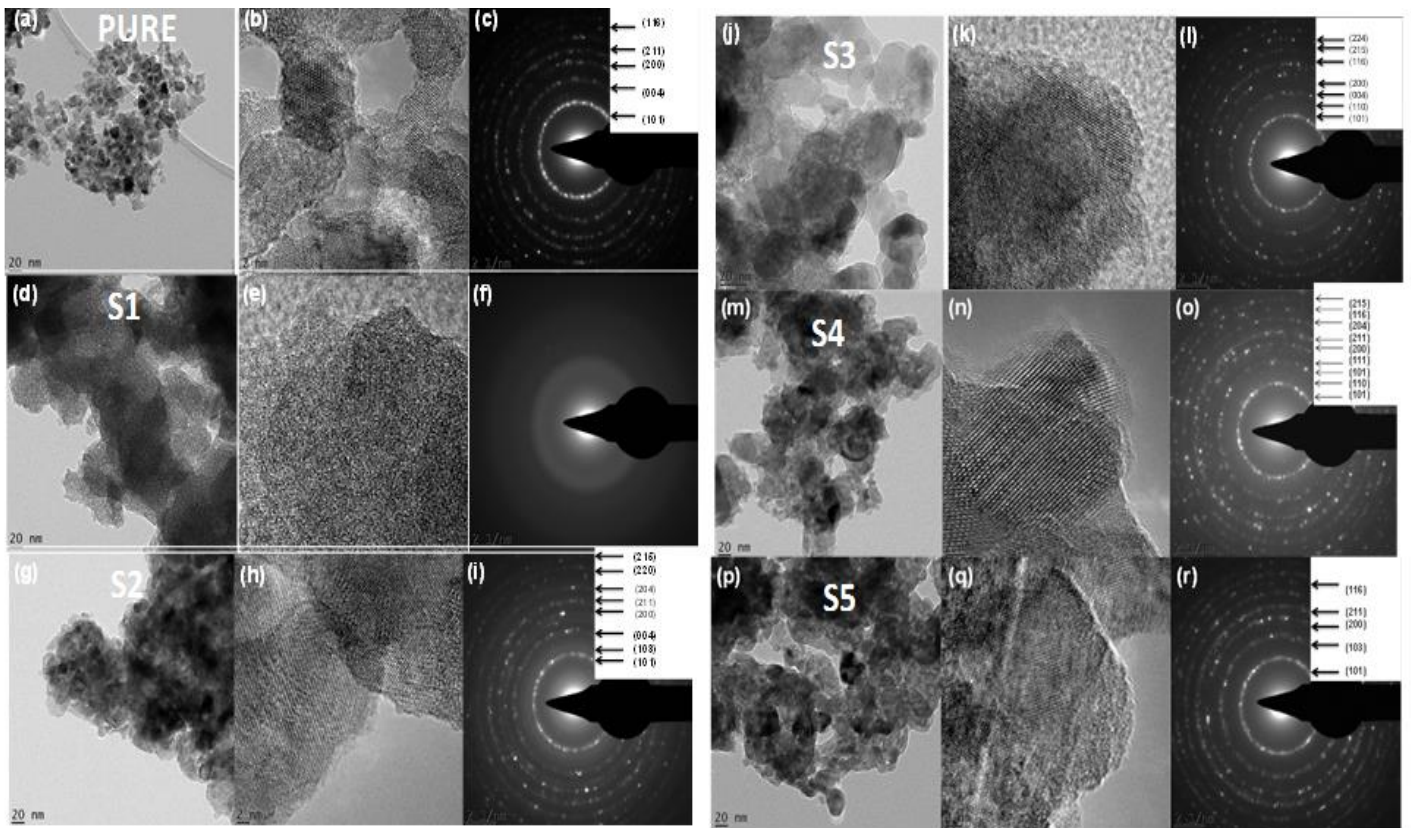


Fig. 6.3: HR-TEM and SAED micrographs for (a-c) Pure and Mn doped TiO_2 nanoparticles, namely (d-f) S1, (g-i) S2, (j-l) S3, (m-o) S4 and (p-r) S5.

The high angle annular dark field-scanning transmission electron microscope (HAADF-STEM) analysis was carried out to confirm the existence and distribution of Mn ions on the TiO_2 surface. Fig. 6.4a and b shows the HAADF image of S1, the direct mapping of each element (Ti, Mn and O) at high resolution z-contrast (Fig 6.4a) were carried out at 200 kV. The surfaces of the Mn- TiO_2 particles were evenly bright. No isolations of elements or regions were observed on the map as the elements evenly overlap the entire selected area. This indicates that, the Mn ions were incorporated into the TiO_2 lattice and no phase/elemental segregation occurred. Similar behaviour was observed from XRD and XPS analyses.

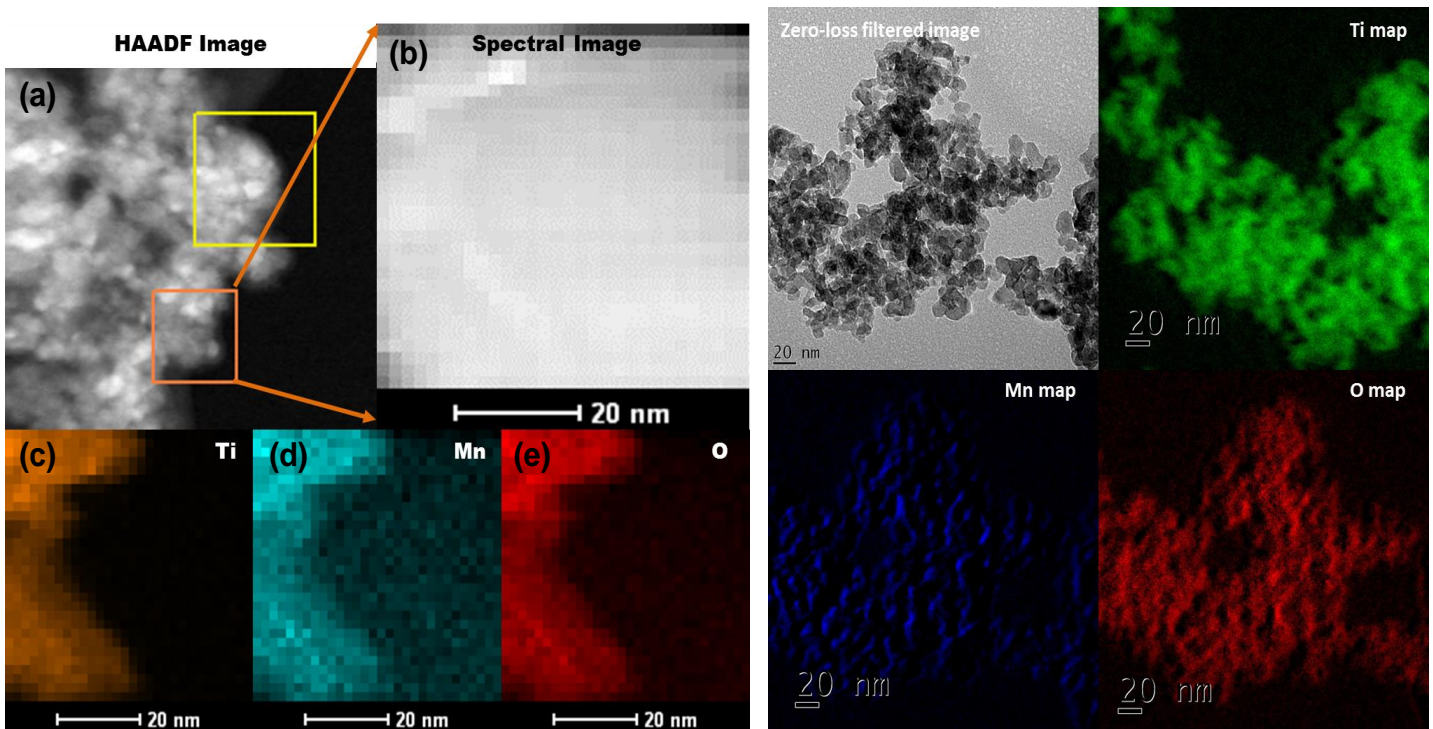


Fig 6.4: STEM coupled EDS Map analysis of sample S1 for the nanoscale mapping of Ti, Mn and O.

6.3.2. Surface Morphology

Fig. 6.5 shows the SEM images of the pure and Mn doped TiO₂ nanoparticles with different Mn concentrations. It is obviously seen from the SEM micrographs that, when incorporating Mn ions in the TiO₂ structure, the particle size grows, and this observation is consistent with the XRD results. The pure TiO₂ sample in Fig 6.5 shows a porous surface made of small nanoparticles with diameter of about 6.5 nm. Additionally, the sample has a fluffy like texture. However, upon incorporating the Mn, Fig. 6.5, the particles aggregated, showing almost a flat surface. When increasing the doping concentration (S2-S5), the particles sizes increases more and becomes more elongated. Moreover, the S3 sample shows larger porous behaviour compared to its counter parts.

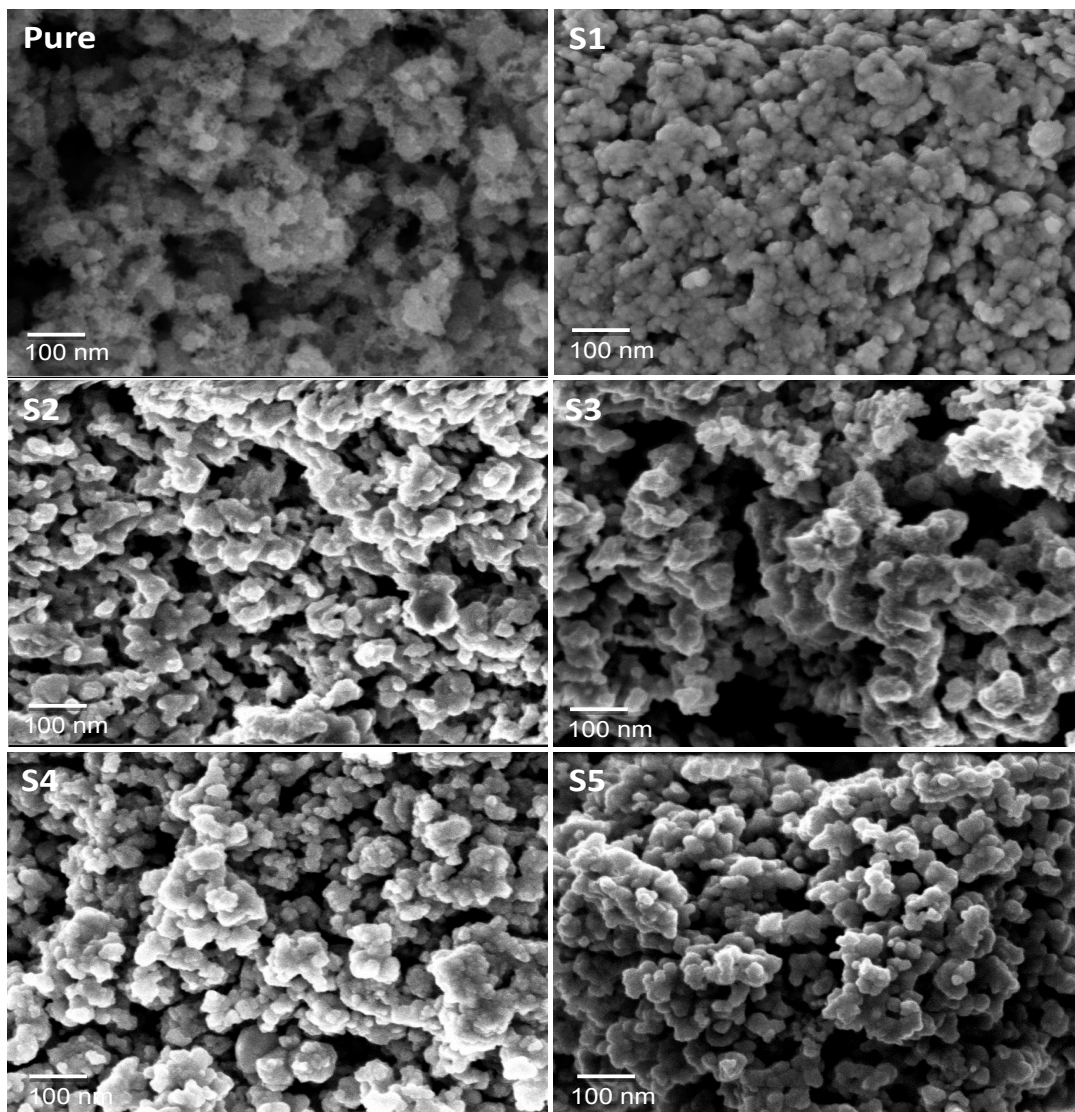


Fig. 6.5: SEM micrographs of Pure and Mn doped TiO₂ nanoparticles.

6.3.3. BET Surface area analysis.

Fig. 6.6 shows the nitrogen adsorption and desorption analysis of pure and Mn doped TiO₂ nanoparticles. As demonstrated in Fig. 6.6, the isotherms of the doped nanostructures shift downwards while the hysteresis loop at relatively high pressure increases, disclosing a higher pore (mesopore) diameter distribution. As

evidenced in Table 6.2, sample S1 disclose a higher surface area which is beneficial to gas adsorption. However, the relative smaller pore diameter results to quick saturation during gas sensing. The S2 sample shows a smaller surface area compared to rest of the samples. However, the S3 sample reveals a higher pore diameter of about 39.9034 nm, compared to its counter parts. It is well known that the higher pore diameter is beneficial for gas sensing, since it allows more gas adsorption. Therefore, a higher sensing response may be anticipated for this sample (Pure, S1, S5).

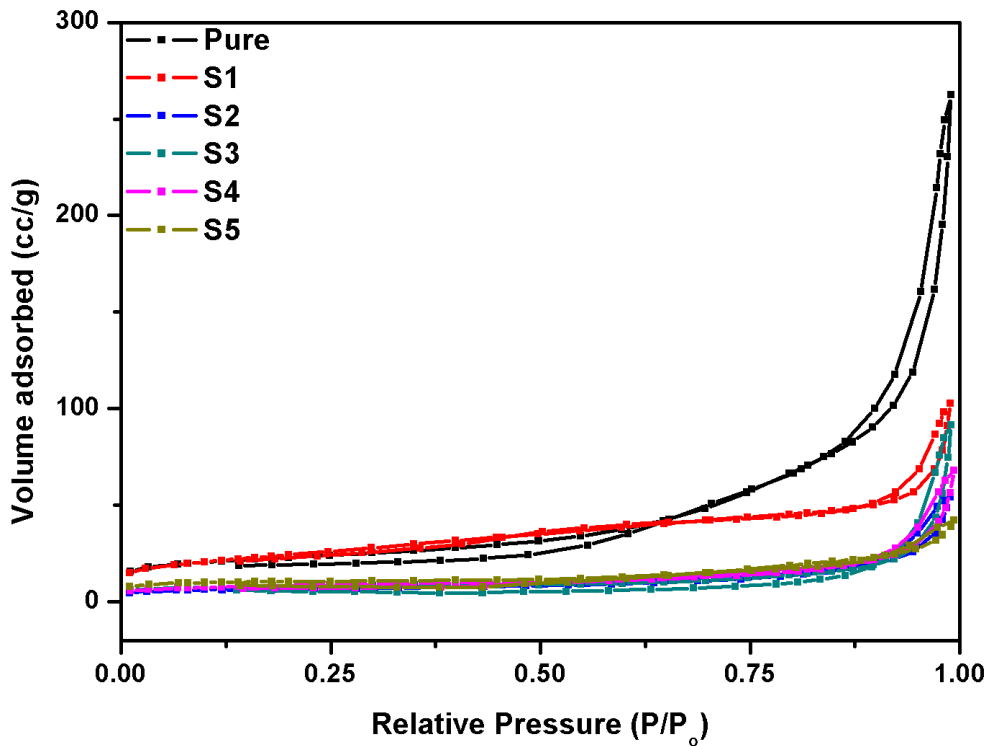


Fig. 6.6: NO₂ adsorption isotherms for a pure and Mn doped TiO₂ nanoparticles.

Table 6.2: Summary of the BET surface, pore volume and diameter.

| Sample | BET surface area (m²g⁻¹) | Pore diameter (nm) | Pore volume (cm³g⁻¹) |
|---------------|-----------------------------------------------------------|-------------------------------|-------------------------------------------------------|
| Pure | 80.3301 ± 0.5149 | 21.5196 | 0.417041 |
| S1 | 87.6667 ± 0.1203 | 8.7716 | 0.159813 |
| S2 | 25.5697 ± 0.0667 | 18.3846 | 0.082793 |
| S3 | 27.1535 ± 0.4188 | 39.9034 | 0.139456 |
| S4 | 29.1115 ± 0.1939 | 22.1619 | 0.103300 |
| S5 | 35.3524 ± 0.5958 | 16.1174 | 0.058135 |

6.3.4. Photoluminescence analysis

The Photoluminescence spectra of pure and Mn doped TiO₂ nanoparticles are shown in Fig. 6.7a-g. A broad emission peak centred at 410-430 nm is observed for all samples with a blue shift to smaller wavelength as the Mn concentration increases. A broad hump in the green emission range intensifies with an increase in Mn concentration and is clearer in sample S3. Furthermore, upon doping, the PL intensity quenches. Similar behaviour was observed by Sharma *et al.* [6.30] and was attributed to the reduction of exciton concentration due to the transfer of photo excited electrons to Mn ions on the crystallite surface. The emission peaks for all samples were deconvoluted using Gaussian fitting. The spectra in Fig 6.7b-f display a UV emission peak at 386 nm (peak 1)

attributed to band edge emission [6.24, 6.30]. A violet emission centred at 420 nm (peak 2 and peak 3 for S2 and S3) due to self-trapped excitons in the TiO_6 octahedra [6.8, 6.24, 6.31]. Two blue emission peaks centred at (peak 3 and peak 4) 440 nm and 490 nm and green emission peaks at 540 nm (peak 5) were assigned to shallow trapped oxygen vacancy associated with Ti^{3+} centres [6.24, 6.30, 6.31]. Sample S2 and S3 display two new peaks at lower wavelength and at higher wavelength, peak 1 centred at 360 nm and 359 nm and peaks 6 and 7 centred at 555 nm and 573 nm, respectively were not reported before in pure sample. These peaks are due to incorporation of Mn Mn^{2+} ions into the TiO_2 lattice. Mn^{2+} (0.08 nm) has larger ionic radii than Ti^{4+} (0.064 nm) thus result to lattice distortion and induces a number of defects such as doubly charged oxygen vacancies in order to compensate for charge imbalance [6.32].

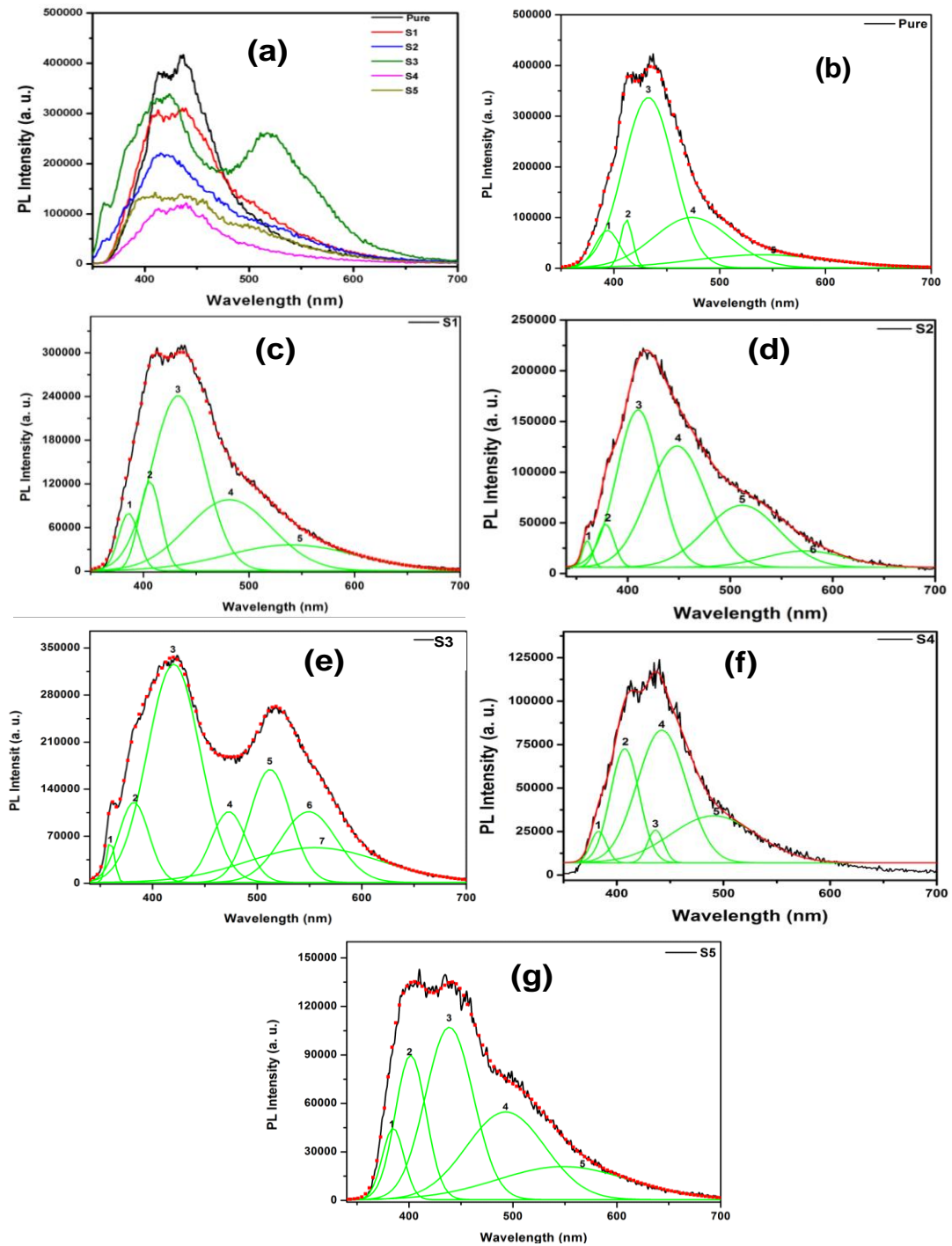


Fig. 6.7: (a) Photoluminescence spectra of pure TiO_2 nanoparticles and those doped with various concentration of Mn. Note: (b-g) corresponds to peaks fitted using Gaussian fit.

6.3.5. X-ray photoelectron spectroscopy analysis

X-ray Photoelectron Spectroscopy (XPS) analysis was carried in order to study the elemental composition and the electronic valence state of pure and Mn doped TiO₂ nanoparticles. The Ti 2p, O 1s and Mn 2p core levels spectra are shown in Figs. 6.8 and 6.9. As seen in Fig. 6.8a-d, the pure TiO₂ show Ti 2p_{3/2} and 2p_{1/2} doublet centred at 458.08 eV and 463.76 eV corresponding to Ti³⁺. A shift to higher binding energy with introduction of dopant is observed. This shift is attributed to Mn²⁺ ions being substituted into the TiO₂ lattice [6.30, 6.32]. Fig. 6.6b-d shows the Ti 2p core levels spectra of S1, S3 and S5. The Ti 2p doublets for S1 sample were deconvoluted by fitting two Gaussian peaks on each. The 2p_{3/2} peaks centred at 458.28 eV and 459.96 eV were attributed to Ti³⁺ and Ti⁴⁺ ions [6.33, 6.34]. The S3 sample shows the Ti 2p_{3/2} peaks centred at 458.26 eV and 460.56 eV assigned to Ti³⁺ and Ti⁴⁺ respectively. The Ti 2p_{1/2} peaks centred at 463.21 eV and 465.79 eV assigned to Ti³⁺ and Ti⁴⁺ respectively [6.8, 6.24, 6.30]. The S5 sample displayed two 2p_{3/2} peaks and one 2p_{1/2} peak centred at 458.33 eV, 460.73 eV and 464.38 eV assigned to Ti³⁺ and Ti⁴⁺.

The O 1s was fitted with 2 peaks centred at 529.31 eV and 530.58 eV attributed to Ti⁴⁺ and O²⁻ ions in the TiO₂ crystal lattice as shown in Fig. 6.9a [6.24]. The asymmetric O 1s peaks for S1, S3 and S5 are shown in Fig. 6.9b-d, disclosing broader peaks than the pure TiO₂ nanoparticles, indicating that there are several oxygen defects present in the doped samples. The Ti⁴⁺-O oxidation state is dominating on the Mn doped samples. The peaks corresponding to S1, S3, and S5 centred at 529.83 eV, 529.27 eV and 530.04 eV, and 529.09 eV were

assigned to Ti^{4+} and O^{2-} in the crystal lattice [6.8, 6.24, 6.33]. A peak centred at 531.52 eV assigned to Ti^{3+} -O bond on the surface was observed in S1 and S3 [6.8, 6.24, 6.34, 6.35]. An O-H peak due to chemisorbed water was observed at 532.37 eV and 532.30 eV in S3 and S5. A peak due to surface atmospheric carbon contamination at 533.67 eV is observed in S1 [6.24, 6.35].

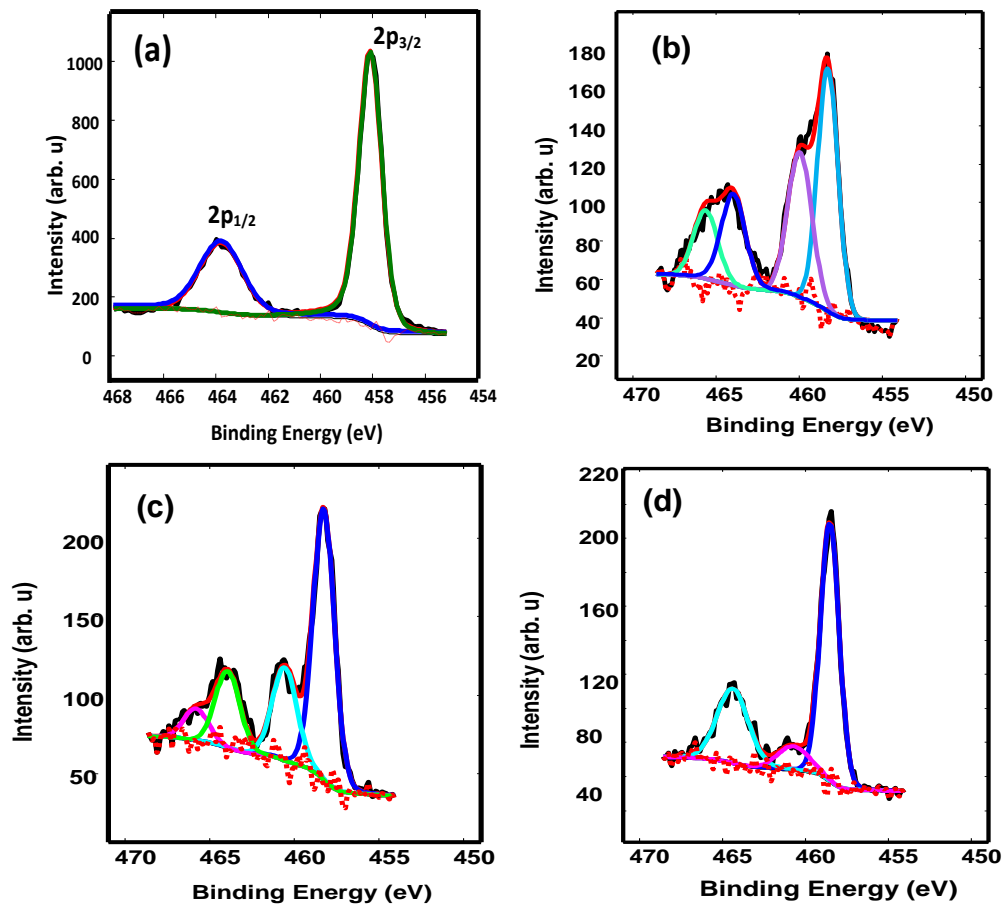


Fig. 6.8: XPS spectra for (a), the pure TiO_2 , (b) S1, (c) S3 and (d) S4 Ti 2p core levels spectra.

The Mn 2p core level spectra for S1, S3 and S5 are shown in Fig. 6.9e-g
The Mn $2p_{3/2}$ peaks centred at 641.37, 641.51, and 641.93 eV and $2p_{1/2}$ peaks

centred at 653.55, 653.72 and 652.31 eV were all assigned to Mn^{2+} ions for S1 S3 and S5 respectively. This is evident that the Mn^{2+} ions are in divalent state by substituting the Ti^{4+} ions in the TiO_2 lattice [6.30, 6.32, 6.34, 6.36].

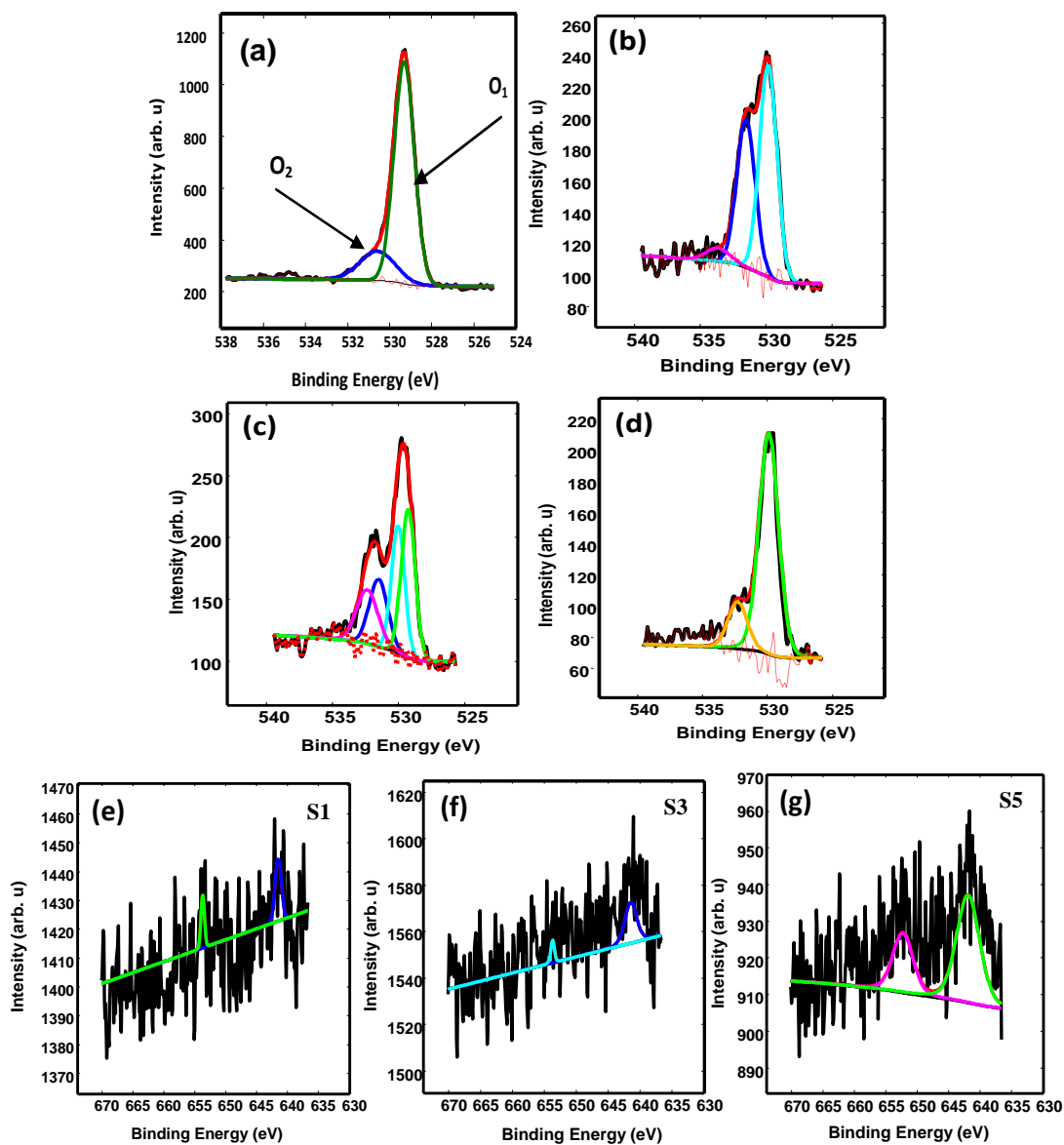


Fig. 6.9: XPS O 1s core level spectra of (a) pure TiO_2 , (b) S1, (c) S3, (d) S5 and (e-g) correspond Mn to 2p core level spectra of S1, S3 and S5, respectively.

6.3.6 Electron paramagnetic resonance analysis

To get more information on the defect states the electron paramagnetic resonance (EPR) analysis was carried out by detecting the spin polarization charge state of pure and Mn doped TiO₂ nanoparticles. Room temperature EPR spectra are shown in Fig. 6.10 as the microwave adsorption derivative $\left(\frac{dP}{dH}\right)$ as a function of magnetic flux density. The pure TiO₂ nanoparticles in Fig. 6.10 displays an isotropic signal related to ferromagnetic and a sharp peak related to paramagnetic behaviour with a g-factor of 1.9738 corresponding to Ti³⁺ in the lattice [6.24]. The Mn doped samples S2-S5 display a ferromagnetic signal with hyperfine splitting in the 282-313 mT range. Arroyo *et al.* [6.13] and Alaria *et al.* [6.37] have reported a hyperfine splitting of Mn nuclei in Mn doped semiconductors and assigned it to ferromagnetic ordering caused by isolated Mn²⁺ ions. As shown in Fig. 6.10, S1 displays a six hyperfine structure embedded between 299 and 350 mT with g factors of 1.9603, and 2.0145 attributed to lattice Ti³⁺ and single ionized oxygen in F⁺ centre [6.38]. As the dopant concentration increases we observe a shoulder peak (see arrow) with g values at 1.8294, 1.8324, 1.8394 and 1.8399 assigned to oxidize Mn²⁺, forming Mn⁴⁺ which is substitutionally incorporated into TiO₂ lattice. Additionally, an absorption centres with g values at 2.0498 and 2.0838 in S2, 2.0394 and 2.0817 in S3, 2.0404 in S4 and 2.0307 in S5 are observed. These signals can be assigned to adsorbed oxygen on the TiO₂ surface forming superoxide (O₂⁻) ions [6.24, 6.38, 6.39]. More interestingly new signals at 2.2272, 2.24782, 2.24941 and 2.2401 in lower

fields are observed and these signals were also observed by Santara *et al.* [6.38] at 2.22 and 2.27 in Fe-doped TiO₂ nanoribbons. They assigned these signals to Fe³⁺ in the TiO₂ lattice; thus, we attribute these signals to the presence of Mn²⁺ ions in the lattice and also oxygen vacancies. A peak is observed with g factor of 4.9398, 4.8790, 4.7326, 4.9454, and 4.7104 in all the doped samples. A similar behaviour was observed by Arroyo *et al.* [6.13] at a g-factor of 5.16 and assigned it to the increase in paramagnetic ion from the Mn²⁺ ions concentrated in the octahedral.

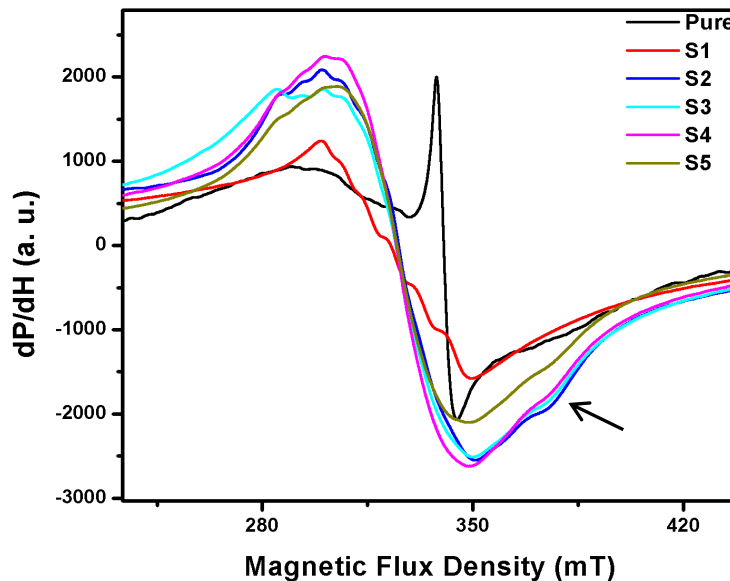


Fig. 6.10: EPR pure TiO₂ nanoparticles and those doped with various concentration of Manganese.

6.3.7. Gas sensing analysis

Gas sensing properties of doped TiO₂ nanoparticles with different concentrations of Mn were studied in conjunction with the pure TiO₂

nanoparticles. The sensing material was exposed to 60 ppm of NH_3 , NO_2 , CO , CH_4 and H_2 , while varying the temperature from room temperature (RT) 25 °C to 400 °C, in order to determine the optimum working temperature which provides a maximum sensor response. Generally, a response is given by R_a/R_g , in presence of reducing gas and R_g/R_a , in presence of oxidizing gas; where R_a and R_g are the sensor resistance in the air and in presence of target gas. As shown in Fig. 6.11a-e, both pure and doped nanoparticles have maximum response at room temperature and their sensing response decreases with increasing the operating temperature. The pure sample shows a good response towards all the gases at RT, with a maximum response of 1093 towards NO_2 . More remarkably the pure sensing material shows no response towards CO at all temperatures (see Fig. 6.11c). However, Mn doped samples show enhanced response to all the gases including CO at RT. In comparison with other doped samples (S2, S3, S4 and S5), sample S1 shows a good response towards all the gases except NO_2 (Fig. 6.11b). As shown in Fig. 6.11, maximum responses of approximately 1293, 983, 631, and 285 were observed towards NH_3 , CO , CH_4 and H_2 gases, respectively. The poor response displayed by S1 when exposed to oxidizing gas NO_2 indicates that, it is only sensitive to reducing gases, more specifically NH_3 . S2 shows a moderate response towards all the gases with average response between 450-700. However, when exposed to NO_2 a significant increase in response value to approximately 1158 is observed. Sample S3 is a good candidate for hydrogen sensing applications, as it displayed selectivity towards H_2 with maximum response of 561 (greater than all other samples) as observed in Fig. 6.11e. A

peculiar behaviour is observed for sample S4, as shown in Fig. 6.11. The S4 sample only shows a response towards NH_3 and NO_2 at RT and no response is observed at higher temperatures or even to any other tested gases. As seen from the XRD results (Fig. 6.1), there is a shift in diffraction peaks of sample S4 to lower angles, indicating a lattice distortion as Mn^{2+} ions are substituted into the TiO_2 lattice. The presence of the ions induces defects states which enhance UV emission (see Fig. 6.7) and provides active sites for gas adsorption giving enhanced response; however we observe the opposite with the S4 sensing material, meaning:

- (1) Whether the ions are substitutes into the lattice or are interstitially incorporated determines the phase (rutile and anatase respectively) and also determines whether the dopant ion is a donor or acceptor **[6.13]**.
- (2) Based on the XRD, Raman and PL results, it was found that the diffraction peaks shifted to lower angles, and a quenching was observed on the Raman and PL analyses, which indicated that the Mn^{2+} was substituted within the TiO_2 surface.
- (3) Regarding the substitution of Mn into the TiO_2 , there is an optimum concentration of Mn^{2+} that should be substituted, however, if the solubility (or concentration) is exceeded, then, the contribution of Mn on the sensing properties becomes minimal **[6.40]**.

- (4) Therefore this denotes that number of defects is reduced (see PL results) on the surface, when doping at high concentrations, which then resulted to a decrease in sensitivity and poor sensing response as observed for S4 in Fig. 6.9. Similar behaviour was observed by Stella *et al.* [6.41] in Mn doped Co_3O_4 gas sensor.
- (5) Additionally, if the number of defects is reduced at room temperature, therefore, it is expected that, at higher operating temperature the number will reduce more, which therefore causes the sensing material not to be active.

Therefore, the above possible reasons explain the enhanced response of S5 toward all gases with selectivity towards NO_2 (Fig. 6.11b). Previous studies [6.23, 6.42] have reported that incorporation of Mn on the MOX surface improves the gas sensing properties of MOX nanostructures. As stated above that, the selective doping of elements in semiconductor materials can highly modify the surface of the sensing material and improve its gas sensing activities. However, to the best of our knowledge, there are no reports on the gas the sensing properties of Mn- TiO_2 .

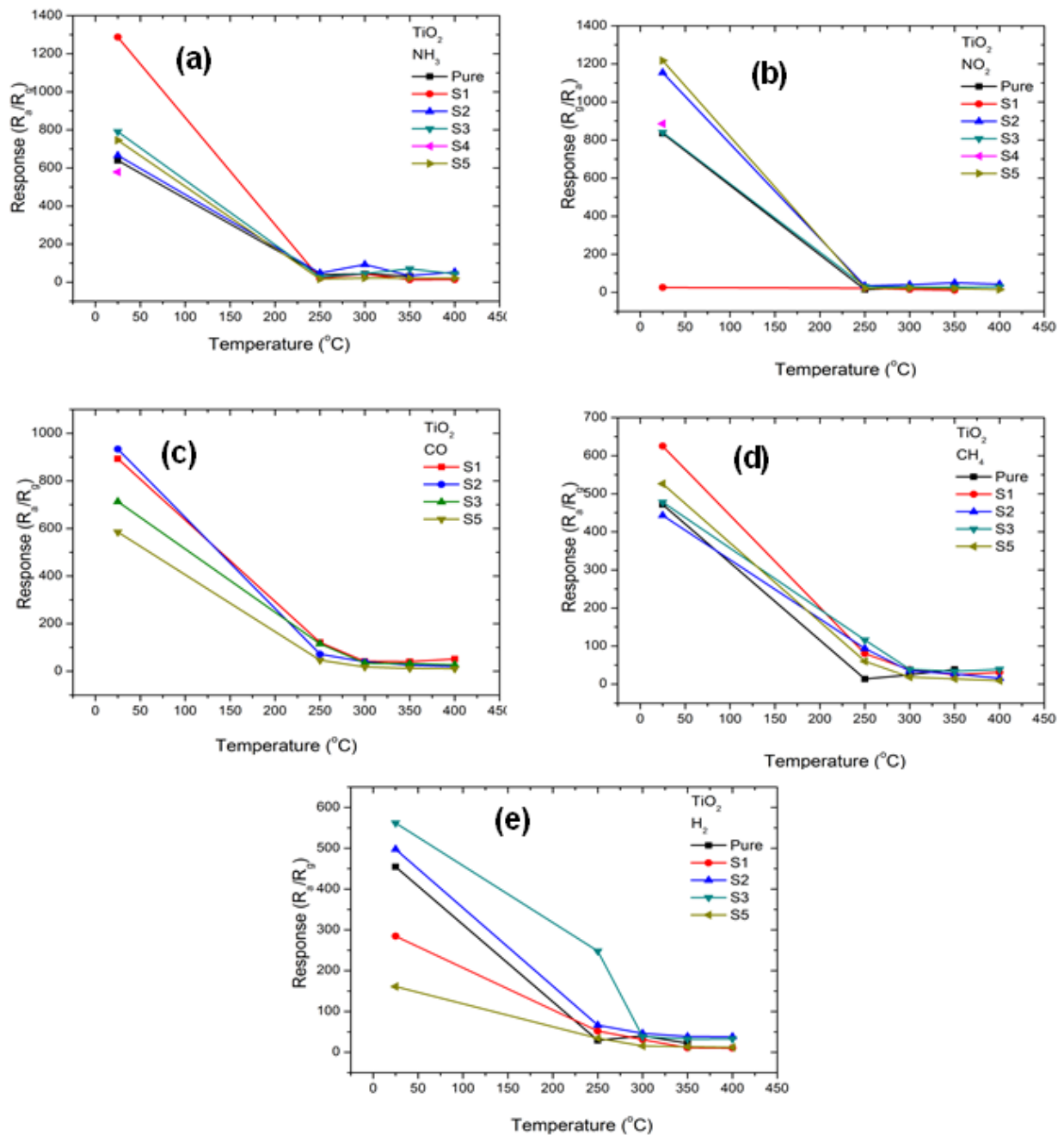


Fig. 6.11: Sensor response against working temperature of pure and Mn doped TiO_2 nanoparticles exposed to 60 ppm of NH_3 , NO_2 , CO , CH_4 and H_2 .

Fig. 6.12a and b shows the response against gas concentration measured at room temperature. As shown in Fig. 6.12a, the pure TiO₂, S2, S3, S4 and S5 sensing material show a linear increase in response as concentration increases up to 40 ppm, the sensors saturate thereafter, denoting that they are not stable at higher concentration of NH₃ gas. Furthermore, it is clear that sample S1 shows a higher response compared to other sensing materials, disclosing a sensing response of approximately 1681 at 20 ppm. Although our sensing material (S1) is not stable at higher concentrations, however, it is able to disclose a higher response even at low concentration of 20 ppm, at room temperature.

When the sensors are exposed to different concentrations of NO₂, the pure TiO₂ sensing material shows a linear increase up to 40 ppm NO₂ showing a maximum response of about 1093 and saturate thereafter, showing that it is only stable up to 40 ppm. However, when the Mn doped sensing materials (except S1) are exposed to NO₂, their response increase rapidly with the growth of the gas concentration without showing any saturation up to 80 ppm, denoting that, they are very stable to NO₂, even at higher sensing concentration. Based on the results, it is clear that S5 has higher sensing response at 60-80 ppm. The adsorption of Mn-doped TiO₂ sensing materials even at higher NO₂ concentration is probably due to incorporation of Mn²⁺ ions, leads to the improvement of surface activity, since Mn has a low ionization energy compared to that of TiO₂. Thus, the gas surface chemisorption activation energy reduces, resulting to the enhancement of NO₂ gas absorption.

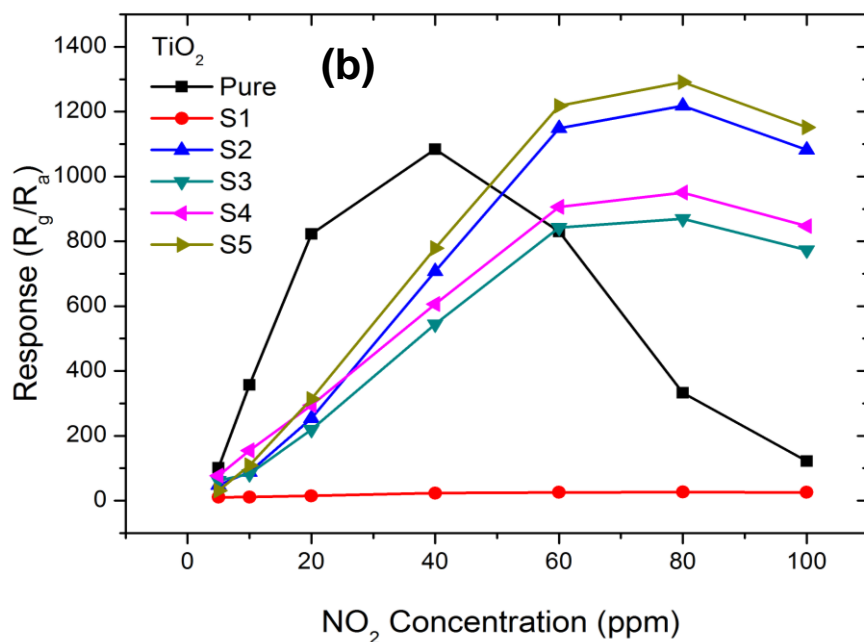
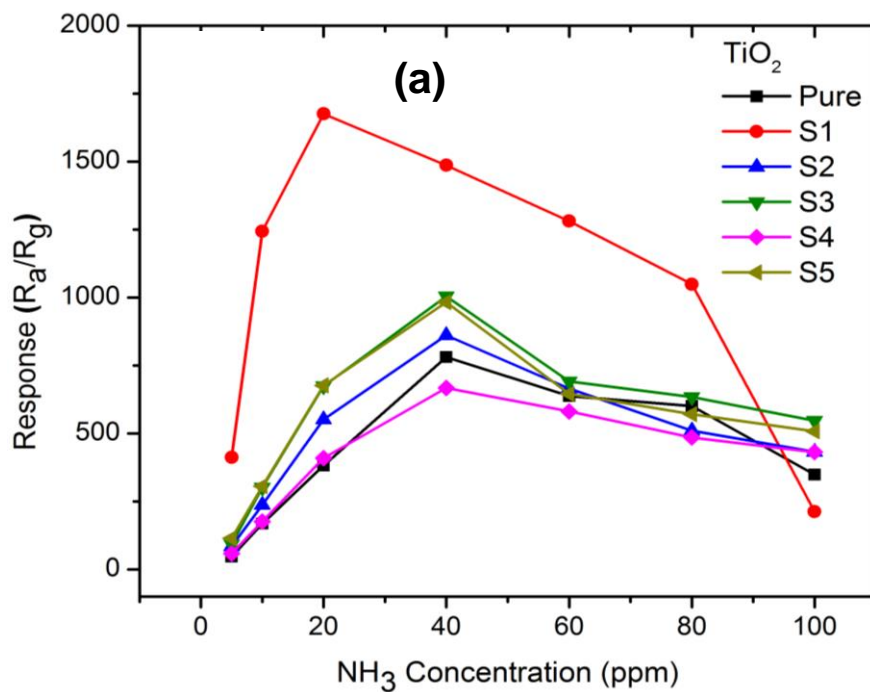


Fig. 6.12: Sensor response against (a) NH_3 and (b) NO_2 gas concentration at room temperature.

The response and recovery characteristics for Mn doped TiO₂ nanoparticles, S1 and S5 exposed to NH₃ and NO₂ respectively are shown in Fig. 6.13a-b. The two curves show the changes in response of a sensor when exposed to ambient air and target gas at different operational temperatures. The sensors display good reversibility as they return back to baseline after exposure to NH₃ and NO₂. Enhanced response is observed at RT; however as the operation temperature increases poor response is observed, more interestingly S1 show no response at 400 °C. Similar behaviour was observed by Yang *et al.* [6.43] in Mn- doped SnO₂ flower-like spheres and stated that at higher temperatures; oxygen molecules with high activation energy are not permanent on the surface of the metal oxide therefore less oxygen can be chemisorbed to oxygen ion species. When the target gas reacts with the sensing material not enough electrons are re-injected into the surface therefore the depletion layer increases more thus further increase in resistance.

The response time is the time required by the sensor to reach about 90% of the equilibrium value of the sensor resistance, after being exposed to target gas, and while the recovery time is the time needed by the sensing resistance to return to about 10% below the original resistance in air, after realising the tested gas. Therefore, as shown in Table 6.3, the Mn-TiO₂ sensing materials show better response-recovery times towards NH₃ gas compared to the pure TiO₂. To be specific, the S5 reveals a shorter response time of 13 s to NH₃ gas at room temperature. Additionally, the sensitivity (S), listed in Table 6.3 was estimated using the slopes of the curves in Fig. 6.12. The sensitivity of the pure and Mn-

doped TiO₂ was estimated at 40 ppm, where the sensing materials showed a linear increase from 5 ppm to 40 ppm. While, the S1 sample, showed a linear increase in the range of 5-20 ppm NH₃ gas, disclosing a sensitivity of 85 ppm⁻¹ at room temperature. However, when the pure and Mn doped TiO₂ samples were tested to NO₂ gas, a pure TiO₂ revealed a linear increase up to 40 ppm, while the Mn doped samples showed a linear up to 60 ppm, demonstrating sensitivity values of 47.85, 0.337, 21.66, 15.40, 15.01, ppm⁻¹ related to pure TiO₂, S1, S3, S4 and S5, respectively.

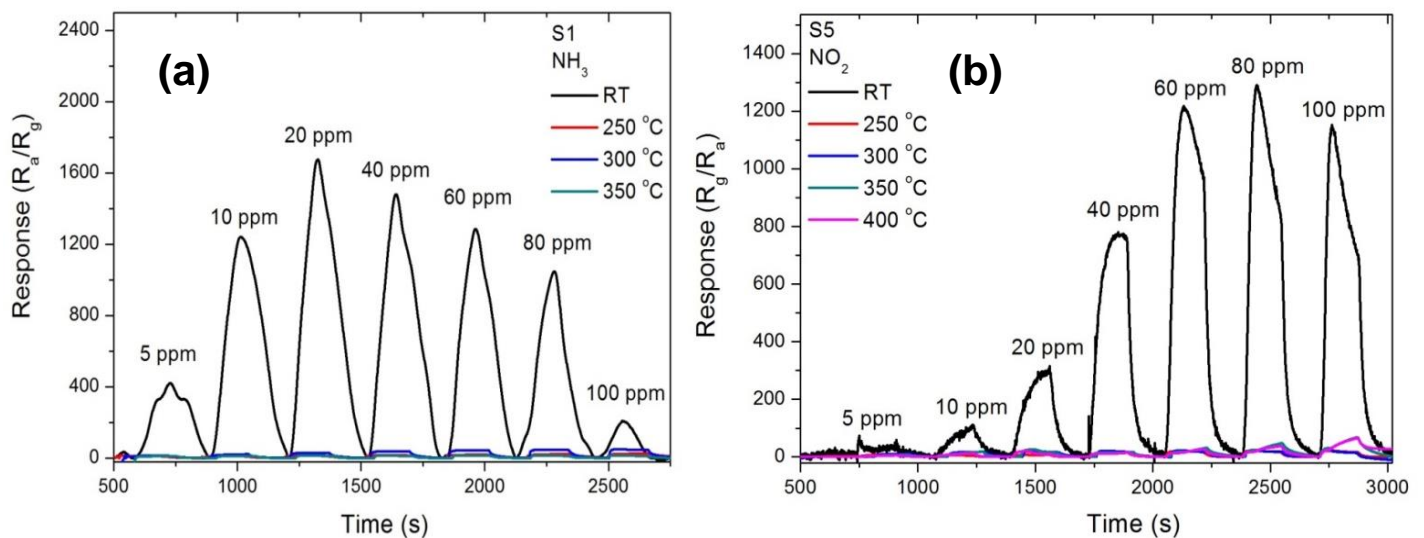


Fig. 6.13: Response curve of (a) S1 and (b) S5 exposed to NH₃ and NO₂ at room temperature.

Table 6.3: Summary of sensing properties, response time (t_{res}), recovery time (t_{rec}) and sensitivity of TiO₂ nanostructures.

| Sample | NH ₃ (20 ppm) | | | NO ₂ (20 ppm) | | |
|-----------------------|--------------------------|---------------|------------------------|--------------------------|---------------|------------------------|
| | t_{res} (s) | t_{rec} (s) | S (ppm ⁻¹) | t_{res} (s) | t_{rec} (s) | S (ppm ⁻¹) |
| Pure TiO ₂ | 33 | 101 | 22.19 | 48 | 52 | 47.85 |
| S1 | 32 | 80 | 85.39 | 25 | 30 | 0.337 |
| S2 | 26 | 22 | 22.70 | 36 | 22 | 21.66 |
| S3 | 18 | 22 | 26.40 | 36 | 27 | 15.40 |
| S4 | 26 | 13 | 18.94 | 28 | 12 | 15.01 |
| S5 | 13 | 27 | 25.48 | 22 | 20 | 22.184 |

To the best of our knowledge there are few/no reports on Mn- doped TiO₂ gas sensors therefore to highlight the novelty in this work Table 6.4 list reports on Mn doped MOX, showing their working temperature and response when exposed to various gases. Although, SnO₂ and ZnO doped with Mn are the mostly studied MOX for gas sensing application; however there are no reports on room temperature NH₃ and NO₂ gas sensing on these materials. Additionally, it is worthy to mention that there are no reports on these materials demonstrating higher sensing response to other gases, except NO₂, NH₃ gases at room temperature. Therefore, in this work we show for the first time ultra-high sensitive and selective room sensing materials (S1, S5) with high response (see Table 4).

Table 6.4: Summary of literature survey showing Mn doped MOX structures tested to various gasses.

| Sensing material | Temperature (°C) | Gas | Gas concentration (ppm) | Response | | Refs. |
|-----------------------------------------|------------------|-----------------|-------------------------|----------|-------|---------------------|
| | | | | Pure | Doped | |
| Mn-ZnO nanofibers | 340 | Acetone | 1200 | 76.2 | 262.5 | [6.44] |
| Mn-SnO₂ nanoflowers | 360 | Ethanol | 1000 | 156.8 | 360.2 | [6.43] |
| Mn-ZnO nanoparticles | 350 | NO ₂ | 50 | 1.9 | 2700 | [6.36] |
| Mn-ZnO nanorods | RT | O ₂ | 15 | 1% | 3% | [6.23] |
| Mn-ZnO thin film | 100 | TMA | 75 | | 300 | [6.45] |
| Mn-SnO₂ thin film | 250 | H ₂ | 500 | 3.9 | 2.4 | [6.46] |
| Mn-ZnO nanoparticles | 200 | Formaldehyde | 205 | 5.6 | 20 | [6.47] |
| | 400 | Toluene | 5000 | 400 | 1050 | |
| | 300 | NH ₃ | 200 | 6.1 | 4.8 | |
| | 400 | CO | 9000 | 14 | 8 | |
| | 200 | Humidity | 70% | 1.9% | 5.8% | |
| Mn-TiO₂ nanoparticles | RT | NH ₃ | 60 | 750 | 1293 | In this work |
| | | NO ₂ | 60 | 1093 | 1224 | |

Selectivity test for the pure and the Mn-doped TiO₂ were conducted at 60 ppm using different gases, including CH₄, H₂, NH₃, NO₂ and CO gases. The sensor response towards all the gases at 60 ppm is reported as a histogram, as shown in Fig. 6.14. As reported in **[6.24]**, the pure TiO₂ nanoparticles sensor showed good response valued 1093 and selectivity to 40 ppm NO₂ at room temperature. It is interesting to note that, sensor S1 shows enhanced response of 1600 and improved selectivity towards 20 ppm NH₃ at room temperature. The

improved sensor performance displayed by S1 may be attributed to addition of Mn^{2+} ions improving the surface activity. Therefore, this observation validates that, our sensing materials (S1 and S5) can be considered as potential candidates for detection of NH_3 and NO_2 gases at room temperature.

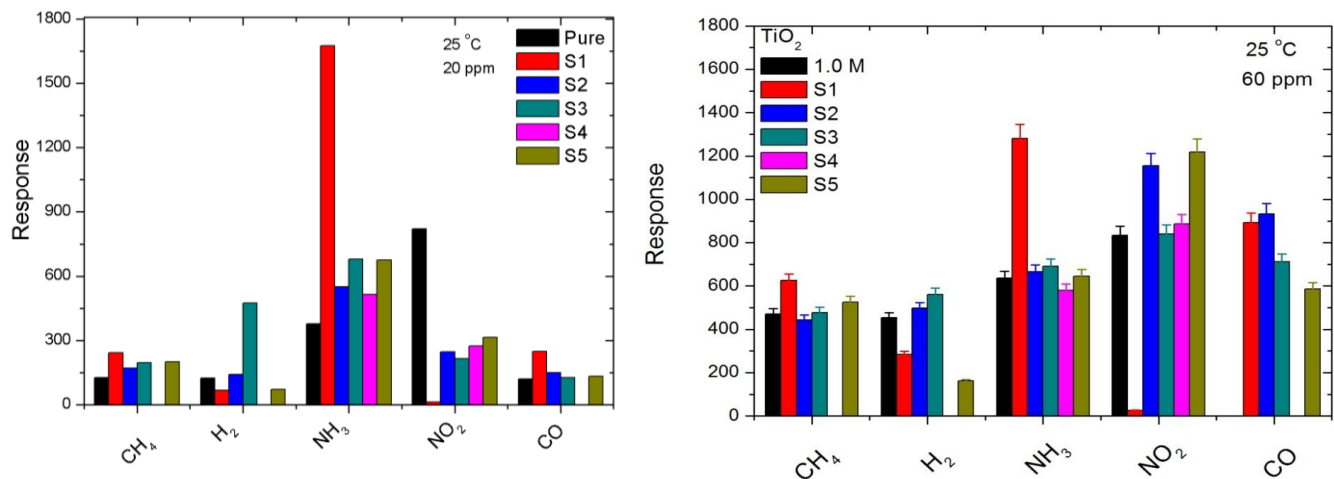
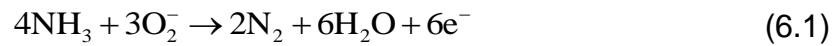


Fig. 6.14: Selectivity tests for all the sensors exposed to (a) 20 ppm and (b) 60 ppm CH_4 , CO , H_2 , NO_2 , and NH_3 at room temperature.

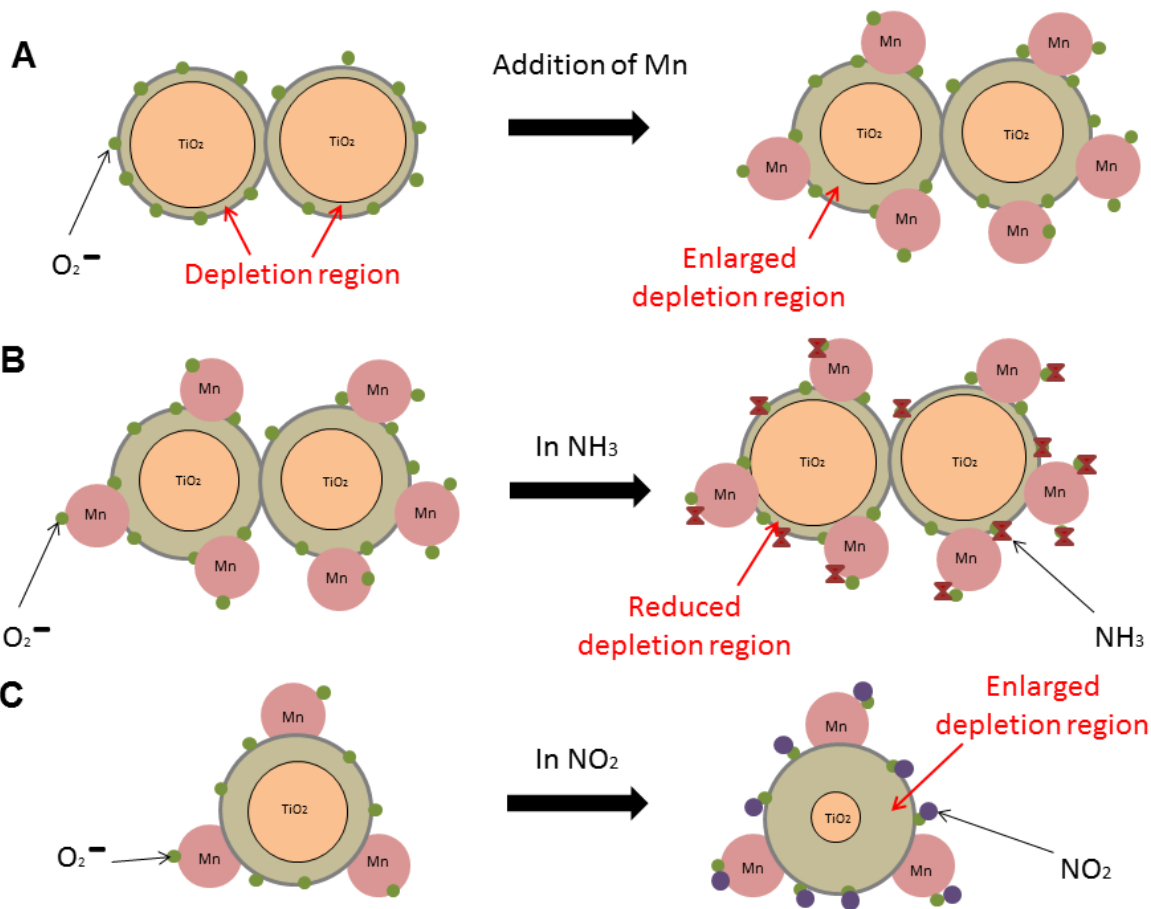
Based on our proposed sensing mechanisms, at room temperature, oxygen molecules from air are adsorbed on the surface of $Mn-TiO_2$ and the oxygen (O_2^-) molecules accept electrons from the oxide surface decreasing the carrier concentration of electrons resulting to an increase in a depletion layer and an increase in a sensor resistance. As shown in **Scheme 1A**, the thickness of the depletion layer of the pure TiO_2 is thinner compared to that doped with Mn , disclosing a thicker depletion region due to adsorption of O_2^- ions at the

equilibrium. However, when sample S1 is exposed to a reductive gas such as NH₃ (**Scheme 1B**), the NH₃ gas reacts with the Mn-TiO₂ surface and is oxidised by the Mn²⁺ ions and form active surface species that react with the adsorbed oxygen molecules on the TiO₂ surface via the spill-over process. An electron is injected back into the material decreasing the depletion layer and thus electron conductivity is improved due to a decrease in resistance.



However at high concentration of Mn- doping (S5) sensing mechanism follows the electronic mechanism due to high content of Mn²⁺ ions in the TiO₂ lattice (as seen by the intense Mn²⁺ peak in XPS Fig. 6k). The Mn²⁺ ions exchange electrons with host material and are oxidized to higher oxidation states and increase the depletion layer, thus increasing the sensor's resistance. When exposed to an oxidative gas like NO₂ (**Scheme 1C**), Mn ions give electrons and the gas is reduced to NO₂⁻. The loss of electrons results to further increase in depletion layer, thus further increase in resistance and this results to higher sensing response towards NO₂ gas. Similar behaviour was observed by Tamaekong *et al.* [6.36] at lower concentrations (0.25 mol %) of Mn doped zinc nanoparticles.





Scheme 1: Schematic diagram showing (A) change in TiO₂ depletion layer due to Mn -doping, and the gas sensing mechanism of Mn-TiO₂ on (B) NH₃ and (C) NO₂.

6.4. CONCLUSION

TiO₂ nanoparticles doped with manganese were synthesized using a simple hydrothermal method and washed with a 1.0 M HCl aqueous solution and tested for gas sensing at various operating temperatures. Gas sensing studies

demonstrated that the incorporation of Mn^{2+} ions on the TiO_2 surface improved the NO_2 and NH_3 sensing performances in terms of response and selectivity. The improved response is associated with the Mn^{2+} ions that leads to the improvement of surface activity, therefore results to reduced gas surface chemisorption activation energy reduces. Moreover, combination of X-ray photoelectron spectroscopy and the electron paramagnetic resonance studies revealed that the Mn doped TiO_2 contain higher concentration of Ti^{4+} , Ti^{3+} and single ionized oxygen vacancies which contribute to gas sensing properties. Raman and PL studies disclosed that the Mn doped TiO_2 nanoparticles possess enhanced UV-Vis emission and a broad shoulder at 540 nm denoting induced defects by substituting Ti^{4+} ions with Mn^{2+} . Therefore, based on these finding the Mn-doped TiO_2 nanoparticles would be of great potential for gas sensing applications.

6.5. ACKNOWLEDGEMENTS

The Department of Science and Technology and the Council for Scientific and Industrial research financially supported this work. Authors are highly thankful to the NCNSM characterization team for TEM, SEM and BET measurements and the UFS team for XPS measurements.

6.6. REFERENCES

- [6.1] A. Fujishima, K. Honda, *Nature* 23 (1972) 37-38.
- [6.2] M. Gratzel, *Nature* 414 (2001) 338.
- [6.3] D.K. Hwang, J.H. Moon, Y.G. Shul, K.T. Jung, D. H. Kim, D.W. Lee, J. *Sol-Gel Sci. Technol.* 26 (2003) 783.
- [6.4] A.E. Shalan, M.M. Rashad, Y. Yu, M. Lira-Cantu, M.S.A. Abdel-Mottaleb, *Electrochim. Acta.* 89 (2013) 469.
- [6.5] J.H. Braun, *J. Coat. Technol.* 69 (1997) 59.
- [6.6] S.H. Lim, J. Luo, Z. Zhong, W, Ji, J. Lin, *Inorg. Chem.* 44 (2005) 4124.
- [6.7] K. Ninomiya, C. Ogino, S, Oshima, S. Sonoke, S. Kuroda, N. Shimizu, *Ultrason. Sonochem.* 19 (2012) 607-614.
- [6.8] A.S. Bolokang, F.R. Cummings, B.P. Dhonge, H.M.I. Abdallah, T. Moyo, H.C. Swart, C.J. Arendse, T.F.G. Muller, D.E. Motaung, *Appl. Surf. Sci.* 331 (2015) 362-372.
- [6.9] X. Chen, S.S. Mao, *Chem. Rev.* 107 (2007) 2891-2959.
- [6.10] X. Liu, S. Cheng, H. Liu, S. Hu, D. Zhang, H. Ning, *Sensors* 12 (2012) 9635-9665.
- [6.11] M.H. Razali, A. Noor, M. Yusoff, *Aust. J. Basic and Appl. Sci.*, 9 (2015) 139-143.
- [6.12] Y. Wang, R. Zhang, J. Li, S. Lin, *Nano. Res. Lett.* 9 (2014) 46.
- [6.13] R. Arroyo, G. Cordoba, J. Padilla, V. H. Lara, *Mater. Lett.* 54 (2002) 397-402.

- [6.14] A.R. Bally, E. N. Korobeinikova, P. E. Schmid, F. Levy, F. Bussy, J. Phys. D: Appl. Phys. 31 (1998) 1149.
- [6.15] G.G. Belmonte, V. Kytin, T. Dittrich, J. Bisquert, J. Appl. Phys. 94 (2003) 5261.
- [6.16] Q.R. Deng, X.H. Xia, M.L. Guo, Y. Gao, G. Shao, Mater. Lett. 65 (2011) 2051-2054.
- [6.17] L. Lu, X. Xia, J. K. Luo, G. Shao, J. Phys. D: Appl. Phys. 45 (2012) 485102-485110.
- [6.18] V. D. Binas, K. Sambani, T. Maggos, A. katsanaki, G. Kiriakidis, Appl. Catal., B 113-114 (2012) 79-86.
- [6.19] X. Wei, R. Skomski, B. Balamurugan, Z. G. Sun, S. Ducharme, D. J. Sellmyer, J. Appl. Phys. 105 (2009) 07C517.
- [6.20] B. B. Straumal, A. A. Mazilkin, S. G. Protasova, A. A. Myatiev, P.r B. Straumal, G. Schütz, P. A. van Aken, E. Goering, B. Baretzky, Phys. Rev. B 79 (2009) 205206.
- [6.21] Y. J. Kim, S. Thevuthasan, T. Droubay, A. S. Lea, C. M. Wang, V. Shutthanandan, S. A. Chambers, R. P. Sears, B. Taylor, B. Sinkovic , Appl. Phys. Lett. 84 (2004) 3531-3533.
- [6.22] Z. Li, D. Ding, Q. Liu, C. Ning, X. Wang, Nano. Res. Lett. 9 (2014) 118.
- [6.23] F. Ahmed, N. Arshi, M. S. Anwar, R. Danish, B. H. Koo, Curr. Appl. Phys. 13 (2013) s64-s68.
- [6.24] Z.P. Tshabalala, D.E. Motaung, G.H. Mhlongo, O.M. Ntwaeaborwa, Sens. Actuators B 224 (2016) 841–856.

- [6.25] L. Vergard, M. Shjelderup, Z. Phys. 18 (1917) 93.
- [6.26] M. M. Rashad, E. M. Elsayed, M. S. Al-Kotb, A. E. Shalan, J. Alloys Compd. 581 (2013) 71-78.
- [6.27] F. Tian, Y. Zhang, J. Zhang, C. Pan, J. Phys. Chem. C 116 (2012) 7515-7519.
- [6.28] W. Ma, Z. Lu, M. Zhang, Appl. Phys. A, 66 (1998) 612-627.
- [6.29] J.P. Xu, S.B. Shi, L. Li, J. F. Wang, L. Y. Lv, F. M. Zhang, Y. W. Du, J. Phys. Chem. Solids, 70 (2009) 511-515.
- [6.30] S.D. Sharma, K.K. Saini, C. Kant, C.P. Sharma, S.C. Jain, Appl. Catal., B 84 (2008) 233-240.
- [6.31] T. Sahoo, G.K. Pradhan, M.K. Rath, B.Pandey, H.C. Verma, S. Nandy, K.K. Chattopadhyay, S. Anand, Mater. Lett. 61 (2007) 4821-4823.
- [6.32] S. Paul, P. Chetri, A. Choudhury, J. Alloys Compd. 583 (2014) 578-586.
- [6.33] A. Lapcha, C. Maccato, A. Mettenborger, T. Andreu, L. Mayrhofer, M. Walter, S. Olthof, T.-P. Ruoko, A. Klein, M. Moseler, K. Meerholz, J. R. Morante, D. Barreca, and S. Mathur, J. Phys. Chem. C 119 (2015) 18835-18842.
- [6.34] D.E. Motaung, I. Kortidis, D. Papadaki, S.S. Nkosi, G.H. Mhlongo, J. Wesley-Smith, G.F. Malgas, B.W. Mwakikunga, E. Coetsee, H.C. Swart, G. Kiriakidis, S.S. Ray, Appl. Surf. Sci. 311 (2014) 14-26.
- [6.35] B. Santara, P.K. Giri, K. Imakita, M. Fujii, J. Phys. Chem. C 117 (2013) 23402-23411.

- [6.36] N. Tamaekong, C. Liewhiran, A. Wisitsoraat, A. Tuantranont, S. Phanichphant, *Sens. Actuators, B* 204 (2014) 239-249.
- [6.37] J. Alaria, P. Turek, M. Bernard, M. Bouloudenine, A. Berbadj, N. Brihi, G. Schmerber, S. Colis, A. Dinia, *Chem. Phys. Lett.* 415 (2005) 337–341.
- [6.38] B. Santara, P.K. Giri, S. Dhara, K. Imakita, M. Fujii, *J. Phys. D: Appl. Phys.* 47 (2014) 235304-235317.
- [6.39] B. Santara, K. Imakita, M. Fujii, S. Dhara, *J. Alloys Compounds* (2015), doi: 10.1016/j.jallcom.2015.11.066.
- [6.40] H.S. Kang, S.K. Hong, Y.C. Kang, K.Y. Jung, Y.G. Shul, S.B. Park, *J. Alloys Compd.* 402 (1-2) (2005) 246.
- [6.41] C. Stella, N. Soundararajan, K. Ramachandran, *J. Mater. Sci: Mater. Electron.* 26 (2015) 4178–4184.
- [6.42] P. Rajeshwaran, A. Sivarajan, *J. Mater. Sci.: Mater. Electron.* 26 (2015) 539.
- [6.43] F. Yang, Z. Guo, *J. Colloid Interface Sci.* 448 (2015) 265-274.
- [6.44] Y. Mao, S. Ma, X. Li, C. Wang, F. Li, X. Yang, J. Zhu, L. Ma, *Appl. Surf. Sci.* 298 (2014) 109-115.
- [6.45] D. Sivalingam, J.B. Gopalakrishnan, J.B.B. Rayappan, *Sens. Actuators B* 166–167 (2012) 624–631.
- [6.46] C.-H. Lin, W.-C. Chang, X. Qi, *Procedia Engineering* 36 (2012) 476 – 481.
- [6.47] N. Han, H. Liu, X. Wu, D. Li, L. Chai, Y. Chen, *Appl. Phys. A* 104 (2011) 627–633.

SUMMARY AND CONCLUSION

In summary, ultra-high sensitive and selective TiO₂-based sensors for selective detection of NO₂, CH₄ and NH₃ gases at room temperature were synthesized using a simple hydrothermal method in a sodium hydroxide aqueous solution and washed with distilled water and different concentrations of hydrochloric acid annealed at various temperatures.

Surface morphology analyses denoted that, the size of the nanoparticles and crystallization behaviour of TiO₂ are highly dependent on the concentration of HCl. XRD analysis revealed a phase transformation from mixture of both anatase and rutile in a commercial P25 to pure anatase phase, after hydrothermal treatment. An amorphous structure was observed on the TiO₂ nanoparticles after hydrothermal treatment and their crystallinity improved with an increase in HCl concentration. The as prepared nanoparticles (i.e. after hydrothermal treatment without annealing) were agglomerated with highly porous surfaces and the particle size decreased as the acid was introduced resulting in a higher surface area. The 1.0 M sample showed greater response toward target gases at room temperature than the other samples. This was attributed to relatively high concentration of V_o and Ti³⁺ defects states and surface porosity allowing more interaction of the adsorbed gas with the sensing material.

When subjected to thermal annealing at different temperatures (300, 450, 700 °C), the TiO₂ sensing materials demonstrated that the sensing properties are dependent on the annealing temperature. The 1.0 M TiO₂ nanoparticles annealed at higher temperatures (700 °C) transformed to rods and displayed enhanced sensing response disclosing a response time of 45 s and recovery time of 33 s, and higher sensitivity of 199 ppm⁻¹ and as well as improved selectivity to CH₄ gas at room temperature. This is due to its higher surface area of 180.51 m²g⁻¹ and point defects related to Ti³⁺ and as well as their high surface to volume ratio.

The Mn-loaded TiO₂ nanoparticles displayed no change in structure as it remained tetragonal and no peaks corresponding to Mn²⁺ or impurities were observed. Raman spectroscopy and PL revealed quenching, peak broadening and enhance UV-Vis emission due to lattice disorder as Mn²⁺ ions concentration increases and substituted Ti⁴⁺ ions. The increase in lattice parameter c from 0.9403 (pure) to 1.1151 (S5) as Mn²⁺ concentration increases was evident to lattice growth and distortion. We observed an increase in the crystallite sizes and particle aggregation of doped samples on SEM micrographs. The XPS spectroscopy and the EPR studies revealed the presence of Ti⁴⁺, Ti³⁺ and single ionised oxygen vacancies in both pure and Mn²⁺ loaded nanoparticles. Hyperfine split due to Mn²⁺ ferromagnetic ordering was observed, confirming the incorporation of Mn²⁺ ions into the TiO₂ lattice. Enhanced sensor performance and sensitivity at low ppm level of NH₃ was observed for Mn loaded samples due to the Mn²⁺ ions that leads to the improvement of surface activity and reduced surface chemisorption activation energy. Therefore, the Mn-loaded TiO₂

nanoparticles would be of great potential for detection of NH_3 gas at low ppm concentration and at room temperature.

In conclusion, since CH_4 poses a threat to underground mine workers due to the fact that it is combustible and explosive in air. Furthermore, NO_2 is a very toxic gas and an air pollutant that can cause respiratory diseases when over exposed to concentration ≥ 4 ppm. NH_3 causes severe irritation to the eyes, nose and throat and result to suffocation and permanent lung damage after prolonged exposure. Therefore, monitoring such gases and the ability to detect at low concentration in the ppm range is vital to preserve human life and ensure safety in work places. The materials synthesized and studied in this work, have displayed capability to this application.